Key Points:

- Hematite with/without cation substitution can be identified and quantified effectively by combining magnetic and color spectral analyses
- Hematite can be useful for reconstructing paleoclimate variations on Earth
- Terrestrial hematite may be analogous to Martian hematite and provide evidence for the former presence of water on Mars

Correspondence to:

Z. Jiang and Q. Liu,
jiangzhaoxia@ouc.edu.cn;
qsliu@sustech.edu.cn

Author Contributions:

Writing – original draft: Qingsong Liu, Andrew P. Roberts, Mark J. Dekkers, Vidal Barrón, José Torrent, Sanzhong Li

The Magnetic and Color Reflectance Properties of Hematite: From Earth to Mars

Zhaoxia Jiang[1,2] , Qingsong Liu[2,3], Andrew P. Roberts[4] , Mark J. Dekkers[5] , Vidal Barrón[6] , José Torrent[6], and Sanzhong Li[1,2]

[1]Frontiers Science Center for Deep Ocean Multispheres and Earth System, Key Laboratory of Submarine Geosciences and Prospecting Techniques, Ministry of Education, College of Marine Geosciences, Ocean University of China, Qingdao, China, [2]Laboratory for Marine Geology, and Laboratory for Marine Mineral Resources, Qingdao National Laboratory for Marine Science and Technology, Qingdao, China, [3]Southern University of Science and Technology, Shenzhen, China, [4]Research School of Earth Sciences, Australian National University, Canberra, ACT, Australia, [5]Department of Earth Sciences, Faculty of Geosciences, Utrecht University, Utrecht, The Netherlands, [6]Departamento de Agronomía, Universidad de Córdoba, Edificio C4, Campus de Rabanales, Córdoba, Spain

Abstract Hematite is a canted antiferromagnet with reddish color that occurs widely on Earth and Mars. Identification and quantification of hematite is conveniently achieved through its magnetic and color properties. Hematite characteristics and content are indispensable ingredients in studies of the iron cycle, paleoenvironmental evolution, paleogeographic reconstructions, and comparative planetology (e.g., Mars). However, the existing magnetic and color reflectance property framework for hematite is based largely on stoichiometric hematite and tends to neglect the effects of cation substitution, which occurs widely in natural hematite and influences the physical properties of hematite. Thus, magnetic parameters for stoichiometric hematite are insufficient for complete analysis of many natural hematite occurrences and can lead to ambiguous geological interpretations. Remagnetization, which occurs pervasively in red beds, is another ticklish problem involving hematite. Understanding red bed remagnetization requires investigation of hematite's formation and remanence recording mechanisms. We elaborate on the influence of cation substitution on the magnetic and color spectral properties of hematite, and on identifying hematite and quantifying its content in soils and sediments. Studies of remagnetization mechanisms are discussed, and we summarize methods to discriminate between primary and secondary remanences carried by hematite in natural samples to aid primary remanence extraction in partially remagnetized red beds. Although there remain unknown properties and unresolved issues that require future work, recognition of the properties of cation-substituted hematite and remagnetization mechanisms for hematite will aid identification and interpretation of the magnetic signals that it carries, which is environmentally important and responsible for magnetic signals on Earth and Mars.

Plain Language Summary Hematite is red in powdered form and is a common magnetic mineral on Earth and Mars. It carries significant information on ancient climates and environments. Well-dated terrestrial hematite records enable detailed monsoon reconstructions while hematite occurrences on Mars tend to be interpreted as associated with the former presence of water. Hence, hematite-bearing regions are considered key to the search for potential ancient life on Mars. Hematite can have stable magnetizations, so hematite-bearing rocks are key targets for tectonic reconstructions. Identification and quantification of hematite is conveniently achieved through its magnetic and color properties. However, two major hurdles in hematite studies include cation substitution and remagnetization. The former can strongly affect its physical properties, while the latter evidently complicates geological interpretation of the natural remanent magnetization carried by hematite. Here, we review the influence of cation substitution on the magnetic and color spectral properties of hematite and summarize methods for its identification and quantification in nature by combining magnetic and color spectral analyses. In addition, we summarize remagnetization mechanisms and illustrate methods to discriminate primary and remagnetized remanences carried by hematite. Finally, current challenges pertaining to hematite research on Earth and Mars are highlighted along with discussion of future avenues for how to resolve these issues.

1. Introduction

Hematite (α-Fe_2O_3) derives its name from the Greek *haimatite* meaning blood-like, which refers to its distinct red color (Morrish, 1994). Hematite is one of the most widely occurring iron oxides on Earth, Mars, the Moon, and some asteroids (S. Li, Lucey, et al., 2020; Y. Li, Yang, et al., 2020), and is significant in environmental studies of soils and sediments (Barrón & Torrent, 2013; Colombo et al., 2017; Cornell & Schwertmann, 2003; Deng et al., 2006; Schwertmann, 1985, 1988, 1993; Torrent et al., 1980). It is also responsible for the natural remanent magnetization (NRM) carried by most "red beds"—the red sandstones and shales that have been a major paleomagnetic data source in classic plate tectonic reconstructions (Collinson, 1966, 1974; Løvlie & Torsvik, 1984; Walker, 1967a, 1967b; Walker et al., 1981). In addition, hematite is the dominant iron oxide in subducted rocks at depths of 300–600 km (Kupenko et al., 2019) when magnetite has decomposed thermally (Woodland et al., 2012). This observation is relevant when inverting geomagnetic data in crustal magnetic anomaly studies (Y. Li & Oldenburg, 1996), especially in studies of planetary bodies that no longer have a dynamo, such as Mars (Stevenson, 2001). Hematite is also abundant as a nanophase reddish pigment that covers much of the surface of Mars (Allen et al., 2001, 2004; Christensen, Bandfield, Clark, et al., 2000; Christensen et al., 2001; R. V. Morris & Golden, 1998; R. V. Morris et al., 1993) and as coarse-grained crystalline gray specular hematite that is an important contributor to magnetic anomalies on Mars (Catling, 2004; Chan et al., 2004; R. Morris et al., 2005).

Hematite formation is controlled largely by surface environmental conditions (e.g., temperature, humidity/aridity; Dong et al., 2009; Schwertmann & Cornell, 2000; Schwertmann & Murad, 1983; Šubrt et al., 2000; Sugimoto & Wang, 1998). Thus, concentration and magnetic property variations of hematite are important proxies for geological processes and environmental evolution (Balsam et al., 2004; Ji et al., 2004; Jiang et al., 2012; Jiang, Liu, Dekkers, et al., 2014; Z. Liu et al., 2013). This makes hematite a critically important mineral in paleoenvironmental, iron cycle, tectonic, and comparative planetology studies (Bailey et al., 2011; Dunlop & Kletetschka, 2001; Ge et al., 2017; Kletetschka et al., 2000a, 2000b, 2000c; K. P. Kodama, 2012; Q. Liu et al., 2012; Tan et al., 2003).

Hematite has a hexagonal crystal structure in which alternating planes contain Fe^{3+} ions that are magnetized in almost opposite directions (Dzyaloshinsky, 1958; Moriya, 1960). Slight departure ($\sim$0.065°) from perfectly antiparallel spins, or spin canting, gives rise to its magnetization (Morrish, 1994). This changes hematite from an ideal antiferromagnetic mineral with no net magnetization to an imperfect antiferromagnet with a weak spontaneous magnetization of $\sim$0.4 $Am^2\,kg^{-1}$ and a Curie temperature of $\sim$675°C (Aharoni et al., 1962; Lin, 1959, 1960; Morrish, 1994). Thus, although its magnetization is more than 200 times weaker than that of magnetite, the contribution of hematite to magnetic anomalies cannot be ignored (Dunlop & Kletetschka, 2001; Kletetschka et al., 2000a, 2000b, 2000c). In addition, hematite has characteristic color reflectance properties, that is, peaks in diffuse reflectance spectroscopy (DRS) second derivative curves (Torrent & Barrón, 2003, 2008; Torrent et al., 1983). As instrument precision increases, considerable attention has been paid to understanding magnetic and color information carried by hematite on Earth and Mars (Fabian et al., 2011; Jacob & Abdul Khadar, 2010; Lu & Meng, 2010; Özdemir & Dunlop, 2014; Reufer et al., 2011; Suber et al., 2010; Tadić et al., 2011), which is valuable for understanding magnetic properties, structure, identification, and quantification of hematite in environmental, tectonic, and planetary studies (Allen et al., 2001; Bercoff & Bertorello, 2010; C. Liu, Deng, et al., 2007; Chan et al., 2004; Hargraves et al., 2000; Harrison et al., 2010; Jacob & Abdul Khadar, 2010; Kletetschka & Wasilewski, 2002; R. Morris et al., 2005; Özdemir & Dunlop, 2005, 2006; Özdemir et al., 2008; Robinson et al., 2002; S. Ono et al., 2004, 2011; S. A. McEnroe, Robinson, & Panish, 2001). However, much of this magnetic property framework is based on stoichiometric hematite. In natural hematite, other cations (e.g., Al, Ti, etc.) are invariably present in either single crystal or polycrystalline particles (Cornell & Schwertmann, 2003; Nagata & Akimoto, 1956). Furthermore, the color and magnetic properties of hematite may change, either slightly or significantly, depending on the substituted cation and on the parameter of interest (Barrón & Torrent, 1984; Jiang, Liu, Colombo, et al., 2014; Jiang, Liu, Dekkers, et al., 2016; Jiang et al., 2012, 2013; Liu, Roberts, et al., 2007; Morrish, 1994; Wells et al., 1999). Typical magnetic and color parameters for "pure" hematite do not apply readily to cation-substituted hematite and may lead to ambiguous geological interpretations (Jiang, Liu, Colombo, et al., 2014; Jiang, Liu, Dekkers, et al., 2014; Jiang et al., 2012; P. Hu et al., 2016; Q. Liu et al., 2011).

In addition to issues involving the usefulness of the existing magnetic parameter framework for studying naturally variable hematite, remagnetization is a further issue in research involving hematite. Remagnetization can be pervasive in red beds and complicates the geological interpretation of paleomagnetic data (Creer, 1968; E. Cox

et al., 2005; Kent et al., 1987; McCabe & Elmore, 1989; Van der Voo & Torsvik, 2012). In red beds and some hematite-bearing carbonate rocks, hematite has two modes of occurrence: fine-grained pigment and coarser detrital (specular) particles. The former is the most frequent carrier of a chemical remanent magnetization (CRM) in red beds and can overprint a detrital remanent magnetization (DRM) carried by primary hematite and lead to remagnetization (Tauxe & Kent, 1984; Tauxe et al., 1980). Therefore, discriminating between DRM and CRM is central to red bed paleomagnetism (Iosifidi et al., 2010; Jiang, Liu, Dekkers, et al., 2015; Jiang et al., 2017; Van der Voo & Torsvik, 2012). However, to develop methods to recognize and isolate different NRM types, the hematite formation process and accompanying remanence recording processes should be investigated. In addition, hematite formation mechanisms, magnetic recording, and shock impact effects on its magnetic properties are significant for paleoclimatic, magnetic field, and tectonic studies of Mars. Hematite studies have, thus, been extended to Martian environments to assess the presence of water and potential for life and a former Martian magnetic field and dynamo action expressed by crustal magnetic anomalies (e.g., Fraeman et al., 2013; Grotzinger et al., 2015; Haberle et al., 2017; Mangold et al., 2016; R. Morris et al., 2005; Sato et al., 2018; Thomas et al., 2018).

To address many of the issues listed above, we combine chemical synthesis, magnetic, and color reflectance methods with systematic investigation of synthetic and natural hematite samples (Jiang, Liu, Colombo, et al., 2014; Jiang, Liu, Dekkers, et al., 2014; Jiang, Liu, Dekkers, et al., 2015; Jiang, Liu, Dekkers, et al., 2016; Jiang, Liu, Zhao, et al., 2015; Jiang, Liu, Zhao, et al., 2016; Jiang et al., 2012, 2013, 2017, 2018). It is now timely to provide a detailed overview of the magnetic and color spectral properties of hematite. We elaborate systematically on the influence of cation substitution on the magnetic and color reflectance properties of hematite and summarize methods to identify and quantify hematite in soils and sediments by combining magnetic and color reflectance properties. In addition, remagnetization mechanisms of red beds are discussed based on laboratory modeling and natural sample analyses, with a summary of the methods available to discriminate between CRM and DRM or thermal remanent magnetization (TRM) carried by hematite in natural samples. This is critical for extracting primary NRM signals from (partially) remagnetized red beds. Also, the high-pressure magnetic behavior of hematite from laboratory experiments is assessed in relation to impacts of cosmic material on Mars. Based on all of the above, the implications of signals due to hematite in environmental, tectonic, Earth interior, and planetary (particularly Mars) studies are discussed. Finally, we discuss remaining unknown properties and issues concerning hematite that require future work. For example, is hematite on Earth and Mars comparable? Is hematite on Mars also cation-substituted? If so, how can we quantify cation contents? Can this be done with a color reflectance spectrometer on a Mars lander or orbiter? Are weak magnetic anomalies on Mars due to a former weak dynamo field or did they result from impact demagnetization? We summarize progress on these issues and focus on major outstanding questions associated with hematite in environmental magnetism, paleomagnetism, tectonics, paleoclimate, soil science, and comparative planetology.

2. Hematite Occurrences and Formation on Earth and Mars

Hematite and other ferric iron oxides and oxyhydroxides occur widely on Earth and Mars and form via diverse processes. Understanding hematite formation pathways is critical for interpreting information carried by hematite in terms of climate, environment, tectonics, and planetary evolution. Hematite occurrences and formation pathways are, thus, discussed at length throughout the rest of this section.

2.1. Forms of Iron Oxyhydroxide (FeOOH) and Fe_2O_3

In nature, there are six polymorphs of iron oxyhydroxide (FeOOH) and three of Fe_2O_3; the oxyhydroxides can be dehydroxylated to their oxide counterparts (Cornell & Schwertmann, 2003). The dominant oxyhydroxides include: goethite (α-FeOOH), akaganéite (β-FeOOH), lepidocrocite (γ-FeOOH), feroxyhyte (δ-FeOOH), ferrihydrite ($Fe_5HO_8 \cdot 4H_2O$), and green rusts ($Fe^{3+}_xFe^{2+}_y(OH)_{3x+2y-z}(A^-)_z$), where A is Cl, CO_3^{2-}, or SO_4^{2-}. Goethite is one of the thermodynamically most stable iron oxides at ambient temperatures, and it is either the first well-crystalline oxide to form or the final product after many transformations. Pure goethite powder is typically yellow and is responsible for the yellowish color of many rocks and soils (Hao et al., 2009). Fine grained goethite is beige-brown, while Mn substituted goethite can be blackish (Cornell & Schwertmann, 2003). Orange-colored lepidocrocite occurs in rocks, soils, and rust, and is often an oxidation product of Fe^{2+} bearing minerals (Schwertmann & Cornell, 2000). Akaganéite occurs rarely in nature and is found mainly in Cl-rich environments such as hot brines and in rust in marine environments (Bishop et al., 2015; Remazeilles & Refait, 2007). In contrast,

the reddish-brown ferrihydrite is widespread in surface environments (Jambor & Dutrizac, 1998). It exists exclusively as nanocrystals; unless it is stabilized in some way, it transforms with time into more stable iron oxides (Hiemstra, 2018). Ferrihydrite is, thus, an important precursor of more stable, more crystalline Fe oxides (Jiang et al., 2018). Green rusts form as corrosion products and are a group of Fe oxides consisting of layers of $Fe^{2+}OH$ octahedra in which some Fe^{2+} is replaced by Fe^{3+}. To maintain charge neutrality, anions, especially Cl^- and SO_4^{2-}, are bound between layers (Génin et al., 2002).

The dominant Fe_2O_3 polytypes are hematite (α-Fe_2O_3), maghemite (γ-Fe_2O_3), and ε-Fe_2O_3 (Cornell & Schwertmann, 2003). Hematite is extremely stable and is often the end member of transformations of other iron oxides. Maghemite has a cubic crystal structure and occurs in soils as a weathering product of magnetite (Fe_3O_4) or as a heating product of other Fe oxides, usually in the presence of organic matter. ε-Fe_2O_3 occurs in disordered pure forms and in ordered forms along with hematite or maghemite. ε-Fe_2O_3 is orthorhombic (Tronc et al., 1998) and has a broad geographical distribution in bricks and baked clays (McIntosh et al., 2011) with high coercivity and low Curie temperature (López-Sánchez et al., 2017; McIntosh et al., 2007). ε-Fe_2O_3 can transform to hematite at 500°C–750°C depending on the preparation method.

2.2. Hematite Occurrences on Earth and Mars

Hematite is one of the most widely occurring iron oxides in nature; it is distributed widely in red soils, red beds, marine sediments, and wind-blown dust on Earth and Mars (Figure 1). On Earth, hematite is abundant in many aerobic soils under warm, humid climates or in sediments of various ages in tropical and subtropical areas (Figures 1b–1d; Van Houten, 1968, 1973; Walker, 1967a; Walker et al., 1981). Hematite also occurs in Archean and Paleoproterozoic banded iron formation (BIF; Figure 1e) sediments that record evolution of Earth's early atmosphere and ocean (Cloud, 1973; Hoashi et al., 2009; Klein, 2005). Moreover, hematite is the dominant pigment in oceanic red beds (Figure 1a), which are reddish to pinkish pelagic marine sedimentary rocks (Wang et al., 2004, 2005) that document global oceanic and climate changes during the Cretaceous greenhouse world (X. Hu, Scott, et al., 2012). High pressure and temperature experiments on hematite and its polymorphs suggest that they can be dominant magnetic carriers down to ∼600 km depth, that is, in (cold portions of) subducted slabs (Ferré et al., 2021; Kupenko et al., 2019). Two dominant kinds of hematite, specular grains and red pigment, occur in soils and red beds. Fine-grained chemically formed hematite pigment is responsible for the characteristic red bed color; it is the dominant magnetic carrier in some red beds in warm, humid climates (Robb, 1949; Torrent & Schwertmann, 1987; Van Houten, 1968; Walker, 1967a). Detrital hematite, black specularite, is typically coarser-grained and may record the primary NRM of certain red beds (Van der Voo & Torsvik, 2012).

Hematite is the most common pigment and magnetic mineral on the surface of Mars and is responsible for its nickname as the "Red Planet." Hematite on Mars occurs in three forms with different physicochemical and spectral properties: nanophase, red crystalline, and gray crystalline hematite (R. V. Morris et al., 1985, 1989). The former two are the dominant contributors to the eye-catching color of bright regions of Mars (Figure 1f; R. V. Morris et al., 1989, 1993, 1997). In contrast, gray hematite is absent in visible/near-IR (VNIR) spectra for Fe^{3+}-containing bright regions on Mars. Significant gray hematite deposits are inferred to exist from spectra from Sinus Meridiani (2°S and 4°W), Aram Chaos (2°N and 21°W), and numerous smaller areas in Valles Marineris, covering areas of >175,000, ∼5,000, and 25–800 km², respectively (Figure 2; Christensen, Bandfield, Clark, et al., 2000; Christensen, Bandfield, Hamilton, et al., 2000; Christensen, Bandfield, Smith, et al., 2000; Christensen et al., 2001). Two other small gray hematite-rich regions have been identified at Aureum (4.4°S and 333.0°E) and Iani (2.0°S and 342.3°E) Chaos using thermal emission spectroscopy (TES) and Thermal Emission Imaging System data (Glotch & Rogers, 2007). *In situ* images from the Mars Exploration Rover "Opportunity" indicate that hematite in Sinus Meridiani occurs as spherical balls, typically a few millimeters in diameter and embedded in rock outcrops like "blueberries in muffins" (Figure 1g; Catling, 2004; Chan et al., 2004). Specifically, hematite has been detected by miniature TES in spherical particle accumulations on a sulphate-rich outcrop surface and in channel lag deposits in Meridiani Planum (Bell et al., 2004; Christensen et al., 2004; Herkenhoff et al., 2004; Squyres et al., 2004). Spherules embedded in the outcrop have a 4.2 ± 0.8 mm mean diameter (McLennan et al., 2005). Gray hematite consists of crystalline particles >10 μm in diameter or polycrystalline aggregates of such particles (R. V. Morris et al., 1989), and is distributed throughout the spherules rather than forming concentric surface shells (McLennan et al., 2005).
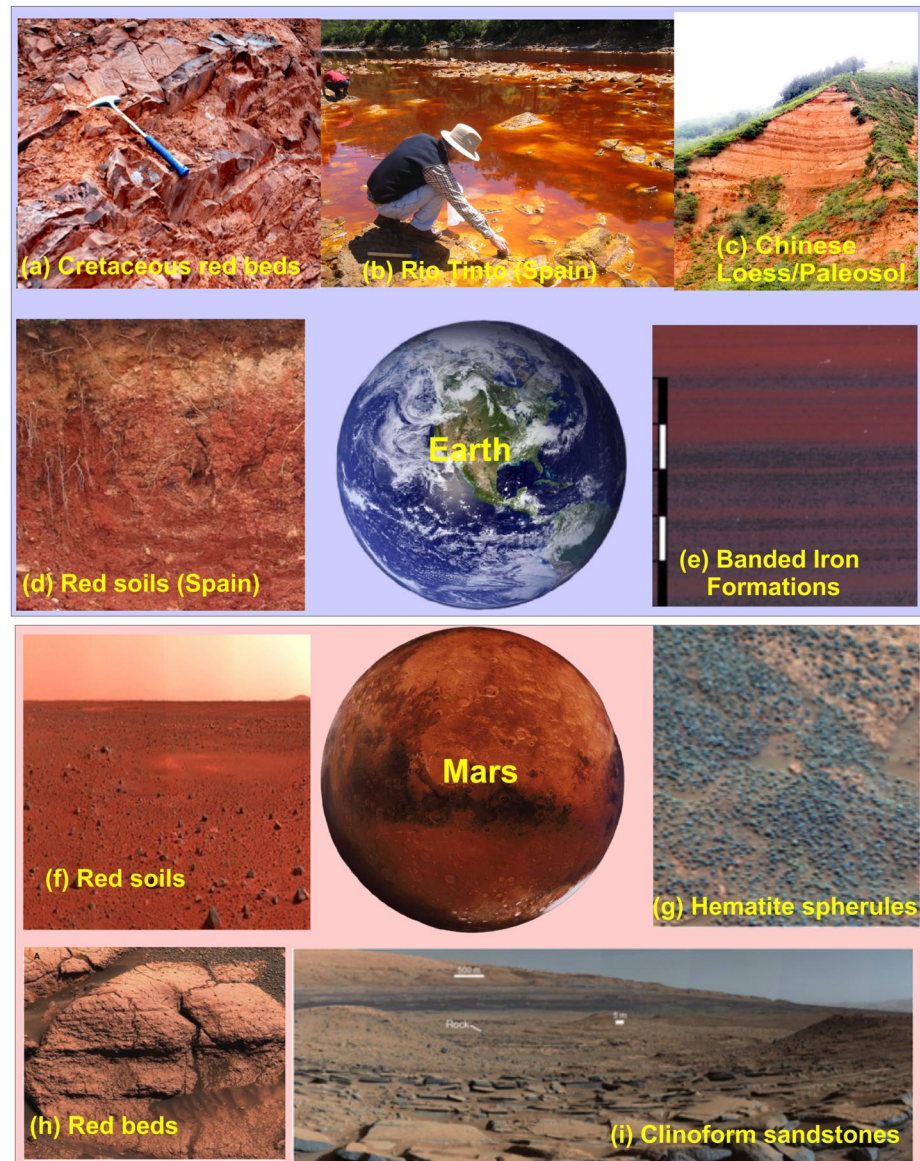
Figure 1. Hematite-rich environments on Earth and Mars. (a) Late Cretaceous red beds from Fenghuoshan Group in the Hoh Xil Basin, Tibetan Plateau (provided by Dr. Chunsheng Jin); (b) iron oxides in leachates from acid mine drainage, Rio Tinto, Spain (provided by Vidal Barrón); (c) Weinan loess/paleosol profile, Chinese Loess Plateau (provided by Dr. Chunsheng Jin); (d) iron oxide enriched horizons in an Acrisol, Spain (provided by Vidal Barrón); (e) banded iron formation, Mamatwan Manganese Mine, Hotazel, Northern Cape Province, South Africa (from Posth et al. (2011)); (f) Martian red soils (from NASA) and (g) hematite spherules (from Bell et al. (2004)); (h) red beds from a mosaic image, El Capitan (from Squyres et al. (2004)); and (i) clinoform sandstones from an ancient lake deposit, Gale crater, Mars (from Grotzinger et al. (2015)).

2.3. Hematite Formation Cycle on Earth and Mars

On Earth and Mars, three dominant pathways occur for hematite formation (Figure 3). The first is crystallization from solution (labeled I in Figure 3), which can occur by (a) direct precipitation from hydrolysis of Fe^{3+}- or Fe^{2+}-rich fluids (Schwertmann & Cornell, 2000) or (b) hydrothermal transformation of precursor ferrihydrite in soils (Cornell & Schwertmann, 2003), aerobic sedimentary environments (Drodt et al., 1997; Eren & Kadir, 1999; Spencer & Percival, 1952; Van der Zee et al., 2003), iron-rich waters, which are typical of BIFs (Klein, 2005; Posth et al., 2011), or hot spring deposits (Wade et al., 1999). The second pathway is dehydroxylation of Fe oxyhydroxides at high temperatures (labeled II in Figure 3), for example, during lava baking, burning of coal measures (de Boer, Dekkers, & Van Hoof, 2001), or forest fires (Iglesias et al., 1997; Ketterings et al., 2000;

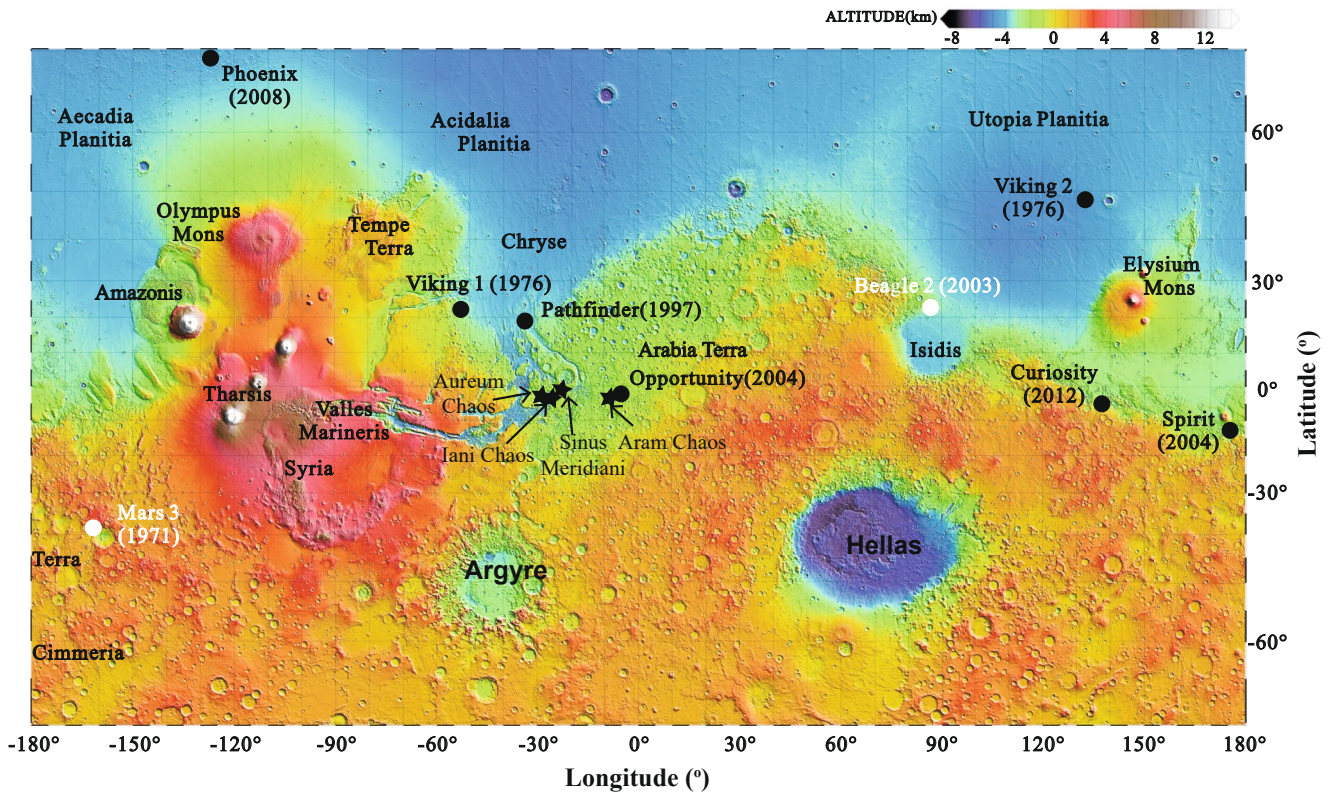**Figure 2.** Global topographic map of Mars from Mars Orbit Maser Altimeter data with major surface features labeled. Black and white dots are spacecraft landing sites.
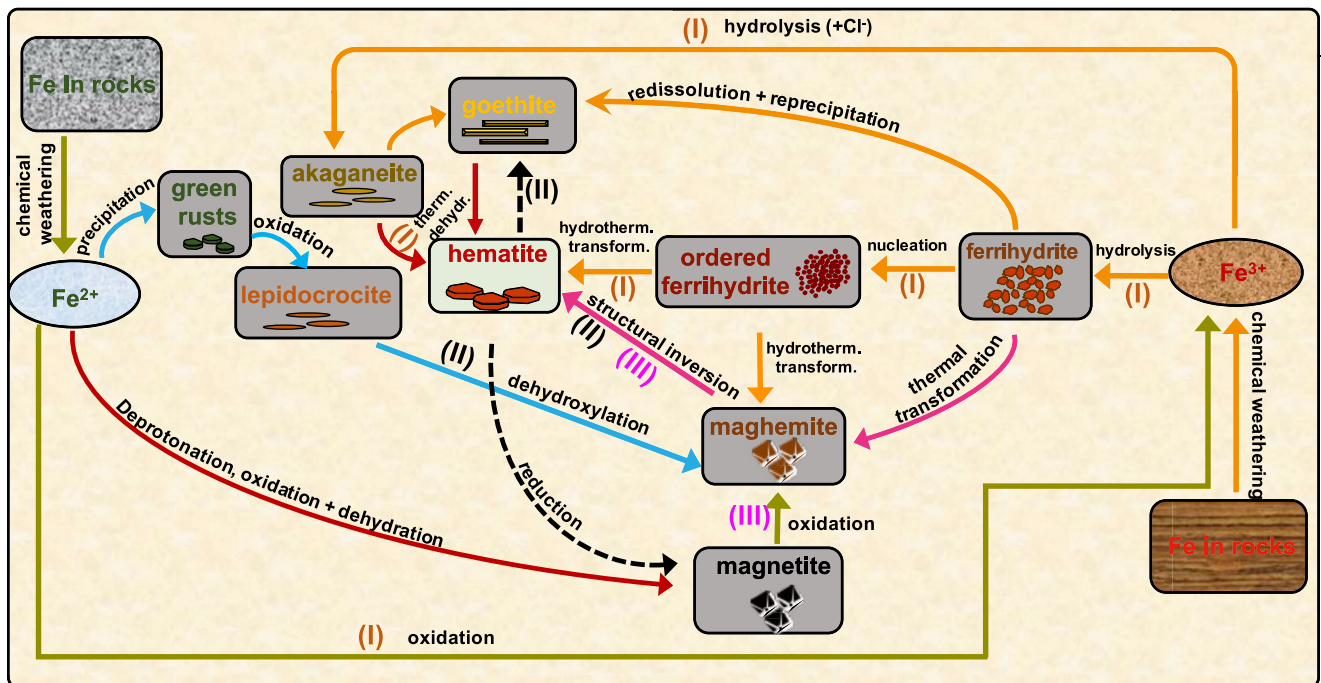

Figure 3. Schematic illustration of formation and transformation pathways of common iron oxides, where *therm. dehydr.* and *hydrotherm. transform.* are abbreviations for thermal dehydroxylation and hydrothermal transformation.

Nornberg et al., 2009). The third pathway is via magnetite oxidation or maghemite inversion at ambient temperatures (labeled III in Figure 3), which occurs widely in soils and sediments (e.g., Chen et al., 2005, 2010; Dunlop & Özdemir, 1997). Hematite formation is controlled by many geological processes, so its abundance and magnetic and color properties are important proxies in studies of geological and environmental processes. Therefore, determining its properties is useful in studies of paleoenvironmental evolution, the iron cycle, marine biology, tectonics, and comparative planetology.

2.3.1. Hematite Formation From Hydrolysis of Iron-Rich Solutions

Precipitation of ultra-fine hematite from iron-rich solutions in the pore spaces of clastic sediments produces the distinctive purple to red hues of red beds (Dunlop & Özdemir, 1997; Walker, 1967a). In deep-sea sediments, hematite occurs mainly in oxidizing environments, so it is a useful indicator of such conditions, and it eventually dissolves in reducing conditions (Roberts, 2015). Its abundance decreases from typically ~20 wt% of the total Fe-oxide population near the sediment surface to about zero at the Fe^{3+}-Fe^{2+} redox boundary, which results in a sediment color change from brown/red to green (Drodt et al., 1997; Eren & Kadir, 1999; Lyle, 1983). Precambrian BIFs formed via diagenesis (biologically driven and below 120°C) and by subsequent metamorphism (abiogenically at higher temperatures; Klein, 2005; Köhler et al., 2013; Konhauser et al., 2005; Posth et al., 2013; Rasmussen et al., 2014). Deposition of Fe-rich layers in BIFs requires certain geochemical conditions and processes to have occurred in Archean-Paleoproterozoic oceans. Fe^{3+} is poorly soluble in oxic seawater at circumneutral pH, so ancient oceans must have been anoxic to transport significant dissolved Fe^{2+} to BIF deposition sites (Cornell & Schwertmann, 2003; Halama et al., 2016). On the Martian surface, most hematite is thought to have been formed from Fe-rich aqueous fluids under ambient conditions or from hydrothermal fluids. The presence of crystalline hematite has been suggested to provide evidence for aqueous environments on Mars (Christensen, Bandfield, Clark, et al., 2000; Christensen et al., 2001; Yoshida et al., 2018).

Once Fe^{3+} ions appear in solution due to dissolved Fe^{2+} oxidation, they are likely to form poorly crystalline hydrous ferric oxide gels or ferrihydrite through hydrolysis (Figure 3; Burns, 1993a; Schwertmann & Cornell, 2000). Subsequently, the gels age to different crystalline phases depending on the oxidation rate of dissolved Fe^{2+} to Fe^{3+}, Fe^{3+} ion concentration, the nature of anions present, pH, temperature, and aging time (Gálvez et al., 1999; Schwertmann & Cornell, 2000; Schwertmann & Murad, 1983; Schwertmann et al., 2000; Torrent et al., 1982). Ferrihydrite forms initially by hydrolysis of Fe^{3+} ions and ages to form goethite, hematite, or mixtures of the two, depending on pH, temperature, and soil moisture (Guyodo et al., 2003; Schwertmann & Murad, 1983). Hematite formation is favored at elevated temperatures, low water activity, and neutral pH, whereas goethite predominates at both low temperature and high pH. Ambient magnetic fields can also play a role in hematite versus goethite growth from ferrihydrite. Hematite and goethite mixtures are obtained in fields <~60 μT; higher fields favor hematite formation by accelerating magnetic ferrihydrite aggregation (Jiang, Liu, Dekkers, et al., 2016). Carbonate can enhance ferrihydrite transformation to hematite by buffering the pH at ~7–8, which is critical for understanding the fate and transport of carbonate and Fe^{3+}-bearing mineral transformation (Y. Li, Yang, et al., 2020).

Investigations of hematite formation have proposed a transformation pathway of ferrihydrite → a maghemite-like mineral → hematite (Barrón & Torrent, 2002; Gutiérrez et al., 2016; L. Cao et al., 2017; Michel et al., 2010; Q. Liu et al., 2008). The intermediate ferrimagnetic maghemite-like phase (originally proposed to be hydromaghemite) was considered an important contributor to soil magnetic enhancement (Barrón et al., 2003). However, it was later suggested to be a ferrimagnetically ordered ferrihydrite (Michel et al., 2010), or a core-shell structured ferrihydrite (Hiemstra, 2018; L. Cao et al., 2017). Torrent et al. (2006, 2007) ascribed correlation between the amount of the pedogenic maghemite-like phase and hematite contents to multiple factors, including prevailing climate, chemical environment (e.g., sorbed ligands and organic acids), and degree of weathering. Concentration variations of these two minerals are, therefore, used widely as climatic or environmental proxies (J. M. Sun et al., 2008; Z. Liu et al., 2013). However, the results of Jiang et al. (2018) suggest that this ferrihydrite-hematite conversion is not a simple three-stage process, but a more complex five-stage process. The five stages are: (I) formation of magnetically ordered (or core-shell structured) superparamagnetic (SP) ferrihydrite, (II) rapid hematite formation from SP ferrihydrite, (III) relative hematite stabilization, (IV) maghemite nanoparticle neoformation, and (V) complete transformation from maghemite to hematite (Figure 4). Unlike previous models in which pedogenic maghemite forms mainly in stages I and II, it forms dominantly in stage IV of the model of Jiang et al. (2018). Iron oxide growth under natural conditions occurs mainly via an aggregation-based nucleation pathway (Banfield et al., 2000). Recrystallization and transformation are enhanced by particle aggregation, which
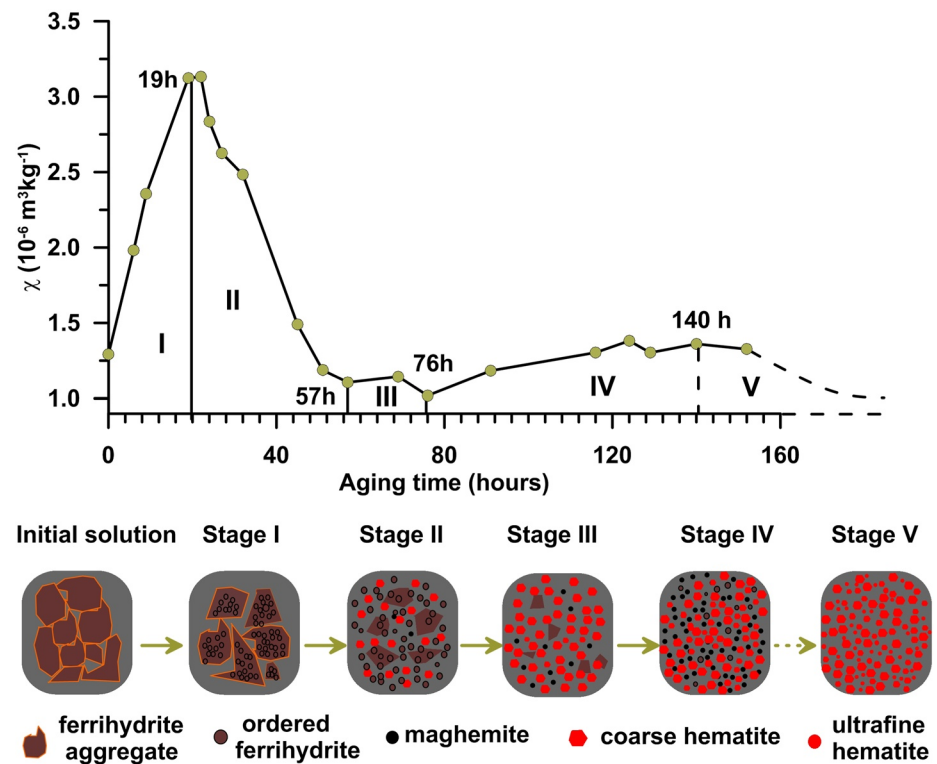
Figure 4. Five-stage model for transformation of ferrihydrite to hematite from magnetic susceptibility (χ) versus aging time (from Jiang et al. (2018)). The initial solution contains fresh ferrihydrite aggregates. Stage I: fresh ferrihydrite is magnetically ordered and transforms into ferrimagnetic ferrihydrite. Stage II: magnetically enhanced ferrihydrite particles convert abruptly to SD hematite. Stage III: massive SD hematite formation. Stage IV: the remaining ferrihydrite transforms to ultrafine maghemite. Stage V: maghemite transforms ultimately to fine-grained hematite after strong weathering (stage V). Stage V is inferred and was not detected directly by Jiang et al. (2018) (dashed line in the magnetic susceptibility aging curve).

is controlled by many factors, for example, initial precipitate content, ligands, pH, temperature, oxygen, etc. (Burns, 1993a; Penn, 2004; Schwertmann et al., 1999). In near-neutral and alkaline solutions, reaction kinetics are so rapid that dissolved Fe^{3+} is removed almost instantaneously. Therefore, in early stages, abundant ferrihydrite forms in aggregates with sizes of a few nanometers and recrystallizes to form ferrimagnetic ferrihydrite, which dehydrates rapidly to larger hematite particles (Michel et al., 2010). Hematite is produced in larger quantities when ferrihydrite supply is abundant in stages I and II of Jiang et al. (2018), which is consistent with results for soils where the parent material determines the amount of magnetic mineral produced during pedogenesis (Boyle et al., 2010). However, after stage III of Jiang et al. (2018), few ferrihydrite clusters remain and ferrimagnetic ferrihydrite transforms preferentially into ultrafine maghemite rather than hematite. Maghemite concentration builds up rapidly with a decreasing precursor concentration (Ayyub et al., 1988) because less entropy is needed for ultrafine maghemite formation compared to hematite, which may be the reason why maghemite exists as ultrafine particles (McHale et al., 1997; Navrotsky et al., 2008). This is why maghemite particles are also produced during nanocrystalline hematite synthesis (Ayyub et al., 1988). However, maghemite will transform to hematite eventually because of its metastability (Özdemir & Dunlop, 1988). This transformation pathway provides clues for maghemite and hematite co-formation on Earth and Mars.

2.3.2. Hematite Formation via Dehydroxylation of Fe Oxyhydroxide (FeOOH)

The second hematite formation pathway is by thermal dehydroxylation or mechanochemical decomposition of a precursor Fe oxyhydroxide (i.e., $2FeOOH \rightarrow Fe_2O_3 + H_2O$; Figure 3), which is considered the main hematite formation pathway in sedimentary rocks during burial and metamorphism (de Boer & Dekkers, 2001; Dekkers, 1990; Gendler et al., 2005; González et al., 2000; Rendón et al., 1983). Goethite is thermodynamically less stable than hematite, and is expected to dehydroxylate to hematite during burial (Langmuir, 1971). At moderate depths (e.g., 5 km), water is either bound in chemical compounds or adsorbed onto grains within sediments.

All compounds that consist of a combined volatile and solid phase exert a vapor pressure as a function of temperature, pressure, and grain size. Goethite dehydroxylation and hematite recrystallization will occur at a depth where the geotherm intersects the dehydration line for bound water (Catling & Moore, 2003). High temperatures, such as those experienced during wildfires or movement of hot lava flows (on Earth and Mars), can also trigger goethite dehydration to hematite (Iglesias et al., 1997; Ketterings et al., 2000; Nornberg et al., 2009). In addition, mechanical grinding can induce goethite transformation to hematite through the impact of forces, attrition, shear, and compression (e.g., González et al., 2000; Lemine, 2014; Rendón et al., 1983).

Despite the above, intricacies of the dehydration process remain disputed. At low pressures (<1 kbar), temperatures between 70°C and 130°C are sufficient for goethite to transform to hematite in the presence of saturated water vapor (Bischoff, 1969; Johnston & Lewis, 1983), which is consistent with temperatures deduced for coarse hematite formation in the best-preserved ancient terrestrial BIFs. The transition temperature differs from the dehydration temperature required to transform a dry goethite powder into hematite because in aqueous systems, crystal growth lowers the transition temperature (Pollack et al., 1970; R. V. Morris & Lauer, 1981). Differential thermal analysis and differential scanning calorimetry results indicate a conversion temperature of 175°C–400°C or higher, which depends on cation substitution in goethite (e.g., Al substitution stabilizes goethite; Fey & Dixon, 1981), while Gialanella et al. (2010) found that recrystallization and partial sintering of hematite occurs only >800°C, with coarser crystalline material reacting at higher temperatures.

In addition, goethite dehydr(oxyl)ation involves removal of hydrogen and one-quarter of the oxygen, without disturbing the network of remaining oxygen, and atomic rearrangement of Fe^{3+}, to form hematite: $2\alpha\text{-FeOOH} \rightarrow \alpha\text{-Fe}_2\text{O}_3 + \text{H}_2\text{O}$. Watari, Delavignette, and Amelinckx (1979) proposed, based on X-ray diffraction (XRD) data, that this transformation involves direct goethite dehydration to hematite without an intermediate phase. Walter et al. (2001) argued that the so-called intermediate hydrohematite described in the literature (e.g., Gualtieri & Venturelli, 1999; Wolska & Schwertmann, 1989) does not exist as a discrete intermediate during dehydration from goethite to hematite; instead they observed a dependence of the dehydration mechanism on particle size. Prasad et al. (2006) and W.-J. Zhang et al. (2010) confirmed that no intermediate phase exists during the transformation through in situ Fourier transform infrared spectroscopy analysis and molecular dynamics simulations, respectively. However, Özdemir and Dunlop (2000) found that an intermediate magnetite forms during the transformation. Thus, formation of intermediate products in the goethite-hematite reaction remain disputed. These studies were conducted on pure goethite without considering other ions, for example, Al, which is ubiquitous in nature and can significantly influence the behavior of newly formed minerals (Jiang, Liu, Colombo, et al., 2014; Jiang et al., 2012).

In contrast to the goethite-hematite transformation, there is consensus on the mechanism for lepidocrocite transformation. Clear phase transformations occur as follows: lepidocrocite → maghemite → hematite (Özdemir & Dunlop, 1993). This pathway has been cited as a possible explanation for magnetic enhancement of Chinese paleosol/loess samples during heating at ~280°C (Deng et al., 2001). It is also considered to be the dominant mode of maghemite and hematite formation in Martian soils (Torrent & Barrón, 2000). Gendler et al. (2005) showed that some maghemite transforms rapidly to hematite, so the intermediate phase production/destruction is a dynamic simultaneous rather than consecutive process. Acicular hematite formation from goethite or lepidocrocite dehydroxylation has received much attention due to its application in materials science (Watari, Delavignette, & Amelinckx, 1979; Watari, Van Landuytet al., 1979; Watari et al., 1983). Acicular hematite has a substantially higher coercivity and lower magnetization compared to chemical precipitates from solution (Dekkers, 1990; Dunlop, 1971; Jiang et al., 2012).

2.3.3. Hematite Formation via Oxidation of Ferrimagnetic Phases

The third hematite formation pathway involves low and high temperature oxidation (Figure 3). Magnetite oxidation and maghemite transformation are ubiquitous in soils and igneous rocks. Hematite particles that preserve the characteristic (1 1 1) planes of magnetite after pseudomorphous transformation to hematite are named martite (e.g., Steiner, 1983). Low temperature oxidation of magnetite to maghemite is a topotactic reaction, as is the subsequent inversion of maghemite to hematite (Dunlop & Özdemir, 1997). This has been confirmed experimentally where hematite forms first on edges and surfaces of maghemite formed by oxidation of eolian magnetite in a mature paleosol (Chen et al., 2005). Transmission electron microscope (TEM) and XRD results for loess/paleosol samples from the Chinese Loess Plateau (CLP) indicate that magnetite oxidation is stronger in paleosols than in loess, even though it also occurs in source areas before loess transportation and deposition (Chen et al., 2010).

Titanomagnetite is the dominant magnetic mineral in most igneous rocks. In terrestrial igneous rocks, hematite is usually a late-stage oxidation product that forms during hydrothermal oxidation or low-temperature (LT) surface oxidation (Catling & Moore, 2003). Deuteric titanomagnetite oxidation is considered a two-stage process that often occurs during initial lava cooling. The first deuteric oxidation stage (exsolution) involves development of oriented ilmenite lamellae along (1 1 1) planes in host titanomagnetite. The second stage involves magnetite and ilmenite replacement by hematite and pseudobrookite, respectively (H. Li & Beske-Diehl, 1991). Low-Ti hematite produced by deuteric oxidation of iron silicates does not contribute significantly to the magnetization of these basalts. Magnetic remanence intensity and stability should increase when Ti moves out of the titanomagnetite lattice and ilmenite lamellae form, which subdivide the grain during deuteric oxidation. Subdivision of a large mineral by lamellae effectively decreases the magnetic crystal size, which influences profoundly its magnetic stability (Feinberg et al., 2006; Tauxe, 2010). Also, magnetic exchange interactions among atoms at lamellar interfaces can give rise to so-called lamellar magnetism (Harrison et al., 2010; Robinson et al., 2002, 2004). Upon further oxidation, magnetic intensity should correlate inversely with oxidation state as strongly magnetic titanomagnetite is oxidized to weakly magnetic hematite.

2.3.4. Hematite Formation in Banded Iron Formations

BIFs are sedimentary rocks that contain >15 wt% iron, with alternating iron-rich and iron-poor (usually silica-rich) layers. Specularite occurs frequently in terrestrial BIFs (Halama et al., 2016; Katsuta et al., 2012). In the consensus model of terrestrial BIF genesis, Fe^{2+} was exhaled into Earth's early oceans from seafloor vents and circulated to continental shelves where it was oxidized and deposited as BIFs (Holland, 1984; Klein, 2005). BIF banding records changing atmosphere-hydrosphere interactions near the ancient sea surface (Klein & Beukes, 1989), which induced dissolved Fe^{2+} oxidation, precipitation of insoluble ferric oxides and silica, and regulation of oxygen in Earth's early atmosphere (Holland, 1984; Kasting, 1987).

In standing water bodies, iron precipitates as fine-grained reddish hematite, not as gray crystalline hematite. There are three ways in which the Fe^{2+} could be precipitated initially: chemical oxidation, oxygenic photosynthesis, or biologically mediated oxidation (e.g., Klein & Beukes, 1989; Konhauser et al., 2002; Rasmussen et al., 2014). Fe^{2+} oxidation in solution proceeds via an intermediate amorphous, insoluble red-brown ferrihydrite gel. Ferrihydrite is unstable and converts irreversibly to goethite, which may in turn convert to hematite depending on environmental conditions and the presence of other dissolved species. Hematite may form directly from ferrihydrite, competing with goethite. In general, goethite formation is favored in alkaline solutions at moderate temperatures. Hematite is dominant at near-neutral pH and higher temperatures. Iron oxides in BIFs could also be photo-oxidized abiotically. Initial sedimentary Fe^{3+} deposition in BIFs is thought to have been likely, with microbes providing the oxidizing power to change soluble Fe^{2+} to insoluble Fe^{3+} (e.g., Konhauser et al., 2002). For example, some purple bacteria can couple Fe^{2+} oxidation to CO_2 reduction during anoxic photosynthesis (e.g., Cloud, 1973; Holland, 1984; Posth et al., 2013). However, the hematite that forms via the three sedimentary oxidation processes is reddish and fine-grained. Temperatures of ∼100°C or more are needed to form large platy hematite crystals. To convert sediments to lithified BIFs, fine-grained iron oxide-rich sediments were likely later altered at depth by burial metamorphism or by hydrothermal activity. Thermal processing converted microcrystalline or amorphous iron oxides to coarse crystalline hematite (Barley et al., 1999; D. Taylor et al., 2001; Powell et al., 1999). If coarsely crystalline hematite on Mars started with aqueous deposition in a standing water body, this must have been followed by either deep burial or some other large-scale thermal perturbation due to igneous activity.

2.3.5. Reduction of Hematite to Magnetite During Burial

Hematite can be reduced to magnetite when environments are sufficiently reducing. Hematite reduction is an important process that gives rise to magnetite formation in surface soils or sediments (Bloemendal & Liu, 2005; Gedye et al., 2000; Geiss et al., 2008; Kletetschka & Banerjee, 1995; Tite & Mullins, 1971). For example, wildfires can heat the topmost centimeters of organic-rich soils to 800°C and produce reducing soil-pore atmospheres, for example, mixing CO and CO_2 (Haliuc et al., 2016; Tunstall et al., 1976), which causes hematite and/or goethite to transform to magnetite (C. Zhang et al., 2012; Jiang, Liu, Zhao, et al., 2015; Swann & Tighe, 1977). Hematite also forms as an intermediate phase during reduction of goethite to magnetite (e.g., Till et al., 2015) and during underground burning of peat or coal seams, which can reach temperatures >2,000°C (de Boer & Dekkers, 2001). In addition to hematite and goethite, ferrihydrite and siderite can transform into magnetite or maghemite in the presence of organic matter during soil and sediment heating (Hanesch et al., 2006). Clay minerals can also lead

to reduction of hematite to magnetite by releasing Fe^{2+}; details of the chemical reactions involved require further study (C. Zhang et al., 2012; Jiang, Liu, Zhao, et al., 2015).

Neoformed magnetite has also been detected in fault gouge (Hirono et al., 2006; Mishima et al., 2009; R. Han et al., 2007; Tanikawa et al., 2007; Yang et al., 2012, 2020) produced by frictional heating generated during large earthquakes (Scholz, 2002). Rapidly elevated temperatures (flash heating to >1,000°C) within fault slip zones induce thermochemical reactions, such as hematite and clay mineral decomposition (Ferré et al., 2005; Tanikawa et al., 2007, 2008), where temperature depends on the distance to the slip surface (Yang et al., 2016). Jiang, Liu, Zhao, et al. (2016) found that magnetite formed via high temperature conversion can inherit the parent hematite morphology. Moreover, some magnetite samples that transformed from hematite may have surficial micro-pores that may be due to structural water release during heating (Jiang, Liu, Zhao, et al., 2016). Surface micro-pores could, thus, serve as a practical fingerprint of fire or other high-temperature (HT) mineralogical alteration processes in natural environments.

2.3.6. Hematite Formation on Mars

Understanding the origin of Martian hematite is essential to unravel its geologic, aqueous and, possibly, even its climatic history. Due to the rarity of Martian samples (e.g., from Martian meteorites), it is difficult to investigate hematite formation mechanisms on Mars, so we must rely on appropriate Earth analogs. The formation process for coarsely crystalline hematite is also different from the oxidative weathering that ubiquitously forms the familiar red, fine-grained hematite. Therefore, to consider Martian hematite, we address first the formation pathway of nano-phase hematite before discussing formation of so-called gray hematite, which is distinctly coarser.

2.3.6.1. Nano-Phase Hematite

Newsom (1980) and Allen et al. (1982) suggested that nanophase hematite in Martian soil could be an erosion product of hydrothermally altered impact melt sheets. This hematite type corresponds to hematite pigment on Earth of which the Manicouagan impact melt sheet (Canada) is a terrestrial analog. Crystalline hematite with subordinate nanophase iron oxide are the primary iron-bearing oxidized alteration products of hydrothermal alteration due to impact melting (R. V. Morris et al., 1995). Burns (1993a) proposed that iron formations on Mars could have formed similarly to Archean BIFs. Iron-rich aqueous or hydrothermal environments, including water-filled basins rich in basaltic sands, are plausible candidate settings for these deposits on Mars (Bandfield, 2002). Bell et al. (1993) inferred that crystalline hematite can form naturally from palagonitic tephra by heating and suggested this can occur on Mars by impact heating. Hematite with a narrow size distribution can precipitate from aqueous solutions in the laboratory. Hematite with specific morphologies can also form during forced hydrolysis at ~100°C in the presence of additives and/or by altering reaction conditions (Schwertmann & Cornell, 2000; Sugimoto & Sakata, 1992; Sugimoto & Wang, 1998; Sugimoto et al., 1993, 1996, 1998). For example, chloride in acidic solutions can promote formation of spherical hematite particles with sizes of ~0.05–0.5 μm (Sugimoto et al., 1998). Phosphate, which has high concentrations (~3 g/kg) in Martian soils (e.g., Dreibus et al., 1999), favors hematite over goethite formation (Gálvez et al., 1999; Ren et al., 2020; Torrent & Barrón, 2000). Alteration of jarosite $(KFe_3(SO_4)_2(OH)_6)$ to hematite under low temperature acidic conditions is a further mechanism for nanophase hematite formation on Mars, which suggests a transient period with liquid water at Meridiani Planum (Barrón et al., 2006).

2.3.6.2. Gray Hematite Spherules (Hematite "Blueberries")

Limited gray hematite spherule occurrences on Mars suggest that its formation required a restricted combination of abundant water, temperature, pH, Eh, and rock composition conditions that may have been rare through Martian history. Crystalline gray hematite is uncommon on the Martian surface, yet in all known occurrences it is associated with layered, sedimentary units (Christensen et al., 2001). Most proposed formation mechanisms for these gray hematite spherules include: (a) direct precipitation from standing, oxygenated, iron-rich water (Herkenhoff et al., 2004; Squyres et al., 2004); (b) precipitation, oxidation, and crystallization from iron-rich hydrothermal fluids (Golden et al., 2008); (c) LT dissolution and precipitation through mobile groundwater leaching (McLennan et al., 2005); (d) sulfur-bearing water reaction of volcanic ash and basaltic pyroclastic deposits (Hynek et al., 2002); (e) oxidation of jarosite or other iron sulfide/sulphate minerals (Squyres & Knoll, 2005); (f) accretionary lapilli from an impact surge (Knauth et al., 2005); (g) fine hematite coatings (Kirkland et al., 2004); and (h) diagenesis of hematite-rich spherules following sediment transport and deposition (Fan et al., 2010). Association with layered deposits and strong correlation with these geological units led Christensen et al. (2001)
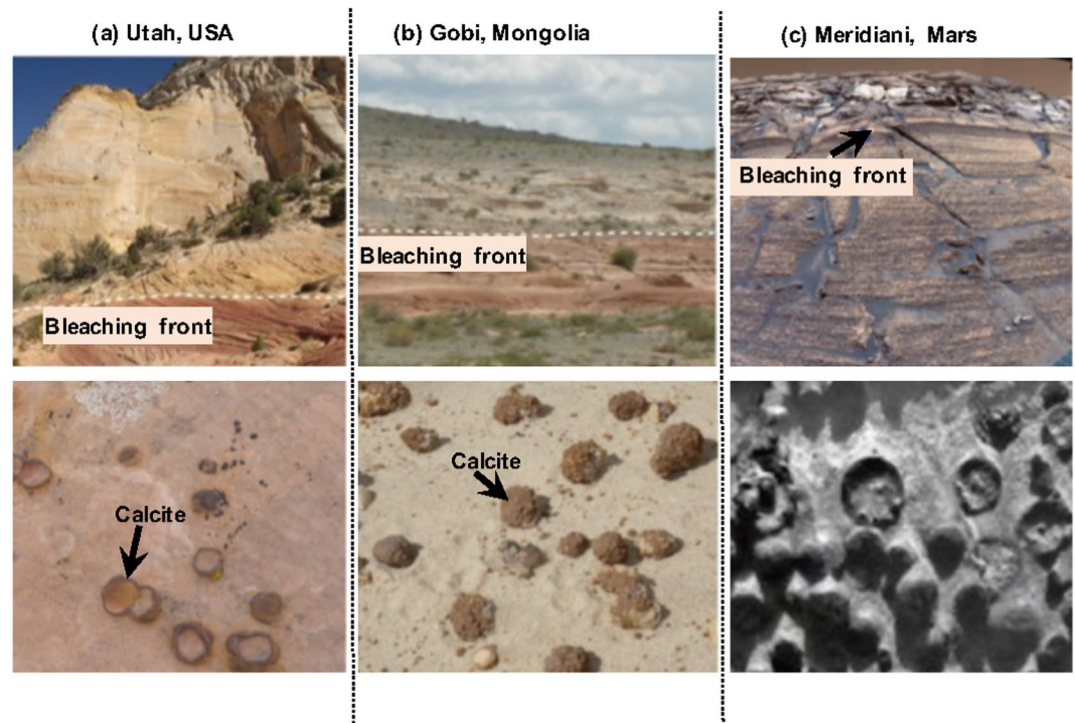
Figure 5. Similarity of hematite-bearing concretions on Earth (Utah and Mongolia) and Mars (Meridiani Planum), which occur dominantly in the upper part just above a bleaching front. From Yoshida et al. (2018).

to favor precipitation from Fe-rich water, either in a LT subaqueous environment or a hydrothermal system. The strongest hematite signature occurs adjacent to a paleolake basin, which supports the role of water in hematite formation. Water could have been responsible for hematite formation in several ways, including deposition in lakes, and precipitation as surface coatings due to groundwater wetting (Newsom et al., 2003). Abundant Fe^{3+} as electron acceptors and abundant H_2 as electron donors would have provided favorable redox environments for simple life on Mars if it ever arose.

Hematite "blueberries" on Mars are strikingly similar to the larger hematite "marbles" found in Utah, Mongolia (Figure 5), and Australia (Bowen et al., 2008; Chan et al., 2004; Potter et al., 2011; West et al., 2010; Yoshida et al., 2018). These terrestrial hematite concretions are examples of early diagenetic formation in acid and saline conditions that may be analogous to past conditions on Mars (e.g., Bowen et al., 2008; McLennan et al., 2005; West et al., 2010; Zolotov & Shock, 2005). However, Martian hematite is pure, crystalline, and gray. In contrast, the Utah concretions are mostly quartz, with a secondary brownish-black hematite cement (Catling, 2004). It is, therefore, reasonable to ask whether the Utah concretions are a good analog for those on Mars. On Mars, acidic water probably mobilized iron (Burns, 1993a; Clark & Van Hart, 1981) compared to reducing, hydrocarbon-rich fluids in Utah. Regardless, formation of spherical hematite concretions requires a permeable host rock, ground-water flow, and a chemical reaction front (Chan et al., 2004). Therefore, Chan et al. (2006) proposed a conceptual Fe redox cycling model for Fe oxide concretion formation. Early hematite grains are present as coatings in original red sandstone, which were reduced to Fe^{2+} by fluids that bleach buried sandstone. Bleached sandstone pores were then saturated with Fe^{2+}-containing reduced waters. Then, oxidizing groundwater influx created a redox front where concretions precipitated. Concretions formed along a reaction front with organized distribution and spherical shape. However, this model does not explain development of spherical concretions with Fe-rich crusts. Loope and Kettler (2015) proposed a siderite formation and microbial oxidation model (Table 1) in which a spherical concretion is both an Fe source and a precursor of a spherical Fe-oxide encrusted concretion. If a siderite concretion undergoes oxidative dissolution, which is possibly microbially mediated, it provides an internal Fe^{2+} source for a Fe^{3+}-oxide crust to form on the concretion exterior. However, no siderite concretions have been identified, either in outcrop or in deeper environments in Utah or Mongolia. Yoshida et al. (2018) then proposed different stages of calcite and Fe-oxide concretion formation in Utah and Mongolia. First, calcite

Table 1
Comparison of Formation Models for Gray Hematite

Model	Precursor	Reaction fluid/liquid	Fe-oxide mineralization	Fe state	Equation	Reference
Redox-oxic reaction model	None	Buoyant, reducing fluid due to hydrocarbons	Precipitation of goethite	Fe^{2+}	$2Fe^{2+} + 0.5O_2 + 3H_2O = 2FeOOH + 4H^+$	Chan et al. (2004)
Siderite formation & microbial oxidation model	Siderite	Reducing groundwater with dissolved methane	Internal Fe source (siderite)	Fe^{2+}	$4FeCO_3 + O_2 + 10H_2O = 4Fe(OH)_3 + 4HCO_3^- + 4H^+$	Loope and Kettler (2015)
Calcite-acid reaction model	Calcite	Penetration of CO_2-charged acidic groundwater	Inward precipitation of goethite by Fe-rich acidic water from outside	Fe^{3+}	$CaCO_3 + 2H^+ = Ca^{2+} + H_2O + CO_2$; $Fe^{3+} + 2H_2O = FeOOH + 3H^+$	Yoshida et al. (2018)

concretions with different sizes and shapes formed from carbonate-saturated groundwater within buried eolian sandstones, and then acidic water penetration episodes dissolved the calcite concretions. Mobile Fe in acidic waters precipitated on preexisting calcite concretion surfaces due to increased pH, thereby producing outer rinds consisting of FeOOH. When FeOOH-encrusted calcite was exposed at the surface by erosion, any remaining calcite was dissolved to preserve Fe-oxide-encrusted concretions. This model explains why many Fe-oxide-encrusted concretions are observed near bleached fronts. Similarity between Fe-oxide concretions on Earth and hematite spherule occurrences in Meridiani Planum, combined with evidence of acid sulphate-bearing water influence on Mars, suggest that the hematite spherules also formed from dissolution of preexisting carbonate spherules possibly in a dense early Martian CO_2-rich atmosphere, the process of which has been well studied for hematite ore bodies formed from a siderite precursor on Earth (e.g., Kim et al., 2013; Loope & Kettler, 2015; Seguin, 1966).

As illustrated above, hematite can form via several mechanisms, most of which involve water. Although a fully defined hematite formation pathway has yet to be discerned for Mars, the origin of crystalline hematite can provide chemical clues about the early Martian environment, especially pertaining to the existence of (liquid) water, which is an indispensable requirement for evolution and sustenance of life.

3. Magnetic Structure and Properties of Hematite

Hematite carries potentially valuable signals about climate, environments, tectonics, and planetary evolution on Earth and Mars. Knowledge of the pathways by which hematite forms, as discussed above, can be important for interpreting such signals, which requires robust methods for identifying its presence both from direct measurements and through remotely sensed spectroscopic measurements. In this section, we discuss magnetic and color spectroscopic methods for identifying hematite. This requires understanding of its crystal structure and physical properties, which provide a starting point for understanding how magnetism and color spectroscopy are used to identify hematite.

3.1. Crystal Structure of Hematite

Hematite can be indexed with a hexagonal unit cell, with a three-fold symmetry axis perpendicular to the basal plane, which is sometimes called the principal crystal plane (Blake et al., 1966; Pauling & Hendricks, 1925; Smith, 1916). Hematite (α-Fe_2O_3) and corundum (α-Al_2O_3) share the same crystal structure, so hematite is often said to have the corundum structure. The hexagonal unit cell has parameters $a = b = 5.038$ Å and $c = 13.77$ Å and contains six formula units (Blake et al., 1966; Figure 6). The hematite structure consists of hexagonally close packed oxygen ion arrays stacked in the [0 0 1] direction. Two-thirds of the octahedral lattice interstices are filled with Fe^{3+} ions that are arranged regularly with two filled sites followed by one vacant site along the [0 0 1] axis to form six-fold rings in the (0 0 1) plane. The cation arrangement produces pairs of adjacent $Fe(O)_6$ octahedra. Each octahedron shares edges with three neighboring octahedra in the same plane and one face with an octahedron in
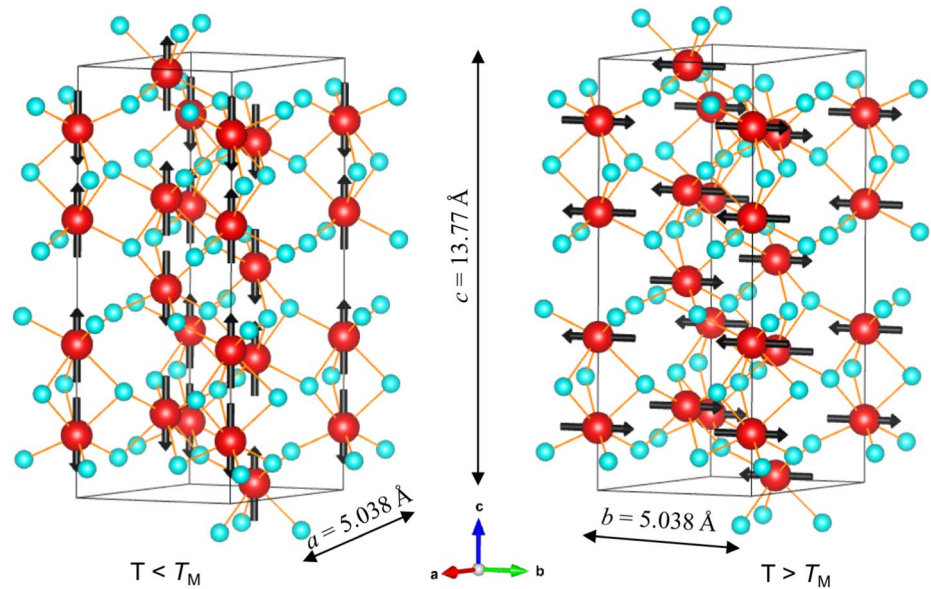
Figure 6. Crystallographic and magnetic structure of hematite below ($T < T_M$) and above ($T > T_M$) the Morin transition temperature (T_M). The unit cell is hexagonal with $a = b = 5.038$ Å and $c = 13.77$ Å (Blake et al., 1966). Spins are aligned parallel to the c axis [0 0 1] below T_M and lie in the (0 0 1) plane; spins lie in the (1 1 1) plane above T_M.

an adjacent plane, which is responsible for distortion of the cation arrangement from ideal hexagonal packing (Cornell & Schwertmann, 2003).

3.2. Magnetic Structure of Hematite

Magnetic moments of Fe^{3+} ions in hematite are arranged in almost opposite directions in alternating lattice planes (A and B sublattices), so that the spins in adjacent layers largely cancel each other. Such an arrangement leads to no net macroscopic magnetization in a perfect antiferromagnetic structure (Appendix A). Early explanations attributed the weak ferromagnetism of hematite to crystal defects (e.g., crystal dislocations; Néel, 1955) or to pinning of domain wall magnetizations by lattice imperfections (Y. Y. Li, 1956). However, these mechanisms employ crystal inhomogeneities, which means that the net magnetism is not an intrinsic property of hematite and would disappear in an ideal crystal. Dzyaloshinsky (1958) showed that canting of spin sublattices within the basal plane can produce an anisotropic moment, and Moriya (1960) demonstrated that the canting is produced by anisotropic exchange interaction. Thus, in the Dzyaloshinsky-Moriya model, hematite is a canted or imperfect antiferromagnet. Hematite is considered to have an archetypical canted antiferromagnetic structure (Morrish, 1994).

3.3. Key Magnetic Properties of Stoichiometric Hematite

3.3.1. Weak Magnetism

As an imperfect antiferromagnetic mineral, hematite has a weak spontaneous magnetization ($M_s = 0.4$ Am^2 kg^{-1}) at room temperature. Above the Morin transition temperature (T_M), this weak magnetism is an intrinsic feature that arises from canting of spin moments in hematite. Below T_M, spin canting should vanish and with it the weak magnetism (Figures 6 and 7). However, a small magnetic moment survives (Figure 7), which is generally ascribed to distortion of the hematite spin structure by lattice defects and is referred to as the defect moment. As defined by Özdemir and Dunlop (2006), the defect moment is responsible for the remanent magnetization below T_M. The defect moment also contributes to the magnetization of hematite above T_M; it is sometimes named the isotropic moment (Gallon, 1968a; R. Smith & Fuller, 1967). The total magnetization of hematite is, thus, a combination of spin-canted and defect moments. The defect moment can be altered by stress or heating and may record unstable paleomagnetic information (Dunlop, 1970). NRM stability in hematite depends on its imperfect antiferromagnetism. The saturation remanent magnetization (M_{rs}) of hematite is particle size dependent. It increases with particle size from 30 to 500 nm and then remains almost stable with further particle size increase (Figure 8a).
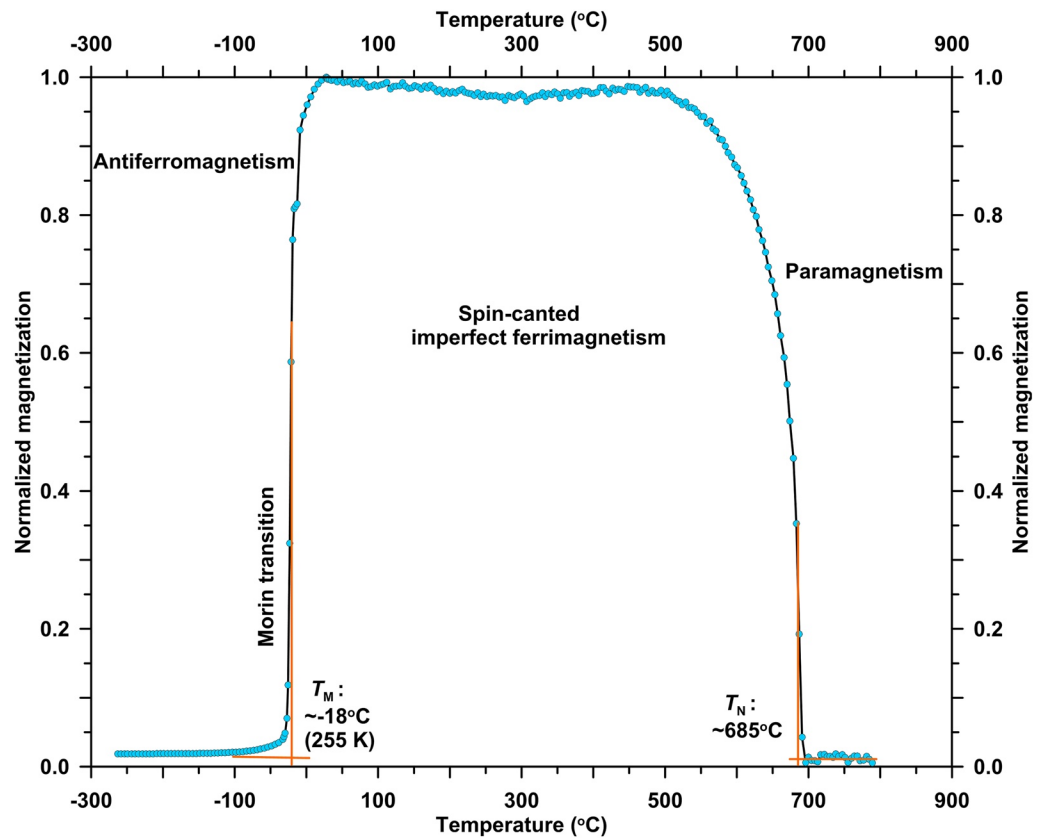
Figure 7. Temperature dependence of magnetization for hematite (data from Jiang et al. (2012)) normalized to the room-temperature value (~ 0.085 Am^2 kg^{-1}).

3.3.2. High Coercivity

A distinctive characteristic of hematite is its strong resistance to alternating field (AF) demagnetization, that is, its high coercivity. For particles <20 μm, the coercive force (B_c) can be hundreds of mT (Figure 8b), which means that the NRM cannot be removed easily with AF demagnetization. Some synthetic and natural hematite pigments do not saturate magnetically even in 4–5 T inducing fields (Abrajevitch et al., 2018; Jiang et al., 2012). This makes hematite the most stable paleomagnetic carrier. Dunlop (1970) suggested that the defect remanence of fine-grained hematite is magnetically softer than the spin-canted remanence, which can be annealed out by heating. Dekkers and Linssen (1989) also found that the coercivity can increase by hundreds of mT after annealing; Abrajevitch et al. (2018) reported a $\sim$1 T coercivity increase after annealing. Annealing largely removes defect moments, so the high coercivity does not result from defects.

Generally, coercivity originates from shape, magnetoelastic, and/or magnetocrystalline anisotropies (Dunlop & Özdemir, 1997). The weak magnetization of hematite means that shape anisotropy (which is proportional to M_s) is irrelevant, and magnetocrystalline anisotropy cannot explain the high coercivity of hematite (Flanders & Schuele, 1964). Urquhart and Goldman (1956) reported a magnetostrictive effect in hematite crystals, so Stacey (1963) proposed that magnetoelastic anisotropy arising from internal strain (Dunlop, 1971; Porath, 1968) is responsible for high coercivities in SD hematite. The saturation magnetostriction for hematite, λ_s, is $\sim 8 \times 10^{-6}$, so the coercivity B_c can be estimated by (Dunlop & Özdemir, 1997):

$$B_c = 3\lambda_s P/(2M_s), \tag{1}$$

where P is the internal stress. A B_c value of 500 mT can be obtained using $P = 100$ MPa, which is expected in the vicinity of dislocations (Dunlop & Özdemir, 1997). The spin-canted magnetic moment in fine-grained natural hematite is harder than the defect moment and is dominated by uniaxial magnetoelastic anisotropy.
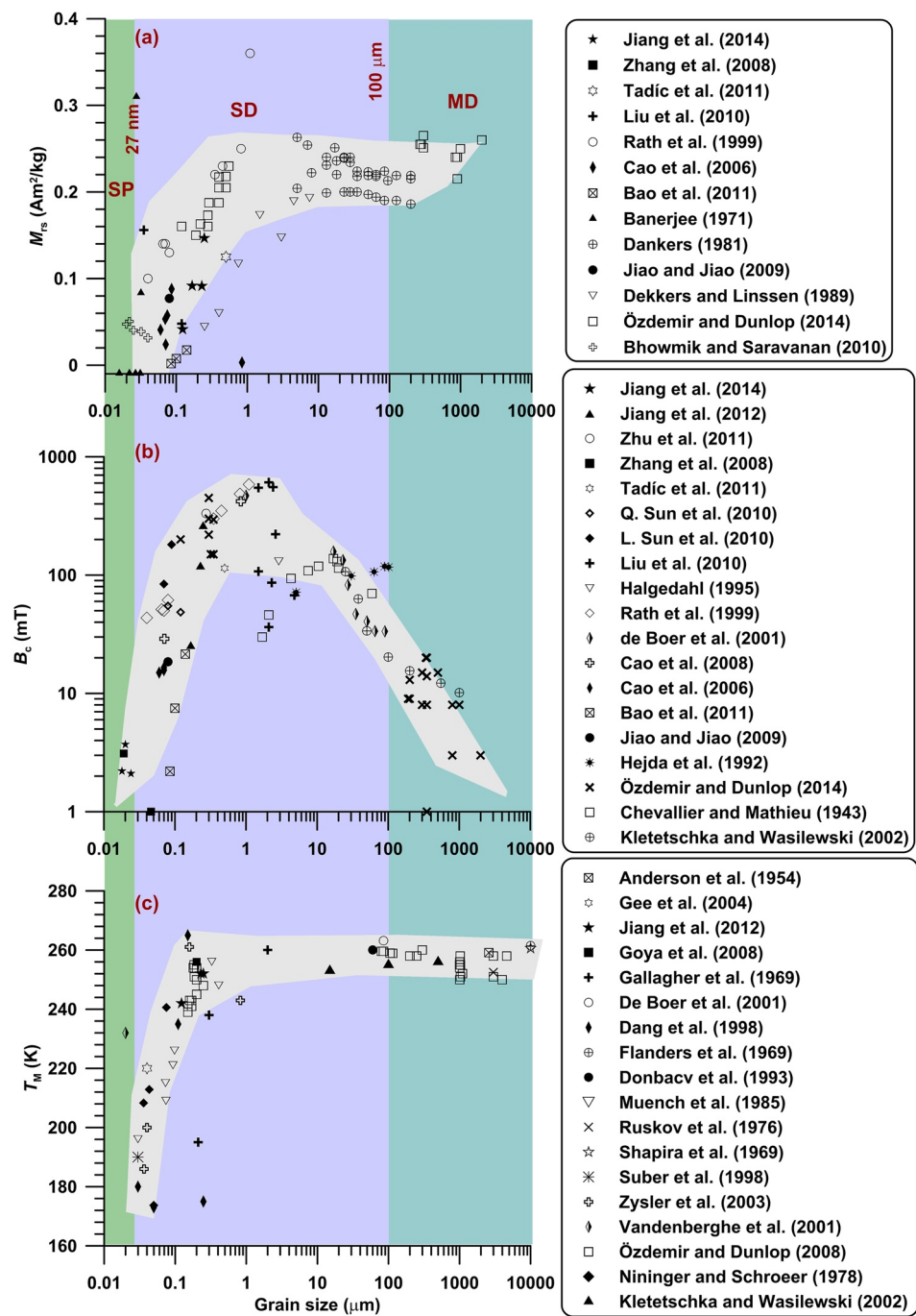
Figure 8. Grain size dependence of magnetic parameters for hematite. (a) M_{rs}; (b) B_c; and (c) T_M with respect to grain size. Data sources are listed in the figure.

B_c in hematite is also grain size dependent, with values decreasing from ∼600 mT at ∼1–10 μm to 3 mT at ∼2 mm (Figure 8b). B_c–grain size trends for diverse synthetic and natural hematites (Bao et al., 2011; de Boer, Mullender, & Dekkers, 2001; Dekkers & Linssen, 1989; H. Cao et al., 2008, 2006; Halgedahl, 1995, 1998; Jiang, Liu, Colombo, et al., 2014; Jiang et al., 2012; Jiao & Jiao, 2009; Kletetschka & Wasilewski, 2002; L. Sun, Cao, et al., 2010; Özdemir & Dunlop, 2014; Q. Liu, Barrón, et al., 2010; Q. Sun, Lu, et al., 2010; Rath et al., 1999; Tadić et al., 2011; Y. C. Zhang et al., 2008; Zhu et al., 2011) indicate that B_c first increases with increasing grain size, reaching a maximum between 1 and 3 μm, and then decreases slowly as grain size increases to 2 mm

(Figure 8b). The reason for this size dependence is increased thermal stability as SP behavior gives way to stable SD behavior over a broad size range, which is followed by increased thermal instability with the transition into the coarser MD state. Furthermore, different hematite synthesis methods lead to wide variations in crystal shape, morphology (e.g., rods, cubes, plates, disks, pod-like, shuttle-like, and trapezoidal), and degree of crystallinity, which contribute to considerable B_c dispersion for particles of nominally the same size (Figure 8b).

3.3.3. Morin Transition

The Morin transition is named after Morin (1950) who reported an abrupt magnetic susceptibility decrease in a hematite polycrystalline powder below 250 K (Figure 7). Powder neutron diffraction studies demonstrated that this magnetic transition is caused by a change in spin moment alignment of Fe^{3+} ions in the hematite lattice (Shull et al., 1951). Dzyaloshinsky (1958) predicted this spin-flop transition at 250 K from thermodynamic calculations using group theory, where spins are aligned parallel to the crystallographic c axis [0 0 1] below T_M where the weak magnetism of hematite vanishes, and above T_M, spins lie in the (0 0 1) plane, perpendicular to the [0 0 1] axis (Figure 6; Dzyaloshinsky, 1958; Moriya, 1960). The Morin transition has been identified with diverse methods, including domain observations (Gallon, 1968b; Williams et al., 1958), magnetic remanence (Lin, 1959, 1960, 1961), and Mössbauer spectroscopy (K. Ôno & Ito, 1962). This magnetic transition results from competition between the local single-ion anisotropy and a long-range dipolar anisotropy. These two anisotropy terms have comparable magnitude with opposite signs and different temperature dependencies such that they cross at the Morin transition temperature, at ~250 K for well-crystalline stoichiometric hematite (Artman et al., 1965; Levinson et al., 1969; Özdemir & Dunlop, 2006). The sign of the overall anisotropy constant changes at T_M, which induces a spin flop from the basal plane to an orientation along the crystallographic c direction (Artman et al., 1965; Levinson et al., 1969).

When hematite is given a M_{rs} at room temperature that is cycled through T_M in zero field, it loses much of its remanence during cooling and regains a fraction of M_{rs} during heating (Haigh, 1957). Something must be guiding the spin-canted magnetization into a given easy direction in the basal plane as it re-nucleates during warming through T_M; the only likely candidate for this so-called "memory" is the defect magnetization that survives below T_M (Gallon, 1968b). Özdemir and Dunlop (2006) compared memory ratio and defect magnetization values in submicron and millimeter size crystals and found that high M_{rs} memory ratios are associated with higher defect moments. They suggested that the defect moment of these spins serves to restore preferred spin directions and magnetic domains during zero-field warming through T_M. The defect moment is, thus, responsible for the memory phenomenon.

The Morin transition is sensitive to variations in applied field, pressure, grain size, impurities, and lattice strain originating from crystal defects, which all affect the balance between single-ion and long-range dipolar anisotropies. Based on magnetic studies of hematite with 70–602 nm particle sizes, Amin and Arajs (1987) provided an empirical relation between T_M and particle size: $T_M = 264.2 - 2.194/d$, where d is the particle diameter expressed in Å and where the unit for T_M is K. Furthermore, the Morin transition does not occur in non-substituted hematite particles <~8 nm. Zysler et al. (2003) showed that T_M increases for increasing crystallite size from 36 to 159 nm, which indicates that this variation is mainly driven by surface effects. Özdemir et al. (2008) summarized literature T_M values and found two clear trends. T_M has a positive relationship with grain size for mean sizes between ~30 and 100 nm, with values from 230 to 165 K (Figure 8c). However, for samples with mean sizes above 100 nm, T_M values hover between 250 and 260 K and do not vary significantly. Therefore, except for the finest SD samples, which likely include a <100 nm fraction, T_M values between 250 and 260 K seem to be an intrinsic hematite property that depends only on the spin orientation and is independent of domain structure. In addition, a field applied along the basal plane stabilizes its weak magnetism, which causes T_M to decrease linearly with increasing field (Amin & Arajs, 1987; Bhowmik & Saravanan, 2010; Goya et al., 2005; Muench et al., 1985; Suber et al., 2010). Therefore, for comparable results, T_M should be measured in or extrapolated to zero field (Özdemir et al., 2008).

3.3.4. High Néel and Blocking Temperatures

A further noteworthy characteristic of hematite is its high T_N of ~675°C–690°C (Figure 7). This means that hematite NRMs can survive significant metamorphic heating that would reset the NRM of other magnetic minerals (Dunlop & Özdemir, 1997). Hematite-bearing sedimentary rocks were, therefore, favored in early paleomagnetic studies and yielded some of the first convincing paleomagnetic data (Irving & Major, 1964).

The blocking temperature (T_b) is the temperature at which a remanent magnetization disappears (Butler, 1992). T_b for natural hematite varies up to ~600–675°C (i.e., $\leq T_N$) and increases with particle size throughout the SD size range (Dunlop & Özdemir, 1997). However, for SP particles, T_b correlates positively with particle size below 16–17 nm and then has a negative relationship with particle size between 17 and 25 nm, which is explained as follows. From Néel theory (Dunlop & Özdemir, 1997; O'Reilly, 1984), the relaxation time τ of a magnetic particle is given by:

$$\tau = \tau_0 \exp\left(KV/\kappa_b T_b\right), \qquad (2)$$

where K is the anisotropy constant (in J/m^3), V is grain volume (in m^3), κ_b is the Boltzmann constant (1.380649×10^{-23} J/K), and τ_0 is the so-called attempt frequency or pre-exponential factor, which typically has values of 10^{-8} to 10^{-9} s^{-1}. T_b (in K) is related positively to V because the anisotropy constant K is assumed to be constant for SD particles. However, this is not entirely correct for SP particles. The total anisotropy is due to surface and magnetoelastic anisotropy contributions. The former was proposed by Néel (1954) as the magnetocrystalline anisotropy of surface regions where spins deflect from that of the bulk particle due to broken chemical bonds and surface irregularities (e.g., R. Kodama, 1999). As a result, SP hematite has enhanced anisotropy compared to bulk samples because the surface area to volume ratio is much larger than for coarser particles. Furthermore, for particle sizes below 16–17 nm, the anisotropy is primarily thought to be controlled by the surface layer Fe^{3+} content, while bulk properties dominate particles >17 nm. A low surface layer Fe^{3+} content would result in a low surface anisotropy for particles <16–17 nm. As particle size increases, long-range spin coupling extends over more Fe^{3+} ions so that the anisotropy energy increases. T_b will, therefore, increase with increasing particle size for samples with sizes <17 nm. However, at some size the surface layer contribution becomes small and bulk spin properties become dominant. Once particle size exceeds a critical value (i.e., here 17 nm) the surface anisotropy becomes less pronounced, and the total anisotropy decreases (Jiang, Liu, Dekkers, et al., 2014). Thus, T_b has different trends with increasing particle size. It will not continue decreasing in large grains: at some point, T_b rises abruptly because the surface contribution is insignificant and particles have constant bulk anisotropy. T_b will continue to increase with grain size.

3.4. Grain Size Thresholds for the SP/SD and SD/MD Transitions in Hematite

The magnetic properties of hematite are particle-size and domain state dependent. Banerjee (1971) estimated a stable SD grain-size range from 27.5 ± 5 nm (SP/SD threshold size) to 15 μm (SD/MD threshold size) based on compiled data (Figure 8b). The SP threshold is defined by the sharp M_{rs} decrease to zero at 27.5 nm (Banerjee, 1971), while the SD threshold size, where B_c and B_{cr} have maximum values, is from the hysteresis data of Chevallier and Mathieu (1943) without slope correction. Dekkers and Linssen (1989) argued that the SD threshold size depends on hematite crystallinity; crystalline hematite has a larger SD threshold size. Microcrystalline natural hematite has an upper boundary for the SD size range at ~1 μm. Furthermore, Kletetschka and Wasilewski (2002) argued that the SD to MD transition in hematite can extend to ~100 μm, based principally on a break slope in B_c data at ~100 μm. However, Özdemir and Dunlop (2014) suggested that evidence for a SD/MD transition from B_c data is tenuous (Figure 8b), and that it would be more useful to identify this boundary with direct domain observations. The wide size range for SD behavior in hematite means that natural hematite is expected to be dominantly in the SD state. SD hematite records stable NRMs in red beds (Collinson, 1966; Jiang et al., 2017; Tan & Kodama, 2002; Walker et al., 1981; Z. Sun et al., 2006) and red soils (C. Liu, Deng, et al., 2010; Deng et al., 2007), which makes it paleomagnetically useful (C. Liu, Deng, et al., 2010; Dekkers & Linssen, 1989; Özdemir & Dunlop, 2002). Also, although MD hematite is magnetically less stable than SD hematite, it can carry a stronger NRM than MD magnetite, which may be significant for Martian magnetic anomaly analysis (Clark, 1983; Dunlop & Kletetschka, 2001; Kletetschka et al., 2000b, 2000c; Özdemir & Dunlop, 2005).

3.5. Color Reflectance Properties of Hematite

The most eye-catching color characteristic of hematite is its conspicuous red hue (3.5R-4.1YR; Figures 9a and 9b), which contributes dominantly to the typical yellow-red to purple-red colors of red beds and red soils (Cornell & Schwertmann, 2003). Redder hematite hues are due to its face-sharing octahedra with Fe-Fe distance of only 0.29 nm. This strongly enhances electron pair transitions (EPTs). In contrast, other iron oxide minerals, for example, goethite contains only edge- and corner-sharing octahedra and Fe-Fe centers are 0.30–0.33 and
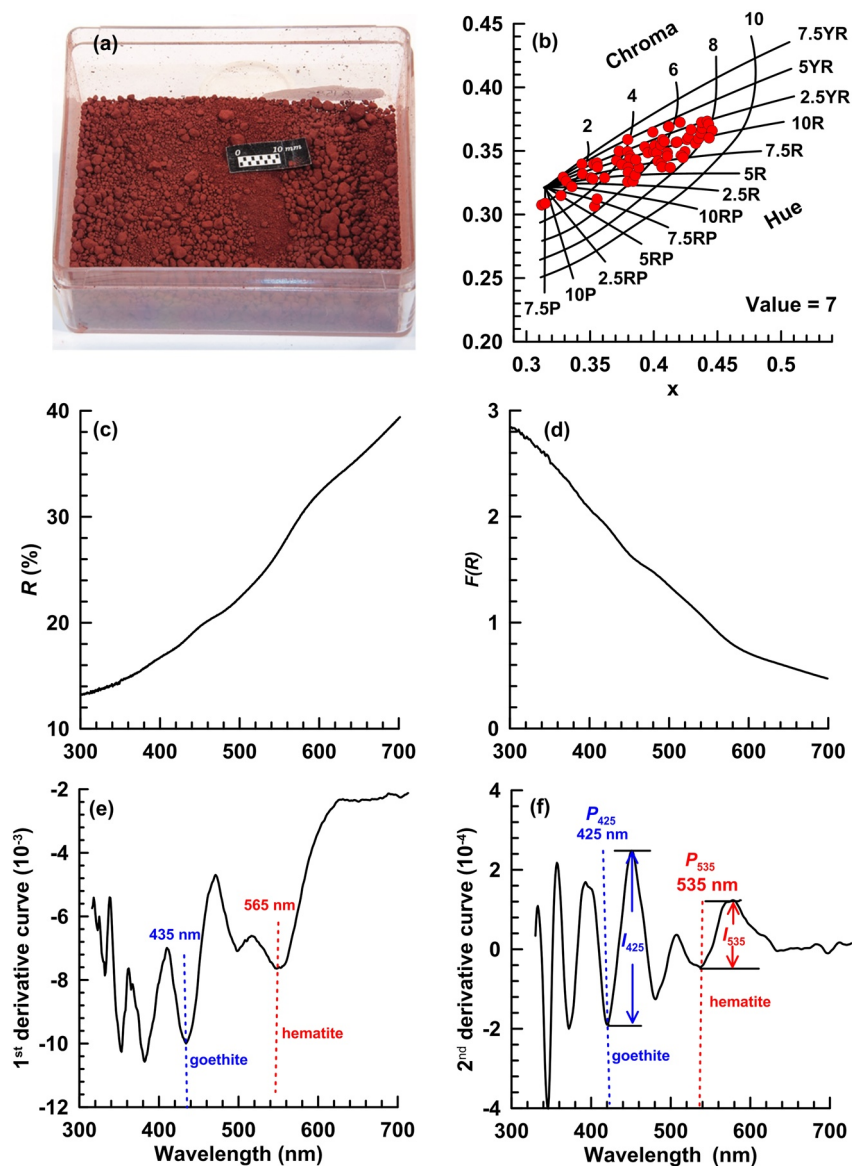
Figure 9. Color spectral characteristics of hematite. (a) Image of hematite pigment; (b) color parameters for hematite (P = purple, R = red, and Y = yellow), where red dots represent data for individual samples; (c) raw diffuse reflectance spectroscopy (DRS) data; (d) transferred $F(R)$ from DRS data based on the function $F(R) = (1 - R)^2/2R$, where R is the reflectance of a thick sample layer; (e) first derivative curve of $F(R)$; and (f) second derivative curve of $F(R)$.

0.35 nm apart, respectively, which leads to yellow hues. In contrast, the black color of magnetite is because its structure contains both Fe^{2+} and Fe^{3+}, which causes intervalence charge transfer (Cornell & Schwertmann, 2003).

Redness has been used to quantify soil hematite contents (Barrón & Torrent, 1986; Torrent et al., 1983). Hematite powder color varies with particle size. Hematite suspensions with particle sizes <0.1 μm are orange, while suspended 0.1–0.5 μm particles are red, and those with >1.5 μm sizes are purple (Kerker et al., 1979). Thus, hematite spectra have increased reflectance in the red range as particle size decreases from 0.48 to 0.11 μm (Hund, 1981). Red hematite can be converted to purple hematite, for example, by heating to >800°C because oriented aggregates of small, platy, hematite crystals can cause a shift toward purple hues (Torrent & Schwertmann, 1987).

DRS in the visible (VIS, ~400–700 nm) and near infrared (NIR) ranges (~700–2,500 nm) has been used to obtain color information for hematite (Figures 9c–9f; e.g., Cornell & Schwertmann, 2003; Torrent & Barrón, 2002, 2008). Reflectance in soils and sediments includes two components, *specular* and *diffuse* reflectance.

When an incident light beam impinges on a powder surface, a small fraction is reflected specularly (*specular reflectance*); the rest penetrates the mass as wavelength-dependent absorption within colored materials or is scattered (as multiple reflections, refractions, and diffractions in all directions). Part of this radiation ultimately leaves the material in all directions and constitutes *diffuse reflectance* (Torrent & Barrón, 2002, 2008). The color of hematite is related to the position and/or intensity of the main visible spectrum absorption bands. To enhance characteristic reflection identification, Deaton and Balsam (1991) calculated the first derivative of a measured DRS curve (Figure 9e) and obtained characteristic peaks for goethite (primary peak: 535 nm and secondary peak: 435 nm) and hematite (575 nm), the intensity of which can be used to estimate goethite and hematite contents. However, Kosmas et al. (1984, 1986) and Scheinost et al. (1998) used the second derivative of raw spectra and the Kubelka-Munk (K-M) function ($F(R) = (1 - R)^2/2R$, where R is the reflectance of a thick sample layer), respectively, to detect and quantify soil and sedimentary iron oxides (Figure 9f). The K-M function is a proxy for the typical absorption spectrum, which can be approximated for a soil sample by the absorption coefficient in the K-M function. As illustrated in Figure 9f, the characteristic hematite (P_{535}) and goethite (P_{425}) peak positions can be used to identify these minerals; the ordinate difference between the minimum and the next longer wavelength maximum (band intensity) of the second derivative curve is used as a proxy for true band amplitude. Band amplitudes at ~425 nm (I_{425}) and ~535 nm (I_{535}) are proportional to the goethite and hematite concentration, respectively (Figure 9f), and are used as proxies for their relative mass concentration changes (Scheinost et al., 1998). Torrent et al. (2007) proposed empirical equations for hematite and goethite quantification through I_{425} and I_{535}, as discussed in Section 5.

3.6. Spectral Characteristics of Hematite on Mars

Constrained by sparse direct surface measurements of Mars, the foremost methods to characterize the three Martian hematite forms are optical, X-ray spectrometer, VNIR spectra, and TES, which are often acquired via remote sensing. Instruments include Earth-based telescopes, the imaging spectrometer for Mars (ISM; Mustard & Bell, 1994), and the TES instrument deployed on the Mars Global Surveyor (MGS) spacecraft (Christensen, Bandfield, Clark, et al., 2000) and Mars Surveyor Lander (Grotzinger et al., 2015; R. Morris et al., 2006). Based on telescopic and ISM data, a composite spectrum for the Olympus-Amazonis region has a shallow band minimum near 860 nm, a reflectivity maximum near 740 nm, a distinct inflection near 600 nm, and a shallow absorption edge from ~400 to 740 nm (Figure 10a; Mustard & Bell, 1994). The presence of red hematite in this region is deduced from spectral results of laboratory simulations, for example, spectral analysis on known nanophase ferric oxide plus subordinate red hematite mixtures (R. V. Morris et al., 1997), hematite, and goethite (R. V. Morris & Golden, 1998). The 600-, 740-, and 860-nm features are associated with red hematite. A conservative upper limit for the red hematite content of the optical surface of Mars is 5%, while the typical Fe content of Martian rocks is 100 g/kg (Rieder et al., 1997; R. V. Morris et al., 1997). Hematite could also account for much or all spectral behavior of the Martian surface in the 0.4–1.0 µm region (Bell et al., 1990). The degree of crystallinity and particle diameter of hematite can be detected by comparing TES results and available Hubble Space Telescope VNIR multispectral data with corresponding data for nanophase, red, and gray hematite, although detailed interpretation will likely require sample return to Earth.

Nanophase hematite (<5–10 nm in size) is X-ray amorphous. The reddish color of the surface and sky of Mars is due to the optical properties of finely or poorly crystalline hematite on the surface and in airborne dust. Nanosized samples have neither a well-defined reflectivity maximum near 750 nm nor a well-defined reflectivity minimum near 860 nm in VNIR spectra (R. V. Morris et al., 1989). In addition, they do not have well-developed absorption bands above noise level (~1%) in the 450–700 cm^{-1} region, which is consistent with the properties of SP hematite on Earth (Christensen, Bandfield, Clark, et al., 2000).

Red hematite consists of crystalline particles ~10 nm to ~5–41 µm in diameter, which have a well-defined reflectivity maximum and minimum near ~750 and ~860 nm, respectively. Crystalline red hematite is a minor component of VNIR spectral observations (<5 wt%) in certain Martian bright regions such as Olympus and Amazonis (Figure 2). Together with nanophase ferric oxide particles, it gives these regions their conspicuous red color (Bell et al., 1990; R. V. Morris et al., 1997). Spectral data of the Martian bright regions have a shallow band minimum near 860 nm, a reflectivity maximum near 740 nm, a distinct inflection near 600 nm, and a shallow absorption edge from ~400 to 740 nm. These responses are attributed to nanophase ferric oxide plus subordinate red hematite (Figure 10a). Even though the red hematite is extremely fine grained, which results in low spectral
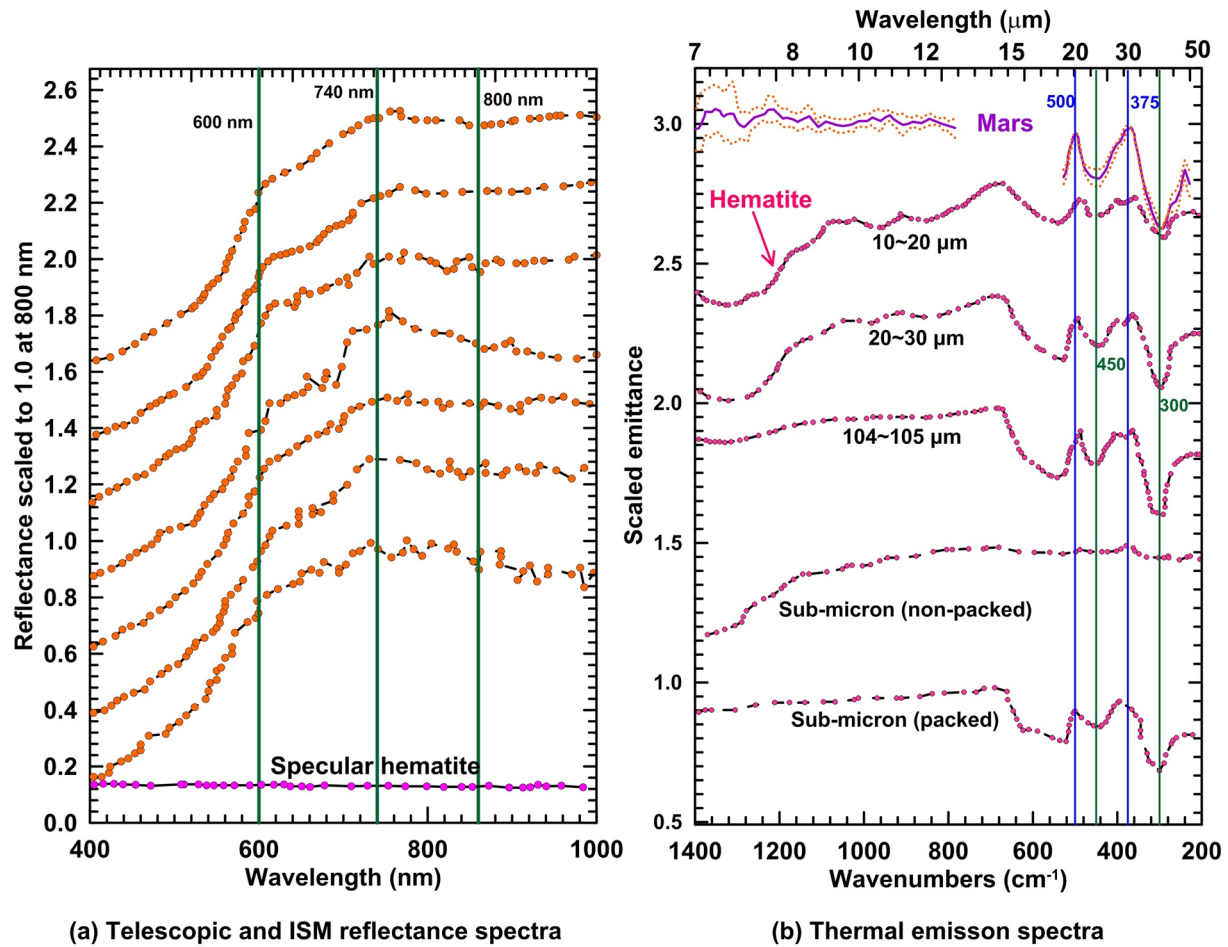
Figure 10. Spectral characteristics of the Martian surface. (a) Telescopic and imaging spectrometer for Mars (after Mustard and Bell (1994)); (b) thermal emission spectroscopy results for Sinus Meridiani, Mars, and for hematite as a function of particle diameter and packing (from Christensen, Bandfield, Clark, et al. (2000)).

contrast, TES data have discernable absorption features at 450 and 550 cm^{-1}. Nanophase and red hematite detected in high-albedo regions are mainly thought to form by weathering and alteration processes, that is, they are considered erosion products of hydrothermally altered impact melt sheets (R. V. Morris et al., 1995).

Unlike fine-grained hematite, gray hematite is spectrally neutral (nearly flat reflectivity) at visible wavelengths (400–700 nm; R. V. Morris et al., 1989), and is not detected in color spectra from Fe^{3+}-bearing bright regions on Mars (Lane et al., 2002). Gray hematite also has distinct TES features with minima at about 300, 450, and >525 cm^{-1} and maxima at about 375 and 500 cm^{-1} (Figure 10b), which results from the ordered symmetry of FeO_6 octahedra. Detailed hematite TES features for the Sinus Meridiani region (Figure 2) indicate that the spectrum is consistent with emission dominated by the crystallographic *c*-faces of platy hematite (Lane et al., 2002), which suggests that platy grains dominate the hematite particle suite. These hematite plates are inferred to have formed by low-grade metamorphism (Lane et al., 2002).

4. Complex Properties of Cation Substituted Hematite

The discussion so far has focused mainly on stoichiometric hematite. However, in natural single crystal or polycrystalline hematite, cations other than Fe^{3+} (e.g., Al^{3+}, Ti^{4+}, and Mn^{2+}) are always present to some extent (Morrish, 1994; Wells et al., 1999). Aluminum is abundant in Earth's crust. It substitutes easily for Fe in natural hematite to form Al-hematite because Fe^{3+} and Al^{3+} have a roughly similar ionic radius: 0.65 Å for Fe^{3+} versus 0.53 Å for Al^{3+} (Morrish, 1994; Morrish & Eaton, 1971; Schwertmann et al., 1977). Although it is not common in magmatic or metamorphic rocks, Al-hematite occurs widely in Al-rich tropical and subtropical soils, for example,

Brazilian and South African oxisols (Curi & Franzmeier, 1984, 1987; Fitzpatrick & Schwertmann, 1982; Fontes et al., 1991; Fontes & Weed, 1991; Zeese et al., 1994), and red soils in West Java, Indonesia (Prasetyo & Gilkes, 1994), and South China (Deng et al., 2007; Jiang, Liu, Zhao, et al., 2015). In these warm and humid environments, Al is easily incorporated into iron oxides during chemical weathering, so Al-hematite is usually of chemical origin. Long-weathered, often polygenetic soils typically have variable Al-substitution levels within profiles that reflect their Fe mobilization and precipitation stages. However, the hematite-corundum ($\alpha-Al_2O_3$) series is not a complete solid-solution series. Al substitution is limited in hematite, with maximum values of 15–18 mol.% (Schwertmann & Murad, 1988).

Magnetic and other physical properties of hematite change with cation substitution, such as unit cell parameters (e.g., Schwertmann et al., 2000; Stanjek & Schwertmann, 1992; Vandenberghe et al., 2001), T_M (De Grave et al., 1988, 2002; Sváb & Krén, 1979; Van San et al., 2001; Vandenberghe et al., 2001), T_N (Krén et al., 1974), crystalline field (Morrish, 1994), and coercivity and magnetization (Jiang et al., 2012; Liu, Roberts, et al., 2007; Roberts et al., 2006; Wells et al., 1999). Thus, studies of hematite properties with diverse cation substitution levels are important and discussion of the magnetic and color reflectance properties of hematite must consider the effects of cation substitution. Natural or synthetic doped hematite samples can provide insights into the extent of such variations.

4.1. Al Substitution

4.1.1. Influence of Al on the Unit Cell Parameters of Hematite

Cell edge lengths a and c decrease consistently with increasing Al substitution to follow Vegard's rule (Figures 11a and 11b; Barrón et al., 1984; R. Taylor & Schwertmann, 1980; Schwertmann et al., 1979; Stanjek & Schwertmann, 1992). The smaller ionic radius of Al^{3+} (0.53 Å) compared to Fe^{3+} (0.65 Å) controls this behavior. As smaller Al^{3+} ions are incorporated and occupy Fe^{3+} positions, the internal balance of $(Fe, Al)O_6$ octahedra adjusts by shrinkage and distortion to produce a disordered lattice with low crystallinity and smaller crystals (Cornell & Schwertmann, 2003).

Al substitution inevitably leads to macroscopic morphological changes. Hematite particle size (from TEM observations) decreases from several hundreds of nm to tens of nm with increasing Al substitution (Figure 11c). Thus, Al retards hematite particle growth, but this effect does not apply similarly to all crystal axes (Barrón et al., 1984; Cornell & Schwertmann, 2003; Schulze, 1984). For hematite grown from a ferrihydrite suspension, the length in the [1 0 4] direction increases with Al substitution (Jiang et al., 2012); while in the [1 1 0] direction it decreases with Al substitution. This is manifested in a larger radius but smaller hematite platelet thickness with increasing Al content. Highly substituted hematite particles have ~3 times larger platelets than non-substituted hematite while, in contrast, their thickness can decrease by ~25% (Barrón et al., 1984).

4.1.2. Influence of Al on the Magnetic Properties of Hematite

The magnetic properties of hematite depend on its crystallinity, particle size, and crystal morphology (Cornell & Schwertmann, 2003; Dunlop, 1971). Al substitution exerts a profound influence on the crystallinity and crystal habit of hematite. Therefore, the magnetic properties of hematite vary systematically with Al content.

For stoichiometric hematite without cation substitution, the SP/SD threshold size at room temperature is 27.5 ± 5 nm, and the upper SD limit is >15 μm (Banerjee, 1971; Dunlop & Özdemir, 1997; Kletetschka & Wasilewski, 2002). However, based on the grain size-dependence of B_c, M_{rs}, and T_b for Al contents >16 mol.%, the SP/SD threshold is lowered to 17 nm (Jiang, Liu, Dekkers, et al., 2014; Figure 12). As particle size decreases, room temperature hysteresis loops narrow (Figure 12a), which reflects a change from solely SD, to SP/SD mixtures, to an entirely SP assemblage (Evans & Heller, 2003; Roberts et al., 1995). Simultaneously, the Morin transition becomes weaker, T_M shifts to lower temperatures, and the isothermal remanent magnetization (IRM) imparted at 10 K (IRM_{10K}) is no longer temperature-independent but decreases with increasing temperature (Figure 12b), which leads to curling of low temperature curves with increasing SP behavior. The Morin transition disappears in a sample with 23.5 nm mean particle size, but IRM_{10K} remains after warming to 300 K, which demonstrates the existence of SD particles (Figure 12b). For samples with mean particle size below 17 nm, IRM_{10K} is nearly zero at 300 K, which indicates a dominance of SP particles. Room temperature B_c and M_{rs} approach zero at
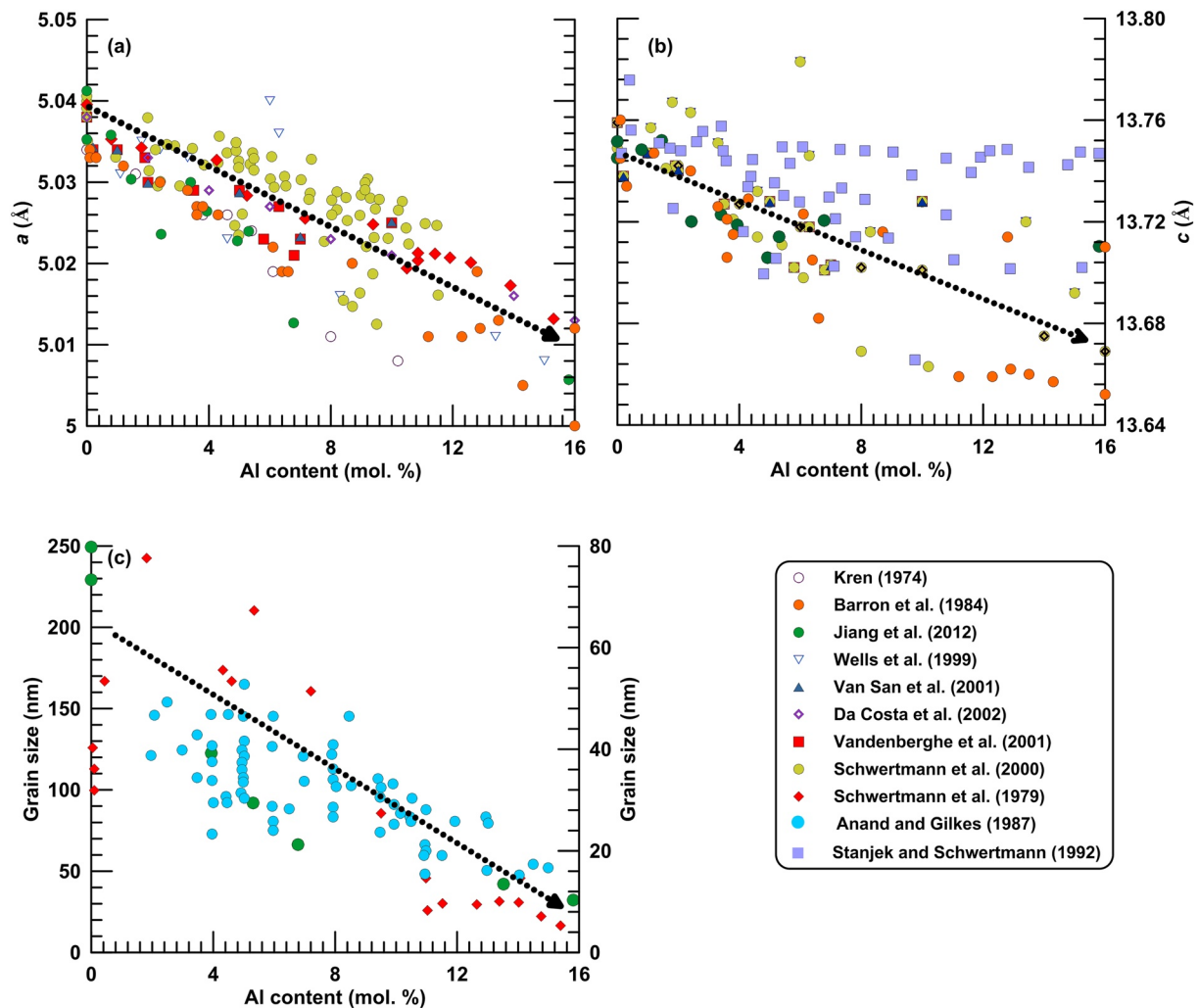
Figure 11. Dependence of unit cell parameters and particle size on Al content. (a) Unit cell parameter *a*; (b) unit cell parameter *c*; and (c) grain size, all with respect to Al content in mol.%. The left-hand axis is for data from Jiang et al. (2012); the right-hand axis is for data from Anand and Gilkes (1987) and Vandenberghe et al. (2001). The dashed lines with arrows represent overall data trends.

~17 nm, while T_b drops from 800 to 200 K at the same size, which defines the SP/SD threshold size for Al-Hm with Al content above 16 mol.% at room temperature (Figure 12c).

Magnetic parameters for hematite also depend on the amount of Al-substitution (Figure 13). T_N is controlled by the magnetic energy and magnetic exchange interaction of Fe ions (O'Reilly, 1984). Substituting nonmagnetic Al ions decreases the exchange interaction energy, so less thermal energy is needed to overcome the magnetic energy. Therefore, T_N decreases continuously with increasing Al substitution. Magnetic susceptibility (χ) and coercivity have different trends. For Al contents <~8 mol.%, χ correlates negatively with Al content, while it increases for higher Al contents (Figure 13a; Jiang, Liu, Colombo, et al., 2014; Jiang et al., 2012; Wells et al., 1999). In contrast, compared to χ, B_c has an opposite relationship with Al content (Jiang, Liu, Dekkers, et al., 2014; Jiang et al., 2012; Liu, Roberts, et al., 2007; Roberts et al., 2006; Wells et al., 1999). For Al contents <~7–8 mol.%, B_c increases steadily and non-linearly with increasing Al content from several tens of mT for pure hematite to several hundreds of mT (Figure 13b). For Al contents >8 mol.%, B_c correlates negatively with Al content (Figure 13b). This could be due to continuously dropping T_N. Thus, Al-substitution magnetically hardens hematite but lowers its T_N at the same time. At low substitution levels, hardening dominates but for higher levels the effects of falling T_N dominate. Unlike χ and B_c, M_{rs} decreases continuously with Al substitution (Figure 13c). T_M decreases linearly with increasing Al substitution (Figure 13d; da Costa et al., 2002; De Grave et al., 2002; Jiang, Liu, Dekkers, et al., 2014; Jiang, Liu, Zhao, et al., 2015; Jiang et al., 2012; Krén et al., 1974; Srivasta & Sharma, 1972; Sváb &
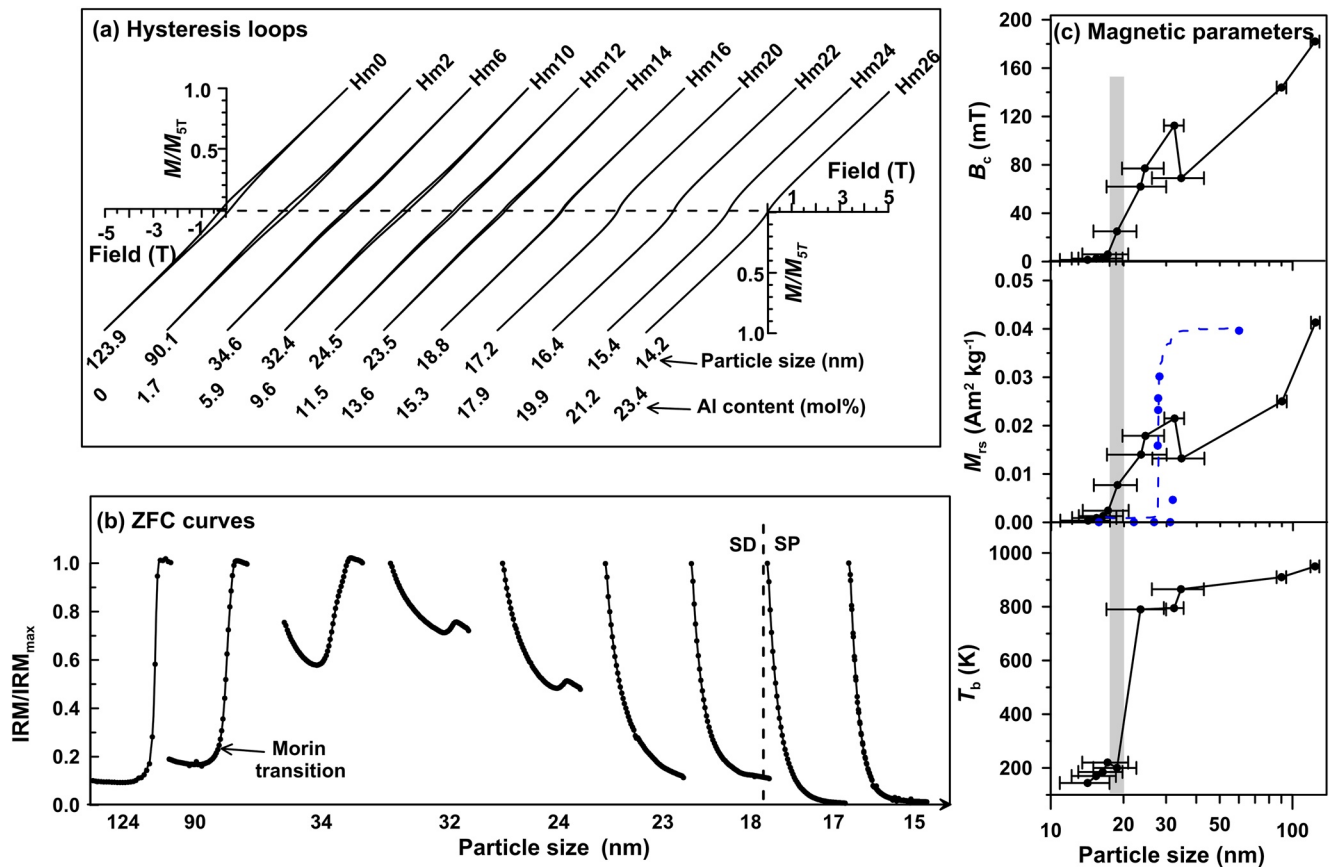
Figure 12. Particle size dependence of magnetic parameters for Al-substituted hematite (from Jiang, Liu, Dekkers, et al. (2014)). (a) Room temperature hysteresis loops for Al-substituted hematite with particle sizes ranging from 14.2 to 123.9 nm; numbers below loops indicate the average particle size and Al content in samples; (b) warming curves (from 10 to 300 K) of an isothermal remanent magnetization imparted in a 5 T field at 10 K ($IRM_{10 K}$) after zero-field cooling from 300 to 10 K; and (c) particle size dependence of B_c, M_{rs}, and T_b. The shaded area represents the particle size at which the three parameters decrease abruptly. Blue solid circles are data for pure hematite from Banerjee (1971).

Krén, 1979; Vandenberghe et al., 2001; Van San et al., 2001). In addition, the amount of "spin flopping" during the Morin transition decreases with increasing Al substitution (Sváb & Krén, 1979).

In summary, Al substitution influences the magnetic properties of hematite mainly by modifying its crystallinity and particle size. When Al replaces Fe in the hematite structure, then some Fe-O bonds are replaced by Al-O bonds (Cornell & Schwertmann, 2003). The symmetrical octahedral hematite structure is distorted, which enhances internal strain. Thus, magnetoelastic anisotropy arising from internal strain increases, which increases coercivity in Al-hematite (Jiang et al., 2012, 2013). Also, nonmagnetic Al ions are incorporated randomly into A and B layers of the hematite structure (Ruan & Gilkes, 1995), so Fe ions are diluted, which decreases its magnetism (e.g., χ, M_{rs}) with increasing Al content (Jiang, Liu, Zhao, et al., 2015; Jiang et al., 2012, 2013). However, for higher Al levels, B_c decreases and χ increases (Figures 13a and 13b) as the Al-hematite particle size shifts from the SD to SP state with Al substitution (Figure 11c).

4.2. Ti Substitution

4.2.1. Magnetic Properties of Titanohematite as a Function of Ti Content

Ti can also substitute for Fe in the hematite lattice to form titanohematite ($Fe_{2-y}Ti_yO_3$) for which a complete solid solution series exists between hematite (α-Fe_2O_3) and ilmenite ($FeTiO_3$) (Bozorth et al., 1957; Hunt et al., 1995; Nagata & Akimoto, 1956; Thorpe et al., 1977). Titanohematite occurs widely in rapidly cooling extrusive rocks (Kent et al., 1978; Kletetschka et al., 2002; S. A. McEnroe, Brown, et al., 2004; S. A. McEnroe et al., 2009).
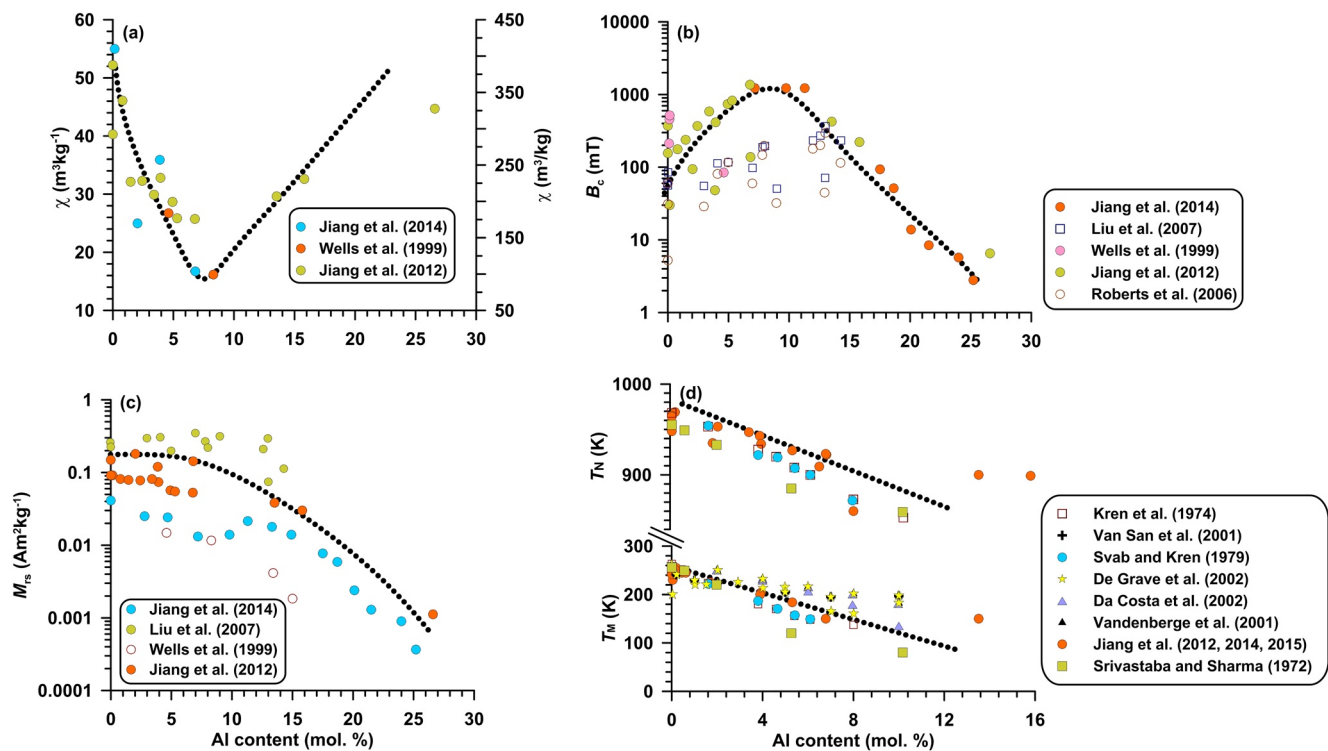
Figure 13. Magnetic parameter trends versus Al substitution in hematite. (a) χ (the left-hand axis represents data from Jiang et al. (2012), and the right-hand axis is for data from Wells et al. (1999) and Jiang, Liu, Dekkers, et al. (2014)); (b) B_c, (c) M_{rs}, and (d) T_N and T_M, all with respect to Al content in mol.%.

Ti^{4+} not only replaces Fe^{3+}, but another Fe^{3+} ion must be converted to Fe^{2+} to preserve charge balance (Bayer et al., 1972; Nagata & Akimoto, 1956), which makes Ti substitution different from Al substitution (Hartstra, 1982).

Unlike Al substitution, the unit cell parameter a increases approximately linearly with Ti content, which is attributed to the larger ionic radii of Ti^{4+} (0.74 Å) and Fe^{2+} (0.78 Å) compared to Fe^{3+} (0.65 Å) (Thorpe et al., 1977). Magnetic parameters also vary with Ti incorporation (Figure 14). The T_N of titanohematite decreases linearly with Ti content and drops below room temperature at $y = 0.75$ (Burton et al., 2008; Hunt et al., 1995; Nagata & Akimoto, 1956). However, T_C or T_N can change with annealing for 10^{-1} to 10^3 hr at 350°C–400°C due to high temperature cation reordering in Fe-Ti oxides (Bowles et al., 2012, 2013). Moreover, B_c values for titanohematite increase for $y = 0$–0.22 and then decrease as Ti content increases (Nagata & Akimoto, 1956), which is similar to the B_c trend with increasing Al substitution (Figure 13b).

M_s varies with increasing Ti content in three stages (Bozorth et al., 1957). For $0 < y < 0.55$ (stage I), Fe^{2+}, Fe^{3+}, and Ti^{4+} are distributed randomly over the titanohematite A and B sublattices, which leads to a weak net magnetism. These compositions are antiferromagnetic like endmember hematite with nearly zero M_s (Nagata & Akimoto, 1956; Robinson et al., 2002). Starting at $y = 0.55$, stages II and III have an ordered cation distribution across the A and B sublattices with Fe^{2+} and Fe^{3+} layers alternating with Fe^{3+} and Ti^{4+} layers. All Fe^{2+} occurs selectively in either the A or B sublattice, which leads to an appreciable net magnetic moment (Figure 14d). M_s increases abruptly at $y = 0.55$ and has its largest value (~40 $Am^2 kg^{-1}$) at $y = 0.67$ (stage II) (Dunlop & Özdemir, 1997; Hunt et al., 1995). For higher Ti contents, M_s drops again because T_C lowers with increasing Ti (Figure 14c) and drops below room temperature at $y \geq 0.75$. This marks stage III with M_s dropping to zero as titanohematite becomes paramagnetic at room temperature with T_N around 56 K (Hunt et al., 1995). Below T_N, stage III Ti-bearing hematite is purely antiferromagnetic with spins parallel to the basal plane even at low temperature, with the Morin transition eliminated (e.g., Harrison et al., 2010; Morrish, 1994). Thus, ferrimagnetic Ti-rich titanohematite has a distinctly stronger M_s than pure hematite while retaining the high coercivity and thermal properties of SD hematite.
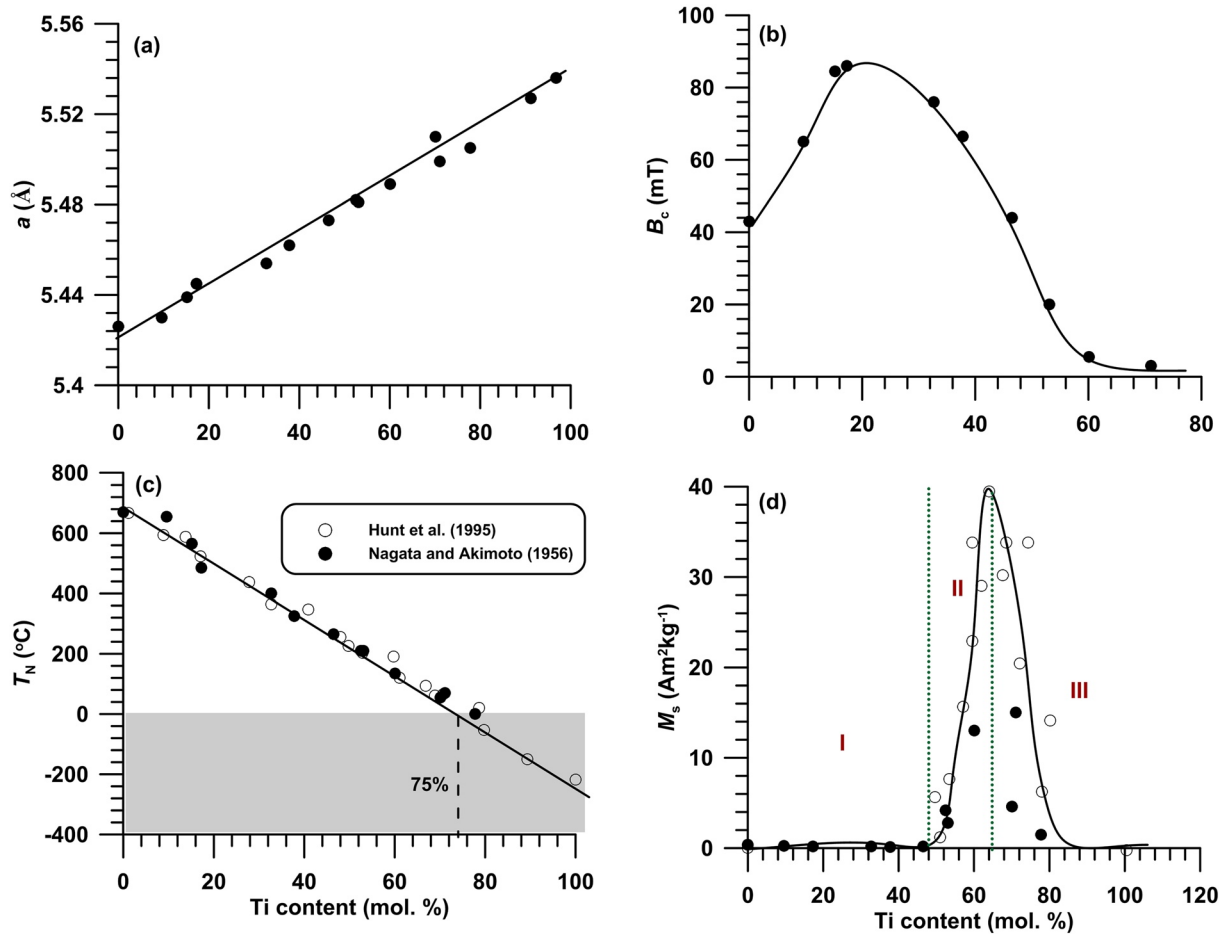
Figure 14. Magnetic parameter variations with Ti content in the titanohematite ($Fe_{2-y}Ti_yO_3$) solid-solution series. (a) Unit cell parameter a; (b) B_c; (c) T_N; and (d) M_s, all with respect to Ti content. Data are from Nagata and Akimoto (1956) (solid circles) and the compilation of Hunt et al. (1995) (open circles).

4.2.2. Lamellar Magnetism

Hematite and ilmenite intergrowths occur in some slowly cooled igneous and metamorphic rocks. Exsolution lamellae with thicknesses from 100 µm to ∼1 nm can carry an unusually strong and stable remanent magnetization (Robinson et al., 2002, 2004; McEnroe, Harrison, et al., 2001; McEnroe, Robinson, & Panish, 2001; McEnroe et al., 2016). A ferrimagnetic substructure is created by reduced charge balance along Fe^{2+}-Fe^{3+} interfaces between antiferromagnetic hematite and paramagnetic ilmenite (Fabian et al., 2008; Robinson et al., 2002, 2004). For ultrafine lamellae with an odd number of Fe-layers, spins are uncompensated and locked to the hematite structure, which produces a large magnetic moment within the interface that cannot be demagnetized. The hematite host contains a lamellar NRM that is inclined at 30° with respect to the hematite basal plane (0 0 1) (Robinson et al., 2017). Titanohematite with abundant nanoscale ilmenite exsolution (lamellar magnetism) is, thus, a major contributor to crustal magnetic anomalies, for example, the area of negative remanent magnetization near Modum, Norway (Langlais et al., 2004; S. McEnroe, Langenhorst, et al., 2004). McEnroe et al. (2009) proposed that lamellar magnetism is a potential large remanent magnetic anomaly source on Mars, which has no present-day magnetic field.

4.2.3. TRM Self-Reversal in Titanohematite

Titanohematite is often a deuteric oxidation product of titanomagnetite (e.g., H. Li & Beske-Diehl, 1991), which can carry a self-reversed TRM. Self-reversal occurs when a mineral is magnetized antiparallel to the ambient magnetic field direction (e.g., Nagata, 1952; Nagata & Uyeda, 1959). This phenomenon has been studied widely in natural and synthetic samples (Burton et al., 2008; Doubrovine & Tarduno, 2004; Fabian et al., 2008; Garming et al., 2007; Heller et al., 1986; Hoffman, 1992; Ozima et al., 2003; Sprain et al., 2016; Westcott-Lewis, 1971;

Yoshikazu & Yasuhiko, 1963). Titanohematite was studied intensively after discovery of reversed TRM in the Haruna dacite tuff from Japan (Nagata, 1952), which complicated early recognition of geomagnetic polarity reversals (A. Cox et al., 1963; McDougall & Tarling, 1963). The primary control on self-reversal in titanohematite appears to be the coexistence of two phases in a crystal (ordered and disordered ferrimagnetic phases, respectively) and their exchange interactions, rather than interactions between repeating, geometric microstructures (e.g., Hoffman, 1992; Nagata & Uyeda, 1959; Sprain et al., 2016). If ordered and disordered regions are both in the SD state, cation moments in the ordered phase couple antiparallel to, and outweigh, the weak moments of disordered domains, resulting in self-reversed TRM. Therefore, micro-intergrowths of ordered and disordered phases promote self-reversal (Dunlop & Özdemir, 1997).

4.3. Substitution of Other Cations

Some other cations can also substitute into the hematite lattice (e.g., Cr, Ni, Mn, and V). Such substitutions are less relevant in natural environments and are significant in materials science, for example, ceramic properties can be modified by various substitutions (Sileo et al., 2007; Varshney & Yogi, 2011, 2013; Yogi & Varshney, 2013). Unit cell parameters for hematite with Mn^{3+}, Cr^{3+}, or V^{3+} substitutions follow Vegard's rule, and decrease with increasing dopant content because the doped ions have smaller ionic radii (Mn^{3+}: 0.645 Å; Cr^{3+}: 0.615 Å; and V^{3+}: 0.64 Å) than Fe^{3+} (0.65 Å) (D. E. Cox et al., 1962; Sileo et al., 2007; Varshney & Yogi, 2011, 2013; Yogi & Varshney, 2013). Unit cell parameters become larger for Ni^{2+} substitution because it has a larger ionic radius of 0.69 Å (Wells et al., 1999, 2001). In contrast to Al-for-Fe substitution, Cr, Ni, or Mn substitution enhances the magnetization of hematite (Figure 15), which is due to the magnetic moment of these doped ions. When these dopants (e.g., Cr^{3+} with net moment of 3 Bohr magnetons (μ_B)) are incorporated into hematite, Fe^{3+}, with 5 μ_B moment, is replaced to produce a higher uncompensated moment than that due to spin-canting (Jiang, Liu, Zhao, et al., 2016). For Al substitution, dilution dominates because Al^{3+} is not magnetic. For all substitutions (i.e., including Ti^{4+} and Al^{3+}) T_N decreases linearly with increasing substitution, but at a different rate for each cation (Figures 13d, 14c & 15d; D. E. Cox et al., 1962; Sileo et al., 2007; Sváb & Krén, 1979) because anisotropic cell contraction provokes Fe-O angle and bond length changes that affect superexchange (Catti et al., 1995).

4.4. Influence of Cation Substitution on Hematite DRS Properties

Replacement of Fe by other metals can modify the color and DRS properties of hematite. Structural Al does not significantly influence the hue and chroma of synthetic Al-hematite, although crystals become lighter (Barrón & Torrent, 1984; Kosmas et al., 1986). The Al dependence of DRS characteristic peak positions and amplitudes for hematite are summarized in Figure 16. P_{535} and I_{535} correlate negatively with Al content, decreasing to lower wavelengths with increasing Al content. This is similar to the Al dependence of P_{425} and I_{425}, the characteristic peaks for goethite (Jiang, Liu, Colombo, et al., 2014). Al incorporation in hematite is, therefore, an important factor for its DRS properties.

Al substitution influences the DRS properties of hematite in two ways. With increasing substitution, FeO_6 octahedra in hematite are increasingly replaced by AlO_6 octahedra. Thus, Al incorporation changes Fe^{3+}-Fe^{3+} magnetic coupling between face-sharing octahedra, thereby decreasing the EPT band energy (Kosmas et al., 1986; Scheinost et al., 1999; Torrent & Barrón, 2003). Linkages between smaller AlO_6 octahedra and larger FeO_6 octahedra will also produce lattice distortions. Octahedral distortions alter Fe-O distances, which in turn alter the ligand field and shift the energy transition band positions (Burns, 1993b; Sherman & Waite, 1985). Hematite particle size also changes with Al incorporation (Figure 11c), which shifts the characteristic peak from 530 to 570 nm (Torrent & Barrón, 2003). Therefore, cation substitution should be considered when interpreting DRS data for hematite.

5. Hematite Identification and Quantification From Magnetic and DRS Properties

Based on the above-discussed crystallographic and physical properties of hematite, and key controls on their variations (e.g., particle size and cation substitution), we now explore how hematite can be identified and quantified. The main magnetic and color reflectance properties of hematite, as outlined above, are exploited for these purposes in the methods discussed below.
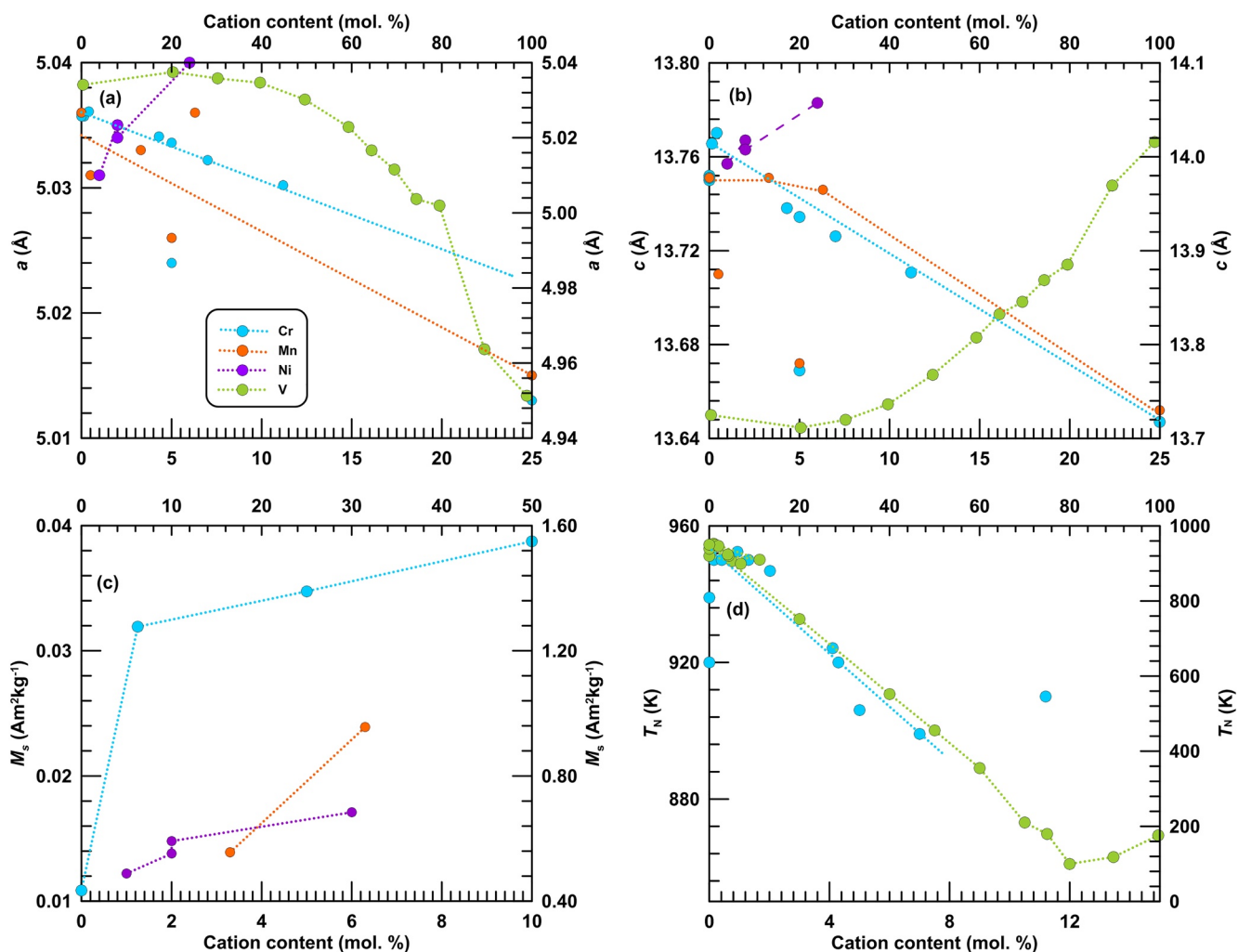
Figure 15. Relationship of unit cell and magnetic parameters versus cation substitution. (a) a and (b) c versus cation content, where Cr data are from Sileo et al. (2007) and Varshney and Yogi (2013), Mn data from Varshney and Yogi (2011, 2013) and Wells et al. (1999), Ni data from Wells et al. (1999), and V data from Cox et al. (1962). The right-hand vertical axis is for V, while the left-hand vertical axis is for Cr, Mn, Ni; (c) M_s versus cation content, where Cr data are from Yogi and Varshney (2013), Mn data are from Wells et al. (1999), and Ni data are from Wells et al. (1999). The right-hand vertical axis is for Mn and Ni, while the left-hand vertical axis is for Cr; (d) T_N versus cation content, where Cr data (left-hand vertical axis) are from Sileo et al. (2007) and Sváb and Krén (1979), and V data (right-hand vertical axis) are from Cox et al. (1962).

5.1. Hematite Identification in Natural Samples

XRD is the most direct and effective method for identifying crystalline structures. However, its detection limit is high ($\sim$2%) for fine particles. Thus, in many geological materials, where hematite is often fine-grained and occurs in trace amounts, hematite identification is not straightforward for bulk samples. Therefore, XRD analysis to determine the presence of hematite (and other iron(oxy)(hydr)oxides) is often carried out on magnetic extracts. However, hematite is magnetically weak, which makes it difficult to raise its concentration in magnetic extracts to enable identification with XRD. If adequate hematite concentrations are obtained, XRD enables its identification. Likewise, scanning electron microscope (SEM) or TEM observations coupled with X-ray microanalysis enable hematite identification.

Magnetic techniques have been used widely to identify hematite. The two most typical characteristics of hematite are its high T_N (670°C–690°C), which is noticeably different from other magnetic minerals, and the Morin transition at $\sim$250–260 K. In addition, DRS can be advantageous because its detection limit is $\sim$0.5% (Kosmas et al., 1984, 1986; Torrent et al., 1983). The typical peak and amplitude at $\sim$535 nm (P_{535} and I_{535}) in DRS second derivative curves (Figure 9f) is used widely to identify and quantify hematite in soils and sediments (e.g., Lepre
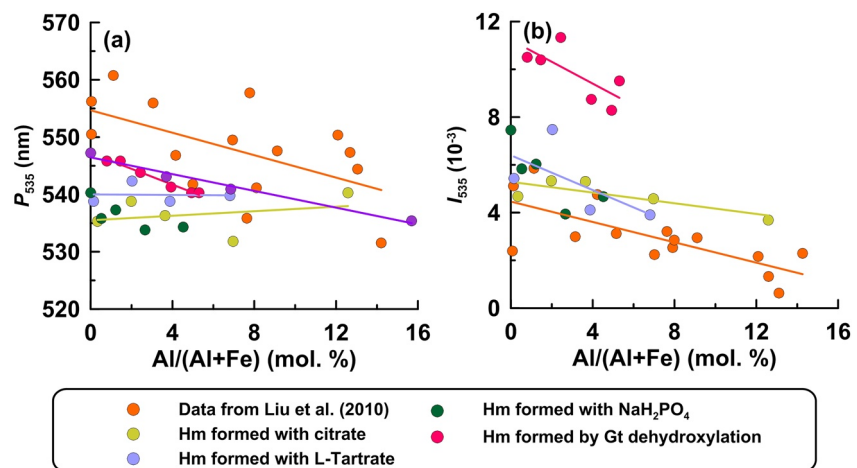
Figure 16. Diffuse reflectance spectrum parameters versus Al content for hematite. (a) Characteristic peak position (P_{535}); and (b) characteristic peak amplitude (I_{535}), both versus Al content. All data are from Jiang (2014) and Q. Liu, Barrón, et al. (2010). Different colors indicate hematite formation with various complexes in solution.

& Olsen, 2021; Q. Zhang et al., 2018; Torrent et al., 2007, 2010a, 2010b). Therefore, combined use of magnetic and DRS measurements is ideal for identifying hematite in natural samples.

Hematite is weakly magnetic and stable SD particles have high coercivity, so it can be easily confused with goethite based on magnetization and coercivity parameters, although goethite is magnetically weaker with generally considerably harder coercivity than hematite (Table 2; Reynolds et al., 2014; Rochette et al., 2005; Till et al., 2015). Moreover, the Morin transition is suppressed by small grain sizes, crystal defects, and cation substitutions. Hematite nanoparticles occur commonly in both the magnetically unstable SP state and in the magnetically stable SD state, so that use of SD-indicative parameters will underestimate its presence (e.g., Roberts et al., 2020). In addition, cation substitution affects the magnetic and DRS properties of hematite. For example, Al substitution can lower the coercivity of hematite to tens of mT or even a few mT. Similarly, T_N decreases to 850 K (~580°C) for a ~10% Al content, so that it could be mistaken for magnetite or maghemite (Jiang, Liu, Zhao, et al., 2015; Jiang, Liu, Zhao, et al., 2016; Jiang et al., 2012). Also, Ti incorporation can enhance the magnetization of hematite to 40 Am² kg⁻¹, which complicates differentiation from other ferrimagnetic minerals in igneous rocks based only on magnetization. Simultaneously, hematite color varies; for example, Mn or Ti incorporation may make hematite black. Cation substitution can, therefore, cause potential confusion between hematite and magnetite or maghemite, so that discriminating between these minerals is not straightforward.

To resolve such ambiguities, a flowchart for combined methods (magnetic, DRS, etc.) is presented in Figure 17. Its eye-catching red color provides the most direct initial evidence to identify hematite. Hematite (Hm) and maghemite (Mh) are red or brown-red, while magnetite and titanohematite (Ti-Hm) or Mn-hematite (Mn-Hm) are black, which divides these magnetic iron oxides into two branches (Figure 17). DRS can discriminate between Hm and Mh because the former has a characteristic peak at ~535 nm (P_{535}) while the peak for the latter is <500 nm (Scheinost et al., 1998). What is left is to distinguish stoichiometric from Al-substituted hematite. Key characteristics of SD and MD stoichiometric hematite are its T_N at ~680°C and T_M at ~255 K (e.g., Lagroix & Guyodo, 2017). If both parameters decrease simultaneously to lower temperatures, Al-hematite is indicated (Figure 13d). Then, for phases with black colors, the Verwey transition is the most characteristic signature of magnetite, although it is not always observed in low temperature curves when magnetite is fine-grained or partially oxidized (Chang et al., 2013; Özdemir & Dunlop, 1993). In addition, the T_N of Ti-Hm can decrease to 580°C; nevertheless, B_c for such titanohematite is higher than for magnetite. Thus, combining B_c and T_N can help to distinguish between magnetite and Ti-Hm.

5.2. Hematite Quantification in Natural Samples

The abundance of hematite in natural environments makes its quantification important in paleoenvironmental studies of soils and sediments. The main challenge for quantifying hematite is its weak spontaneous magnetization

Table 2
Summary of Magnetic and DRS Methods for Hematite Identification and Quantification

Purpose	Method	Parameter	Advantage(s)	Disadvantage(s)	Additional information
Identification	Magnetic methods	T_N	Not sensitive to non-magnetic matrix; no grain size control	Time-consuming and destroys samples	Insensitive to non-magnetic matrix; lower limit exists for detecting weak magnetic phases; detects both pigmentary and specular hematite
		Morin transition	Clear indicator of the presence of hematite	Suppressed by fine grain sizes, crystal defects, and cation substitution	
		M_{rs}, B_c, and B_{cr}	Rapidly measured	Indicator of hematite, although goethite can have similar properties	
	DRS	Positions of characteristic DRS (P_{535}) peaks	Lower detection limit, rapid measurement	Influenced by non-magnetic matrix and grain size; cannot discriminate between specularite and pigment	
Quantification	Magnetic methods	HIRM	Estimate of absolute hematite concentration	Cut-off field of 300 mT can be ambiguous for separating ferrimagnetic minerals with coercivity tail >300 mT and hematite softer than 300 mT	
		S-ratio	Estimate of relative hematite concentration		
		M_{fr}	Decreases strong magnetic background; isolates weak imperfect antiferromagnetic signal	Sensitive to applied field errors	
		$IRM_{0.9T}@AF_{120\,mT}$	Useful for u-channel samples	Ambiguous when soft goethite is present	
		Remanence after $TD_{120°C}$ and $AF_{80\,mT}$	Removes goethite and soft ferrimagnetic contributions	Soft hematite fraction will also be demagnetized	
		$^{1.5-0.3T}$IRM cycling: 300–400–300 K	Removes goethite and ferrimagnetic contributions	Magnetically soft nanohematite particles (<~200 mT) may also be demagnetized; time-consuming	
	DRS	Redness ratings	Rapidly and easily measured	Influenced by other red or brown magnetic minerals, for example, maghemite	Rapidly measured; sensitive to matrix composition; effective in soil and sediment (lacustrine, eolian, marine) studies
		Calibrated DRS functions	Effective for Chinese loess/paleosol samples	Influenced by other red or brown magnetic minerals, for example, maghemite; not proven for other regions	
		I_{425} and I_{535}	Low detection limit; rapidly measured	Influenced by non-magnetic matrix	

Note. DRS, diffuse reflectance spectroscopy.

($M_s = \sim 0.4$ Am^2/kg) compared to ferrimagnetic minerals (e.g., magnetite, $M_s = 92$ Am^2/kg), so hematite information must be extracted from a potentially strongly magnetic background. It is also often poorly crystalline, which poses challenges for mineralogical, spectroscopic, and magnetic identification. Many parameters have been proposed to quantify hematite by magnetic or color reflectance methods, as summarized by Roberts et al. (2020).

5.2.1. Hard Isothermal Remanent Magnetization (HIRM) and S-Ratio

Hematite can have such high coercivity that it is difficult to saturate without specialized magnetic instruments, while strongly magnetic ferrimagnetic minerals have low coercivity and tend to dominate magnetic measurements. Use of magnetic properties to extract information about hematite usually exploits distinct coercivity differences between hematite and ferrimagnetic minerals. As detailed by Roberts et al. (2020), the S-ratio and
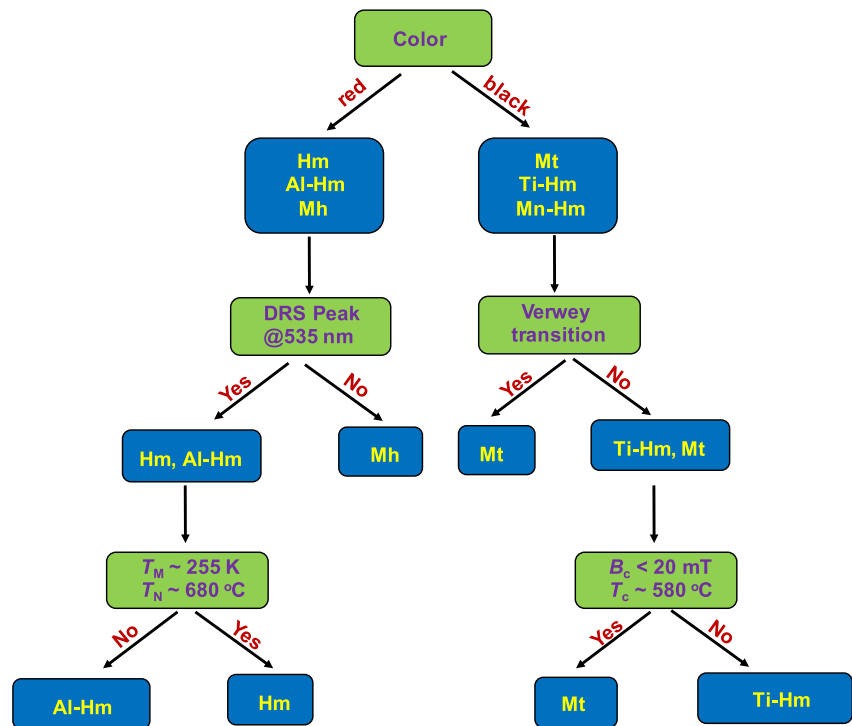
Figure 17. Flow chart for identifying hematite (Hm), magnetite (Mt), and maghemite (Mh) by combining color characteristics and magnetic properties.

HIRM have limitations for quantifying hematite without independent constraints on the magnetic mineralogy. Nonetheless, we detail here the ideas behind use of these parameters and highlight their value and limitations.

Collinson (1968) reported that IRM acquisition in direct current (DC) fields above 300 mT is effectively due to hematite-type minerals only, so this field is used as a cutoff to separate IRM acquisition due to hematite compared to magnetically "soft" minerals. The S-ratio ($S = -\mathrm{IRM}_{-300\,\mathrm{mT}}/M_{rs}$) was proposed to calculate the relative proportions of magnetically "soft" versus "hard" minerals in samples (Bloemendal, 1983; Bloemendal et al., 1988; J. W. King & Channell, 1991; Robinson, 1986). An alternative formulation was proposed by Bloemendal et al. (1992): S-ratio = $[(-\mathrm{IRM}_{-300\,\mathrm{mT}}/M_{rs}) + 1]/2$. Users should be aware of which S-ratio version is used when comparing data between studies. S-ratios vary between +1 and −1 in the former definition and between +1 and 0 in the latter. A value of +1 is interpreted to indicate that only ferrimagnetic minerals (e.g., magnetite) are present. In contrast, low or negative values indicate that significant hematite contributions are likely. Robinson (1986) also suggested that the remanence that remains unreversed after applying a DC backfield of −300 mT is carried by the magnetically hard minerals, hematite and goethite. Therefore, he proposed the "hard" IRM (HIRM = $(M_{rs} + \mathrm{IRM}_{-300\,\mathrm{mT}})/2$) to express the difference between the backfield magnetization at −300 mT and the initial M_r of a sample to quantify hematite or goethite contents. Goethite is far from saturation even in a 57 T field (Rochette et al., 2005), so HIRM can be a quantification proxy for hematite concentration that is largely saturated in ∼3 T applied fields (Dunlop, 1971) and has been used extensively and valuably for this purpose (Abrajevitch et al., 2018; Bailey et al., 2011; Bloemendal & Liu, 2005; Hao et al., 2009; Larrasoaña et al., 2003; Lyons et al., 2010; Nie et al., 2010; Yamazaki & Ioka, 1997). However, it should be remembered that phases such as pyrrhotite, partially oxidized magnetite, greigite, and titanomagnetite can have a coercivity tail above 300 mT and that some hematite will be softer than 300 mT.

5.2.2. Residual Remanent Magnetization After Demagnetization

The magnetization of natural samples is often dominated by the strong magnetism of ferrimagnetic minerals (magnetite and maghemite). Detecting weakly magnetic antiferromagnetic minerals (hematite and goethite), thus, becomes more challenging. To remove interference from strongly magnetic minerals, Liu et al. (2002) proposed a method to separate a weak imperfect antiferromagnetic signal from a strong ferrimagnetic background signal

by measuring M_{fr}, a residual or final remanence after hysteretic demagnetization of M_{rs}. The hysteretic demagnetization process includes imparting a saturation IRM (SIRM) in a 1 T or 2 T field using a vibrating sample magnetometer, then subjecting samples to successive reversed fields with decreasing peak levels to mimic a low frequency AF demagnetization with an alternating DC field. The maximum demagnetization field then provides a measure of the remanent coercivity of the undemagnetized magnetic mineral assemblage within a sample. This treatment almost completely removes signals due to strongly magnetic minerals and leaves information due to hematite. Compared to classic AF demagnetization (with typical maximum peak fields of ∼100–120 mT), higher fields can be used for hysteretic demagnetization (e.g., up to ∼1–2 T) with this approach. Compared to HIRM, M_{fr} is the residual SIRM after direct demagnetization, so no errors are propagated by subtracting terms. Hysteretic demagnetization decreases the effects of a strongly magnetic background, for example, initial non-zero HIRM offsets for partially oxidized magnetite, to enable isolation of the weak imperfect antiferromagnetic signal.

Additionally, unreliable IRM$_{0.9\,T}$ and IRM$_{-0.3\,T}$ values can be obtained for u-channel samples because IRM intensities often exceed the dynamic range of the SQUID magnetometers used for such measurements (Weeks et al., 1993). To avoid this and other uncertainties related to HIRM calculation (Q. Liu et al., 2002), Larrasoaña et al. (2003) developed a hematite concentration proxy (IRM$_{0.9\,T}$@AF$_{120\,mT}$) by AF demagnetizing the IRM$_{0.9\,T}$ at 120 mT, which removes contributions due to magnetite. They used this parameter to investigate Saharan dust input to eastern Mediterranean sediments and found that IRM$_{0.9\,T}$@AF$_{120\,mT}$ is a useful hematite concentration proxy that correlates with an acknowledged eolian proxy (Ti/Al). Combined with the different LT magnetic behavior of hematite and goethite (i.e., hematite IRM is temperature independent below the Morin transition, while goethite IRM increases almost linearly to 4 K), this approach has value in identifying and separating magnetic contributions due to hematite and goethite (Maher et al., 2004). K. P. Kodama and Dekkers (2004) proposed that hematite remanences can be isolated by thermal demagnetization at 120°C to remove goethite contributions, followed by AF demagnetization to remove soft ferrimagnetic contributions, although a soft hematite fraction will also be demagnetized by this procedure. Separating signals due to goethite and hematite is important for isolating hematite contributions. Carter-Stiglitz et al. (2006) proposed a parameter named $^{1.5\text{-}0.3T}$IRM to quantify hematite using a two-step procedure with a superconducting magnet and magnetometer system: (1) samples are magnetized in a 0.3 T direct field, partially AF demagnetized with a 0.2 T field, and the remanence is measured; (2) then it is remagnetized in a 1.5 T field followed by partial demagnetization as in step 1 and the resulting $^{1.5\text{-}0.3T}$IRM is measured. A 300 → 400 → 300 K thermal cycling in zero field will then thermally demagnetize any goethite, so that $^{1.5\text{-}0.3T}$IRM is due solely to hematite. Lagroix and Guyodo (2017) used an oscillation mode to sweep the field to make a coarse effective AF demagnetization without sample removal to allow continuous temperature cycling. Bilardello (2019) summarized this approach and outlined caveats that inhibit separation of contributions to $^{1.5\text{-}0.3T}$IRM. For example, nano hematite can have softer coercivity than larger SD grains and can be demagnetized below 200 mT. Such grains will generally be attributed to the soft magnetite fraction. Also, some maghemitized grains can survive 200 mT AF demagnetization but lose part of their remanence by 400 K, which affects determination of the relative contributions of all phases. This parameter and related tests are generally useful for soils and sediments, although the above caveats should be considered.

5.2.3. Redness Ratings

Hematite is the most important pigmenting agent in organic-poor soils and sediments, so color is useful for approximating hematite contents in soils and paleosols (Torrent et al., 1980). Redness ratings (RR) from visual or spectroscopic measurements correlate with hematite content and are used for hematite quantification (Torrent et al., 1983). The RR is defined as:

$$RR = \frac{(10 - H) \times C}{V} \ , \tag{3}$$

where C and V are numerical values of the Munsell chroma and value, respectively, and H (hue) is the number preceding YR in the Munsell color coding scheme. For example, H is 10 for 10YR and H is 0 for 10R. This parameter provides discrimination between yellowish brown and red colors. Another redness index (RI, Torrent et al., 1983) is defined as:

$$RI = \frac{(x - 0.35)^2}{(y - 0.35)Y} \ , \tag{4}$$

where x and y are the chromaticity coordinates, and Y is the luminosity based on the des Séances (1931) definition. The 0.35 subtracted from x and y are the x, y values of the Munsell color 10YR 7/2.3 (very pale brown), which is typical of a hematite-free reference soil. Both RR and RI correlate linearly with hematite content in European soils (Torrent et al., 1983).

5.2.4. Diffuse Reflectance Spectroscopy

Magnetically "hard" goethite and hematite coexist in many terrestrial environments, so it is difficult to exclude goethite when using magnetic methods to quantify hematite. Also, the large fields required to magnetically saturate hematite and goethite, and their relatively weak magnetizations, make it difficult to estimate their absolute abundances accurately with magnetic methods. DRS in the VIS (~400–700 nm) and NIR (~700–2,500 nm) ranges is more suited to identification and semi-quantitative determination of goethite and hematite abundance in soils (Balsam et al., 2004; Cornell & Schwertmann, 2003; Ji et al., 2004; Torrent et al., 2007) and sediments (Balsam & Deaton, 1996; Y. G. Zhang et al., 2007). Iron oxides have different colors and reflectance (Scheinost & Schwertmann, 1999). Thus, DRS analysis is useful for identifying and characterizing iron oxides, especially hematite and goethite.

5.2.4.1. Calibrated DRS Functions

Color spectra can be divided into six bands: violet = 400–450 nm, blue = 450–490 nm, green = 490–560 nm, yellow = 560–590 nm, orange = 590–630 nm, and red = 630–700 nm (Judd, 1952). Total sample reflectance or brightness is calculated by summing reflectance values from 400 to 700 nm (Balsam et al., 1999). The reflectance percentage in these standard color bands is calculated by dividing the reflectance percentage in a given color band by the total sample reflectance. Ji et al. (2002) produced a natural matrix material to which hematite and goethite were added in known weight percentages to produce calibration standards. The reflectance of standard color bands and brightness were measured to provide independent variables for multiple linear regression analysis. The next empirical calibration functions were then used to estimate hematite and goethite contents in Chinese loess/paleosols (Figure 18a):

$$\text{Hematite (\%)} = -1.261 - 0.0791 \times \text{green (\%)} + 0.208 \times \text{blue (\%)} + 0.103 \times \text{orange (\%)} - 0.0863 \times \text{violet (\%)} \, (R^2 = 0.985), \tag{5}$$

$$\text{and Goethite (\%)} = -10.6 + 1.084 \times \text{yellow (\%)} - 0.718 \times \text{orange (\%)} + 0.34 \times \text{red (\%)} \, (R^2 = 0.938). \tag{6}$$

The reliability of these empirical equations has been demonstrated with Chinese loess/paleosol samples, which indicates that the hematite/goethite ratio is higher in paleosols than in loess because of their redness (Balsam et al., 2004; Ji et al., 2004). However, these equations are only applicable to loess and paleosol samples because each sample type requires its own set of standard samples.

5.2.4.2. DRS Derivative Curves

The color of hematite is related to the position and intensity of the main absorption bands in the visible light spectrum. To enhance the resolution of reflectance features, Deaton and Balsam (1991) calculated the first derivative of a DRS curve to obtain characteristic goethite (primary and secondary peaks at 535 and 435 nm) and hematite peaks (prominent peak at 575 nm), the intensities of which are used to measure their contents. However, to improve resolution compared to raw DRS curves and their first derivative, Kosmas et al. (1984, 1986) and Scheinost et al. (1998) used the second derivative of raw spectra and the K-M function (Section 3.5), respectively, to detect and quantify iron oxides in soils and sediments. The ordinate difference between a minimum and the next maximum at a longer wavelength (band intensity) is used as a proxy for band amplitude (Figure 9f). Work on natural soil samples indicates a significant correlation between hematite content and I_{535}, and goethite content and I_{425}, where hematite and goethite contents were determined by differential XRD (Figure 18b). Therefore, I_{425} and I_{535} are proportional to goethite and hematite concentrations, respectively, and serve as proxies for their mass concentration changes (Scheinost et al., 1998). Second derivative curves of DRS spectra are, thus, used widely to "fingerprint" iron oxides in soils and sediments (Balsam et al., 2004; Hao et al., 2009; Q. Zhang et al., 2018; Torrent et al., 2007).
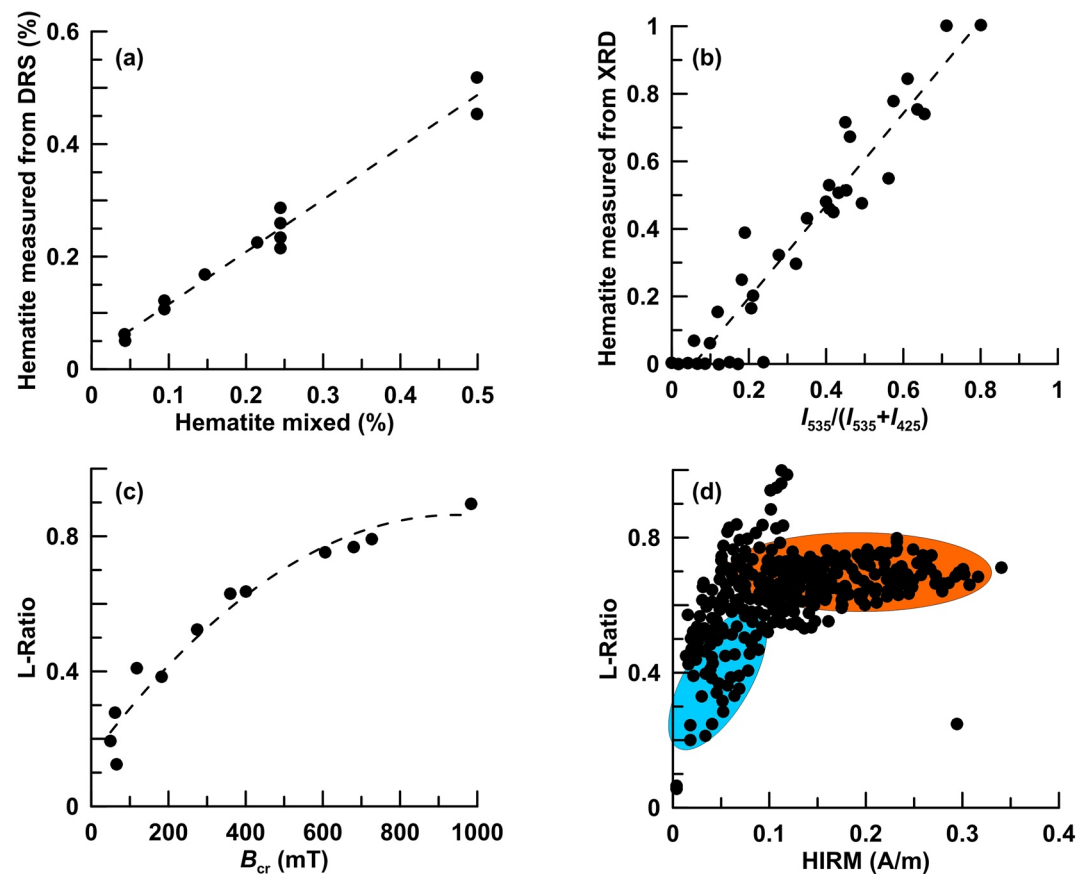
Figure 18. (a) Hematite measured from diffuse reflectance spectroscopy (DRS) versus hematite mixed in the matrix (Ji et al., 2002); (b) relationship between hematite/(hematite + goethite) as determined by differential X-ray diffraction, and $I_{535}/(I_{535}+I_{425})$ determined by DRS (Scheinost et al., 1998); (c) L-ratio versus B_{cr} for Al-hematite (Liu, Roberts, et al., 2007); and (d) L-ratio versus HIRM for samples from ODP 967, eastern Mediterranean Sea (Liu, Roberts, et al., 2007). Blue and orange shaded areas indicate samples for which HIRM cannot and can be used, respectively, to estimate hematite concentration.

Based on DRS band intensity (I_{535} and I_{425}), the hematite to goethite ratio (Hm/Gt) is determined as I_{535}/I_{425}. However, it is difficult to obtain the absolute hematite concentration. To address this issue, Torrent et al. (2007) used citrate-bicarbonate-dithionite (CBD)-extractable Fe (Fe_d) to aid DRS quantification, in which Fe_d is extracted with a CBD reagent at 25°C for 16 hr. Fe_d is assigned to the combination of Fe in stoichiometric hematite and goethite (Q. Liu et al., 2004; Torrent et al., 2007). Then, the following two empirical equations were obtained:

$$Y = -0.133 + 2.871X - 1.709\ X^2,\ \text{and} \tag{7}$$

$$Fe_d = Hm/1.43 + Gt/1.59, \tag{8}$$

where Y is the Hm/(Hm + Gt) ratio and X is $I_{535}/(I_{425} + I_{535})$. Hematite and goethite concentrations can be calculated from these equations. DRS has been used widely to quantify hematite in Chinese loess/paleosol units (P. Hu et al., 2013, 2015) and European soils (Buggle et al., 2014; Torrent et al., 2010a, 2010b).

5.2.5. Limitations of Hematite Quantification Methods and Ways Forward

Despite widespread use of the above quantitative parameters in environmental magnetism, their interpretation is not straightforward because the magnetic and color properties of hematite are controlled by both grain size and cation substitution. The advantages and disadvantages of magnetic and DRS methods for hematite identification and quantification are summarized in Table 2. As reviewed by Roberts et al. (2020), HIRM, S-ratio, $IRM_{AF@x\ mT}$, and other parameters all exploit hematite coercivity based on the assumption that hematite does not make large contributions to remanence below the 300 mT cutoff field (Table 2). However, cation-substituted hematite

(e.g., Al-hematite) is widespread in nature and its coercivity ranges from several tens of mT to several T (Jiang, Liu, Dekkers, et al., 2014; Jiang et al., 2012, 2013; Wells et al., 1999), which may partially overlap with that of ferrimagnetic minerals. Thus, a considerable portion of hematite IRM can reside in particles with coercivity <300 mT in pure and natural hematite samples (Roberts et al., 2020). The remanence of hematite is also lowered by cation substitution (Figure 13c; Jiang et al., 2012; Liu, Roberts, et al., 2007), which makes it difficult to discriminate between low hematite concentrations and widespread cation substitution. The same ambiguity exists in DRS proxies because the DRS bands at 425 and 535 nm (I_{425} and I_{535}) are also influenced by the degree of Al substitution (Figure 16) and hematite surface area (Jiang, Liu, Colombo, et al., 2014; Q. Liu et al., 2011; Torrent & Barrón, 2003). Therefore, these parameters should be interpreted with caution.

To circumvent these issues and to trace coercivity variations, Liu, Roberts, et al. (2007) defined the L-ratio, which is the ratio of two remanences after AF demagnetization of an IRM imparted in a 1 T field with 100 and 300 mT peak AFs: $IRM_{AF@300\ mT}/IRM_{AF@100\ mT}$. If the L-ratio is close to 1, HIRM and S-ratio reflect hematite concentration changes. Conversely, L-ratio fluctuations indicate variable coercivities that can reflect wide grain size ranges or cation substitution in hematite (Figures 18c and 18d). Thus, the L-ratio reduces ambiguities associated with interpretation of widely used parameters such as the HIRM and S-ratio (Hao et al., 2008, 2009; Lyons et al., 2010). Additionally, contributions to remanence below the 300 mT cutoff field can be tested using the median coercivity and width of the IRM acquisition peak (dispersion parameter; see Figure 7 of Abrajevitch et al. (2009)).

In addition, to reduce ambiguities caused by variable cation substitution, Liu et al. (2011) and Jiang, Liu, Colombo, et al. (2014) proposed parameters to indicate Al substitution, for example, T_N or T_b, which vary linearly with Al content. Based on this, Hu et al. (2016) tested the feasibility and limitations of estimating Al-hematite and Al-goethite concentrations by combining DRS and magnetic analyses. They found that for limited Al substitution (Al mol.% < ~8%), DRS amplitudes can provide reliable Gt/Hm estimates. Empirical relationships between DRS band intensity ratio and the true Gt/Hm concentration are, thus, proposed: Gt/Hm = $1.56 \times (I_{425}/I_{535})$ or Gt/Hm = $6.32 \times (I_{480}/I_{535})$) (P. Hu et al., 2016). Therefore, combining DRS and magnetic analyses can aid hematite quantification, along with knowledge of the Al substitution level.

6. Natural Remanent Magnetizations Recorded by Hematite

In addition to identifying hematite and quantifying its content to understand natural environmental processes, hematite is paleomagnetically important. Complexities associated with magnetic remanence acquisition must be considered to understand its recorded paleomagnetic signals.

6.1. Different Magnetic Remanence Types in Hematite

The NRM in most red beds and soils is due to a combination of detrital hematite, also termed specularite, and authigenic, pigmentary hematite (Collinson, 1966, 1974; Tauxe et al., 1980). The former records a DRM while the latter records a CRM. Authigenic hematite may have formed long after red bed deposition (Van der Voo & Torsvik, 2012). In such cases the red beds record a CRM that may partially or completely overprint a primary DRM, thus markedly complicating paleomagnetic interpretation (e.g., Dekkers, 2012; Deng et al., 2007; K. Huang & Opdyke, 1996; Stearns & Van der Voo, 1987), although this distinction is not absolute. For example, martite is a form of hematite that results from chemical conversion of magnetite. Even though it forms chemically, it is a specularite and is assumed to carry a DRM if it is deposited as martite (e.g., Steiner, 1983). Conversion from magnetite to martite can also occur in situ after DRM acquisition (e.g., Reynolds, 1982; Walker et al., 1981) and hematite can form at high temperatures to carry a TRM. MD hematite carries a comparable TRM to that of MD magnetite (Dunlop & Kletetschka, 2001; Kletetschka et al., 2000c), which has been suggested to make it an important contributor to magnetic anomalies on Mars. These remanence types are discussed in more detail below.

6.1.1. DRM in Hematite

Detrital hematite grains, released from their parent rock by weathering, and then transported and incorporated within sediments, can have their magnetic moments align partially with the ambient geomagnetic field during deposition or shortly after, thus contributing to a DRM, which is a statistical ensemble of partially aligned grains. DRMs carried by hematite have been identified in paleomagnetic studies of red beds from the Tibetan Plateau (Tan et al., 2003; Yan et al., 2006), Northwest China (Z. Sun et al., 2006), South China (Faure et al., 2016; K.
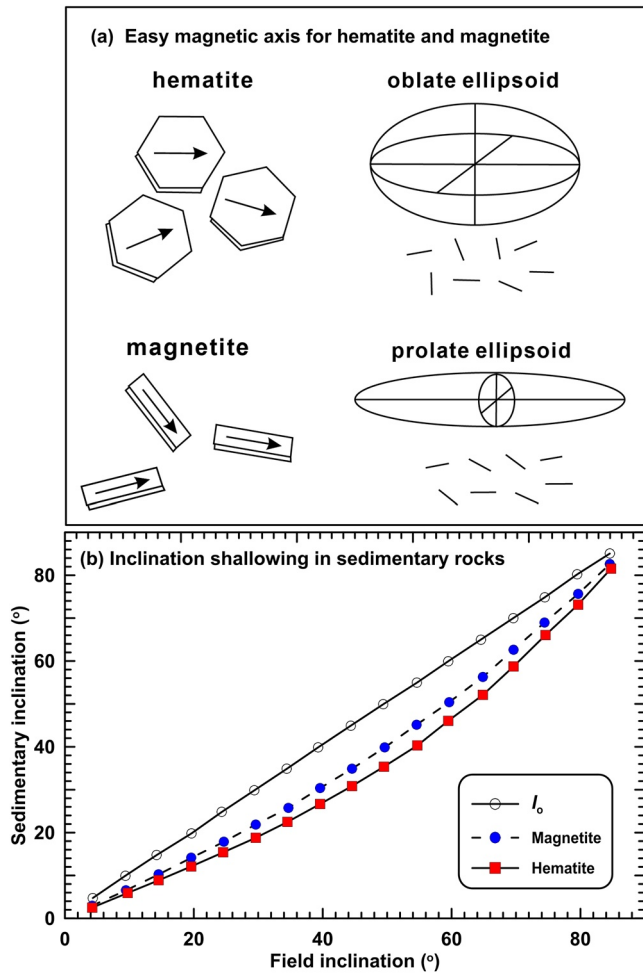
Figure 19. Contrasting magnetic easy axes and paleomagnetic inclination shallowing for hematite and magnetite (from Kodama (2012)). (a) Easy magnetic axes for hematite hexagonal plates and for magnetite particles. Oblate and prolate ellipsoids graphically represent orientation distributions of particle magnetic easy axes. (b) Inclination shallowing magnitude for typical magnetite and hematite-bearing sedimentary rocks.

Huang & Opdyke, 1991, 1993, 1998; K. Huang et al., 2000), North America (Elston & Purucker, 1979; Kent & Opdyke, 1985; Kodama, 1997; Steiner, 1983; Swanson-Hysell et al., 2019; Walker et al., 1981), and Europe (Iosifidi et al., 2010; Kruiver et al., 2000), and provide important data for chronological and tectonic reconstructions. Detrital hematite may be of HT origin with unblocking temperatures up to T_N. Therefore, to isolate a primary red bed DRM, best practice is to undertake detailed stepwise thermal demagnetization to >600°C, or even >650°C (Swanson-Hysell et al., 2019). DRM-carrying hematite consists of relatively large particles that yield a block-shaped unblocking spectrum with limited unblocking below 600°C. Such a block-shaped unblocking spectrum can then be related to the hematite deposition mode in red beds because hydrodynamic sorting associated with detrital hematite transportation will generally produce a narrower and coarser grain size distribution (Swanson-Hysell et al., 2019). Authigenic pigmentary hematite is fine grained with a broad size range and wide remanence unblocking spectrum.

For a hematite DRM, inclination shallowing caused by either flattening of hematite plates into the bedding plane or burial compaction during deposition is unavoidable. It has been detected in many studies, including of Miocene Siwalik Group red beds, Pakistan (Tauxe & Kent, 1984), Cretaceous and Early Tertiary rocks of Western China (Dupont-Nivet, Butler, et al., 2002; Dupont-Nivet, Guo, et al., 2002; Gilder et al., 2003; Tan et al., 2010; Yuan et al., 2020), central Asia (Gilder et al., 2001), Pennsylvanian Mauch Chuck Formation red beds, USA (Bilardello & Kodama, 2009, 2010), Permo-Carboniferous sediments, Ukraine (Iosifidi et al., 2010), and in laboratory redeposition experiments (Bilardello et al., 2012; Tan et al., 2002). Hematite-bearing rocks appear to be more affected by inclination shallowing than magnetite-bearing rocks with 25°–30° shallowing often observed (Figure 19; Gallet et al., 2012; Iosifidi et al., 2010; K. P. Kodama, 2012). This could be due to particle shape differences between the two minerals. For magnetite, magnetic "easy" axis alignment is controlled by particle shape anisotropy that lies parallel to particle long axes. Easy axis directions are controlled crystallographically in hematite, and typically lie in the basal crystallographic plane. However, particle shape is still important. If hematite plates are present, they will flatten into the bedding plane, which contributes to greater inclination shallowing than is the case for magnetite (Figure 19). The degree of flattening depends on inclination, as given by (R. F. King, 1955):

$$\tan I_o = f \ \tan I_f, \tag{9}$$

where I_o and I_f are the observed and applied field inclinations, respectively, and f is the so-called flattening factor. Bilardello and Kodama (2010) summarized reported f factors for hematite-bearing rocks from which inclination-shallowing corrections have been made. For 15 studies, they found an average f of 0.59. Inclination shallowing does not occur in all red beds. For example, Z. Sun et al. (2006) compared results from Cretaceous red beds and basalts from the Qaidam Block, China, and found no inclination shallowing in the red beds. Thus, while inclination shallowing is common in hematite-bearing sedimentary rocks, it is not universal and needs to be assessed case by case.

6.1.2. CRM in Hematite

CRM is acquired during mineral growth below T_C or T_N within an ambient magnetic field. This can occur during crystallization, weathering, diagenesis, or metamorphism. Two CRM types are distinguished: (a) growth-CRM (g-CRM), which results from hematite crystal growth through its blocking volume; and (b) alteration-CRM (a-CRM), where hematite forms from parent minerals, for example, by oxidation (e.g., Haigh, 1958; Stokking & Tauxe, 1990a). Stable CRM acquisition requires magnetic mineral growth through the SP threshold size. Once
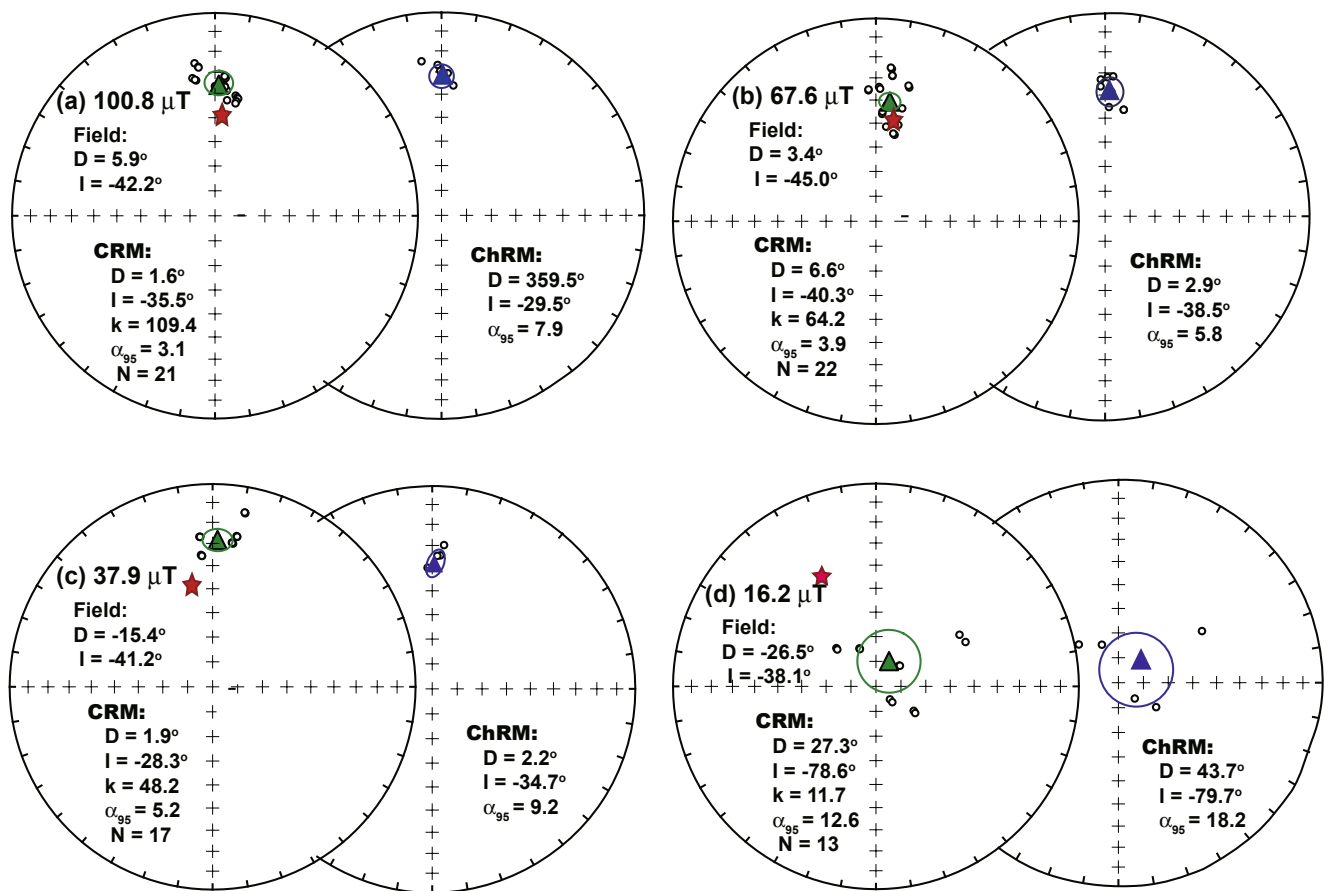
Figure 20. Equal area stereographic projections of magnetic directions for a starting chemical remanent magnetization (CRM), applied magnetic field (red star), and characteristic remanent magnetization (ChRM) isolated after stepwise thermal demagnetization (from Jiang, Liu, Dekkers, et al. (2015)). Green and blue triangles are mean CRM and ChRM directions, respectively; ellipsoids represent 95% confidence limits (α_{95}). D and I represent declination and inclination of remanence.

particles grow into stable SD sizes, they lock in the ambient magnetic field direction and any external field direction and/or intensity changes have little or no effect on the recorded CRM.

CRM acquisition by hematite in laboratory experiments (Bailey & Hale, 1981; Gendler et al., 2005; Hedley, 1968; Özdemir & Dunlop, 1993; Stokking & Tauxe, 1987, 1990a, 1990b) reveals different behaviors for the CRM types. For hematite crystals grown on a substrate in an aqueous ferric nitrate solution in ambient magnetic fields, the g-CRM direction is essentially parallel to the applied field direction (Stokking & Tauxe, 1987). However, a-CRM acquired by submarine basalts during laboratory heating in air in a 50 µT field recorded a direction between that of the ambient field and the pre-existing NRM (Bailey & Hale, 1981). When two perpendicular fields were applied during hematite growth in two stages, CRM behavior becomes complex (Stokking & Tauxe, 1990b). Also, CRM acquisition has been investigated either at certain field values or over a range of strong fields up to 7.5 mT (Stokking & Tauxe, 1987, 1990b). No study has investigated CRM acquisition systematically in Earth-like magnetic fields.

Jiang, Liu, Dekkers, et al. (2015) synthesized hematite in controlled Earth-like fields (<100 µT). Recorded CRM directions closely track the growth field orientation for field intensities >~40 µT (Figure 20). Hence, CRM recorded shortly after deposition can record an ambient field direction and will be suitable for paleomagnetic studies. However, for applied fields <~40 µT, the recorded CRM does not track the applied field direction (Figures 20c and 20d). This deviation may be due to the synthesis route from ferrihydrite, which mainly involves dehydration and solid-state rearrangement but not dissolution followed by precipitation. Alternatively, it could be caused by inefficient magnetization alignment at such low applied fields. This could be an underappreciated uncertainty source in red bed paleomagnetic studies. Some intervals of stable polarity in red bed magnetostratigraphic studies appear to record randomly oriented directions, particularly in paleosols (e.g., Tauxe &
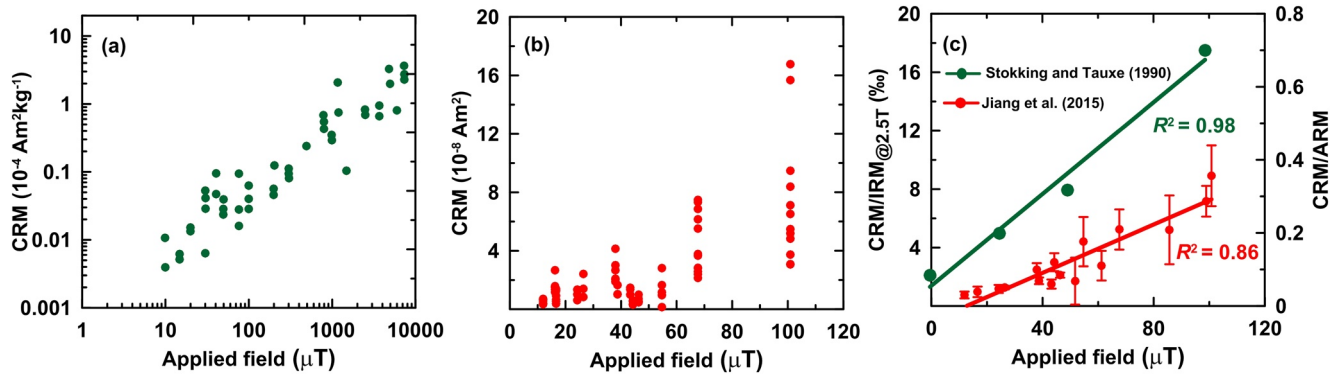
Figure 21. Chemical remanent magnetization (CRM) intensity versus applied field (after Jiang, Liu, Dekkers, et al. (2015)). (a) CRM data from Stokking and Tauxe (1990a)) versus applied field (10–7,500 µT); (b) CRM intensity versus applied field from Jiang, Liu, Dekkers, et al. (2015); (c) CRM/IRM$_{@2.5T}$ (IRM$_{@2.5T}$, isothermal remanent magnetization acquired in a 2.5 T field; red dots, from Jiang, Liu, Dekkers, et al. (2015)) or CRM/ARM (green dots, from Stokking and Tauxe (1990a)) versus applied field.

Opdyke, 1982), which could be due to organic activity (e.g., worms, etc.) that disturb grain arrangements. Poor CRM directional recording in fields <~40 µT is also a possible contributor.

CRM intensities in hematite are related almost linearly to applied field intensity from 0.015 to 7.5 mT (Figure 21a; Stokking & Tauxe, 1990a). Jiang, Liu, Dekkers, et al. (2015) compared their results from 10 to 100 µT with those of Stokking and Tauxe (1990a) and found that CRM normalized to IRM@2.5 T (CRM/IRM$_{@2.5\ T}$) increases linearly with applied field from ~0 to 100 µT (Figures 21b and 21c), which is consistent with expectation. CRM of hematite could, in principle, be used for relative paleointensity studies in Earth-like fields. However, interpretation of CRM records in terms of relative paleointensity must consider potentially prolonged CRM growth. Undefined growth timespans represent a significant uncertainty; red bed relative paleointensity records could represent a time-averaged field that will average out short-lived intensity variations (Deenen et al., 2011). Also, multiple growth stages complicate interpretation (Stokking & Tauxe, 1990b). SEM analyses of the Moenkopi Formation, USA, indicate multiple secondary hematite growth periods (Walker et al., 1981). Meaningful red bed CRM interpretation in terms of relative paleointensity should require identification of dominantly early diagenetic hematite growth.

6.1.3. TRM in Hematite

In volcanic and high-grade metamorphic rocks, primary hematite typically acquires a TRM upon cooling through T_N (675°C–690°C) in Earth's magnetic field. Theoretically, TRM should be lower for MD grains because of domain interactions (Dunlop & Özdemir, 1997). For example, an average TRM is three orders of magnitude larger in SD (~10 kA/m) than in MD magnetite (~0.01 kA/m) (Kletetschka et al., 2000a). In contrast, hematite acquires a more intense TRM in MD than in SD particles (Clark, 1983; Hartstra, 1982). Kletetschka et al. (2000c) showed that hematite has an inverse grain size dependence for TRM, with MD hematite acquiring a TRM comparable to that of sub-micron magnetite and only an order of magnitude less than SD magnetite (Figure 22). Two factors have been proposed to explain the high TRM intensity in MD hematite. First, the demagnetization energy of hematite has a lower influence on domain wall pinning energy at temperatures almost up to T_N (Dunlop & Kletetschka, 2001). Second, magnetostatic energy is more important in an applied field, which dominates the total energy at high temperatures (Kletetschka et al., 2000c). The internal demagnetizing energy, which is proportional to M_s, is much lower for MD hematite and allows it to approach saturation in weak fields. The low demagnetizing energy of hematite can also approach the domain wall pinning energy, so defects can control the magnetization and allow local magnetic minima close to M_s, which causes MD hematite to stay in a SD-like state (Kletetschka et al., 2000c; Stacey, 1958). Consequently, metamorphic MD hematite formed in the lower and middle crust may contribute significantly to an NRM (e.g., Moskowitz et al., 2015), as observed in Labrador, Canada (Kletetschka & Stout, 1998), and Norway (Schlinger & Veblen, 1989) where hematite or titanohematite are dominant remanence carriers. Hematite is also a candidate source for Martian crustal anomalies based on magnetic observations from the Viking and Pathfinder missions (Madsen et al., 1999). TES measurements from the MGS mission reveal that areal hematite abundances vary with particle size, with some areas dominated by coarse hematite (>30 µm;
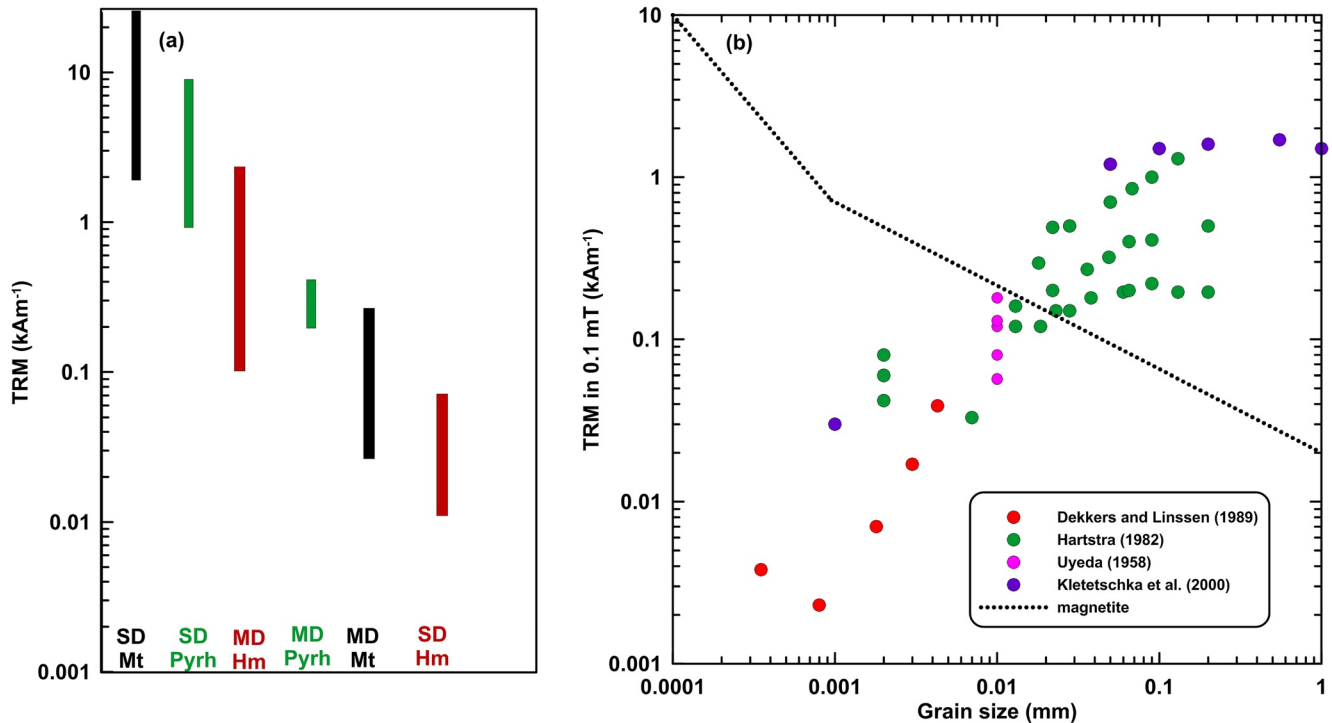
Figure 22. Characteristics of thermoremanent magnetization (TRM) for different magnetic minerals. (a) TRM intensity ranges acquired in the geomagnetic field (~50 μT; from Kletetschka et al. (2000c)); and (b) comparison of the grain size dependence of the weak-field TRM in hematite and magnetite (from Kletetschka et al. (2000c)).

Christensen, Bandfield, Clark, et al., 2000) that might be in the MD state. Thus, a MD hematite TRM might be a significant magnetic anomaly source on Mars (Dunlop & Kletetschka, 2001).

6.2. Identifying Red Bed Remagnetization: Separating DRM From CRM

A central aspect of red bed paleomagnetic studies is to discriminate CRM from DRM to discern the primary NRM component—if possible (e.g., Collinson, 1965a, 1965b; K. P. Kodama & Dekkers, 2004; Kruiver et al., 2000). Recognition of the remanence type residing in hematite (DRM or CRM) would substantiate paleomagnetic interpretation of red bed data. In general, a CRM is associated with LT hematite authigenesis, whereas detrital hematite can record a DRM with an original HT origin. The magnetic behavior of hematite depends on its thermal history. Thus, rock magnetic analysis of red beds has potential for recognizing CRM and DRM. The magnetic properties of HT hematite are relatively well established from fine-grained hematite synthesized between 400°C and 600°C. Based on this, Tauxe et al. (1980) identified these two hematite types in Siwalik red beds (Pakistan). Red pigment has a lower and comparatively broad T_b spectrum and higher coercivity, while black specular hematite has higher T_b and lower coercivity. The former can be removed by chemical dissolution and was interpreted to record a CRM, while the latter most likely carries a DRM (Tauxe et al., 1980). However, a near-primary CRM also records the magnetic field direction faithfully. When a DRM is overprinted by a CRM, it is difficult to interpret the resulting magnetization as a geomagnetic record (Deng et al., 2007; Iosifidi et al., 2010; McCabe & Elmore, 1989) because of the composite nature of the magnetization. More robust separation of DRM from CRM carried by hematite is indispensable and is more complex than identifying fine pigmentary and larger specularite (or martite) particles; it can also depend on the age and polarity of each remanence type.

Dekkers and Linssen (1989) proposed that TRM and CRM in hematite can be discriminated with annealing experiments. Coercivity and LT behavior differences can be related to thermal history in hematite. TRM has a HT origin, whereas CRM has a LT origin. Hematite with HT features in sediments can then be assigned to a DRM. B_{cr} of LT hematite is lower than for HT hematite with similar grain size. The former has a smeared or no Morin transition, while the latter has a much sharper transition. In addition, B_{cr} increases and M_{rs} decreases after thermal
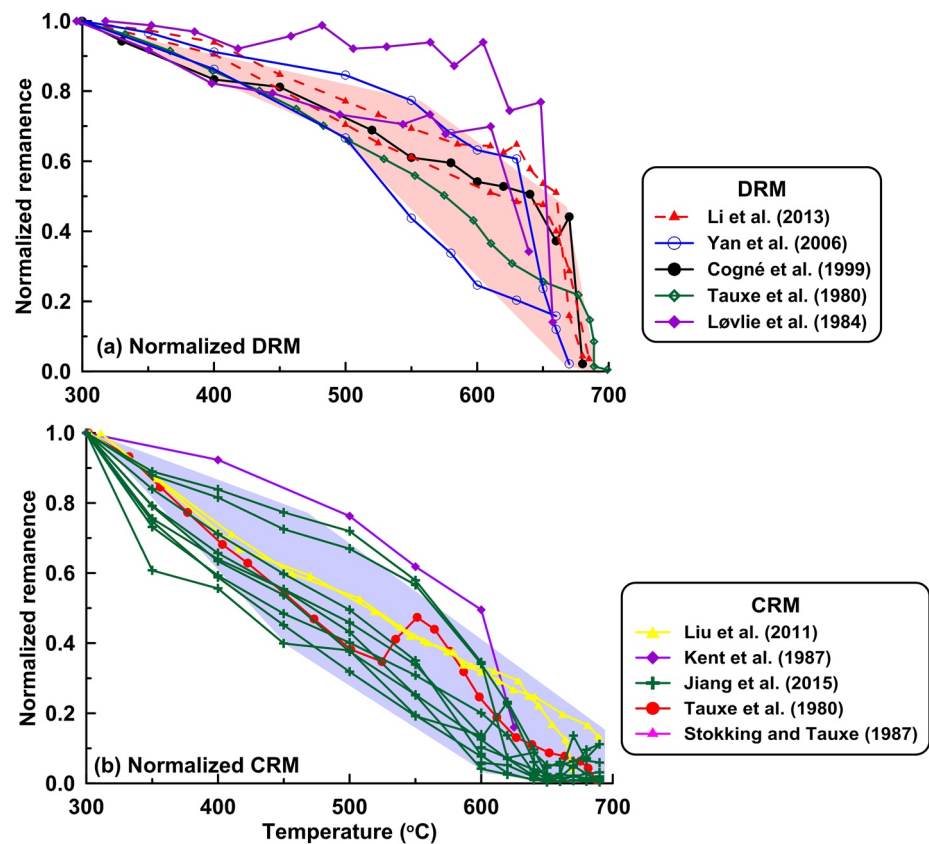
Figure 23. Stepwise thermal demagnetization curves for a (a) detrital remanent magnetization (DRM) and (b) chemical remanent magnetization (CRM; from Jiang, Liu, Dekkers, et al. (2015)). Pink and blue areas indicate the general shapes of DRM and CRM demagnetization curves, respectively.

treatment. Therefore, different remanent coercivity parameters before and after thermal treatment can provide clues to discriminate between TRM (DRM with HT origin) and CRM (LT origin) in red beds.

McClelland-Brown (1982) used T_b spectra to discriminate between TRM and CRM in hematite. Jiang, Liu, Dekkers, et al. (2015) built on this result by summarizing stepwise thermal demagnetization curves for synthetic samples and natural red beds (Figure 23), where data are normalized to the remanence after demagnetization at 300°C to remove viscous magnetization influences. The respective thermal decay curves have different shapes. DRM demagnetization curves generally have a convex shape and drop to zero at ~670°C–680°C (Cogné et al., 1999; Iosifidi et al., 2010; Løvlie et al., 1984; S. H. Li et al., 2013; Tauxe et al., 1980; Yan et al., 2006; Figure 23a). CRM demagnetization curves have a concave shape and decay to zero gradually by 600°C–650°C, which is the maximum T_b for a hematite CRM (Figure 23b). CRM has more distributed T_b spectra (~200°C to 600°C–650°C) than DRM (mostly 600°C–680°C). Also, CRM unblocking spectra can overlap with DRM spectra and extend to near T_N. Thus, to isolate a primary NRM in red beds, best practice is to use detailed thermal demagnetization steps above 600°C to >650°C (Jiang, Liu, Dekkers, et al., 2015; Jiang et al., 2017; Swanson-Hysell et al., 2019). The differences between CRM and DRM can be attributed to grain size and crystallinity differences, which provide clues to distinguish CRM from DRM in red beds, for example, Tibetan red beds (Bian et al., 2020; Meng et al., 2017; W. Zhang et al., 2020) and North American red bed intraclasts (Swanson-Hysell et al., 2019). Although T_b spectra of CRM recorded by coarse particles will overlap with those for DRM and complicate their distinction as NRM components (e.g., Abrajevitch et al., 2014; Whidden et al., 1998), this observation can still be used as a supporting line of evidence to discriminate between red bed CRM and DRM. Paleomagnetic field tests remain the most effective methods to discriminate primary and secondary magnetizations: reversal and fold tests are used often, with occasional use of conglomerate and baked contact tests (Butler, 1992). In the absence of field tests, demagnetization patterns provide circumstantial rather than definitive evidence. For example, protracted hematite pigment growth spanning one or several geomagnetic polarity reversals can record antipodal

magnetizations that pass the reversal test, which has been reported for remagnetized hematite-bearing rocks (e.g., Abrajevitch et al., 2014; Derder et al., 2001; Henry et al., 2004). Alternatively, credible magnetostratigraphic records from red beds can fail a reversal test, with polarity bias resulting from imperfect removal of normal polarity overprints in some samples despite extensive demagnetization treatment (e.g., Ao et al., 2016; Charreau et al., 2005; Dupont-Nivet et al., 2007; Xiao et al., 2012). These issues should be considered when assessing red bed paleomagnetic records. It is desirable to combine multiple approaches when possible.

6.3. Inclination Shallowing Correction in Hematite-Bearing Rocks

DRM carried by detrital hematite can be affected by inclination shallowing. This produces erroneous paleolatitude estimates that strongly affect tectonic reconstructions (e.g., Bilardello & Kodama, 2010; Tan et al., 2007; Tauxe & Kent, 1984). Significant inclination shallowing is particularly evident in central Asia where many paleomagnetic studies have been conducted on Cretaceous-Cenozoic sediments to quantify tectonic shortening associated with India-Eurasia collision (e.g., Dupont-Nivet, Butler, et al., 2002; Dupont-Nivet, Guo, et al., 2002; Dupont-Nivet, Lippert, et al., 2010; Dupont-Nivet, van Hinsbergen, et al., 2010; Lippert et al., 2011; Tan et al., 2010; Yi et al., 2011; Yuan et al., 2020). To maximize the value of such studies, inclination shallowing corrections are needed.

Two dominant inclination shallowing correction methods have been developed. The first is based on magnetic remanent anisotropy measurements (M. J. Jackson et al., 1991; Tan & Kodama, 2002, 2003; Tan et al., 2007; Vaughn et al., 2005), and the second is based on geomagnetic secular variation models (elongation/inclination [E/I] method; Tauxe & Kent, 2004). Anisotropy-based corrections assume that the easy-axes of sedimentary magnetic particles are distributed nearly isotropically soon after deposition and that a bedding-parallel foliated anisotropy is acquired during burial compaction (K. P. Kodama, 2012). Jackson et al. (1991) provided a theoretical basis for this method by assuming that magnetic moments of individual magnetic particles lie parallel to their long axes, which is the case for magnetite-bearing rocks (Figure 19). However, different factors emerge for hematite: its magnetization is controlled by crystal structure rather than grain shape. Hematite nanoparticles have a plate-like habit with the basal plane magnetization confined to the flakes. Tan and Kodama (2003), therefore, modified the approach of Jackson et al. (1991) to include an orientation distribution of disk-shaped grains with magnetizations confined to the disk plane. They derived a new expression for the flattening term f in $\tan I_o = f \tan I_f$ (R. F. King, 1955) used for anisotropy correction:

$$f = \frac{(2a+1)K_{\min} - 1}{(2a+1)K_{\max} - 1} \quad , \tag{10}$$

where a is the individual particle anisotropy, which for hematite is typically ~1.4–1.45 (Kodama, 2009), and $K_{\min}$ and $K_{\max}$ are the minimum and maximum principal remanence anisotropy axes used for inclination correction of hematite-bearing rocks.

The E/I method gives similar inclination corrections that are independent of anisotropy measurements (Tauxe & Kent, 2004). The elongation of an unflattened distribution and its mean inclination are plotted for different f values from $f = 1$ toward $f = 0$. Each f value creates a different E/I pair that plots as a point on an E/I graph. These points are connected to form a curve. The corrected inclination and f factor are determined from the intersection of the E/I curve with the TK03 geomagnetic field model (Figure 24). This method assumes that geomagnetic secular variation has had essentially the same character throughout geological time as for the past 5 Myr. The E/I method uses the sedimentary paleomagnetic site mean distribution to detect and correct inclination shallowing. Paleomagnetic directions will be elongated in a N-S direction during periods long enough to average secular variation. A major difference between the E/I and anisotropy methods is that the E/I method does not use information about the magnetic behavior of analyzed sedimentary rocks; rather, different f factors are used to numerically unflatten the site mean distribution. The E/I method has been used successfully in Tibet (Tan et al., 2010; Yan et al., 2005; Yuan et al., 2020), the Mediterranean, and North America (Tauxe et al., 2008). However, paleomagnetic data are needed for many independently oriented specimens (>100–150) per location/site, which is typically satisfied in magnetostratigraphic studies (Tauxe & Kent, 2004).
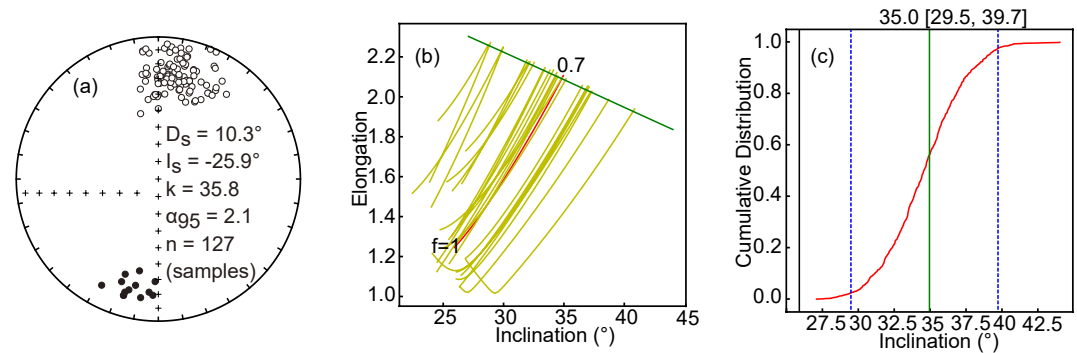
Figure 24. Application of the E/I correction to red bed data from Tibet (from Yuan et al. (2020)). (a) Paleomagnetic directional data; (b) elongation/inclination as a function of ƒ; and (c) cumulative corrected inclination distribution from bootstrapped data.

7. Geological Applications of Hematite Occurrences

Hematite occurrences in the geological record are used to study many processes, including environmental and climate variations, development of crustal magnetic anomalies, and for assessing the potential for life on Mars. The methods discussed above can be used to analyze such processes of interest, which we now discuss below.

7.1. Environmental and Climatic Implications of Hematite Formation

Climate governs the pedogenic formation rate of iron oxides and the hematite to goethite content ratio (Hm/Gt) because these minerals form under different climatic conditions with competitive processes (Schwertmann, 1993). Goethite is favored in cool, moist soils that rarely experience prolonged aridity. By contrast, hematite is more abundant in subtropical, Mediterranean, or tropical soils with frequent prolonged dry episodes (Cornell & Schwertmann, 2003; Kämpf & Schwertmann, 1983; Schwertmann & Murad, 1988). Soils with near-neutral pH and low organic content tend to favor hematite formation over goethite, and *vice-versa* (Maxbauer et al., 2016; Schwertmann & Murad, 1983). Therefore, the Hm/Gt ratio is an important paleoenvironmental indicator of iron oxide formation (Deaton & Balsam, 1991). This ratio remains stable for long periods, so it provides important soil moisture information related to climate changes unless either phase is dissolved reductively (Balsam et al., 2004; Ji et al., 2004; Kämpf & Schwertmann, 1983; Schwertmann et al., 1987; Y. G. Zhang et al., 2007).

7.1.1. Hematite Content in Soils: A Precipitation Proxy

Precipitation plays an important role in pedogenesis besides temperature, bed rock, and slope conditions, so parameters related to pedogenesis can be used as precipitation proxies (Maxbauer et al., 2016), including geochemical weathering indices (e.g., Rb/Sr and Fe_d/Fe_t; Sheldon & Tabor, 2009)). χ is used as a precipitation proxy due to the positive correlation between pedogenic ferrimagnet formation and annual rainfall (Balsam et al., 2004, 2011; Geiss et al., 2008; J. M. Han et al., 1996; Maher et al., 1994, 2003). Therefore, most precipitation studies have focused on ferrimagnetic minerals, and have neglected the magnetic properties of hematite and goethite. Nevertheless, antiferromagnetic minerals provide more robust climatic information than ferrimagnets and form over a wider climate range (Cornell & Schwertmann, 2003). Based on the ferrihydrite → hematite transformation pathway, short periods of seasonal rainfall, <350 mm/yr under warm conditions, are sufficient to form significant hematite (Maher, 1998). Balsam et al. (2004) found high hematite concentrations and low to moderate χ values for moderate precipitation of 550–600 mm/year in loess/paleosol sequences on the CLP. Absolute χ in CLP soils is affected by initial eolian input and climatic factors, so C. Liu, Deng, et al. (2007) suggested a hematite/ferrimagnet ratio as a rainfall proxy. The ratio of hematite concentration (Hm) to the frequency dependence of magnetic susceptibility (χ_{fd}, expressed as the absolute value between low and high frequency measurements) relates to mean annual precipitation (MAP) in six loess/paleosol profiles from five CLP locations (Torrent et al., 2006). For CLP data, Hm content and χ_{fd}/HIRM reach maxima for rainfall of 550–600 mm/yr (Figure 25a; Balsam et al., 2004), and ~1,000 mm/yr (Figure 25c), respectively (Balsam et al., 2011; J. M. Han et al., 1996; Z. Liu et al., 2013).
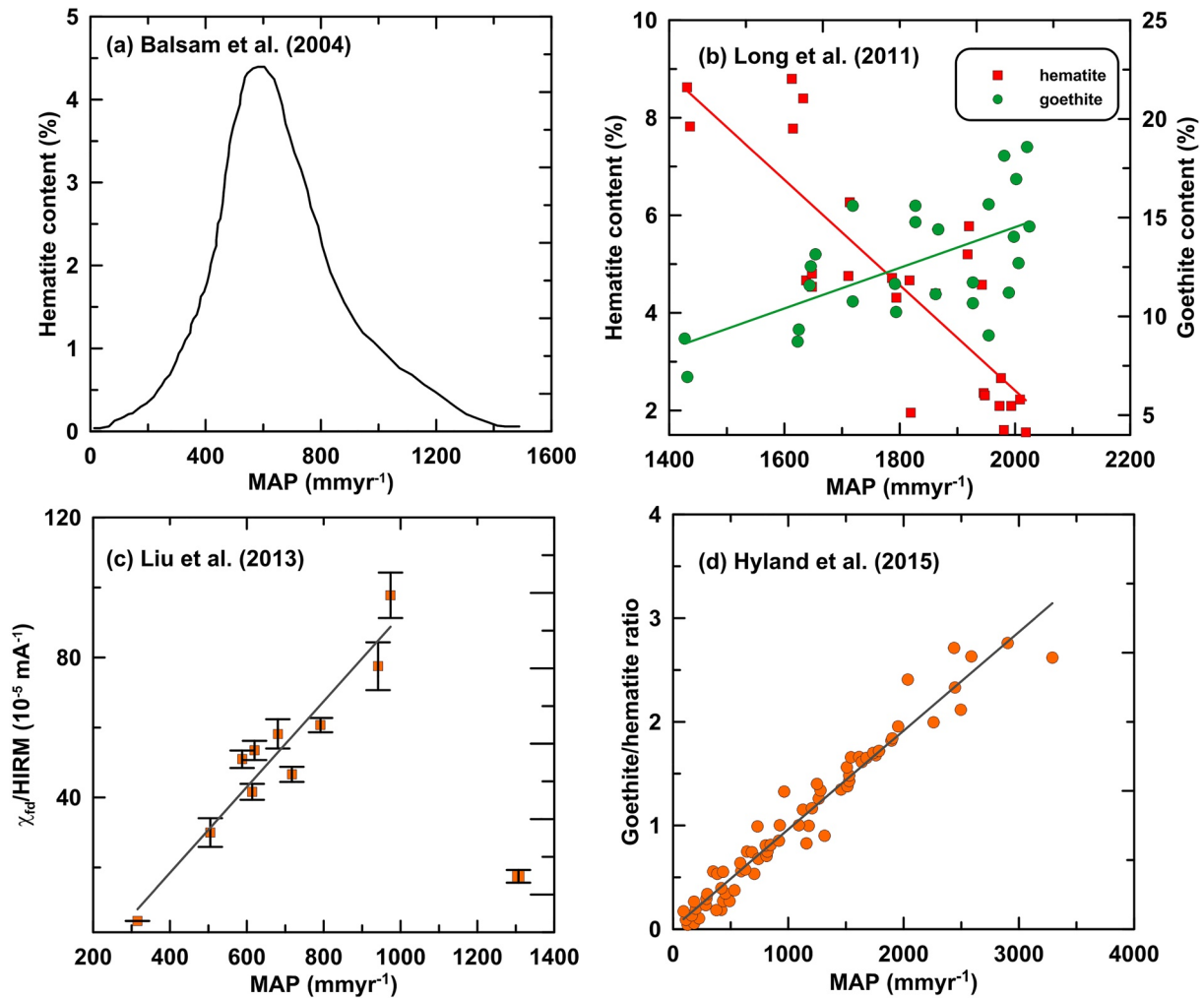
Figure 25. Relationship between hematite content parameters and mean annual precipitation (MAP) used for hematite paleoprecipitation proxies. χ_{fd} is frequency magentic susceptibility. Data are from Balsam et al. (2004), Long et al. (2011), Liu et al. (2013), and Hyland et al. (2015).

Liu et al. (2013) later proposed χ_{fd}/HIRM (Figure 25c), which is the slope in a bivariate plot of χ_{fd} versus HIRM, as a precipitation proxy and established a paleoprecipitation transfer function by combining both ferrimagnetic and antiferromagnetic parameters. Ferrimagnetic particles appear to form more rapidly than hematite and goethite, so χ_{fd}/HIRM increases with MAP first; when MAP exceeds the thresholds mentioned above, magnetic depletion occurs due to dissolution. Magnetite and maghemite dissolution are much more rapid than for hematite and goethite in soils (e.g., Long et al., 2011; P. Hu et al., 2013). Therefore, the positive relationship between χ_{fd}/HIRM and MAP breaks down at a turning point. χ_{fd}/HIRM reflects pedogenic partitioning of iron between ferrimagnets and hematite, which removes the need to construct an enhancement ratio, and can partly eliminate the effects of parent material, wildfires, and human activity (Maxbauer et al., 2016; Z. Liu et al., 2013).

Long et al. (2011) quantified relationships between precipitation and hematite and goethite abundances in soils with high rainfall (up to 3,000 mm/yr) based on the hematite and goethite concentration ratio (Hm/Gt) calculated from DRS data. For high rainfall, pedogenic ferrimagnetic mineral dissolution is often accompanied by a pedogenic hematite decrease while goethite increases (Figure 25b). Competition between hematite (warm and dry) and goethite (cold and wet) formation means that relative goethite and hematite proportions depend on environmental hydration; higher Hm/Gt ratios represent a drier environment (Cornell & Schwertmann, 2003). Hyland et al. (2015) calculated Gt and Hm abundances using the remanence unmixing method of Kruiver et al. (2001) by inputting the IRM acquisition curve from 0 to 4.7 T, saturation IRM, mean coercivity, and the IRM distribution width or dispersion. From literature and measured Gt/Hm ratios and MAP estimates for globally distributed
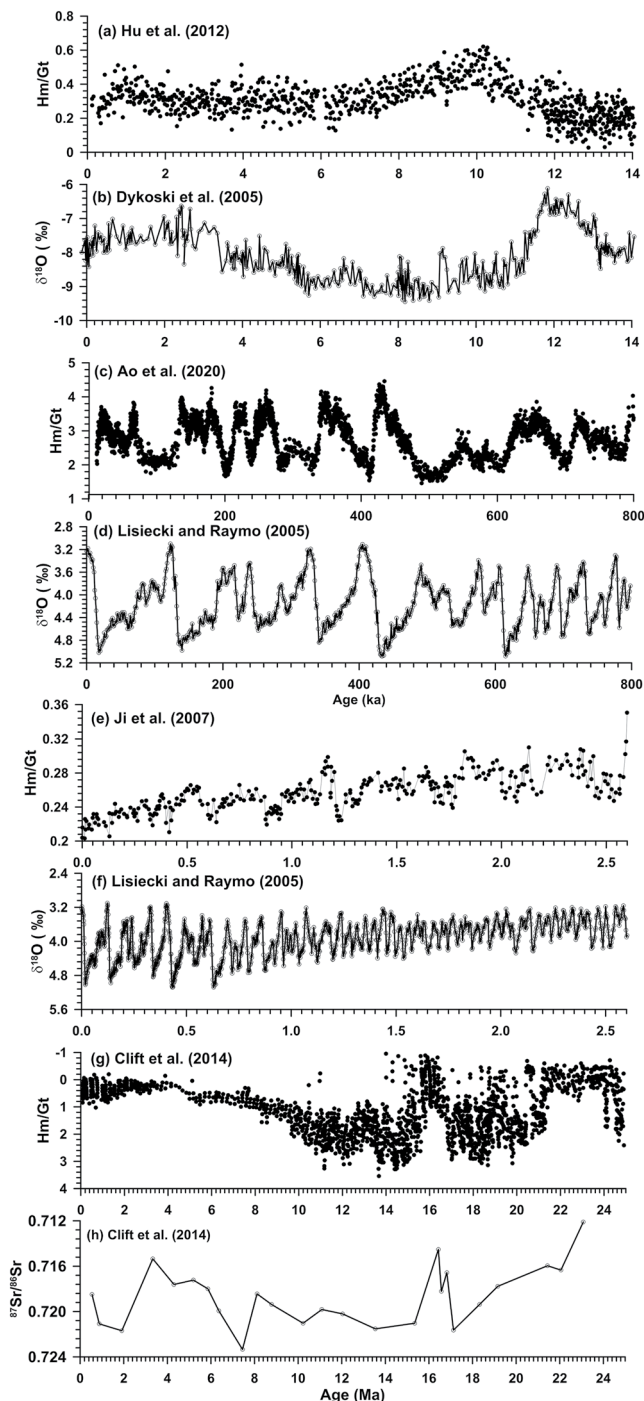
Figure 26. Comparison of hematite and goethite content variations and marine $\delta^{18}O$ over different time scales: (a and b) 0–14 ka (D. Hu, Böning, et al., 2012; Dykoski et al., 2005); (c and d) 0–800 ka (Ao et al., 2020; Lisiecki & Raymo, 2005); (e and f) 0–2.6 Ma (Ji et al., 2007; Lisiecki & Raymo, 2005); and (g and h) 0–25 Ma (Clift et al., 2014) with $^{87}Sr/^{86}Sr$.

modern soils, Hyland et al. (2015) found a strong linear relationship between Gt/Hm of soil B horizons and MAP that can be used to estimate paleoprecipitation for diverse climatic regimes (MAP 100–3,300 mm/yr) and soil types (Figure 25d). However, Maxbauer et al. (2016) noted several inherent challenges to the analytical approach of Hyland et al. (2015). First, minor cation substitution (e.g., Al) in goethite or hematite can dramatically alter coercivity (Jiang, Liu, Colombo, et al., 2014; Jiang et al., 2012; Q. Liu et al., 2006; Roberts et al., 2006), so identified magnetic components may not represent true goethite or hematite concentrations. In addition, converting magnetic moments to moles remains a challenge. Thus, proxy-based MAP estimates must be reported with realistic uncertainty estimates (Heslop & Roberts, 2013; Maxbauer et al., 2016). Integration of magnetic and DRS approaches is an attractive theme for future research.

7.1.2. East Asian Monsoon Variations

The Hm/Gt ratio is a sensitive East Asian Monsoon (EAM) dry/wet indicator for the CLP and marine sediment records (e.g., Ao et al., 2020; Balsam et al., 2004; Clift et al., 2008, 2014; Hao et al., 2009; Ji et al., 2004; Torrent et al., 2007; X. Hu, Scott, et al., 2012). A Hm/Gt record from ODP Site 1144, South China Sea (SCS), tracks summer rain intensity since the last glacial maximum, particularly monsoon strengthening between 11 and 18 ka, which correlates well with speleothem records, most notably Dongge Cave, SW China (Clift et al., 2014; X. Hu, Scott, et al., 2012; Figures 26a and 26b). Hm/Gt from the Binxian section, CLP, over the last 800 Kyr matches marine benthic $\delta^{18}O$ glacial-interglacial cycles (Ao et al., 2020). Higher Hm/Gt values in interglacial red paleosol layers than in glacial yellow loess layers indicate stronger interglacial summer and weaker winter monsoons (Ao et al., 2020; Figures 26c and 26d). Hm/Gt in the Luochuan section (CLP) has decreased continuously since 2.6 Ma, which indicates a wetter environment and periodic (400–500 Kyr) EAM enhancement since 2.6 Ma (Ji et al., 2007; Figures 26e and 26f). Hm/Gt variations at SCS ODP Site 1148 indicate EAM strengthening over the 22–18 Ma interval, followed by an extended monsoon maximum between 18 and 10 Ma. The summer EAM may have also strengthened since 3–4 Ma after reaching an early Pliocene minimum (Figures 26g and 26h; Clift et al., 2014). Hm/Gt correlates well with $^{87}Sr/^{86}Sr$ variations, which indicates stronger weathering linked to greater monsoon seasonality. However, goethite and hematite have different stability to reductive diagenesis, with pedogenic hematite dissolving preferentially compared to other iron oxides in Chinese loess/paleosol samples (P. Hu et al., 2013), while goethite is more sensitive to dissolution than hematite in marine sediments (e.g., Abrajevitch et al., 2009). These differences are attributed to their different origins, with pedogenic minerals more easily dissolved than detrital ones. Dissolution is also size dependent and removes finer grains first. Dissolution, therefore, influences absolute Gt/Hm contents, which can be traced by magnetic methods but not DRS. Thus, when using Hm/Gt from DRS to study climatic conditions in source areas, it is advisable to combine DRS and magnetic measurements to investigate whether results are influenced by diagenetic changes (e.g., Abrajevitch et al., 2015).

Hematite in pelagic sediments usually has a detrital origin (e.g., Roberts et al., 2013), and hematite contents often reflect continental source area aridity and can be used as eolian tracers (Larrasoaña et al., 2003; Maher, 2011). In the North Pacific Ocean, eolian dust from arid parts of Asia are a major pelagic clay source (Blank et al., 1985). Yamazaki and Ioka (1997) measured HIRM for five pelagic-clay cores from the central North Pacific Ocean. Increasing HIRM and decreasing SIRM is recorded since 2.5 Ma, which indicates the increasing presence of hard
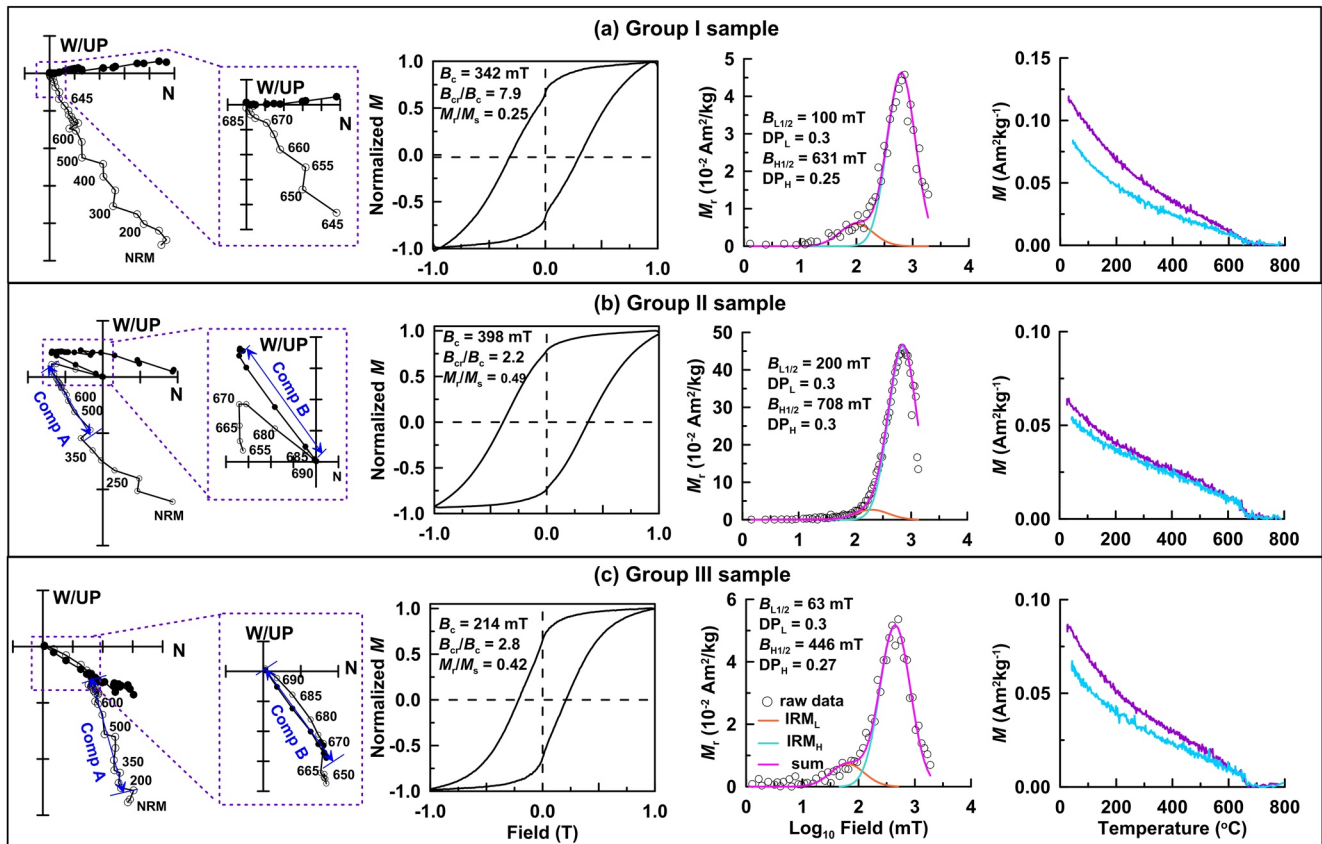
Figure 27. Magnetic characteristics of typical remagnetized red beds (from Jiang et al. (2017)). (a) Characteristics of completely remagnetized samples. The primary remanence is not extracted even after chemical-thermal demagnetization. (b and c) Characteristics for incompletely remagnetized samples. The primary remanence (670°C–690°C) is extracted after chemical-thermal demagnetization.

magnetic minerals (Hm and Gt) and decreasing ferrimagnetic mineral contents. Here, HIRM mainly represents Hm because Gt contributes little to an IRM imparted with a 1 T field due to its high coercivity and weak magnetization (Rochette et al., 2005). In addition, 2.5 Ma is close to the intensification of northern hemisphere glaciation and Chinese loess deposition. Therefore, in North Pacific sediments, HIRM is a proxy for Asian eolian dust. Likewise, Mediterranean sediments record details of Plio-Pleistocene eolian fluxes from North Africa (Larrasoaña et al., 2003, 2015). As is the case for North Pacific dust flux archives, HIRM is a key magnetic parameter that records varying eolian hematite inputs. In the Mediterranean, hematite content variations reflect African summer monsoon evolution, with flux minima associated with processionally driven monsoon intensification; dust maxima correspond to northern hemisphere insolation minima, and weakened monsoon intensity (Larrasoaña et al., 2003). Thus, hematite contents effectively document African monsoon evolution over different timescales.

7.2. Hematite and Remagnetization

As discussed above, hematite can reliably record paleomagnetic information. However, remagnetization is possible, and is a key challenge in paleomagnetic studies, including for hematite-bearing rocks where discriminating primary from secondary NRMs is critical. The shape of thermal demagnetization curves (see Section 6.2) can help to discriminate a primary DRM from a secondary CRM (Figure 23; Jiang, Liu, Dekkers, et al., 2015). Also, use of improved thermal demagnetizers and magnetometers can help to overcome such challenges (Qin et al., 2020). For example, measurement limitations prevented primary NRM identification in Triassic red beds from South China (Kent et al., 1987). By combining chemical and thermal demagnetization, Jiang et al. (2017) removed a remagnetized component and obtained primary NRM information from the 670°C–690°C interval (Figure 27). Ultralow field thermal demagnetizers can also help to obtain low-noise results for weakly magnetic samples (Qin et al., 2020), including Cretaceous oceanic red beds from the Tibetan Plateau (e.g., Yuan et al., 2020). A primary

NRM carried by hematite was demonstrated, which provides evidence for rapid northward drift of the Tethyan Himalayan terrane before the India-Asia collision (Yuan et al., 2020). From thermomagnetic behavior, W. Huang et al. (2019) also suggested that goethite can be used to diagnose red bed remagnetizations from integrated rock magnetic, Mössbauer spectroscopic, and petrographic methods. Moreover, W. Huang et al. (2020) proposed that diagenetic alteration induced by heating and/or fluid circulation is probably the main cause of Tibetan Plateau red bed remagnetizations. They used secondary paleomagnetic components to provide information about coeval field and hydrothermal activity. Secondary remanences, thus, provide important evidence for prevailing geological processes, along with paleolatitude estimations.

7.3. Implications of Hematite for the Presence of Water and Life on Mars

Based on known hematite formation mechanisms, Martian hematite could be associated with the presence of surface water or groundwater (Burns, 1993a; Catling & Moore, 2003; Chan et al., 2006). If the hematite had an aqueous origin, then the possibility of initiation and sustenance of prebiotic or biotic processes exists (Allen et al., 2001) because water is a key ingredient for life (Newsom et al., 2003). Also, several proposed mechanisms for terrestrial hematite formation may include microbial mediation (e.g., R. C. Morris, 1993), such as in BIFs, hydrothermal deposits, iron-rich laterite and ferricrete soils, and rock varnish (Barley et al., 1999; Klein, 2005), which can provide clues about Martian hematite formation. Therefore, Martian hematite deposits may be significant in the search for evidence of extraterrestrial life.

Aqueous Fe^{2+} oxidation is a dominant hematite formation pathway (e.g., Cornell & Schwertmann, 2003). Iron-rich basaltic rocks erupting onto the Martian surface would produce abundant dissolved Fe^{2+}, and dissolved oxygen could be produced by photolysis of atmospheric water vapor and CO_2 (Burns, 1993a). The strongest hematite signature on Mars is adjacent to a paleolake basin in southern Arabia Terra, which supports the role of water in Martian hematite formation (Newsom et al., 2003). Water could have been responsible for Martian hematite formation in several ways, including deposition in lakes, and precipitation as surface coatings due to groundwater wetting (Newsom et al., 2003). The occurrence of diagenetic hematite suggests low pH environments because Fe transport is enhanced in low-pH fluids (L'Haridon et al., 2020; McLennan et al., 2005). On Earth, aqueous Fe^{2+} oxidation reaction kinetics are so rapid at near-neutral pH, particularly in warm surface waters, that Fe^{2+} oxidation would have effectively removed dissolved oxygen from surface waters to maintain low oxygen levels in Earth's Archean atmosphere (Holland, 1984). Thus, Precambrian BIFs might have regulated terrestrial atmospheric pO_2.

It is worth considering whether biological actors could have been involved in redox reactions on Mars. Life thrives via redox chemistry, so it will inevitably leave a large redox imprint on its surroundings (for example, Earth's O_2-rich atmosphere and ocean are the result of photosynthesis, e.g., Lefèbvre and Krasnopolsky (2017)). So, life could provide an oxygen source for Fe^{2+} oxidation. The most significant biochemical implication of Martian hematite concentrations is that Fe^{3+} was being generated in an environment where liquid water and reductants were also readily available. Fe^{3+} and H_2 form an excellent redox couple for most primitive lifeforms without complex enzymes (e.g., Catling & Moore, 2003).

7.4. Piezomagnetic Behavior: Magnetic Anomaly Implications on Earth and Mars

7.4.1. Pressure Demagnetization Behavior of Hematite

The piezomagnetic behavior of hematite has a bearing on our understanding of Earth's interior and on the magnetic expression of impact craters. Under pressure in a magnetically shielded environment, the remanent magnetization of hematite undergoes marked reduction. A 1.44 GPa pressure reduces the IRM by 50% (Jiang et al., 2013; Figure 28a). Repeated loading cycles further reduce the IRM (Bezaeva et al., 2007, 2010; Gilder et al., 2006). Almost 38% of the IRM is lost at 1 atm pressure after the first loading cycle, and a further 18% is lost during a second cycle (Figure 28b).

The pressure dependence of the Morin transition has been investigated theoretically (Searle, 1967) and with diverse techniques such as nuclear magnetic resonance (Wayne & Anderson, 1967), neutron scattering (Klotz et al., 2013; Parise et al., 2006; Umebayashi et al., 1966; Worlton et al., 1967), Mössbauer spectroscopy (Vaughan & Drickamer, 1967), and static magnetic measurements (Bezaeva et al., 2015; Kawai & Ono, 1966). T_M increases with increasing pressure at a rate of ~30–40 K/GPa (Searle, 1967; Umebayashi et al., 1966; Wayne &
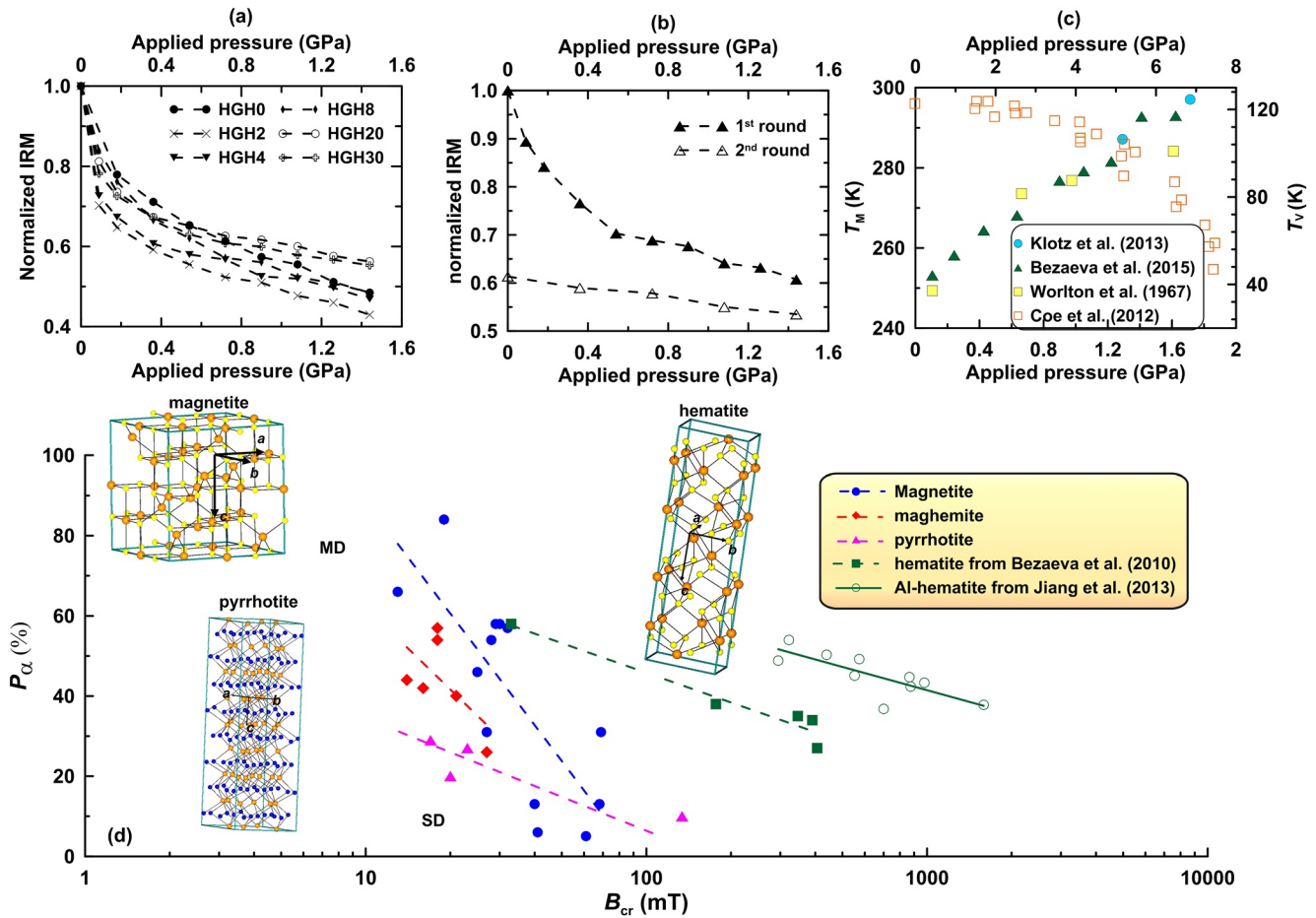
Figure 28. Pressure dependence of hematite remanence and Morin transition temperature. (a) Residual isothermal remanent magnetization (IRM; normalized with initial IRM) under applied compressive pressure (from Jiang et al. (2013)); (b) data for two compression cycles for hematite (from Jiang et al. (2013)); (c) Morin temperature (T_M) and Verwey transition temperature (T_V) versus applied pressure; T_M data are from Klotz et al. (2013), Bezaeva et al. (2015), and Worlton et al. (1967); T_V data are from Coe et al. (2012); and (d) correlation between the pressure demagnetized degree and B_{cr} for different magnetic minerals (from Jiang et al. (2013)).

Anderson, 1967; Worlton et al., 1967). This behavior contrasts with that of the Verwey transition temperature in magnetite, which decreases with increasing hydrostatic pressure at about −3 K/GPa (Coe et al., 2012). Bezaeva et al. (2015) found that T_M changes with pressure at 25 K/GPa. T_M thus reaches room temperature at 1.38–1.61 GPa (Figure 28c). Thus, applied pressures result in a perfect antiferromagnetic state with no net magnetization in hematite at ambient temperatures with spin alignment along the crystallographic c-axis. The magnetic properties of meteorites, which are commonly shocked to pressures well above 1 GPa (e.g., Martian meteorites) may, therefore, not be representative of the magnetic properties of their parent bodies (Gattacceca et al., 2007, 2010).

To quantify pressure effects on magnetic minerals, Jiang et al. (2013) proposed the parameter P_α, which is given by (IRM$_{initial}$ − IRM$_{pressed}$)/IRM$_{initial}$ × 100%. For each iron mineral, P_α correlates linearly and inversely with log (B_{cr}) with a different rate (Figure 28d). Magnetite/titanomagnetite and maghemite have higher slopes and hematite and pyrrhotite have lower slopes. Each of these mineral groups has similar trends. This dichotomy can be attributed to crystal structure differences. Magnetite/titanomagnetite and maghemite have cubic crystal structures (Figure 28d; Cornell & Schwertmann, 2003; Dunlop & Özdemir, 1997), while hematite and pyrrhotite have rhombohedral structures (Cornell & Schwertmann, 2003; Dunlop & Özdemir, 1997; Morrish, 1994; Pauling & Hendricks, 1925). Trends of P_α versus log (B_{cr}) behavior may, thus, be controlled by the crystal structure of the respective mineral. A clear conclusion from Figure 28 is that hematite is by far the most pressure sensitive mineral in the SD state.

Magnetically soft MD particles (lower B_{cr}) are also demagnetized more easily by pressure than magnetically harder SD particles. Domain wall movement in MD particles also influences pressure demagnetization behavior (Bezaeva et al., 2007, 2010, 2007; Gilder, 2007; Gilder et al., 2002, 2004, 2006, 2011; Jiang et al., 2013; K. Louzada et al., 2007; K. L. Louzada et al., 2010; M. Jackson et al., 1993; Rochette et al., 2003). In addition, higher B_{cr} can inhibit spin rotation under compression, and decrease pressure demagnetization sensitivity. Moreover, Al substitution may also increase the resistance to pressure effects by decreasing particle size and generating lattice defects that increase coercivity. The Al-substituted hematite samples of Jiang et al. (2013) have a significantly higher P_a for the same B_{cr} in the SD state as the hematite of Bezaeva et al. (2010) (Figure 28d). In summary, P_a is controlled by multiple factors, such as mineralogy, crystal structure, domain state, and B_{cr}. This makes it difficult to directly compare P_a for different minerals, but P_a can be quantified using the relationship between P_a and log (B_{cr}).

7.4.2. Implications for Magnetic Anomalies on Mars

Martian crust has experienced large meteoroid impacts after the demise of an early planetary magnetic field at least at 4 Ga or earlier (e.g., Acuña et al., 1999; Stevenson, 2001; Lillis et al., 2008, 2013). Impact craters mostly coincide with regions of low or no crustal magnetization (e.g., Acuña et al., 1999), which is likely due to ancient crust modification in impact basins, although no association between individual craters and magnetic sources has been found (Acuña et al., 1999). As discussed above, hydrostatic pressure significantly affects the magnetic properties of rocks and minerals (Bezaeva et al., 2007, 2010; Gilder et al., 2002, 2004, 2006; Rochette et al., 2003). The most relevant hydrostatic pressure range for terrestrial and Martian crustal conditions is up to 1.5 GPa (Bezaeva et al., 2015). Hematite-bearing rocks or regolith will be strongly pressure demagnetized, or remagnetized in an ambient field, even for modern impacts. No magnetic signals have been detected over Tharsis, Elysium, Valles Marineris, or any other major Martian volcanic edifice (Figure 29; Acuña et al., 1999; Lillis et al., 2004, 2008). The large impacts that formed the Hellas and Argyre basins are thought to have formed in the early Noachian epoch (~4 Ga) and are not associated with magnetic sources. The absence of crustal magnetism in these impact basins and their surroundings implies that the Martian core dynamo had already ceased to operate when the basins formed at ~3.9 Ga (Acuña et al., 1999; Lillis et al., 2008). Impacts that occurred after dynamo cessation only modified the ancient, magnetized, thin crust. Therefore, magnetic anomalies observed above impact basins may provide clues for the presence or absence of an active dynamo at the time of impact.

8. Conclusions and Future Work

Our knowledge of the magnetic and spectroscopic properties of hematite has increased considerably in recent years, which has significant applications for studies on Earth and Mars. For example, terrestrial hematite provides information about monsoon evolution and paleoenvironments, while on Mars hematite provides tantalizing indicators of the former existence of water. However, the properties of hematite vary with grain size, grain shape, and cation substitution, which increase the complexity of geological interpretations based on hematite contents and properties. Recent studies indicate that cation substitution markedly changes the magnetic and spectroscopic properties of hematite by modifying the grain size, crystal strain, and magnetic ion dilution, which complicates identification and quantification of hematite. However, combining magnetic and DRS methods can help to overcome such issues and enable hematite quantification. Furthermore, with improved instrumentation and protocols, future progress is expected in identifying remagnetized NRMs in red beds. The following topics are particularly attractive for future research.

8.1. Environmental Magnetic Ambiguities: Is Hematite Cation Substituted?

Magnetic and color parameters that relate to hematite content (HIRM, S-ratio, I_{535}/I_{425}) are important for assessing paleoenvironmental trends, for example, paleoprecipitation, aridity, monsoon evolution. However, cation substitution in hematite can strongly affect magnetic and color parameters and have a bearing on interpretations. Although general trends are known, and combining magnetic and color parameters is powerful (Jiang, Liu, Colombo, et al., 2014; P. Hu et al., 2016; Q. Liu et al., 2011), full parameter space variability has not been explored sufficiently. Therefore, informed judgment of possible cation substitution is required to avoid ambiguity in environmental studies involving hematite.
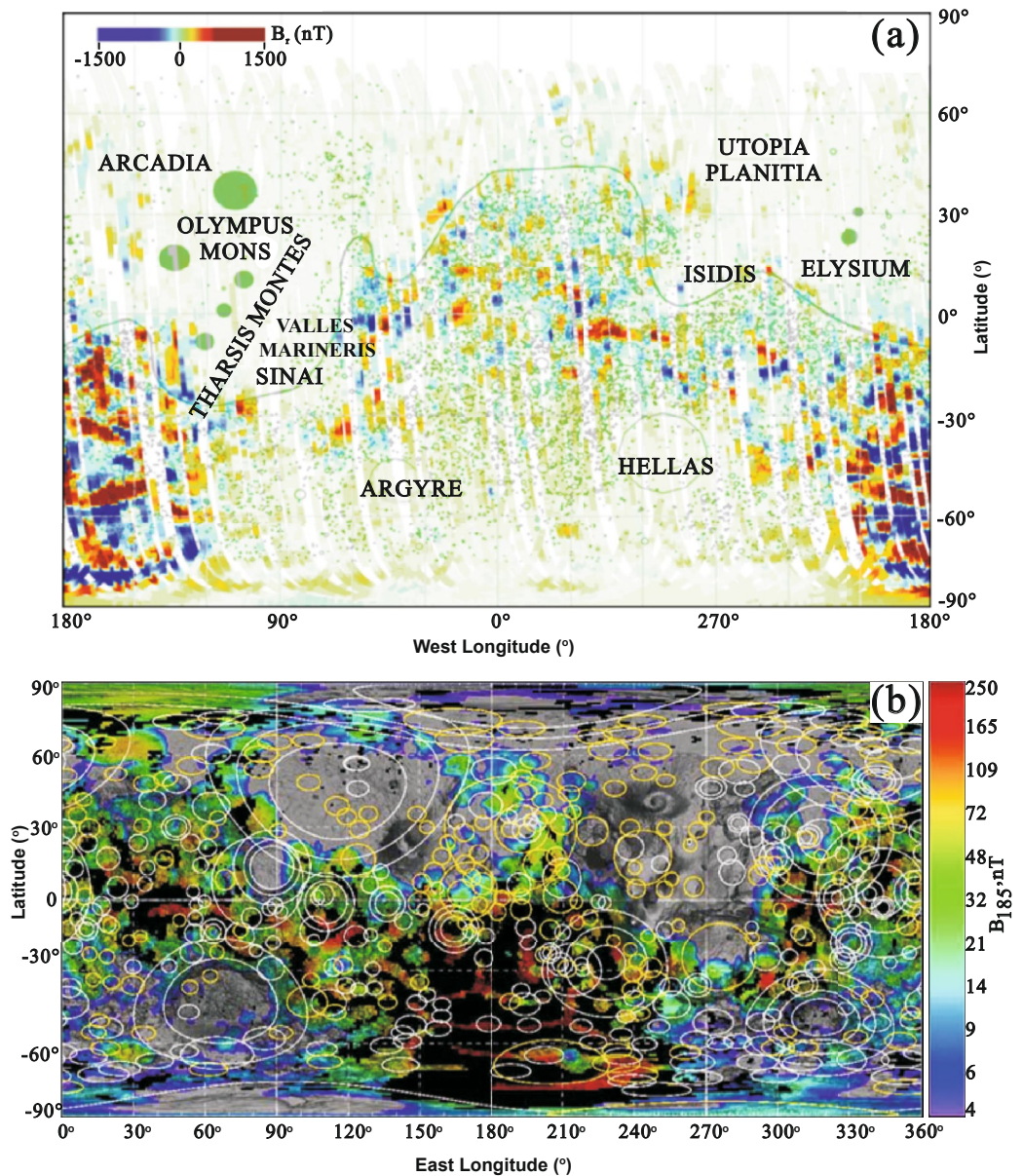
Figure 29. Distribution of crustal magnetic field sources superimposed on a map of Mars with >15 km diameter craters and the dichotomy boundary (solid line) from (a) Acuña et al. (1999) and (b) Lillis et al. (2008).

8.2. Identifying CRMs Carried by Hematite

CRM formation by hematite is a prominent cause of remagnetizations in red beds, soils, and carbonates. Laboratory CRM acquisition experiments constrain interpretation of the NRM record of rocks. However, the laboratory set-ups used for these experiments underestimate natural environmental complexity. For example, the effects of pressure, temperature, and cation substitution on CRM acquisition in hematite deserve investigation to provide better insights into remagnetization mechanisms.

8.3. Developing a Reflectance Spectral and Magnetic Parameter Database for Hematite on Earth and Mars

Although terrestrial hematite has been investigated systematically, a database for hematite properties does not exist. Furthermore, due to the scarcity of Martian meteorite samples, it remains difficult to investigate hematite

from Mars. Thus, the main ways to measure hematite on Mars involve optical, XRD, VNIR spectra, and TES observations. Instruments include Earth-based telescopes (Bell et al., 1990), the ISM (Mustard & Bell, 1994), and TES deployed on the MGS spacecraft (Christensen, Bandfield, Clark, et al., 2000; Christensen, Bandfield, Hamilton, et al., 2000; Christensen, Bandfield, Smith, et al., 2000) and the Mars Surveyor lander (Grotzinger et al., 2015; R. Morris et al., 2006). Systematic studies of the properties of terrestrial hematite are indispensable to provide an interpretive framework for Martian hematite. However, hematite properties are complex and depend critically on formation conditions. Key questions are: how comparable is hematite on Earth and Mars? Is hematite on Mars cation-doped? If so, how can cation content be quantified? Can this be done with color reflectance measurements? A robust database of these hematite properties on Earth and Mars is required to inform such questions along with a full understanding of its formation mechanisms. Integrated analysis should provide significant reference data for future studies of Martian soils or rocks. For example, by comparing with Al-substituted terrestrial reference hematite, it may be deduced whether hematite on Mars is also Al-substituted. This will provide necessary ground-truthing for spectral and other remote Martian surface observations.

8.4. Origin of Weak Magnetic Anomalies on Mars

Martian magnetic anomalies are often weak, especially around large impact craters. This raises the question of whether the magnetic signal is due to a weak (or non-existent) early dynamo field or to high-pressure impacts. Therefore, the crust in these magnetic minima needs to be dated precisely. Paleomagnetic analysis of Martian rocks and dynamo modeling will also be indispensable for understanding dynamo evolution.

Appendix A

A1. Magnetic Terms

A1.1. A and B Sublattices

Two magnetic sublattices with oppositely directed spins and magnetic moments, with negative interaction.

A1.2. Alternating Field (AF) Demagnetization

Progressive demagnetization of samples by exposing them to a sinusoidally alternating magnetic field of gradually decreasing magnitude in the presence of a zero-direct field. This treatment is used to identify different magnetic components with variable coercivities. However, it is less effective for magnetically hard minerals, for example, hematite or goethite.

A1.3. Antiferromagnetism

A magnetic material in which alternating planes (A and B sublattices) contain the same number of Fe^{3+} ions with equal and opposite magnetic moments, so that there is no net M_s. Hematite and goethite are imperfect antiferromagnets. For hematite, slight departure ($\sim$0.065°) from antiparallel spin alignment (Spin canting) gives rise to its magnetization. This changes hematite from an ideal antiferromagnetic mineral with no net magnetization to an imperfect antiferromagnet with a weak spontaneous magnetization of $\sim$0.4 $Am^2 kg^{-1}$.

A1.4. Bohr Magneton (μ_B)

An expression for an electron's magnetic moment, or the strength and orientation of the magnetic field produced by an electron. Due to its spin, the magnetic moment of the electron is approximately one Bohr magneton, the value of which is 9.274×10^{-24} Am^2.

A1.5. Chemical Remanent Magnetization (CRM)

The remanence produced by magnetic mineral formation at any temperature below the Curie temperature in the presence of an ambient magnetic field, either by nucleation and growth to a stable blocking volume V_B (growth CRM) or through alteration of an existing magnetic phase (alteration CRM).

A1.6. Detrital Remanent Magnetization (DRM)

Detrital grains are released from their parent rock by weathering, and are then transported and incorporated within sediments. Their magnetic moments can align partially with the ambient geomagnetic field during deposition or shortly thereafter to produce a DRM.

A1.7. Exchange Interaction

When magnetic atoms or ions are incorporated into a crystal lattice they may cooperate to produce an ordered array of magnetic vectors throughout large lattice regions. The mechanism for this cooperation is the exchange interaction resulting from orbital overlap of nearest neighbor atoms or ions.

A1.8. Ferrimagnetism

An antiferromagnetically coupled material with A and B sublattices that contain different numbers of cations, so that the sublattice magnetizations M_A and M_B are not equivalent, which leads to a net spontaneous magnetization M_s.

A1.9. Hysteresis Parameters

When an applied field is decreased to zero, the magnetization M of a magnetic material does not decrease to zero. This magnetic hysteresis leaves a sample with a permanent magnetization, or magnetic remanence. If the field is increased in the opposite direction, M gradually decreases to zero and then reverses and eventually saturates again. Cycling of the applied field from positive to negative and back traces a hysteresis loop. After application of a sufficiently high field, the sample acquires its saturation magnetization (M_s). Removal of this field leaves the sample with its saturation remanence (M_{rs}). Application of a reversed field eventually leads to the point where the overall magnetization is zero. The field necessary to achieve this is called the coercivity (B_c). To reach zero remanence after field removal, a somewhat stronger negative field is required. This point is called the coercivity of remanence (B_{cr}). These four hysteresis parameters are used widely to understand magnetic recording.

A1.10. Hysteretic Demagnetization

Involves use of a vibrating sample magnetometer to subject the IRM of a sample to cyclical reversed DC fields with decreasing peak levels from a starting state (typically 1–2 T) to mimic a low frequency AF demagnetization.

A1.11. Lamellar Magnetism

A ferrimagnetic substructure that occurs between ilmenite ($FeTiO_3$) and hematite lamellae at contact layers parallel to (0 0 1). The intensity of lamellar magnetism depends on the proportion of lamellae with parallel magnetic moments. A lamellar magnetic material could have a saturation magnetization up to 28 Am^2/kg, which is 70 times stronger than for pure hematite, while retaining the high coercivity and thermal stability of SD hematite.

A1.12. Magnetic Exchange Interaction Energy

The exchange interaction between an atom i and its neighbor j can be described by the magnetic exchange interaction energy, $E_{ex} = -2J_{ij}S_i\Sigma S_j$, where J is the exchange energy constant, which has a positive or negative sign to indicate parallel or antiparallel coupling. At finite temperatures, thermal vibrations cause the orientation of spin vectors to make random excursions away from the energy minimum. At high enough temperature, thermal vibrations provide the work needed to rotate one spin vector against the other and the disordering effect of thermal energy (kT) will overcome the ordering exchange force. The temperature at which the spin structure is destroyed is the Curie temperature for ferrimagnetic minerals, and the Néel temperature for an antiferromagnet.

A1.13. Magnetic Susceptibility (χ)

In small fields, magnetization changes approximately linearly with increasing applied field, $M = \kappa H$. κ, the volume magnetic susceptibility, is dimensionless. Mass-specific susceptibility (χ) is the magnetic moment per unit mass divided by the field strength, with units of m^3kg^{-1}. χ depends on the type, grain size, and concentration of a magnetic mineral, and the measurement field and frequency.

A1.14. Multidomain (MD)

With increasing grain size, the magnetostatic energy of a magnetic particle increases. To minimize this energy, a particle begins to nucleate domain walls at a critical grain size threshold. These walls divide the particle into two or more magnetic volumes or domains. The magnetization is uniform in each domain, but it differs in direction from domain to domain. The transition between small grains with only one domain (termed SD) and MD grains is not sharp; a size range exists with a noncollinear spin structure or vortex structure that may contain a few domains.

A1.15. Magnetostriction

A property of magnetic materials that causes shape changes when subjected to a magnetic field. The effect was first identified by James Joule in nickel. A magnetostrictive material deforms mechanically when subjected to an external magnetic field. This phenomenon is attributed to the rotation of small magnetic domains, which are oriented randomly when the material is not exposed to a magnetic field, but become oriented in an applied magnetic field to create a strain field. As the magnetic field intensity increases, more domains become oriented so that their principal anisotropy axes are aligned with the field until magnetic saturation is achieved.

A1.16. Morin Transition

A magnetic phase transition named after Morin (1950) who reported an abrupt magnetic susceptibility decrease in a hematite polycrystalline powder below ~255 K. Above the Morin transition temperature (T_M: 255 K), antiferromagnetic ordering is reorganized from a perpendicular alignment to the crystallographic c axis to a parallel alignment. Below T_M, spin canting and the weak magnetism should vanish.

A1.17. Natural Remanent Magnetization (NRM)

The magnetic remanence of a geological sample prior to laboratory treatment. The NRM is typically composed of more than one component acquired at different times during a sample's history, which can be identified in the laboratory using various stepwise demagnetization procedures.

A1.18. Néel Temperature (T_N)

As temperature increases in antiferromagnetic substances, interatomic distances increase, and the magnetic exchange interaction becomes weaker. At T_N, thermal energy overcomes the exchange energy and magnetic moments become independent so that the material becomes paramagnetic. For ferrimagnetic minerals, this temperature is known as the Curie temperature (T_C). In practice, the terms Curie and Néel temperature are used interchangeably. T_N and T_C are named after the French physicists Louis Néel (1904–2000) and Pierre Curie (1859–1906), respectively.

A1.19. Remagnetization

A phenomenon by which NRM is acquired in an ambient magnetic field at a much younger age than of the surrounding rock or sediment, which complicates paleomagnetic data interpretation from rocks, soils, and sediments. Remagnetizations are generally carried by a CRM acquired long after deposition.

A1.20. Single Domain (SD)

A uniformly magnetized magnetic particle with a single magnetic domain. Noninteracting SD grains are ideal recorders of paleomagnetic information.

A1.21. Superexchange

In magnetic oxides and sulfides, iron atoms are never close enough for direct exchange interaction. Instead, there is an indirect exchange interaction of $3d$ electrons of Fe^{2+} or Fe^{3+} through overlap with $2p$ orbitals of intervening oxygen ions or $3p$ orbitals of sulfur ions, which is known as superexchange.

A1.22. Superparamagnetism (SP)

A term used to describe the magnetic behavior of particles above their blocking temperature or below their blocking volume. These particles act like paramagnetic atoms, with atomic magnetic moments aligning in a magnetic field to produce a strong induced magnetization that is destroyed rapidly by thermal vibrations soon after removing the applied field.

A1.23. Thermoremanent Magnetization (TRM)

When magnetic minerals cool in a weak magnetic field H_0 from above their Curie temperatures, they acquire TRM in the direction of H_0 with an intensity proportional to H_0. TRM is the primary NRM of igneous rocks and some metamorphic rocks.

A1.24. Thermal Demagnetization

Demagnetization carried out by heating magnetic minerals to elevated temperatures below T_c, then cooling to room temperature in zero field. The remanent magnetization of magnetic grains with T_b less than or equal to the demagnetization temperature is randomized by heating. Stepwise increasing temperatures to T_c enable progressive remanent magnetization removal. Heating can thermally alter constituent minerals and obscure results. Nevertheless, thermal treatment is used to demagnetize high-coercivity minerals such as hematite and goethite, which usually cannot be achieved by alternating field (AF) demagnetization.

A1.25. Unblocking Temperature (T_b)

The temperature during warming at which thermal energy overcomes the magnetic exchange energy and the magnetization "unblocks." At this temperature, the magnetic relaxation time decreases so that the particle has SP behavior rather than stable SD behavior (Butler, 1992).

A2. Nonmagnetic Terms

A2.1. Banded Iron Formations (BIFs)

Distinctive sedimentary rock units consisting of alternating iron oxide and iron-poor chert layers. They can be up to several hundred meters thick and extend laterally for several hundred km. Almost all BIFs are of Precambrian age and are thought to record oxygenation of Earth's oceans.

A2.2. Differential XRD

A diffraction pattern for iron minerals in a sample is obtained by subtracting the pattern for a sample free of iron oxides, after appropriate intensity adjustment, from that of an untreated sample.

A2.3. Diffuse Reflectance Spectroscopy

Reflectance in soils and sediments includes two components, specular and diffuse reflectance. When an incident light beam impinges on a powder surface, a small fraction is reflected specularly (specular reflectance); the rest penetrates into the mass as wavelength-dependent absorption within colored materials or is scattered (as multiple reflections, refractions, and diffractions in all directions). Part of this radiation ultimately leaves the material in all directions as diffuse reflectance. Diffuse reflectance spectroscopy in the visible (VIS, ~400–700 nm) and near infrared (NIR, ~700–2,500 nm) ranges is used to obtain color information and characteristic bands for different minerals. Color can be calculated from these spectra and absorption band positions may be extracted mathematically from spectra to enhance the resolution of broad, overlapping bands.

A2.4. Imaging Spectrometer for Mars

ISM, which operated in the NIR range, is the first flown in space for planetary observation. With a 0.76–3.14 μm spectral range, its main goals were to obtain mineralogical composition information from the surfaces of Mars and Phobos, and information on the composition and spatial and temporal variations of the Martian atmosphere.

A2.5. Munsell Hue, Chroma, and Value

Color system developed in the early 1900s by the artist A. H. Munsell. A color point in this system is defined by three parameters: hue, value, and chroma. Hue refers to the spectral colors red (R), yellow (Y), green (G), blue (B), purple (P), and their intermediates (e.g., YR or RP). These 10 major hues are arranged in a 100° circle divided in 1° steps (e.g., 10YR). Chroma refers to color intensity, increasing from 0 in steps of one. The third parameter, value, defines lightness, and extends perpendicular to the hue-chroma plane, with its greatest extension from 0 (black) over shades of gray to 10 (white).

A2.6. Redness Rating (RR)

An index expressed as $RR = [(10 - H) \times C]/V$, where V and C are the numerical values of the Munsell value and chroma, respectively, and H is the figure preceding YR in the Munsell hue (Torrent et al., 1983). RR is used to obtain semiquantitative hematite measurements in soils.

A2.7. Thermal Emission Spectrometer (TES)

A Michelson interferometer/spectrometer that covers the $\sim$6–50 μm (1,655–200 cm^{-1}) wavelength range at moderate spectral resolution (5 and 10 cm^{-1}). It was designed to study the composition and physical properties of the Martian surface, the composition and abundance of atmospheric aerosols and condensates, the three-dimensional atmospheric temperature field structure, and polar region energy balance and processes. TES entered Mars orbit on board the Mars Global Surveyor (MGS) spacecraft on 11 September 1997.

A2.8. Thermal Emission Imaging System (THEMIS)

A camera on board the 2001 Mars Odyssey orbiter. It imaged Mars in the visible and infrared parts of the electromagnetic spectrum to determine surface thermal properties and to refine the mineral distribution on the Martian surface with the TES. It also helps to understand how the mineralogy of Mars relates to its landforms to search for subsurface thermal hotspots.

A2.9. *x*, *y*, and *Y*

Three color coordinates based on the des Séances ([1931](#)). In the CIE-Y*xy* space, all colors lie within a plane resembling a shoe sole. An arbitrary point B within that plane is defined by the Cartesian coordinates *x* and *y*, where the redness increases with *x*, and greenness increases with *y*. The lightness Y, is perpendicular to *x* and *y* out of the plane.

Data Availability Statement

Data to support this article are deposited in Zenodo (https://doi.org/10.5281/zenodo.5606272).

References

Abrajevitch, A., Font, E., Florindo, F., & Roberts, A. P. (2015). Asteroid impact vs. Deccan eruptions: The origin of low magnetic susceptibility beds below the Cretaceous–Paleogene boundary revisited. *Earth and Planetary Science Letters*, *430*, 209–223. https://doi.org/10.1016/j.epsl.2015.08.022

Abrajevitch, A., Pillans, B. J., & Roberts, A. P. (2014). Haematite pigmentation events and palaeomagnetic recording: Implications from the Pilbara Print Stone, Western Australia. *Geophysical Journal International*, *199*(2), 658–672. https://doi.org/10.1093/gji/ggu293

Abrajevitch, A., Pillans, B. J., Roberts, A. P., & Kodama, K. (2018). Magnetic properties and paleomagnetism of Zebra Rock, Western Australia: Chemical remanence acquisition in hematite pigment and Ediacaran geomagnetic field behavior. *Geochemistry, Geophysics, Geosystems*, *19*(3), 732–748. https://doi.org/10.1002/2017GC007091

Abrajevitch, A., Van der Voo, R., & Rea, D. K. (2009). Variations in relative abundances of goethite and hematite in Bengal Fan sediments: Climatic vs. diagenetic signals. *Marine Geology*, *267*(3–4), 191–206. https://doi.org/10.1016/j.margeo.2009.10.010

Acuña, M., Connerney, J., Lin, R., Mitchell, D., Carlson, C., McFadden, J., et al. (1999). Global distribution of crustal magnetization discovered by the Mars Global Surveyor MAG/ER experiment. *Science*, *284*(5415), 790–793. https://doi.org/10.1126/science.284.5415.790

Aharoni, A., Frei, E., & Schieber, M. (1962). Curie point and origin of weak ferromagnetism in hematite. *Physical Review*, *127*(2), 439–441. https://doi.org/10.1103/PhysRev.129.2835.2

Allen, C. C., Gooding, J. L., & Keil, K. (1982). Hydrothermally altered impact melt rock and breccia: Contributions to the soil of Mars. *Journal of Geophysical Research: Solid Earth*, *87*(B12), 10083–10101. https://doi.org/10.1029/JB087iB12p10083

Allen, C. C., Probst, L. W., Flood, B. E., Longazo, T. G., Schelble, R. T., & Westall, F. (2004). Meridiani Planum hematite deposit and the search for evidence of life on Mars-iron mineralization of microorganisms in rock varnish. *Icarus*, *171*(1), 20–30. https://doi.org/10.1016/j.icarus.2004.04.015

Allen, C. C., Westall, F., & Schelble, R. T. (2001). Importance of a Martian hematite site for astrobiology. *Astrobiology*, *1*(1), 111–123. https://doi.org/10.1089/153110701750137495

Amin, N., & Arajs, S. (1987). Morin temperature of annealed submicronic α-Fe$_2$O$_3$ particles. *Physical Review B*, *35*(10), 4810–4811. https://doi.org/10.1103/PhysRevB.35.4810

Anand, R., & Gilkes, R. (1987). Variations in the properties of iron oxides within individual specimens of lateritic duricrust. *Soil Research*, *25*(3), 287–302. https://doi.org/10.1071/SR9870287

Ao, H., Rohling, E. J., Stringer, C., Roberts, A. P., Dekkers, M. J., Dupont-Nivet, G., et al. (2020). Two-stage mid-Brunhes climate transition and mid-Pleistocene human diversification. *Earth-Science Reviews*, *210*, 103354. https://doi.org/10.1016/j.earscirev.2020.103354

Ao, H., Zhang, P., Dekkers, M. J., Roberts, A. P., An, Z. S., Li, Y. X., et al. (2016). New magnetochronology of Late Miocene mammal fauna, NE Tibetan Plateau, China: Mammal migration and paleoenvironments. *Earth and Planetary Science Letters*, *434*, 220–230. https://doi.org/10.1016/j.epsl.2015.11.019

Artman, J. O., Murphy, J. C., & Foner, S. (1965). Magnetic anisotropy in antiferromagnetic corundum-type sesquioxides. *Physical Review*, *138*(3A), A912–A917. https://doi.org/10.1103/PhysRev.138.A912

Ayyub, P., Multani, M., Barma, M., Palkar, V., & Vijayaraghavan, R. (1988). Size-induced structural phase transitions and hyperfine properties of microcrystalline Fe$_2$O$_3$. *Journal of Physics C*, *21*(11), 2229–2245. https://doi.org/10.1088/0022-3719/21/11/014

Bailey, I., Liu, Q., Swann, G. E. A., Jiang, Z., Sun, Y., Zhao, X., & Roberts, A. P. (2011). Iron fertilisation and biogeochemical cycles in the sub-Arctic northwest Pacific during the late Pliocene intensification of northern hemisphere glaciation. *Earth and Planetary Science Letters*, *307*(3–4), 253–265. https://doi.org/10.1016/j.epsl.2011.05.029

Bailey, M. E., & Hale, C. J. (1981). Anomalous magnetic directions recorded by laboratory-induced chemical remanent magnetization. *Nature*, *294*(5843), 739–741. https://doi.org/10.1038/294739a0

Balsam, W., Ji, J., & Chen, J. (2004). Climatic interpretation of the Luochuan and Lingtai loess sections, China, based on changing iron oxide mineralogy and magnetic susceptibility. *Earth and Planetary Science Letters*, *223*(3), 335–348. https://doi.org/10.1016/j.epsl.2004.04.023

Balsam, W. L., & Deaton, B. C. (1996). Determining the composition of late Quaternary marine sediments from NUV, VIS, and NIR diffuse reflectance spectra. *Marine Geology*, *134*(1–2), 31–55. https://doi.org/10.1016/0025-3227(96)00037-0

Balsam, W. L., Deaton, B. C., & Damuth, J. E. (1999). Evaluating optical lightness as a proxy for carbonate content in marine sediment cores. *Marine Geology*, *161*(2), 141–153. https://doi.org/10.1016/S0025-3227(99)00037-7

Balsam, W. L., Ellwood, B. B., Ji, J. F., Williams, E. R., Long, X. Y., & El Hassani, A. (2011). Magnetic susceptibility as a proxy for rainfall: Worldwide data from tropical and temperate climate. *Quaternary Science Reviews*, *30*(19–20), 2732–2744. https://doi.org/10.1016/j.quascirev.2011.06.002

Bandfield, J. L. (2002). Global mineral distributions on Mars. *Journal of Geophysical Research*, *107*(E6), 5042. https://doi.org/10.1029/2001JE001510

Banerjee, S. K. (1971). New grain size limits for palaeomagnetic stability in haematite. *Nature Physical Science*, *232*(27), 15–16. https://doi.org/10.1038/physci232015a0

Banfield, J. F., Welch, S. A., Zhang, H., Ebert, T. T., & Penn, R. L. (2000). Aggregation-based crystal growth and microstructure development in natural iron oxyhydroxide biomineralization products. *Science*, *289*, 751–754. https://doi.org/10.1126/science.289.5480.751

Bao, L., Yang, H., Wang, X., Zhang, F., Shi, R., Liu, B., et al. (2011). Synthesis and size-dependent magnetic properties of single-crystalline hematite nanodiscs. *Journal of Crystal Growth*, *328*(1), 62–69. https://doi.org/10.1016/j.jcrysgro.2011.05.030

Barley, M. E., Pickard, A. L., Hagemann, S. G., & Folkert, S. L. (1999). Hydrothermal origin for the 2 billion year old Mount Tom Price giant iron ore deposit, Hamersley Province, Western Australia. *Mineralium Deposita*, *34*(8), 784–789. https://doi.org/10.1007/s001260050238

Barrón, V., Rendón, J., Torrent, J., & Serna, C. (1984). Relation of infrared, crystallochemical, and morphological properties of Al-substituted hematites. *Clays and Clay Minerals*, *32*(6), 475–479. https://doi.org/10.1346/CCMN.1984.0320605

Barrón, V., & Torrent, J. (1984). Influence of aluminum substitution on the color of synthetic hematites. *Clays and Clay Minerals*, *32*(2), 157–158. https://doi.org/10.1346/CCMN.1984.0320211

Barrón, V., & Torrent, J. (1986). Use of the Kubelka-Munk theory to study the influence of iron oxides on soil colour. *European Journal of Soil Science*, *37*(4), 499–510. https://doi.org/10.1111/j.1365-2389.1986.tb00382.x

Barrón, V., & Torrent, J. (2002). Evidence for a simple pathway to maghemite in Earth and Mars soils. *Geochimica et Cosmochimica Acta*, *66*(15), 2801–2806. https://doi.org/10.1016/S0016-7037(02)00876-1

Barrón, V., & Torrent, J. (2013). Iron, manganese and aluminium oxides and oxyhydroxides. In F. Nieto, K. J. T. Livi, & R. Oberti (Eds.), *Minerals at the nanoscale* (pp. 297–336). Mineralogical Society of Great Britain and Ireland. https://doi.org/10.1180/EMU-notes.14.9

Barrón, V., Torrent, J., & de Grave, E. (2003). Hydromaghemite, an intermediate in the hydrothermal transformation of 2-line ferrihydrite into hematite. *American Mineralogist*, *88*(11–12), 1679–1688. https://doi.org/10.2138/am-2003-11-1207

Barrón, V., Torrent, J., & Greenwood, J. P. (2006). Transformation of jarosite to hematite in simulated Martian brines. *Earth and Planetary Science Letters*, *251*(3), 380–385. https://doi.org/10.1016/j.epsl.2006.09.022

Bayer, G., Felsche, J., Schulz, H., & Rüegsegger, P. (1972). X-ray study and Mössbauer spectroscopy on lunar ilmenites (Apollo 11). *Earth and Planetary Science Letters*, *16*(2), 273–274. https://doi.org/10.1016/0012-821X(72)90202-6

Bell, J. F., McCord, T. B., & Owensby, P. D. (1990). Observational evidence of crystalline iron oxides on Mars. *Journal of Geophysical Research*, *95*(B9), 14447. https://doi.org/10.1029/JB095iB09p14447

Bell, J. F., Morris, R. V., & Adams, J. B. (1993). Thermally altered palagonitic tephra: A spectral and process analog to the soil and dust of Mars. *Journal of Geophysical Research*, *98*(E2), 3373–3385. https://doi.org/10.1029/92JE02367

Bell, J. F., Squyres, S. W., Arvidson, R. E., Arneson, H. M., Bass, D., Calvin, W., et al. (2004). Pancam multispectral imaging results from the opportunity Rover at Meridiani Planum. *Science*, *306*(5702), 1703–1709. https://doi.org/10.1126/SCIENCE.1105245

Bercoff, P. G., & Bertorello, H. R. (2010). Magnetic properties of hematite with large coercivity. *Applied Physics A*, *100*(4), 1019–1027. https://doi.org/10.1007/s00339-010-5983-7

Bezaeva, N. S., Demory, F., Rochette, P., Sadykov, R. A., Gattacceca, J., Gabriel, T., & Quesnel, Y. (2015). The effect of hydrostatic pressure up to 1.61 GPa on the Morin transition of hematite-bearing rocks: Implications for planetary crustal magnetization. *Geophysical Research Letters*, *42*(23), 10188–10196. https://doi.org/10.1002/2015GL066306

Bezaeva, N. S., Gattacceca, J., Rochette, P., Sadykov, R. A., & Trukhin, V. I. (2010). Demagnetization of terrestrial and extraterrestrial rocks under hydrostatic pressure up to 1.2 GPa. *Physics of the Earth and Planetary Interiors*, *179*(1–2), 7–20. https://doi.org/10.1016/j.pepi.2010.01.004

Bezaeva, N. S., Rochette, P., Gattacceca, J., Sadykov, R. A., & Trukhin, V. I. (2007). Pressure demagnetization of the Martian crust: Ground truth from SNC meteorites. *Geophysical Research Letters*, *34*(L23202). https://doi.org/10.1029/2007GL031501

Bhowmik, R., & Saravanan, A. (2010). Surface magnetism, Morin transition, and magnetic dynamics in antiferromagnetic α-Fe_2O_3 (hematite) nanograins. *Journal of Applied Physics*, *107*(5), 053916. https://doi.org/10.1063/1.3327433

Bian, W., Yang, T., Jiang, Z., Jin, J., Gao, F., Wang, S., et al. (2020). Paleomagnetism of the Late Cretaceous red beds from the Far Western Lhasa Terrane: Inclination discrepancy and tectonic implications. *Tectonics*, *39*(8), e2020TC006280. https://doi.org/10.1029/2020TC006280

Bilardello, D. (2019). Tinkering with the wheel: Can the goethite test run more smoothly? *The IRM Quarterly*, *29*(21), 9–13.

Bilardello, D., Jezek, J., & Gilder, S. A. (2012). Role of spherical particles on magnetic field recording in sediments: Experimental and numerical results. *Physics of the Earth and Planetary Interiors*, *214*, 1–13. https://doi.org/10.1016/j.pepi.2012.10.014

Bilardello, D., & Kodama, K. P. (2009). Measuring remanence anisotropy of hematite in red beds: Anisotropy of high-field isothermal remanence magnetization (hf-AIR). *Geophysical Journal International*, *178*(3), 1260–1272. https://doi.org/10.1111/j.1365-246X.2009.04231.x

Bilardello, D., & Kodama, K. P. (2010). Rock magnetic evidence for inclination shallowing in the early Carboniferous Deer Lake Group red beds of western Newfoundland. *Geophysical Journal International*, *181*(1), 275–289. https://doi.org/10.1111/j.1365-246X.2010.04537.x

Bischoff, J. L. (1969). Goethite-hematite stability relations with relevance to sea water and the Red Sea brine system. In E. T. Degens & D. A. Ross (Eds.), *Hot brines and recent heavy metal deposits in the Red Sea: A geochemical and geophysical account* (pp. 402–406). Springer. https://doi.org/10.1007/978-3-662-28603-6_38

Bishop, J. L., Murad, E., & Dyar, M. D. (2015). Akaganeite and schwertmannite: Spectral properties and geochemical implications of their possible presence on Mars. *American Mineralogist*, *100*, 738–746. https://doi.org/10.2138/am-2015-5016

Blake, R. L., Hessevick, R. E., Zoltai, T., & Finger, L. W. (1966). Refinement of the hematite structure. *American Mineralogist*, *51*(1–2), 123–129.

Blank, M., Leinen, M., & Prospero, J. M. (1985). Major Asian aeolian inputs indicated by the mineralogy of aerosols and sediments in the western North Pacific. *Nature*, *314*(6006), 84–86. https://doi.org/10.1038/314084a0

Bloemendal, J. (1983). Paleoenvironmental implications of the magnetic characteristics of sediments from Deep Sea Drilling Project Site 514, Southeast Argentine Basin. In W. J. Ludwig & V. A. Krasheninnikov (Eds.), *Initial reports of the Deep Sea Drilling Project* (pp. 1097–1108). https://doi.org/10.2973/dsdp.proc.71.144.1983

Bloemendal, J., King, J., Hall, F., & Doh, S. J. (1992). Rock magnetism of Late Neogene and Pleistocene deep-sea sediments: Relationship to sediment source, diagenetic processes, and sediment lithology. *Journal of Geophysical Research*, *97*(B4), 4361–4375. https://doi.org/10.1029/91JB03068

Bloemendal, J., Lamb, B., & King, J. (1988). Paleoenvironmental implications of rock-magnetic properties of Late Quaternary sediment cores from the eastern equatorial Atlantic. *Paleoceanography*, *3*(1), 61–87. https://doi.org/10.1029/PA003i001p00061

Bloemendal, J., & Liu, X. (2005). Rock magnetism and geochemistry of two Plio-Pleistocene Chinese loess-palaeosol sequences—Implications for quantitative palaeoprecipitation reconstruction. *Palaeogeography, Palaeoclimatology, Palaeoecology*, *226*(1–2), 149–166. https://doi.org/10.1016/j.palaeo.2005.05.008

Bowen, B. B., Benison, K. C., Oboh-Ikuenobe, F. E., Story, S., & Mormile, M. R. (2008). Active hematite concretion formation in modern acid saline lake sediments, Lake Brown, Western Australia. *Earth and Planetary Science Letters*, *268*(1), 52–63. https://doi.org/10.1016/j.epsl.2007.12.023

Bowles, J. A., Jackson, M. J., Berquó, T. S., Sølheid, P. A., & Gee, J. S. (2013). Inferred time- and temperature-dependent cation ordering in natural titanomagnetites. *Nature Communications*, *4*, 1916. https://doi.org/10.1038/ncomms2938

Bowles, J. A., Tatsumi-Petrochilos, L., Hammer, J. E., & Brachfeld, S. A. (2012). Multicomponent cubic oxide exsolution in synthetic basalts: Temperature dependence and implications for magnetic properties. *Journal of Geophysical Research*, *117*(B3), B03202. https://doi.org/10.1029/2011JB008867

Boyle, J. F., Dearing, J. A., Blundell, A., & Hannam, J. A. (2010). Testing competing hypotheses for soil magnetic susceptibility using a new chemical kinetic model. *Geology*, *38*(12), 1059–1062. https://doi.org/10.1130/G31514.1

Bozorth, R. M., Walsh, D. E., & Williams, A. J. (1957). Magnetization of ilmenite-hematite system at low temperatures. *Physical Review*, *108*(1), 157–158. https://doi.org/10.1103/PhysRev.108.157.2

Buggle, B., Hambach, U., Müller, K., Zöller, L., Marković, S. B., & Glaser, B. (2014). Iron mineralogical proxies and Quaternary climate change in SE-European loess-paleosol sequences. *Catena*, *117*, 4–22. https://doi.org/10.1016/j.catena.2013.06.012

Burns, R. G. (1993a). Rates and mechanisms of chemical weathering of ferromagnesian silicate minerals on Mars. *Geochimica et Cosmochimica Acta*, *57*(19), 4555–4574. https://doi.org/10.1016/0016-7037(93)90182-V

Burns, R. G. (1993b). *Mineralogical applications of crystal field theory*. Cambridge University Press. https://doi.org/10.1017/CBO9780511524899

Burton, B. P., Robinson, P., McEnroe, S. A., Fabian, K., & Ballaran, T. B. (2008). A low-temperature phase diagram for ilmenite-rich compositions in the system Fe_2O_3-$FeTiO_3$. *American Mineralogist*, *93*(8–9), 1260–1272. https://doi.org/10.2138/am.2008.2690

Butler, R. F. (1992). *Paleomagnetism: Magnetic domains to geologic terranes*. Blackwell Scientific Publications.

Cao, H., Wang, G., Wang, J. H., & Watt, A. A. R. (2008). Amino-acid-assisted synthesis and size-dependent magnetic behaviors of hematite nanocubes. *Applied Physics Letters*, *92*(1), 013110. https://doi.org/10.1063/1.2830699

Cao, H., Wang, G., Zhang, L., Liang, Y., Zhang, S., & Zhang, X. (2006). Shape and magnetic properties of single-crystalline hematite ($α$-Fe_2O_3) nanocrystals. *ChemPhysChem*, *7*(9), 1897–1901. https://doi.org/10.1002/cphc.200600130

Cao, L., Jiang, Z.-X., Du, Y.-H., Yin, X.-M., Xi, S.-B., Wen, W., et al. (2017). Origin of magnetism in hydrothermally aged 2-line ferrihydrite suspensions. *Environmental Science & Technology*, *51*(5), 2643–2651. https://doi.org/10.1021/acs.est.6b04716

Carter-Stiglitz, B., Banerjee, S. K., Gourlan, A., & Oches, E. (2006). A multi-proxy study of Argentina loess: Marine oxygen isotope stage 4 and 5 environmental record from pedogenic hematite. *Palaeogeography, Palaeoclimatology, Palaeoecology*, *239*(1–2), 45–62. https://doi.org/10.1016/j.palaeo.2006.01.008

Catling, D. C. (2004). On Earth, as it is on Mars? *Nature*, *429*(6993), 707–708. https://doi.org/10.1038/429707a

Catling, D. C., & Moore, J. M. (2003). The nature of coarse-grained crystalline hematite and its implications for the early environment of Mars. *Icarus*, *165*(2), 277–300. https://doi.org/10.1016/S0019-1035(03)00173-8

Catti, M., Valerio, G., & Dovesi, R. (1995). Theoretical-study of electronic, magnetic, and structural properties of alpha-Fe_2O_3 (hematite). *Physical Review B*, *51*(12), 7441–7450. https://doi.org/10.1103/PhysRevB.51.7441

Chan, M. A., Beard, B. L., Johnson, C. M., Bowman, J. R., & Parry, W. T. (2006). Iron isotopes constrain the pathways and formation mechanisms of terrestrial oxide concretions: A tool for tracing iron cycling on Mars? *Geosphere*, *2*(7), 324–332. https://doi.org/10.1130/GES00051.1

Chan, M. A., Beitler, B., Parry, W. T., Ormo, J., & Komatsu, G. (2004). A possible terrestrial analogue for haematite concretions on Mars. *Nature*, *429*(6993), 731–734. https://doi.org/10.1038/nature02600

Chang, L., Winklhofer, M., Roberts, A. P., Heslop, D., Florindo, F., Dekkers, M. J., et al. (2013). Low-temperature magnetic properties of pelagic carbonates: Oxidation of biogenic magnetite and identification of magnetosome chains. *Journal of Geophysical Research: Solid Earth*, *118*, 6049–6065. https://doi.org/10.1002/2013jb010381

Charreau, J., Chen, Y., Gilder, S., Dominguez, S., Avouac, J. P., Sen, S., et al. (2005). Magnetostratigraphy and rock magnetism of the Neogene Kuitun He section (northwest China): Implications for Late Cenozoic uplift of the Tianshan mountains. *Earth and Planetary Science Letters*, *230*, 177–192. https://doi.org/10.1016/j.epsl.2004.11.002

Chen, T., Xie, Q., Xu, H., Chen, J., Ji, J., Lu, H., & Balsam, W. (2010). Characteristics and formation mechanism of pedogenic hematite in Quaternary Chinese loess and paleosols. *Catena*, *81*(3), 217–225. https://doi.org/10.1016/j.catena.2010.04.001

Chen, T., Xu, H., Xie, Q., Chen, J., Ji, J., & Lu, H. (2005). Characteristics and genesis of maghemite in Chinese loess and paleosols: Mechanism for magnetic susceptibility enhancement in paleosols. *Earth and Planetary Science Letters*, *240*(3–4), 790–802. https://doi.org/10.1016/j.epsl.2005.09.026

Chevallier, R., & Mathieu, S. (1943). Propriétés magnétiques des poudres d'hématites. Influence des dimensions des grains. *Annales de Physique*, *11*(18), 258–288. https://doi.org/10.1051/anphys/194311180258

Christensen, P. R., Bandfield, J. L., Clark, R. N., Edgett, K. S., Hamilton, V. E., Hoefen, T., et al. (2000). Detection of crystalline hematite mineralization on Mars by the thermal emission spectrometer: Evidence for near-surface water. *Journal of Geophysical Research*, *105*(E4), 9623–9642. https://doi.org/10.1029/1999JE001093

Christensen, P. R., Bandfield, J. L., Hamilton, V. E., Howard, D. A., Lane, M. D., Piatek, J. L., et al. (2000). A thermal emission spectral library of rock-forming minerals. *Journal of Geophysical Research*, *105*(E4), 9735–9739. https://doi.org/10.1029/1998JE000624

Christensen, P. R., Bandfield, J. L., Smith, M. D., Hamilton, V. E., & Clark, R. N. (2000). Identification of a basaltic component on the Martian surface from Thermal emission Spectrometer data. *Journal of Geophysical Research*, *105*(E4), 9609–9621. https://doi.org/10.1029/1999JE001127

Christensen, P. R., Morris, R. V., Lane, M. D., Bandfield, J. L., & Malin, M. C. (2001). Global mapping of Martian hematite mineral deposits: Remnants of water-driven processes on early Mars. *Journal of Geophysical Research*, *106*(E10), 23873–23885. https://doi.org/10.1029/2000JE001415

Christensen, P. R., Wyatt, M. B., Glotch, T. D., Rogers, A. D., Anwar, S., Arvidson, R. E., et al. (2004). Mineralogy at Meridiani Planum from the Mini-TES experiment on the opportunity Rover. *Science*, *306*(5702), 1733–1739. https://doi.org/10.1126/science.1104909

Clark, B. C., & Van Hart, D. C. (1981). The salts of Mars. *Icarus*, *45*(2), 370–378. https://doi.org/10.1016/0019-1035(81)90041-5

Clark, D. A. (1983). Comments on magnetic petrophysics. *Exploration Geophysics*, *14*(2), 49–62. https://doi.org/10.1071/EG983049

Clift, P. D., Hodges, K. V., Heslop, D., Hannigan, R., Van Long, H., & Calves, G. (2008). Correlation of Himalayan exhumation rates and Asian monsoon intensity. *Nature Geoscience*, *1*(12), 875–880. https://doi.org/10.1038/ngeo351

Clift, P. D., Wan, S., & Blusztajn, J. (2014). Reconstructing chemical weathering, physical erosion and monsoon intensity since 25 Ma in the northern South China Sea: A review of competing proxies. *Earth-Science Reviews*, *130*, 86–102. https://doi.org/10.1016/j.earscirev.2014.01.002

Cloud, P. (1973). Paleoecological significance of the banded iron-formation. *Economic Geology*, *68*(7), 1135–1143. https://doi.org/10.2113/GSECONGEO.68.7.1135

Coe, R. S., Egli, R., Gilder, S. A., & Wright, J. P. (2012). The thermodynamic effect of nonhydrostatic stress on the Verwey transition. *Earth and Planetary Science Letters*, *319*, 207–217. https://doi.org/10.1016/j.epsl.2011.11.021

Cogné, J., Halim, N., Chen, Y., & Courtillot, V. (1999). Resolving the problem of shallow magnetizations of Tertiary age in Asia: Insights from paleomagnetic data from the Qiangtang, Kunlun, and Qaidam blocks (Tibet, China), and a new hypothesis. *Journal of Geophysical Research*, *104*(B8), 17715–17734. https://doi.org/10.1029/1999JB900153

Collinson, D. (1965a). Depositional remanent magnetization in sediments. *Journal of Geophysical Research*, *70*(18), 4663–4668. https://doi.org/10.1029/JZ070i018p04663

Collinson, D. (1965b). The remanent magnetization and magnetic properties of red sediments. *Geophysical Journal of the Royal Astronomical Society*, *10*(1), 105–126. https://doi.org/10.1111/j.1365-246X.1965.tb03055.x

Collinson, D. (1966). Carrier of remanent magnetization in certain red sandstones. *Nature*, *210*, 516–517. https://doi.org/10.1038/210516a0

Collinson, D. (1968). An estimate of the haematite content of sediments by magnetic analysis. *Earth and Planetary Science Letters*, *4*(6), 417–421. https://doi.org/10.1016/0012-821X(68)90015-0

Collinson, D. (1974). The role of pigment and specularite in the remanent magnetism of red sandstones. *Geophysical Journal of the Royal Astronomical Society*, *38*(2), 253–264. https://doi.org/10.1111/j.1365-246X.1974.tb04119.x

Colombo, C., Iorio, E. D., Liu, Q., Jiang, Z., & Barrón, V. (2017). Iron oxide nanoparticles in soils: Environmental and agronomic importance. *Journal of Nanoscience and Nanotechnology*, *17*(7), 4449–4460. https://doi.org/10.1166/jnn.2018.15294

Cornell, R., & Schwertmann, U. (2003). *The iron oxides: Structure, properties, reactions, occurrences and uses*. John Wiley & Sons. https://doi.org/10.1002/3527602097

Cox, A., Doell, R. R., & Dalrymple, G. B. (1963). Geomagnetic polarity epochs and Pleistocene geochronometry. *Nature*, *198*(4885), 1049–1051. https://doi.org/10.1038/1981049a0

Cox, D. E., Takei, W. J., Miller, R. C., & Shirane, G. (1962). A magnetic and neutron diffraction study of the Fe_2O_3-V_2O_3 system. *Journal of Physics and Chemistry of Solids*, *23*(7), 863–874. https://doi.org/10.1016/0022-3697(62)90143-9

Cox, E., Elmore, R. D., & Evans, M. (2005). Paleomagnetism of Devonian red beds in the Appalachian Plateau and valley and Ridge provinces. *Journal of Geophysical Research*, *110*(B8), B08102. https://doi.org/10.1029/2005JB003640

Creer, K. (1968). Palaeozoic palaeomagnetism. *Nature*, *219*, 246–250. https://doi.org/10.1038/219246a0

Curi, N., & Franzmeier, D. (1984). Toposequence of oxisols from the central plateau of Brazil. *Soil Science Society of America Journal*, *48*(2), 341–346. https://doi.org/10.2136/sssaj1984.03615995004800020024x

Curi, N., & Franzmeier, D. (1987). Effect of parent rocks on chemical and mineralogical properties of some oxisols in Brazil. *Soil Science Society of America Journal*, *51*(1), 153–158. https://doi.org/10.2136/sssaj1987.03615995005100010033x

da Costa, G. M., Van San, E., De Grave, E., Vandenberghe, R. E., Barrón, V., & Datas, L. (2002). Al hematites prepared by homogeneous precipitation of oxinates: Material characterization and determination of the Morin transition. *Physics and Chemistry of Minerals*, *29*(2), 122–131. https://doi.org/10.1007/s002690100201

Deaton, B. C., & Balsam, W. L. (1991). Visible spectroscopy: A rapid method for determining hematite and goethite concentration in geological materials. *Journal of Sedimentary Research*, *61*(4), 628–632. https://doi.org/10.1306/D4267794-2B26-11D7-8648000102C1865D

de Boer, C. B., & Dekkers, M. J. (2001). Unusual thermomagnetic behaviour of haematites: Neoformation of a highly magnetic spinel phase on heating in air. *Geophysical Journal International*, *144*(2), 481–494. https://doi.org/10.1046/j.0956-540X.2000.01333.x

de Boer, C. B., Dekkers, M. J., & Van Hoof, T. A. M. (2001). Rock-magnetic properties of TRM carrying baked and molten rocks straddling burnt coal seams. *Physics of the Earth and Planetary Interiors*, *126*(1–2), 93–108. https://doi.org/10.1016/s0031-9201(01)00246-1

de Boer, C. B., Mullender, T. A. T., & Dekkers, M. J. (2001). Low-temperature behaviour of haematite: Susceptibility and magnetization increase on cycling through the Morin transition. *Geophysical Journal International*, *146*(1), 201–216. https://doi.org/10.1046/j.0956-540x.2001.01443.x

Deenen, M. H. L., Langereis, C. G., van Hinsbergen, D. J. J., & Biggin, A. J. (2011). Geomagnetic secular variation and the statistics of palaeomagnetic directions. *Geophysical Journal International*, *186*(2), 509–520. https://doi.org/10.1111/j.1365-246X.2011.05050.x

De Grave, E., Barrero, C. A., Da Costa, G. M., Vanderberghe, R. E., & Van San, E. (2002). Mossbauer spectra of α- and γ-polymorphs of FeOOH and Fe_2O_3: Effects of poor crystallinity and of Al-for-Fe substitution. *Clay Minerals*, *37*(4), 591–606. https://doi.org/10.1180/0009855023740062

De Grave, E., Bowen, L., Vochten, R., & Vandenberghe, R. (1988). The effect of crystallinity and Al substitution on the magnetic structure and Morin transition in hematite. *Journal of Magnetism and Magnetic Materials*, *72*(2), 141–151. https://doi.org/10.1016/0304-8853(88)90182-5

Dekkers, M., & Linssen, J. (1989). Rock magnetic properties of fine-grained natural low-temperature haematite with reference to remanence acquisition mechanisms in red beds. *Geophysical Journal International*, *99*(1), 1–18. https://doi.org/10.1111/j.1365-246X.1989.tb02012.x

Dekkers, M. J. (1990). Magnetic properties of natural goethite–III. Magnetic behaviour and properties of minerals originating from goethite dehydration during thermal demagnetization. *Geophysical Journal International*, *103*(1), 233–250. https://doi.org/10.1111/j.1365-246X.1990.tb01765.x

Dekkers, M. J. (2012). End-member modelling as an aid to diagnose remagnetization: A brief review. *Geological Society, London, Special Publications*, *371*(1), 253–269. https://doi.org/10.1144/SP371.12

Deng, C., Liu, Q., Wang, W., & Liu, C. (2007). Chemical overprint on the natural remanent magnetization of a subtropical red soil sequence in the Bose Basin, southern China. *Geophysical Research Letters*, *34*(22), L22308. https://doi.org/10.1029/2007GL031400

Deng, C., Shaw, J., Liu, Q., Pan, Y., & Zhu, R. (2006). Mineral magnetic variation of the Jingbian loess/paleosol sequence in the northern Loess Plateau of China: Implications for Quaternary development of Asian aridification and cooling. *Earth and Planetary Science Letters*, *241*(1), 248–259. https://doi.org/10.1016/j.epsl.2005.10.020

Deng, C., Zhu, R., Jackson, M. J., Verosub, K. L., & Singer, M. J. (2001). Variability of the temperature-dependent susceptibility of the Holocene eolian deposits in the Chinese Loess Plateau: A pedogenesis indicator. *Physics and Chemistry of the Earth*, *26*(11–12), 873–878. https://doi.org/10.1016/S1464-1895(01)00135-1

Derder, M., Henry, B., Merabet, N., Bayou, B., & Amenna, M. (2001). Paleomagnetism of the Liassic member of the Zarzatine Formation (stable Saharan craton, Illizi basin, Algeria). *Annals of Geophysics*, *44*(5–6), 995–1010. https://doi.org/10.4401/ag-3551

des Séances, C. R. (1931). *Commission Internationale de l'Eclairage*. Cambridge University Press.

Dong, Q., Wang, D., Yao, J., Kumada, N., Kinomura, N., Takei, T., et al. (2009). Synthesis of hematite particles with various shapes by a simple hydrothermal reaction. *Journal of the Ceramic Society of Japan*, *117*(1363), 245–248. https://doi.org/10.2109/jcersj2.117.245

Doubrovine, P. V., Tarduno, J. A., & (2004). Self-reversed magnetization carried by titanomaghemite in oceanic basalts. *Earth and Planetary Science Letters*, *222*(3–4), 959–969. https://doi.org/10.1016/j.epsl.2004.04.009

Dreibus, G., Brueckner, J., Lugmair, G. W., & Waenke, H. (1999). Possible indication of sedimentary products at the Mars Pathfinder landing site: Phosphorus in APXS X-ray spectra. *EOS Transactions of the American Geophysical Union*, *80*(46), P32A-06.

Drodt, M., Trautwein, A. X., König, I., Suess, E., & Koch, C. B. (1997). Mössbauer spectroscopic studies on the iron forms of deep-sea sediments. *Physics and Chemistry of Minerals*, *24*(4), 281–293. https://doi.org/10.1007/s002690050040

Dunlop, D. J. (1970). Hematite: Intrinsic and defect ferromagnetism. *Science*, *169*(3948), 858–860. https://doi.org/10.1126/science.169.3948.858

Dunlop, D. J. (1971). Magnetic properties of fine-particle hematite. *Annales de Geophysique*, *27*(3), 269–293.

Dunlop, D. J., & Kletetschka, G. (2001). Multidomain hematite: A source of planetary magnetic anomalies? *Geophysical Research Letters*, *28*(17), 3345–3348. https://doi.org/10.1029/2001GL013125

Dunlop, D. J., & Özdemir, Ö. (1997). *Rock magnetism: Fundamentals and frontiers*. Cambridge University Press.

Dupont-Nivet, G., Butler, R. F., Yin, A., & Chen, X. (2002). Paleomagnetism indicates no Neogene rotation of the Qaidam Basin in northern Tibet during Indo-Asian collision. *Geology*, *30*(3), 263–266. https://doi.org/10.1130/0091-7613(2002)030<0263:PINNRO>2.0.CO;2

Dupont-Nivet, G., Guo, Z., Butler, R. F., & Jia, C. (2002). Discordant paleomagnetic direction in Miocene rocks from the central Tarim Basin: Evidence for local deformation and inclination shallowing. *Earth and Planetary Science Letters*, *199*(3), 473–482. https://doi.org/10.1016/S0012-821X(02)00566-6

Dupont-Nivet, G., Krijgsman, W., Langereis, C. G., Abels, H. A., Dai, S., & Fang, X. M. (2007). Tibetan plateau aridification linked to global cooling at the Eocene–Oligocene transition. *Nature*, *445*, 635–638. https://doi.org/10.1038/nature05516

Dupont-Nivet, G., Lippert, P. C., Van Hinsbergen, D. J. J., Meijers, M. J. M., & Kapp, P. (2010). Palaeolatitude and age of the Indo–Asia collision: Palaeomagnetic constraints. *Geophysical Journal International*, *182*(3), 1189–1198. https://doi.org/10.1111/j.1365-246X.2010.04697.x

Dupont-Nivet, G., van Hinsbergen, D. J. J., & Torsvik, T. H. (2010). Persistently low Asian paleolatitudes: Implications for the India-Asia collision history. *Tectonics*, *29*(5). https://doi.org/10.1029/2008TC002437

Dykoski, C. A., Edwards, R. L., Cheng, H., Yuan, D., Cai, Y., Zhang, M., et al. (2005). A high-resolution, absolute-dated Holocene and deglacial Asian monsoon record from Dongge Cave, China. *Earth and Planetary Science Letters*, *233*(1), 71–86. https://doi.org/10.1016/j.epsl.2005.01.036

Dzyaloshinsky, I. (1958). A thermodynamic theory of "weak" ferromagnetism of antiferromagnetics. *Journal of Physics and Chemistry of Solids*, *4*(4), 241–255. https://doi.org/10.1016/0022-3697(58)90076-3

Elston, D. P., & Purucker, M. E. (1979). Detrital magnetization in red beds of the Moenkopi Formation (Triassic), Gray Mountain, Arizona. *Journal of Geophysical Research*, *84*, 1653–1666. https://doi.org/10.1029/JB084iB04p01653

Eren, M., & Kadir, S. (1999). Colour origin of Upper Cretaceous pelagic red sediments within the Eastern Pontides, northeast Turkey. *International Journal of Earth Sciences*, *88*(3), 593–595. https://doi.org/10.1007/s005310050287

Evans, M. E., & Heller, F. (2003). *Environmental magnetism: Principles and applications of enviromagnetics*. Academic Press.

Fabian, K., McEnroe, S. A., Robinson, P., & Shcherbakov, V. P. (2008). Exchange bias identifies lamellar magnetism as the origin of the natural remanent magnetization of titanohematite with ilmenite exsolution from Modum, Norway. *Earth and Planetary Science Letters*, *268*(3–4), 339–353. https://doi.org/10.1016/j.epsl.2008.01.034

Fabian, K., Robinson, P., McEnroe, S. A., Heidelbach, F., & Hirt, A. M. (2011). Experimental study of the magnetic signature of basal-plane anisotropy in hematite. In E. Petrovský (Ed.), *The Earth's magnetic interior, IAGA Special Sopron Book Series 1* (pp. 311–320). https://doi.org/10.1007/978-94-007-0323-0_22

Fan, C., Xie, H., Schulze-Makuch, D., & Ackley, S. (2010). A formation mechanism for hematite-rich spherules on Mars. *Planetary and Space Science*, *58*(3), 401–410. https://doi.org/10.1016/j.pss.2009.11.001

Faure, M., Lin, W., Chu, Y., & Lepvrier, C. (2016). Triassic tectonics of the Ailaoshan Belt (SW China): Early Triassic collision between the South China and Indochina Blocks, and Middle Triassic intracontinental shearing. *Tectonophysics*, *683*, 27–42. https://doi.org/10.1016/j.tecto.2016.06.015

Feinberg, J. M., Harrison, R. J., Kasama, T., Dunin-Borkowski, R. E., Scott, G. R., & Renne, P. R. (2006). Effects of internal mineral structures on the magnetic remanence of silicate-hosted titanomagnetite inclusions: An electron holography study. *Journal of Geophysical Research*, *111*(B12), B12S15. https://doi.org/10.1029/2006JB004498

Ferré, E. C., Kupenko, I., Martín-Hernández, F., Ravat, D., & Sánchez-Valle, C. (2021). Magnetic sources in the Earth's mantle. *Nature Reviews Earth & Environment*, *2*(1), 59–69. https://doi.org/10.1038/s43017-020-00107-x

Ferré, E. C., Zechmeister, M. S., Geissman, J. W., MathanaSekaran, N., & Kocak, K. (2005). The origin of high magnetic remanence in fault pseudotachylites: Theoretical considerations and implication for coseismic electrical currents. *Tectonophysics*, *402*(1), 125–139. https://doi.org/10.1016/j.tecto.2005.01.008

Fey, M. V., & Dixon, J. B. (1981). Synthesis and properties of poorly crystalline hydrated aluminous goethites. *Clays and Clay Minerals*, *29*(2), 91–100. https://doi.org/10.1346/CCMN.1981.0290202

Fitzpatrick, R. W., & Schwertmann, U. (1982). Al-substituted goethite—An indicator of pedogenic and other weathering environments in South Africa. *Geoderma*, *27*(4), 335–347. https://doi.org/10.1016/0016-7061(82)90022-2

Flanders, P., & Schuele, W. (1964). Anisotropy in the basal plane of hematite single crystals. *Philosophical Magazine*, *9*(99), 485–490. https://doi.org/10.1080/14786436408222959

Fontes, M., Bowen, L., & Weed, S. (1991). Iron oxides in selected Brazilian oxisols: II. Mössbauer studies. *Soil Science Society of America Journal*, *55*(4), 1150–1155. https://doi.org/10.2136/sssaj1991.03615995005500040041x

Fontes, M., & Weed, S. (1991). Iron oxides in selected Brazilian oxisols: I. Mineralogy. *Soil Science Society of America Journal*, *55*(4), 1143–1149. https://doi.org/10.2136/sssaj1991.03615995005500040040x

Fraeman, A., Arvidson, R., Catalano, J., Grotzinger, J., Morris, R., Murchie, S., et al. (2013). A hematite-bearing layer in Gale Crater, Mars: Mapping and implications for past aqueous conditions. *Geology*, *41*(10), 1103–1106. https://doi.org/10.1130/G34613.1

Gallet, Y., Pavlov, V., Halverson, G., & Hulot, G. (2012). Toward constraining the long-term reversing behavior of the geodynamo: A new "Maya" supercron ~1 billion years ago from the magnetostratigraphy of the Kartochka Formation (southwestern Siberia). *Earth and Planetary Science Letters*, *339–340*, 117–126. https://doi.org/10.1016/j.epsl.2012.04.049

Gallon, T. (1968a). The remanent magnetization of haematite single crystals. *Proceedings of the Royal Society of London*, *303*(1475), 511–524. https://doi.org/10.1098/rspa.1968.0066

Gallon, T. (1968b). The ferromagnetic domain structure of haematite. *Proceedings of the Royal Society of London*, *303*(1475), 525–274. https://doi.org/10.1098/rspa.1967.0065

Gálvez, N., Barrón, V., & Torrent, J. (1999). Effect of phosphate on the crystallization of hematite, goethite, and lepidocrocite from ferrihydrite. *Clays and Clay Minerals*, *47*, 304–311. https://doi.org/10.1346/CCMN.1999.0470306

Garming, J. F. L., Von Dobeneck, T., Franke, C., & Bleil, U. (2007). Low-temperature partial magnetic self-reversal in marine sediments by magnetostatic interaction of titanomagnetite and titanohematite intergrowths. *Geophysical Journal International*, *170*, 1067–1075. https://doi.org/10.1111/j.1365-246X.2007.03504.x

Gattacceca, J., Boustie, M., Lima, E., Weiss, B., De Resseguier, T., & Cuq-Lelandais, J. (2010). Unraveling the simultaneous shock magnetization and demagnetization of rocks. *Physics of the Earth and Planetary Interiors*, *182*(1–2), 42–49. https://doi.org/10.1016/j.pepi.2010.06.009

Gattacceca, J., Lamali, A., Rochette, P., Boustie, M., & Berthe, L. (2007). The effects of explosive-driven shocks on the natural remanent magnetization and the magnetic properties of rocks. *Physics of the Earth and Planetary Interiors*, *162*(1), 85–98. https://doi.org/10.1016/j.pepi.2007.03.006

Ge, K., Liu, Q., Deng, J., Nobes, D., Wang, Y., Wang, Y., & Chen, X. (2017). Rock magnetic investigation and its geological significance for vein-type uranium deposits in southern China. *Geochemistry, Geophysics, Geosystems*, *18*(4), 1333–1349. https://doi.org/10.1002/2016GC006756

Gedye, S. J., Jones, R. T., Tinner, W., Ammann, B., & Oldfield, F. (2000). The use of mineral magnetism in the reconstruction of fire history: A case study from Lago di Origlio, Swiss Alps. *Palaeogeography, Palaeoclimatology, Palaeoecology*, *164*(1), 101–110. https://doi.org/10.1016/S0031-0182(00)00178-4

Geiss, C. E., Egli, R., & Zanner, C. W. (2008). Direct estimates of pedogenic magnetite as a tool to reconstruct past climates from buried soils. *Journal of Geophysical Research*, *113*, B11102. https://doi.org/10.1029/2008JB005669

Gendler, T. S., Shcherbakov, V. P., Dekkers, M. J., Gapeev, A. K., Gribov, S. K., & McClelland, E. (2005). The lepidocrocite–maghemite–haematite reaction chain—I. Acquisition of chemical remanent magnetization by maghemite, its magnetic properties and thermal stability. *Geophysical Journal International*, *160*(3), 815–832. https://doi.org/10.1111/j.1365-246X.2005.02550.x

Génin, J. M. R., Refait, P., & Abdelmoula, M. (2002). Green rusts and their relationship to iron corrosion; a key role in microbially influenced corrosion. *Hyperfine Interactions*, *139*(1), 119–131. https://doi.org/10.1023/A:1021219021919

Gialanella, S., Girardi, F., Ischia, G., Lonardelli, I., Mattarelli, M., & Montagna, M. (2010). On the goethite to hematite phase transformation. *Journal of Thermal Analysis and Calorimetry*, *102*, 1–873. https://doi.org/10.1007/s10973-010-0756-2

Gilder, S. (2007). Magnetization, piezoremanence and stress demagnetization. In D. Gubbins & E. Herrero-Bervera (Eds.), *Encyclopedia of geomagnetism and paleomagnetism* (pp. 599–603). Springer. https://doi.org/10.1007/978-1-4020-4423-6_195

Gilder, S., Chen, Y., Cogné, J.-P., Tan, X., Courtillot, V., Sun, D., & Li, Y. (2003). Paleomagnetism of Upper Jurassic to Lower Cretaceous volcanic and sedimentary rocks from the western Tarim Basin and implications for inclination shallowing and absolute dating of the M-0 (ISEA?) chron. *Earth and Planetary Science Letters*, *206*(3), 587–600. https://doi.org/10.1016/S0012-821X(02)01074-9

Gilder, S. A., Chen, Y., & Sen, S. (2001). Oligo-Miocene magnetostratigraphy and rock magnetism of the Xishuigou section, Subei (Gansu Province, western China) and implications for shallow inclinations in central Asia. *Journal of Geophysical Research*, *106*(12), 30505–30521. https://doi.org/10.1029/2001JB000325

Gilder, S. A., Egli, R., Hochleitner, R., Roud, S. C., Volk, M. W. R., Le Goff, M., & de Wit, M. (2011). Anatomy of a pressure-induced, ferromagnetic-to-paramagnetic transition in pyrrhotite: Implications for the formation pressure of diamonds. *Journal of Geophysical Research*, *116*, B10101. https://doi.org/10.1029/2011JB008292

Gilder, S. A., Le Goff, M., & Chervin, J. C. (2006). Static stress demagnetization of single and multidomain magnetite with implications for meteorite impacts. *High Pressure Research*, *26*(4), 539–547. https://doi.org/10.1080/08957950601092085

Gilder, S. A., Le Goff, M., Chervin, J. C., & Peyronneau, J. (2004). Magnetic properties of single and multi-domain magnetite under pressures from 0 to 6 GPa. *Geophysical Research Letters*, *31*(10), L10612. https://doi.org/10.1029/2004GL019844

Gilder, S. A., LeGoff, M., Peyronneau, J., & Chervin, J. C. (2002). Novel high pressure magnetic measurements with application to magnetite. *Geophysical Research Letters*, *29*(10), 1392. https://doi.org/10.1029/2001GL014227

Glotch, T. D., & Rogers, A. D. (2007). Evidence for aqueous deposition of hematite- and sulfate-rich light-toned layered deposits in Aureum and Iani Chaos, Mars. *Journal of Geophysical Research*, *112*(E6), E06001. https://doi.org/10.1029/2006JE002863

Golden, D., Ming, D., Morris, R., & Graff, T. (2008). Hydrothermal synthesis of hematite spherules and jarosite: Implications for diagenesis and hematite spherule formation in sulfate outcrops at Meridiani Planum, Mars. *American Mineralogist*, *93*(8–9), 1201–1214. https://doi.org/10.2138/am.2008.2737

González, G., Sagarzazu, A., & Villalba, R. (2000). Study of the mechano-chemical transformation of goethite to hematite by TEM and XRD. *Materials Research Bulletin*, *35*(14), 2295–2308. https://doi.org/10.1016/S0025-5408(00)00434-7

Goya, G. F., Veith, M., Rapalavicuite, R., Shen, H., & Mathur, S. (2005). Thermal hysteresis of spin reorientation at Morin transition in alkoxide derived hematite nanoparticles. *Applied Physics A*, *80*(7), 1523–1526. https://doi.org/10.1007/s00339-003-2381-4

Grotzinger, J. P., Gupta, S., Malin, M. C., Rubin, D. M., Schieber, J., Siebach, K., et al. (2015). Deposition, exhumation, and paleoclimate of an ancient lake deposit, Gale crater, Mars. *Science*, *350*(6257), aac7575. https://doi.org/10.1126/SCIENCE.AAC7575

Gualtieri, A. F., & Venturelli, P. (1999). In situ study of the goethite-hematite phase transformation by real time synchrotron powder diffraction. *American Mineralogist*, *84*, 895–904. https://doi.org/10.2138/am-1999-5-624

Gutiérrez, L., Barrón, V., Andrés-Vergés, M., Serna, C., Veintemillas-Verdaguer, S., Morales, M., & Lázaro, F. (2016). Detailed magnetic monitoring of the enhanced magnetism of ferrihydrite along its progressive transformation into hematite. *Journal of Geophysical Research: Solid Earth*, *121*(6), 4118–4129. https://doi.org/10.1002/2016JB013016

Guyodo, Y., Mostrom, A., Penn, R. L., & Banerjee, S. K. (2003). From nanodots to nanorods: Oriented aggregation and magnetic evolution of nanocrystalline goethite. *Geophysical Research Letters*, *30*(10), 1512. https://doi.org/10.1029/2003GL017021

Haberle, R. M., Clancy, R. T., Forget, F., Smith, M. D., & Zurek, R. W. (2017). *The atmosphere and climate of Mars*. Cambridge University Press.

Haigh, G. (1957). Observations on the magnetic transition in hematite at -15°C. *Philosophical Magazine*, *2*(19), 877–890. https://doi.org/10.1080/14786435708242726

Haigh, G. (1958). The process of magnetization by chemical change. *Philosophical Magazine*, *3*(27), 267–286. https://doi.org/10.1080/14786435808238219

Halama, M., Swanner, E. D., Konhauser, K. O., & Kappler, A. (2016). Evaluation of siderite and magnetite formation in BIFs by pressure–temperature experiments of Fe(III) minerals and microbial biomass. *Earth and Planetary Science Letters*, *450*, 243–253. https://doi.org/10.1016/j.epsl.2016.06.032

Halgedahl, S. L. (1995). Bitter patterns versus hysteresis behavior in small single particles of hematite. *Journal of Geophysical Research*, *100*(B1), 353–364. https://doi.org/10.1029/93JB01228

Halgedahl, S. L. (1998). Barkhausen jumps in large versus small platelets of natural hematite. *Journal of Geophysical Research*, *103*, 30575–30589. https://doi.org/10.1029/98JB00958

Haliuc, A., Hutchinson, S. M., Florescu, G., & Feurdean, A. (2016). The role of fire in landscape dynamics: An example of two sediment records from the Rodna Mountains, northern Romanian Carpathians. *Catena*, *137*, 432–440. https://doi.org/10.1016/j.catena.2015.10.021

Han, J. M., Lü, H., Wu, N., & Guo, Z. (1996). The magnetic susceptibility of modern soils in China and its use for paleoclimate reconstruction. *Studia Geophysica et Geodaetica*, *40*(3), 262–275. https://doi.org/10.1007/BF02300742

Han, R., Shimamoto, T., Ando, J.-I., & Ree, J.-H. (2007). Seismic slip record in carbonate-bearing fault zones: An insight from high-velocity friction experiments on siderite gouge. *Geology*, *35*(12), 1131–1134. https://doi.org/10.1130/G24106A.1

Hanesch, M., Stanjek, H., & Petersen, N. (2006). Thermomagnetic measurements of soil iron minerals: The role of organic carbon. *Geophysical Journal International*, *165*(1), 53–61. https://doi.org/10.1111/j.1365-246X.2006.02933.x

Hao, Q., Oldfield, F., Bloemendal, J., & Guo, Z. (2008). The magnetic properties of loess and paleosol samples from the Chinese Loess Plateau spanning the last 22 million years. *Palaeogeography, Palaeoclimatology, Palaeoecology*, *260*(3), 389–404. https://doi.org/10.1016/j.palaeo.2007.11.010

Hao, Q., Oldfield, F., Bloemendal, J., Torrent, J., & Guo, Z. (2009). The record of changing hematite and goethite accumulation over the past 22 Myr on the Chinese Loess Plateau from magnetic measurements and diffuse reflectance spectroscopy. *Journal of Geophysical Research*, *114*(12), B12101. https://doi.org/10.1029/2009JB006604

Hargraves, R. B., Knudsen, J. M., Bertelsen, P., Goetz, W., Gunnlaugsson, H. P., Hviid, S. F., et al. (2000). Magnetic enhancement on the surface of Mars? *Journal of Geophysical Research*, *105*(E1), 1819–1827. https://doi.org/10.1029/1999je001032

Harrison, R. J., McEnroe, S. A., Robinson, P., & Howard, C. J. (2010). Spin orientation in a natural Ti-bearing hematite: Evidence for an out-of-plane component. *American Mineralogist*, *95*(7), 974–979. https://doi.org/10.2138/am.2010.3402

Hartstra, R. L. (1982). *Some rock magnetic parameters for natural iron-titanium oxides* (Ph.D. thesis). State University of Utrecht.

Hedley, I. (1968). Chemical remanent magnetization of the FeOOH, Fe$_2$O$_3$ system. *Physics of the Earth and Planetary Interiors*, *1*(2), 103–121. https://doi.org/10.1016/0031-9201(68)90055-1

Heller, F., Carracedo, J. C., & Solert, V. (1986). Reversed magnetization in pyroclasts from the 1985 eruption of Nevado del Ruiz, Colombia. *Nature*, *324*(6094), 241–242. https://doi.org/10.1038/324241a0

Henry, B., Merabet, N., Derder, M. E. M., & Bayou, B. (2004). Chemical remagnetizations in the Illizi basin (Saharan craton, Algeria) and their acquisition process. *Geophysical Journal International*, *156*(156), 200–212. https://doi.org/10.1111/j.1365-246X.2003.02106.x

Herkenhoff, K. E., Squyres, S. W., Arvidson, R., Bass, D. S., Bell, J. F., Bertelsen, P., et al. (2004). Evidence from opportunity's microscopic imager for water on Meridiani Planum. *Science*, *306*(5702), 1727–1730. https://doi.org/10.1126/science.1105286

Heslop, D., & Roberts, A. P. (2013). Calculating uncertainties on predictions of palaeoprecipitation from the magnetic properties of soils. *Global and Planetary Change*, *110*, 379–385. https://doi.org/10.1016/j.gloplacha.2012.11.013

Hiemstra, T. (2018). Surface structure controlling nanoparticle behavior: Magnetism of ferrihydrite, magnetite, and maghemite. *Environmental Science Nano*, *5*, 752–764. https://doi.org/10.1039/c7en01060e

Hirono, T., Lin, W., Yeh, E. C., Soh, W., Hashimoto, Y., Sone, H., et al. (2006). High magnetic susceptibility of fault gouge within Taiwan Chelungpu fault: Nondestructive continuous measurements of physical and chemical properties in fault rocks recovered from Hole B, TCDP. *Geophysical Research Letters*, *33*, L15303. https://doi.org/10.1029/2006gl026133

Hoashi, M., Bevacqua, D. C., Otake, T., Watanabe, Y., Hickman, A. H., Utsunomiya, S., & Ohmoto, H. (2009). Primary haematite formation in an oxygenated sea 3.46 billion years ago. *Nature Geoscience*, *2*(4), 301–306. https://doi.org/10.1038/NGEO465

Hoffman, K. A. (1992). Self-reversal of thermoremanent magnetization in the ilmenite-hematite system: Order-disorder, symmetry, and spin alignment. *Journal of Geophysical Research*, *97*(7), 10883–10895. https://doi.org/10.1029/91JB02846

Holland, H. D. (1984). *The chemical evolution of the atmosphere and oceans*. Princeton University Press.

Hu, D., Böning, P., Köhler, C. M., Hillier, S., Pressling, N., Wan, S., et al. (2012). Deep sea records of the continental weathering and erosion response to East Asian Monsoon intensification since 14 ka in the South China Sea. *Chemical Geology*, *326–327*, 1–18. https://doi.org/10.1016/j.chemgeo.2012.07.024

Hu, P., Jiang, Z., Liu, Q., Heslop, D., Roberts, A. P., Torrent, J., & Barrón, V. (2016). Estimating the concentration of aluminum-substituted hematite and goethite using diffuse reflectance spectrometry and rock magnetism: Feasibility and limitations. *Journal of Geophysical Research: Solid Earth*, *121*(6), 4180–4194. https://doi.org/10.1002/2015JB012635

Hu, P., Liu, Q., Heslop, D., Roberts, A. P., & Jin, C. (2015). Soil moisture balance and magnetic enhancement in loess–paleosol sequences from the Tibetan Plateau and Chinese Loess Plateau. *Earth and Planetary Science Letters*, *409*, 120–132. https://doi.org/10.1016/j.epsl.2014.10.035

Hu, P., Liu, Q., Torrent, J., Barrón, V., & Jin, C. (2013). Characterizing and quantifying iron oxides in Chinese loess/paleosols: Implications for pedogenesis. *Earth and Planetary Science Letters*, *369–370*, 271–283. https://doi.org/10.1016/j.epsl.2013.03.033

Hu, X., Scott, R. W., Cai, Y., Wang, C., & Melinte-Dobrinescu, M. C. (2012). Cretaceous oceanic red beds (CORBs): Different time scales and models of origin. *Earth-Science Reviews*, *115*(4), 217–248. https://doi.org/10.1016/j.earscirev.2012.09.007

Huang, K., & Opdyke, N. D. (1991). Paleomagnetism of Jurassic rocks from southwestern Sichuan and the timing of the closure of the Qinling suture. *Tectonophysics*, *200*(1–3), 299–316. https://doi.org/10.1016/0040-1951(91)90021-J

Huang, K., & Opdyke, N. D. (1993). Paleomagnetic results from Cretaceous and Jurassic rocks of South and Southwest Yunnan: Evidence for large clockwise rotations in the Indochina and Shan-Thai-Malay terranes. *Earth and Planetary Science Letters*, *117*(3–4), 507–524. https://doi.org/10.1016/0012-821X(93)90100-N

Huang, K., & Opdyke, N. D. (1996). Severe remagnetization revealed from Triassic platform carbonates near Guiyang, Southwest China. *Earth and Planetary Science Letters*, *143*(1–4), 49–61. https://doi.org/10.1016/0012-821X(96)00152-5

Huang, K., & Opdyke, N. D. (1998). Magnetostratigraphic investigations on an Emeishan basalt section in western Guizhou province, China. *Earth and Planetary Science Letters*, *163*(1), 1–14. https://doi.org/10.1016/S0012-821X(98)00169-1

Huang, K., Opdyke, N. D., & Zhu, R. (2000). Further paleomagnetic results from the Silurian of the Yangtze Block and their implications. *Earth and Planetary Science Letters*, *175*(3), 191–202. https://doi.org/10.1016/S0012-821X(98)00169-1

Huang, W., Jackson, M. J., Dekkers, M. J., Solheid, P., Zhang, Y., Li, S., et al. (2020). Remagnetization of red beds on the Tibetan Plateau: Mechanism and diagnosis. *Journal of Geophysical Research: Solid Earth*, *125*(8), e2020JB020068. https://doi.org/10.1029/2020JB020068

Huang, W., Jackson, M. J., Dekkers, M. J., Solheid, P. A., Zhang, B., Guo, Z., & Ding, L. (2019). Nanogoethite as a potential indicator of remagnetization in red beds. *Geophysical Research Letters*, *46*(22), 12841–12850. https://doi.org/10.1029/2019GL084715

Hund, F. (1981). Inorganic pigments: Bases for colored, uncolored and transparent products. *Angewandte Chemie International Edition*, *20*, 723–730. https://doi.org/10.1002/anie.198107231

Hunt, C. P., Moskowitz, B. M., & Banerjee, S. K. (1995). Magnetic properties of rocks and minerals. *Handbook of physical constants* (pp. 189–204). American Geophysical Union. https://doi.org/10.1029/RF003p0189

Hyland, E. G., Sheldon, N. D., Van der Voo, R., Badgley, C., & Abrajevitch, A. (2015). A new paleoprecipitation proxy based on soil magnetic properties: Implications for expanding paleoclimate reconstructions. *The Geological Society of America Bulletin*, *127*(7–8), 975–981. https://doi.org/10.1130/B31207.1

Hynek, B. M., Arvidson, R. E., & Phillips, R. J. (2002). Geologic setting and origin of Terra Meridiani hematite deposit on Mars. *Journal of Geophysical Research*, *107*(E10), 5088. https://doi.org/10.1029/2002je001891

Iglesias, T., Cala, V., & González, J. (1997). Mineralogical and chemical modifications in soils affected by a forest fire in the Mediterranean area. *The Science of the Total Environment*, *204*(1), 89–96. https://doi.org/10.1016/s0048-9697(97)00173-3

Iosifidi, A. G., Mac Niocaill, C., Khramov, A. N., Dekkers, M. J., & Popov, V. V. (2010). Palaeogeographic implications of differential inclination shallowing in Permo-Carboniferous sediments from the Donets Basin, Ukraine. *Tectonophysics*, *490*(3), 229–240. https://doi.org/10.1016/j.tecto.2010.05.017

Irving, E., & Major, A. (1964). Post-depositional detrital remanent magnetization in a synthetic sediment. *Sedimentology*, *3*(2), 135–143. https://doi.org/10.1111/j.1365-3091.1964.tb00638.x

Jackson, M., Borradaile, G., Hudleston, P., & Banerjee, S. (1993). Experimental deformation of synthetic magnetite-bearing calcite sandstones: Effects on remanence, bulk magnetic properties, and magnetic anisotropy. *Journal of Geophysical Research*, *98*(B1), 383–401. https://doi.org/10.1029/92JB01028

Jackson, M. J., Banerjee, S. K., Marvin, J. A., Lu, R., & Gruber, W. (1991). Detrital remanence, inclination errors, and anhysteretic remanence anisotropy: Quantitative model and experimental results. *Geophysical Journal International*, *104*(1), 95–103. https://doi.org/10.1111/j.1365-246X.1991.tb02496.x

Jacob, J., & Abdul Khadar, M. (2010). VSM and Mössbauer study of nanostructured hematite. *Journal of Magnetism and Magnetic Materials*, *322*(6), 614–621. https://doi.org/10.1016/j.jmmm.2009.10.025

Jambor, J. L., & Dutrizac, J. E. (1998). Occurrence and constitution of natural and synthetic ferrihydrite, a widespread iron oxyhydroxide. *Chemical Reviews*, *98*(7), 2549–2586. https://doi.org/10.1021/cr970105t

Ji, J., Balsam, W., Chen, J., & Liu, L. (2002). Rapid and quantitative measurement of hematite and goethite in the Chinese loess-paleosol sequence by diffuse reflectance spectroscopy. *Clays and Clay Minerals*, *50*(2), 208–216. https://doi.org/10.1346/000986002760832801

Ji, J., Chen, J., Balsam, W., Liu, L., Chen, Y., Zhao, L., & Zhou, W. (2007). Quantitative analysis of hematite and goethite in the Chinese loess-paleosol sequences and its implication for dry and humid variability. *Quaternary Research (in Chinese)*, *27*(2), 221–229. https://doi.org/10.1346/000986002760832801

Ji, J., Chen, J., Balsam, W., Lu, H., Sun, Y., & Xu, H. (2004). High resolution hematite/goethite records from Chinese loess sequences for the last glacial-interglacial cycle: Rapid climatic response of the East Asian Monsoon to the tropical Pacific. *Geophysical Research Letters*, *31*(3), 347–348. https://doi.org/10.1029/2003GL018975

Jiang, Z. (2014). *The magnetic mechanism of antiferromagnetic minerals: Illustrated by the case of Al substituted hematite and goethite* (Ph.D. thesis). University of the Chinese Academy of Sciences.

Jiang, Z., Liu, Q., Barrón, V., Torrent, J., & Yu, Y. (2012). Magnetic discrimination between Al-substituted hematites synthesized by hydrothermal and thermal dehydration methods and its geological significance. *Journal of Geophysical Research*, *117*(B2), B02102. https://doi.org/10.1029/2011JB008605

Jiang, Z., Liu, Q., Colombo, C., Barrón, V., Torrent, J., & Hu, P. (2014). Quantification of Al-goethite from diffuse reflectance spectroscopy and magnetic methods. *Geophysical Journal International*, *196*(1), 131–144. https://doi.org/10.1093/gji/ggt377

Jiang, Z., Liu, Q., Dekkers, M. J., Barrón, V., Torrent, J., & Roberts, A. P. (2016). Control of Earth-like magnetic fields on the transformation of ferrihydrite to hematite and goethite. *Scientific Reports*, *6*, 30395. https://doi.org/10.1038/srep30395

Jiang, Z., Liu, Q., Dekkers, M. J., Colombo, C., Yu, Y., Barrón, V., & Torrent, J. (2014). Ferro and antiferromagnetism of ultrafine-grained hematite. *Geochemistry, Geophysics, Geosystems*, *15*(6), 2699–2712. https://doi.org/10.1002/2014GC005377

Jiang, Z., Liu, Q., Dekkers, M. J., Tauxe, L., Qin, H., Barrón, V., & Torrent, J. (2015). Acquisition of chemical remanent magnetization during experimental ferrihydrite–hematite conversion in Earth-like magnetic field—Implications for paleomagnetic studies of red beds. *Earth and Planetary Science Letters*, *428*, 1–10. https://doi.org/10.1016/j.epsl.2015.07.024

Jiang, Z., Liu, Q., Dekkers, M. J., Zhao, X., Roberts, A. P., Yang, Z., et al. (2017). Remagnetization mechanisms in Triassic red beds from South China. *Earth and Planetary Science Letters*, *479*(C), 219–230. https://doi.org/10.1016/J.EPSL.2017.09.019

Jiang, Z., Liu, Q., Roberts, A. P., Barrón, V., Torrent, J., & Zhang, Q. (2018). A new model for transformation of ferrihydrite to hematite in soils and sediments. *Geology*, *46*(11), 987–990. https://doi.org/10.1130/G45386.1

Jiang, Z., Liu, Q., Zhao, X., Jin, C., Liu, C., & Li, S. (2015). Thermal magnetic behaviour of Al-substituted haematite mixed with clay minerals and its geological significance. *Geophysical Journal International*, *200*(1), 130–143. https://doi.org/10.1093/GJI/GGU377

Jiang, Z., Liu, Q., Zhao, X., Roberts, A. P., Heslop, D., Barrón, V., & Torrent, J. (2016). Magnetism of Al-substituted magnetite reduced from Al-hematite. *Journal of Geophysical Research: Solid Earth*, *121*(6), 4195–4210. https://doi.org/10.1002/2016JB012863

Jiang, Z., Rochette, P., Liu, Q., Gattacceca, J., Yu, Y., Barrón, V., & Torrent, J. (2013). Pressure demagnetization of synthetic Al substituted hematite and its implications for planetary studies. *Physics of the Earth and Planetary Interiors*, *224*, 1–10. https://doi.org/10.1016/J.PEPI.2013.09.005

Jiao, H., & Jiao, G. (2009). Hydrothermal synthesis and characterization of monodisperse α-Fe_2O_3 nanoparticles. *Materials Letters*, *63*(30), 2725–2727. https://doi.org/10.1016/j.matlet.2009.09.054

Johnston, J. H., & Lewis, D. G. (1983). A detailed study of the transformation of ferrihydrite to hematite in an aqueous medium at 92°C. *Geochimica et Cosmochimica Acta*, *47*(11), 1823–1831. https://doi.org/10.1016/0016-7037(83)90200-4

Judd, D. B. (1952). *Color in business, science and industry*. John Wiley & Sons.

Kämpf, N., & Schwertmann, U. (1983). Goethite and hematite in a climosequence in southern Brazil and their application in classification of kaolinitic soils. *Geoderma*, *29*(1), 27–39. https://doi.org/10.1016/0016-7061(83)90028-9

Kasting, J. F. (1987). Theoretical constraints on oxygen and carbon dioxide concentrations in the Precambrian atmosphere. *Precambrian Research*, *34*(3), 205–229. https://doi.org/10.1016/0301-9268(87)90001-5

Katsuta, N., Shimizu, I., Helmstaedt, H., Takano, M., Kawakami, S., & Kumazawa, M. (2012). Major element distribution in Archean banded iron formation (BIF): Influence of metamorphic differentiation. *Journal of Metamorphic Geology*, *30*(5), 457–472. https://doi.org/10.1111/j.1525-1314.2012.00975.x

Kawai, N., & Ono, F. (1966). Effect of hydrostatic pressure on the morin transition point of alpha-hematite crystal. *Physics Letters*, *21*(3), 279–279. https://doi.org/10.1016/0031-9163(66)90814-6

Kent, D. V., Honnorez, B. M., Opdyke, N. D., & Fox, P. J. (1978). Magnetic properties of dredged oceanic gabbros and the source of marine magnetic anomalies. *Geophysical Journal of the Royal Astronomical Society*, *55*(3), 513–537. https://doi.org/10.1111/J.1365-246X.1978.TB05925.X

Kent, D. V., & Opdyke, N. D. (1985). Multicomponent magnetizations from the Mississippian Mauch Chunk Formation of the central Appalachians and their tectonic implications. *Journal of Geophysical Research*, *90*(B7), 5371–5383. https://doi.org/10.1029/JB090iB07p05371

Kent, D. V., Zeng, X., Zhang, W. Y., & Opdyke, N. D. (1987). Widespread late Mesozoic to Recent remagnetization of Paleozoic and lower Triassic sedimentary rocks from South China. *Tectonophysics*, *139*(1), 133–143. https://doi.org/10.1016/0040-1951(87)90202-2

Kerker, M., Scheiner, P., Cooke, D. D., & Kratohvil, J. P. (1979). Absorption index and color of colloidal hematite. *Journal of Colloid and Interface Science*, *71*(1), 176–187. https://doi.org/10.1016/0021-9797(79)90231-5

Ketterings, Q. M., Bigham, J. M., & Laperche, V. R. (2000). Changes in soil mineralogy and texture caused by slash-and-burn fires in Sumatra, Indonesia. *Soil Science Society of America Journal*, *64*(3), 1108–1117. https://doi.org/10.2136/sssaj2000.6431108x

Kim, J. D., Yee, N., Nanda, V., & Falkowski, P. G. (2013). Anoxic photochemical oxidation of siderite generates molecular hydrogen and iron oxides. *Proceedings of the National Academy of Sciences*, *110*, 10073–10077. https://doi.org/10.1073/pnas.1308958110

King, J. W., & Channell, J. E. T. (1991). Sedimentary magnetism, environmental magnetism, and magnetostratigraphy. *Reviews of Geophysics*, *29*(S1), 358–370. https://doi.org/10.1002/rog.1991.29.s1.358

King, R. F. (1955). The remanent magnetism of artificially deposited sediments. *Monthly Notes of the Royal Astronomical Society, Geophysical Supplement*, *7*(3), 115–134. https://doi.org/10.1111/J.1365-246X.1955.TB06558.X

Kirkland, L. E., Herr, K. C., & Adams, P. M. (2004). A different perspective for the Mars rover "Opportunity" site: Fine-grained, consolidated hematite and hematite coatings. *Geophysical Research Letters*, *31*, L05704. https://doi.org/10.1029/2003GL019284

Klein, C. (2005). Some Precambrian banded iron-formations (BIFs) from around the world: Their age, geologic setting, mineralogy, metamorphism, geochemistry, and origins. *American Mineralogist*, *90*(10), 1473–1499. https://doi.org/10.2138/AM.2005.1871

Klein, C., & Beukes, N. J. (1989). Geochemistry and sedimentology of a facies transition from limestone to iron-formation deposition in the early Proterozoic Transvaal Supergroup, South Africa. *Economic Geology*, *84*(7), 1733–1774. https://doi.org/10.2113/GSECONGEO.84.7.1733

Kletetschka, G., & Banerjee, S. K. (1995). Magnetic stratigraphy of Chinese loess as a record of natural fires. *Geophysical Research Letters*, *22*(11), 1341–1343. https://doi.org/10.1029/95GL01324

Kletetschka, G., & Stout, J. H. (1998). The origin of magnetic anomalies in lower crustal rocks, Labrador. *Geophysical Research Letters*, *25*(2), 199–202. https://doi.org/10.1029/97GL03506

Kletetschka, G., & Wasilewski, P. J. (2002). Grain size limit for SD hematite. *Physics of the Earth and Planetary Interiors*, *129*(1–2), 173–179. https://doi.org/10.1016/S0031-9201(01)00271-0

Kletetschka, G., Wasilewski, P. J., & Taylor, P. T. (2000a). Hematite vs. magnetite as the signature for planetary magnetic anomalies? *Physics of the Earth and Planetary Interiors*, *119*(3), 259–267. https://doi.org/10.1016/S0031-9201(00)00141-2

Kletetschka, G., Wasilewski, P. J., & Taylor, P. T. (2000b). Mineralogy of the sources for magnetic anomalies on Mars. *Meteoritics & Planetary Sciences*, *35*(5), 895–899. https://doi.org/10.1111/J.1945-5100.2000.TB01478.X

Kletetschka, G., Wasilewski, P. J., & Taylor, P. T. (2000c). Unique thermoremanent magnetization of multidomain sized hematite: Implications for magnetic anomalies. *Earth and Planetary Science Letters*, *176*(3), 469–479. https://doi.org/10.1016/S0012-821X(00)00016-9

Kletetschka, G., Wasilewski, P. J., & Taylor, P. T. (2002). The role of hematite–ilmenite solid solution in the production of magnetic anomalies in ground-and satellite-based data. *Tectonophysics*, *347*(1), 167–177. https://doi.org/10.1016/S0040-1951(01)00243-8

Klotz, S., Strässle, T., & Hansen, T. (2013). Pressure dependence of Morin transition in α-Fe_2O_3 hematite. *Europhysics Letters*, *104*(1), 16001. https://doi.org/10.1209/0295-5075/104/16001

Knauth, L. P., Burt, D. M., & Wohletz, K. H. (2005). Impact origin of sediments at the Opportunity landing site on Mars. *Nature*, *438*(7071), 1123–1128. https://doi.org/10.1038/nature04383

Kodama, K. P. (1997). A successful rock magnetic technique for correcting paleomagnetic inclination shallowing: Case study of the Nascimiento Formation, New Mexico. *Journal of Geophysical Research*, *102*(B3), 5193–5205. https://doi.org/10.1029/96JB03833

Kodama, K. P. (2009). Simplification of the anisotropy-based inclination correction technique for magnetite- and haematite-bearing rocks: A case study for the Carboniferous Glenshaw and Mauch Chunk Formations, North America. *Geophysical Journal International*, *176*(2), 467–477. https://doi.org/10.1111/j.1365-246X.2008.04013.x

Kodama, K. P. (2012). *Paleomagnetism of sedimentary rocks: Process and interpretation*. Wiley-Blackwell. https://doi.org/10.1002/9781118384138

Kodama, K. P., & Dekkers, M. J. (2004). Magnetic anisotropy as an aid to identifying CRM and DRM in red sedimentary rocks. *Studia Geophysica et Geodaetica*, *48*(4), 747–766. https://doi.org/10.1023/B:SGEG.0000045481.47203.33

Kodama, R. (1999). Magnetic nanoparticles. *Journal of Magnetism and Magnetic Materials*, *200*(1–3), 359–372. https://doi.org/10.1016/S0304-8853(99)00347-9

Köhler, I., Konhauser, K. O., Papineau, D., Bekker, A., & Kappler, A. (2013). Biological carbon precursor to diagenetic siderite with spherical structures in iron formations. *Nature Communications*, *4*(1), 1741. https://doi.org/10.1038/ncomms2770

Konhauser, K. O., Hamade, T., Raiswell, R., Morris, R. C., Ferris, F. G., Southam, G., & Canfield, D. E. (2002). Could bacteria have formed the Precambrian banded iron formations? *Geology*, *30*, 1079. https://doi.org/10.1130/0091-7613(2002)030<1079:cbhftp>2.0.CO;2

Konhauser, K. O., Newman, D. K., & Kappler, A. (2005). The potential significance of microbial Fe(III) reduction during deposition of Precambrian banded iron formations. *Geobiology*, *3*(3), 167–177. https://doi.org/10.1111/j.1472-4669.2005.00055.x

Kosmas, C., Curi, N., Bryant, R., & Franzmeier, D. (1984). Characterization of iron oxide minerals by second-derivative visible spectroscopy. *Soil Science Society of America Journal*, *48*(2), 401–405. https://doi.org/10.2136/SSSAJ1984.03615995004800020036X

Kosmas, C., Franzmeier, D., & Schulze, D. (1986). Relationship among derivative spectroscopy, color, crystalline dimensions, and A1 substitution of synthetic goethites and hematites. *Clays and Clay Minerals*, *34*(6), 625–634. https://doi.org/10.1346/CCMN.1986.0340602

Krén, E., Molnàr, B., Svàb, E., & Zsoldos, É. (1974). Neutron diffraction study of the (1-x) $\alpha Fe_2O_3.xAl_2O_3$ system. *Solid State Communications*, *15*(10), 1707–1710. https://doi.org/10.1016/0038-1098(74)91217-4

Kruiver, P. P., Dekkers, M. J., & Heslop, D. (2001). Quantification of magnetic coercivity components by the analysis of acquisition curves of isothermal remanent magnetisation. *Earth and Planetary Science Letters*, *189*(3–4), 269–276. https://doi.org/10.1016/S0012-821X(01)00367-3

Kruiver, P. P., Dekkers, M. J., & Langereis, C. G. (2000). Secular variation in Permian red beds from Dôme de Barrot, SE France. *Earth and Planetary Science Letters*, *179*(1), 205–217. https://doi.org/10.1016/S0012-821X(00)00104-7

Kupenko, I., Aprilis, G., Vasiukov, D. M., McCammon, C., Chariton, S., Cerantola, V., et al. (2019). Magnetism in cold subducting slabs at mantle transition zone depths. *Nature*, *570*(7759), 102–106. https://doi.org/10.1038/S41586-019-1254-8

Lagroix, F., & Guyodo, Y. (2017). A new tool for separating the magnetic mineralogy of complex mineral assemblages from low temperature magnetic behavior. *Frontiers in Earth Science*, *5*, 61. https://doi.org/10.3389/feart.2017.00061

Lane, M. D., Morris, R. V., Mertzman, S. A., & Christensen, P. R. (2002). Evidence for platy hematite grains in Sinus Meridiani, Mars. *Journal of Geophysical Research*, *107*(E12), 5126. https://doi.org/10.1029/2001JE001832

Langlais, B., Purucker, M., & Mandea, M. (2004). Crustal magnetic field of Mars. *Journal of Geophysical Research*, *109*(E2), E02008. https://doi.org/10.1029/2003JE002048

Langmuir, D. (1971). Particle size effect on the reaction goethite = hematite + water. *American Journal of Science*, *271*, 147–156. https://doi.org/10.2475/ajs.272.10.972

Larrasoaña, J. C., Roberts, A. P., Liu, Q., Lyons, R., Oldfield, F., Rohling, E. J., & Heslop, D. (2015). Source-to-sink magnetic properties of NE Saharan dust in Eastern Mediterranean marine sediments: Review and paleoenvironmental implications. *Frontiers in Earth Science*, *3*, 19. https://doi.org/10.3389/FEART.2015.00019

Larrasoaña, J. C., Roberts, A. P., Rohling, E. J., Winklhofer, M., & Wehausen, R. (2003). Three million years of monsoon variability over the northern Sahara. *Climate Dynamics*, *21*(7), 689–698. https://doi.org/10.1007/S00382-003-0355-Z

Lefèbvre, F., & Krasnopolsky, V. (2017). Atmospheric photochemistry. In M. H. Robert, R. T. Clancy, F. Forget, M. D. Smith, & R. W. Zurek (Eds.), *The atmosphere and climate of Mars* (pp. 405–433). Cambridge University Press. https://doi.org/10.1017/9781139060172.013

Lemine, O. M. (2014). Transformation of goethite to hematite nanocrystallines by high energy ball milling. *Advances in Materials Science and Engineering*, *2014*, 589146. https://doi.org/10.1155/2014/589146

Lepre, C. J., & Olsen, P. E. (2021). Hematite reconstruction of Late Triassic hydroclimate over the Colorado Plateau. *Proceedings of the National Academy of Sciences of the United States of America*, *118*(7), e2004343118. https://doi.org/10.1073/pnas.2004343118

Levinson, L. M., Luban, M., & Shtrikman, S. (1969). Microscopic model for reorientation of the easy axis of magnetization. *Physical Review*, *187*(2), 715–722. https://doi.org/10.1103/PhysRev.187.715

L'Haridon, J., Mangold, N., Fraeman, A. A., Johnson, J. R., Cousin, A., Rapin, W., et al. (2020). Iron mobility during diagenesis at Vera Rubin Ridge, Gale Crater, Mars. *Journal of Geophysical Research: Planets*, *125*(11), e2019JE006299. https://doi.org/10.1029/2019JE006299

Li, H., & Beske-Diehl, S. J. (1991). Magnetic properties of deuteric hematite in young lava flows from Iceland. *Geophysical Research Letters*, *18*(4), 597–600. https://doi.org/10.1029/91GL00816

Li, S., Lucey, P. G., Fraeman, A. A., Poppe, A. R., Sun, V. Z., Hurley, D. M., & Schultz, P. H. (2020). Widespread hematite at high latitudes of the Moon. *Science Advances*, *6*(36), eaba1940. https://doi.org/10.1126/sciadv.aba1940

Li, S. H., Deng, C., Yao, H., Huang, S., Liu, C., He, H., et al. (2013). Magnetostratigraphy of the Dali Basin in Yunnan and implications for late Neogene rotation of the southeast margin of the Tibetan Plateau. *Journal of Geophysical Research: Solid Earth*, *118*(3), 791–807. https://doi.org/10.1002/JGRB.50129

Li, Y., & Oldenburg, D. W. (1996). 3-D inversion of magnetic data. *Geophysics*, *61*(2), 394–408. https://doi.org/10.1190/1.1443968

Li, Y., Yang, M., Pentrak, M., He, H., & Arai, Y. (2020). Carbonate-enhanced transformation of ferrihydrite to hematite. *Environmental Science & Technology*, *54*(21), 13701–13708. https://doi.org/10.1021/acs.est.0c04043

Li, Y. Y. (1956). Domain walls in antiferromagnets and the weak ferromagnetism of alpha-Fe_2O_3. *Physical Review*, *101*, 1450–1454. https://doi.org/10.1103/PhysRev.101.1450

Lillis, R., Frey, H., & Manga, M. (2008). Rapid decrease in Martian crustal magnetization in the Noachian era: Implications for the dynamo and climate of early Mars. *Geophysical Research Letters*, *35*(14), L14203. https://doi.org/10.1029/2008GL034338

Lillis, R., Mitchell, D., Lin, R., Connerney, J., & Acuña, M. (2004). Mapping crustal magnetic fields at Mars using electron reflectometry. *Geophysical Research Letters*, *31*(15), L15702. https://doi.org/10.1029/2004GL020189

Lillis, R., Robbins, S., Manga, M., Halekas, J. S., & Frey, H. V. (2013). Time history of the Martian dynamo from crater magnetic field analysis. *Journal of Geophysical Research: Planets*, *118*(7), 1488–1511. https://doi.org/10.1002/jgre.20105

Lin, S. (1959). Magnetic properties of hematite single crystals. I. Magnetization isotherms, antiferromagnetic susceptibility, and weak ferromagnetism of a natural crystal. *Physical Review*, *116*(6), 1447–1452. https://doi.org/10.1103/PhysRev.116.1447

Lin, S. (1960). Magnetic behavior in the transition region of a hematite single crystal. *Journal of Applied Physics*, *31*, S273–S274. https://doi.org/10.1063/1.1984695

Lin, S. (1961). Remanent magnetization of a synthetic hematite single crystal. *Journal of Applied Physics*, *32*, S394–S395. https://doi.org/10.1063/1.2000488

Lippert, P. C., Zhao, X., Coe, R. S., & Lo, C.-H. (2011). Palaeomagnetism and $^{40}Ar/^{39}Ar$ geochronology of upper Palaeogene volcanic rocks from Central Tibet: Implications for the Central Asia inclination anomaly, the palaeolatitude of Tibet and post-50 Ma shortening within Asia. *Geophysical Journal International*, *184*(1), 131–161. https://doi.org/10.1111/j.1365-246X.2010.04833.x

Lisiecki, L. E., & Raymo, M. E. (2005). A Pliocene-Pleistocene stack of 57 globally distributed benthic $\delta^{18}O$ records. *Paleoceanography*, *20*(1), 1. https://doi.org/10.1029/2004PA001071

Liu, C., Deng, C., Liu, Q., Zheng, L., Wang, W., Xu, X., et al. (2010). Mineral magnetism to probe into the nature of palaeomagnetic signals of subtropical red soil sequences in southern China. *Geophysical Journal International*, *181*(3), 1395–1410. https://doi.org/10.1111/j.1365-246X.2010.04592.x

Liu, Q., Banerjee, S. K., Jackson, M. J., Zhu, R., & Pan, Y. (2002). A new method in mineral magnetism for the separation of weak antiferromagnetic signal from a strong ferrimagnetic background. *Geophysical Research Letters*, *29*(12), 1565. https://doi.org/10.1029/2002GL014699

Liu, Q., Barrón, V., Torrent, J., Eeckhout, S., & Deng, C. (2008). Magnetism of intermediate hydromaghemite in the transformation of 2-line ferrihydrite into hematite and its paleoenvironmental implications. *Journal of Geophysical Research*, *113*(1), B01103. https://doi.org/10.1029/2007JB005207

Liu, Q., Barrón, V., Torrent, J., Qin, H., & Yu, Y. (2010). The magnetism of micro-sized hematite explained. *Physics of the Earth and Planetary Interiors*, *183*(3), 387–397. https://doi.org/10.1016/j.pepi.2010.08.008

Liu, Q., Deng, C., Torrent, J., & Zhu, R. (2007). Review of recent developments in mineral magnetism of the Chinese loess. *Quaternary Science Reviews*, *26*(3–4), 368–385. https://doi.org/10.1016/J.QUASCIREV.2006.08.004

Liu, Q., Jackson, M. J., Banerjee, S. K., Maher, B. A., Deng, C. L., Pan, Y. X., & Zhu, R. X. (2004). Mechanism of the magnetic susceptibility enhancements of the Chinese loess. *Journal of Geophysical Research*, *109*(B12), B12107. https://doi.org/10.1029/2004JB003249

Liu, Q., Roberts, A. P., Larrasoaña, J. C., Banerjee, S. K., Guyodo, Y., Tauxe, L., & Oldfield, F. (2012). Environmental magnetism: Principles and applications. *Reviews of Geophysics*, *50*(4), RG4002. https://doi.org/10.1029/2012RG000393

Liu, Q., Roberts, A. P., Torrent, J., Horng, C. S., & Larrasoaña, J. C. (2007). What do the HIRM and S-ratio really measure in environmental magnetism? *Geochemistry, Geophysics, Geosystems*, *8*(9), Q09011. https://doi.org/10.1029/2007GC001717

Liu, Q., Torrent, J., Barrón, V., Duan, Z., & Bloemendal, J. (2011). Quantification of hematite from the visible diffuse reflectance spectrum: Effects of aluminium substitution and grain morphology. *Clay Minerals*, *46*(1), 137–147. https://doi.org/10.1180/CLAYMIN.2011.046.1.137

Liu, Q., Yu, Y., Torrent, J., Roberts, A. P., Pan, Y., & Zhu, R. (2006). Characteristic low-temperature magnetic properties of aluminous goethite [α-(Fe, Al)OOH] explained. *Journal of Geophysical Research*, *111*, B12S34. https://doi.org/10.1029/2006JB004560

Liu, Z., Liu, Q., Torrent, J., Barrón, V., & Hu, P. (2013). Testing the magnetic proxy χ_{fd}/HIRM for quantifying paleoprecipitation in modern soil profiles from Shaanxi Province, China. *Global and Planetary Change*, *110*(C), 368–378. https://doi.org/10.1016/J.GLOPLACHA.2013.04.013

Long, X. Y., Ji, J. F., & Balsam, W. (2011). Rainfall-dependent transformations of iron oxides in a tropical saprolite transect of Hainan Island, South China: Spectral and magnetic measurements. *Journal of Geophysical Research*, *116*, F03015. https://doi.org/10.1029/2010JF001712

Loope, D. B., & Kettler, R. M. (2015). The footprints of ancient CO_2-driven flow systems: Ferrous carbonate concretions below bleached sandstone. *Geosphere*, *11*(3), 943–957. https://doi.org/10.1130/ges01094.1

López-Sánchez, J., McIntosh, G., Osete, M. L., del Campo, A., Villalaín, J. J., Pérez, L., et al. (2017). Epsilon iron oxide: Origin of the high coercivity stable low Curie temperature magnetic phase found in heated archeological materials. *Geochemistry, Geophysics, Geosystems*, *18*(7), 2646–2656. https://doi.org/10.1002/2017GC006929

Louzada, K., Stewart, S., & Weiss, B. (2007). Effect of shock on the magnetic properties of pyrrhotite, the Martian crust, and meteorites. *Geophysical Research Letters*, *34*(5), L05204. https://doi.org/10.1029/2006GL027685

Louzada, K. L., Stewart, S. T., Weiss, B. P., Gattacceca, J., & Bezaeva, N. S. (2010). Shock and static pressure demagnetization of pyrrhotite and implications for the Martian crust. *Earth and Planetary Science Letters*, *290*(1–2), 90–101. https://doi.org/10.1016/J.EPSL.2009.12.006

Løvlie, R., & Torsvik, T. (1984). Magnetic remanence and fabric properties of laboratory deposited hematite bearing red sandstone. *Geophysical Research Letters*, *11*(3), 229–224. https://doi.org/10.1029/GL011i003p00221

Løvlie, R., Torsvik, T., Jelenska, M., & Levandowski, M. (1984). Evidence for detrital remanent magnetization carried by hematite in Devonian red beds from Spitsbergen; Palaeomagnetic implications. *Geophysical Journal International*, *79*(2), 573–588. https://doi.org/10.1111/J.1365-246X.1984.TB02242.X

Lu, H. M., & Meng, X. K. (2010). Morin temperature and Né́el temperature of hematite nanocrystals. *Journal of Physical Chemistry C*, *114*(49), 21291–21295. https://doi.org/10.1021/jp108703b

Lyle, M. (1983). The brown-green color transition in marine sediments: A marker of the Fe(III)-Fe(II) redox boundary. *Limnology & Oceanography*, *28*(5), 1026–1033. https://doi.org/10.4319/lo.1983.28.5.1026

Lyons, R., Oldfield, F., & Williams, E. (2010). Mineral magnetic properties of surface soils and sands across four North African transects and links to climatic gradients. *Geochemistry, Geophysics, Geosystems*, *11*(8), Q08023. https://doi.org/10.1029/2010GC003183

Madsen, M. B., Hviid, S. F., Gunnlaugsson, H. P., Knudsen, J. M., Goetz, W., Pedersen, C. T., et al. (1999). The magnetic properties experiments on Mars Pathfinder. *Journal of Geophysical Research*, *104*(E4), 8761–8779. https://doi.org/10.1029/1998JE900006

Maher, B. A. (1998). Magnetic properties of modern soils and Quaternary loessic paleosols: Paleoclimatic implications. *Palaeogeography, Palaeoclimatology, Palaeoecology*, *137*(1), 25–54. https://doi.org/10.1016/S0031-0182(97)00103-X

Maher, B. A. (2011). The magnetic properties of Quaternary aeolian dusts and sediments, and their palaeoclimatic significance. *Aeolian Research*, *3*(2), 87–144. https://doi.org/10.1016/J.AEOLIA.2011.01.005

Maher, B. A., Alekseev, A., & Alekseeva, T. (2003). Magnetic mineralogy of soils across the Russian Steppe: Climatic dependence of pedogenic magnetite formation. *Palaeogeography, Palaeoclimatology, Palaeoecology*, *201*(3–4), 321–341. https://doi.org/10.1016/S0031-0182(03)00618-7

Maher, B. A., Karloukovski, V. V., & Mutch, T. J. (2004). High-field remanence properties of synthetic and natural submicrometre haematites and goethites: Significance for environmental contexts. *Earth and Planetary Science Letters*, *226*(3–4), 491–505. https://doi.org/10.1016/J.EPSL.2004.05.042

Maher, B. A., Thompson, R., & Zhou, L. P. (1994). Spatial and temporal reconstructions of changes in the Asian palaeomonsoon: A new mineral magnetic approach. *Earth and Planetary Science Letters*, *125*(1), 461–471. https://doi.org/10.1016/0012-821X(94)90232-1

Mangold, N., Baratoux, D., Witasse, O., Encrenaz, T., & Sotin, C. (2016). Mars: A small terrestrial planet. *Astronomy and Astrophysics Review*, *24*(1), 15. https://doi.org/10.1007/s00159-016-0099-5

Maxbauer, D. P., Feinberg, J. M., & Fox, D. L. (2016). Magnetic mineral assemblages in soils and paleosols as the basis for paleoprecipitation proxies: A review of magnetic methods and challenges. *Earth-Science Reviews*, *155*, 28–48. https://doi.org/10.1016/J.EARSCIREV.2016.01.014

McCabe, C., & Elmore, R. D. (1989). The occurrence and origin of Late Paleozoic remagnetization in the sedimentary rocks of North America. *Reviews of Geophysics*, *27*(4), 471–494. https://doi.org/10.1029/RG027I004P00471

McClelland-Brown, E. (1982). Discrimination of TRM and CRM by blocking-temperature spectrum analysis. *Physics of the Earth and Planetary Interiors*, *30*(4), 405–414. https://doi.org/10.1016/0031-9201(82)90050-4

McDougall, I., & Tarling, D. H. (1963). Dating of polarity zones in the Hawaiian Islands. *Nature*, *200*(4901), 54–56. https://doi.org/10.1038/200054a0

McEnroe, S., Langenhorst, F., Robinson, P., Bromiley, G., & Shaw, C. S. (2004). What is magnetic in the lower crust? *Earth and Planetary Science Letters*, *226*(1), 175–192. https://doi.org/10.1016/J.EPSL.2004.07.020

McEnroe, S. A., Brown, L. L., & Robinson, P. (2004). Earth analog for Martian magnetic anomalies: Remanence properties of hemo-ilmenite norites in the Bjerkreim-Sokndal intrusion, Rogaland, Norway. *Journal of Applied Geophysics*, *56*(3), 195–212. https://doi.org/10.1016/s0926-9851(04)00052-7

McEnroe, S. A., Fabian, K., Robinson, P., Gaina, C., & Brown, L. L. (2009). Crustal magnetism, lamellar magnetism and rocks that remember. *Elements*, *5*(4), 241–246. https://doi.org/10.2113/GSELEMENTS.5.4.241

McEnroe, S. A., Harrison, R. J., Robinson, P., Golla, U., & Jercinovic, M. J. (2001). Effect of fine-scale microstructures in titanohematite on the acquisition and stability of natural remanent magnetization in granulite facies metamorphic rocks, southwest Sweden: Implications for crustal magnetism. *Journal of Geophysical Research*, *106*(B12), 30523–30546. https://doi.org/10.1029/2001JB000180

McEnroe, S. A., Robinson, P., Miyajima, N., Fabian, K., Dyar, D., & Sklute, E. C. (2016). Lamellar magnetism and exchange bias in billion-year-old titanohematite with nanoscale ilmenite exsolution lamellae: I. Mineral and magnetic characterization. *Geophysical Journal International*, *206*(1), 470–486. https://doi.org/10.1093/GJI/GGW155

McEnroe, S. A., Robinson, P., & Panish, P. T. (2001). Aeromagnetic anomalies, magnetic petrology, and rock magnetism of hemo-ilmenite-and magnetite-rich cumulate rocks from the Sokndal Region, South Rogaland, Norway. *American Mineralogist*, *86*(11–12), 1447–1468. https://doi.org/10.2138/am-2001-11-1213

McHale, J., Auroux, A., Perrotta, A., & Navrotsky, A. (1997). Surface energies and thermodynamic phase stability in nanocrystalline aluminas. *Science*, *277*(5327), 788–791. https://doi.org/10.1126/science.277.5327.788

McIntosh, G., Kovacheva, M., Catanzariti, G., Donadini, F., & Osete Lopez, M. L. (2011). High coercivity remanence in baked clay materials used in archeomagnetism. *Geochemistry, Geophysics, Geosystems*, *12*(2), Q02003. https://doi.org/10.1029/2010GC003310

McIntosh, G., Kovacheva, M., Catanzariti, G., Osete, M. L., & Casas, L. (2007). Widespread occurrence of a novel high coercivity, thermally stable, low unblocking temperature magnetic phase in heated archeological material. *Geophysical Research Letters*, *34*(21), L21302. https://doi.org/10.1029/2007GL031168

McLennan, S. M., Bell, J. F., Calvin, W. M., Christensen, P. R., Clark, B. C., de Souza, P. A., et al. (2005). Provenance and diagenesis of the evaporite-bearing Burns formation, Meridiani Planum, Mars. *Earth and Planetary Science Letters*, *240*(1), 95–121. https://doi.org/10.1016/j.epsl.2005.09.041

Meng, J., Coe, R. S., Wang, C., Gilder, S. A., Zhao, X., Liu, H., et al. (2017). Reduced convergence within the Tibetan Plateau by 26 Ma? *Geophysical Research Letters*, *44*, 6624–6632. https://doi.org/10.1002/2017GL074219

Michel, F. M., Barrón, V., Torrent, J., Morales, M. P., Serna, C. J., Boily, J. F., et al. (2010). Ordered ferrimagnetic form of ferrihydrite reveals links among structure, composition, and magnetism. *Proceedings of the National Academy of Sciences of the United States of America*, *107*(7), 2787–2792. https://doi.org/10.1073/pnas.0910170107

Mishima, T., Hirono, T., Nakamura, N., Tanikawa, W., Soh, W., & Song, S.-R. (2009). Changes to magnetic minerals caused by frictional heating during the 1999 Taiwan Chi-Chi earthquake. *Earth Planets and Space*, *61*(6), 797–801. https://doi.org/10.1186/bf03353185

Morin, F. (1950). Magnetic susceptibility of α-Fe$_2$O$_3$ and α-Fe$_2$O$_3$ with added titanium. *Physical Review*, *78*(6), 819–820. https://doi.org/10.1103/PhysRev.78.819.2

Moriya, T. (1960). Anisotropic superexchange interaction and weak ferromagnetism. *Physical Review*, *120*(1), 91–98. https://doi.org/10.1103/PhysRev.120.91

Morris, R., Klingelhöfer, G., Schröder, C., Rodionov, D., Yen, A., Ming, D., et al. (2006). Mössbauer mineralogy of rock, soil, and dust at Meridiani Planum, Mars: Opportunity's journey across sulfate-rich outcrop, basaltic sand and dust, and hematite lag deposits. *Journal of Geophysical Research*, *111*(E12), E12S15. https://doi.org/10.1029/2006je002791

Morris, R., Ming, D., Graff, T., Arvidson, R., Bell, J., Squyres, S., et al. (2005). Hematite spherules in basaltic tephra altered under aqueous, acid-sulfate conditions on Mauna Kea volcano, Hawaii: Possible clues for the occurrence of hematite-rich spherules in the Burns formation at Meridiani Planum, Mars. *Earth and Planetary Science Letters*, *240*(1), 168–178. https://doi.org/10.1016/j.epsl.2005.09.044

Morris, R. C. (1993). Genetic modeling for banded iron-formation of the Hamersley Group, Pilbara Craton. *Precambrian Research*, *60*(1), 243–286. https://doi.org/10.1016/0301-9268(93)90051-3

Morris, R. V., Agresti, D. G., Lauer, H. V., Newcomb, J. A., Shelfer, T. D., & Murali, A. (1989). Evidence for pigmentary hematite on Mars based on optical, magnetic, and Mossbauer studies of superparamagnetic (nanocrystalline) hematite. *Journal of Geophysical Research*, *94*(B3), 2760–2778. https://doi.org/10.1029/JB094iB03p02760

Morris, R. V., & Golden, D. (1998). Goldenrod pigments and the occurrence of hematite and possibly goethite in the Olympus–Amazonis region of Mars. *Icarus*, *134*(1), 1–10. https://doi.org/10.1006/icar.1998.5939

Morris, R. V., Golden, D., & Bell, J. F. (1997). Low-temperature reflectivity spectra of red hematite and the color of Mars. *Journal of Geophysical Research*, *102*(E4), 9125–9133. https://doi.org/10.1029/96JE03993

Morris, R. V., Golden, D., Bell, J. F., Lauer, H. V., & Adams, J. B. (1993). Pigmenting agents in Martian soils: Inferences from spectral, Mössbauer, and magnetic properties of nanophase and other iron oxides in Hawaiian palagonitic soil PN-9. *Geochimica et Cosmochimica Acta*, *57*(19), 4597–4609. https://doi.org/10.1016/0016-7037(93)90185-Y

Morris, R. V., Golden, D. C., Bell, J. F., & Lauer, H. V. (1995). Hematite, pyroxene, and phyllosilicates on Mars: Implications from oxidized impact melt rocks from Manicouagan Crater, Quebec, Canada. *Journal of Geophysical Research*, *100*(E3), 5319–5328. https://doi.org/10.1029/94JE01500

Morris, R. V., & Lauer, H. V., Jr. (1981). Stability of goethite (α-FeOOH) and lepidocrocite (γ-FeOOH) to dehydration by UV radiation: Implications for their occurrence on the Martian surface. *Journal of Geophysical Research*, *86*(B11), 10893–10899. https://doi.org/10.1029/JB086iB11p10893

Morris, R. V., Lauer, H. V., Lawson, C. A., Gibson, E. K., Nace, G. A., & Stewart, C. (1985). Spectral and other physicochemical properties of submicron powders of hematite (α-Fe$_2$O$_3$), maghemite (γ-Fe$_2$O$_3$), magnetite (Fe$_3$O$_4$), goethite (α-FeOOH), and lepidocrocite (γ-FeOOH). *Journal of Geophysical Research*, *90*(B4), 3126–3144. https://doi.org/10.1029/JB090iB04p03126

Morrish, A. (1994). *Canted antiferromagnetism: Hematite* (pp. 1–2). World Scientific Publishing Company Pty. Ltd. https://doi.org/10.1142/9789812831569_0001

Morrish, A., & Eaton, J. (1971). Magnetic transition in rhodium-doped hematite single crystals. *Journal of Applied Physics*, *42*, 1495–1496. https://doi.org/10.1063/1.1660315

Moskowitz, B. M., Jackson, M., & Chandler, V. (2015). Geophysical properties of the near-surface Earth: Magnetic properties. In G. Schubert (Ed.), *Treatise on geophysics* (2nd ed., pp. 139–174). Elsevier. https://doi.org/10.1016/B978-0-444-53802-4.00191-3

Muench, G., Arajs, S., & Matijevic, E. (1985). The Morin transition in small α-Fe$_2$O$_3$ particles. *Physica Status Solidi A*, *92*(1), 187–192. https://doi.org/10.1002/pssa.2210920117

Mustard, J. F., & Bell, J. F. (1994). New composite reflectance spectra of Mars from 0.4 to 3.14 μm. *Geophysical Research Letters*, *21*(5), 353–356. https://doi.org/10.1029/94GL00198

Nagata, T. (1952). Reverse thermo-remanent magnetism. *Nature*, *169*(4304), 704–705. https://doi.org/10.1038/169704a0

Nagata, T., & Akimoto, S. (1956). Magnetic properties of ferromagnetic ilmenites. *Geofisica Pura e Applicata*, *34*(1), 36–50. https://doi.org/10.1007/bf02122815

Nagata, T., & Uyeda, S. (1959). Exchange interaction as a cause of reverse thermo-remanent magnetism. *Nature*, *184*(4690), 890–891. https://doi.org/10.1038/184890a0

Navrotsky, A., Mazeina, L., & Majzlan, J. (2008). Size-driven structural and thermodynamic complexity in iron oxides. *Science*, *319*(5870), 1635–1638. https://doi.org/10.1126/science.1148614

Néel, L. (1954). Anisotropie magnétique superficielle et surstructures d'orientation. *Journal de Physique et le Radium*, *15*(4), 225–239. https://doi.org/10.1051/jphysrad:01954001504022500

Néel, L. (1955). Some theoretical aspects of rock-magnetism. *Advances in Physics*, *4*, 191–243. https://doi.org/10.1080/00018735500101204

Newsom, H. E. (1980). Hydrothermal alteration of impact melt sheets with implications for Mars. *Icarus*, *44*(1), 207–216. https://doi.org/10.1016/0019-1035(80)90066-4

Newsom, H. E., Barber, C. A., Hare, T. M., Schelble, R. T., Sutherland, V. A., & Feldman, W. C. (2003). Paleolakes and impact basins in southern Arabia Terra, including Meridiani Planum: Implications for the formation of hematite deposits on Mars. *Journal of Geophysical Research*, *108*(E12), 8075. https://doi.org/10.1029/2002JE001993

Nie, J., Song, Y., King, J. W., Fang, X., & Heil, C. (2010). HIRM variations in the Chinese red-clay sequence: Insights into pedogenesis in the dust source area. *Journal of Asian Earth Sciences*, *38*(3), 96–104. https://doi.org/10.1016/j.jseaes.2009.11.002

Nornberg, P., Vendelboe, A. L., Gunnlaugsson, H. P., Merrison, J. P., Finster, K., & Jensen, S. K. (2009). Comparison of the mineralogical effects of an experimental forest fire on a goethite/ferrihydrite soil with a topsoil that contains hematite, maghemite and goethite. *Clay Minerals*, *44*(2), 239–247. https://doi.org/10.1180/claymin.2009.044.2.239

Ôno, K., & Ito, A. (1962). A Mössbauer study of the internal field at Fe^{57} in α-Fe$_2$O$_3$. *Journal of the Physical Society of Japan*, *17*(6), 1012–1017. https://doi.org/10.1143/JPSJ.17.1012

Ono, S., Kikegawa, T., & Ohishi, Y. (2004). High-pressure phase transition of hematite, Fe$_2$O$_3$. *Journal of Physics and Chemistry of Solids*, *65*(8–9), 1527–1530. https://doi.org/10.1016/j.jpcs.2003.11.042

O'Reilly, W. (1984). *Rock and mineral magnetism*. Blackie. https://doi.org/10.1007/978-1-4684-8468-7

Özdemir, Ö., & Dunlop, D. J. (1988). Crystallization remanent magnetization during the transformation of maghemite to hematite. *Journal of Geophysical Research*, *93*(B6), 6530–6544. https://doi.org/10.1029/JB093iB06p06530

Özdemir, Ö., & Dunlop, D. J. (1993). Chemical remanent magnetization during γ-FeOOH phase transformations. *Journal of Geophysical Research*, *98*(B3), 4191–4198. https://doi.org/10.1029/92JB02569

Özdemir, Ö., & Dunlop, D. J. (2000). Intermediate magnetite formation during dehydration of goethite. *Earth and Planetary Science Letters*, *177*(1–2), 59–67. https://doi.org/10.1016/s0012-821x(00)00032-7

Özdemir, Ö., & Dunlop, D. J. (2002). Thermoremanence and stable memory of single-domain hematites. *Geophysical Research Letters*, *29*(18), 1877. https://doi.org/10.1029/2002GL015597

Özdemir, Ö., & Dunlop, D. J. (2005). Thermoremanent magnetization of multidomain hematite. *Journal of Geophysical Research*, *110*, B09104. https://doi.org/10.1029/2005JB003820

Özdemir, O., & Dunlop, D. J. (2006). Magnetic memory and coupling between spin-canted and defect magnetism in hematite. *Journal of Geophysical Research*, *111*, B12S03. https://doi.org/10.1029/2006JB004555

Özdemir, Ö., & Dunlop, D. J. (2014). Hysteresis and coercivity of hematite. *Journal of Geophysical Research: Solid Earth*, *119*(4), 2582–2594. https://doi.org/10.1002/2013JB010739

Özdemir, Ö., Dunlop, D. J., & Berquó, T. S. (2008). Morin transition in hematite: Size dependence and thermal hysteresis. *Geochemistry, Geophysics, Geosystems*, *9*, Q10Z01. https://doi.org/10.1029/2008GC002110

Ozima, M., Oshima, O., & Funaki, M. (2003). Magnetic properties of pyroclastic rocks from the later stage of the eruptive activity of Haruna Volcano in relation to the self-reversal of thermo-remanent magnetization. *Earth Planets and Space*, *55*(4), 183–188. https://doi.org/10.1186/BF03351747

Parise, J. B., Locke, D. R., Tulk, C. A., Swainson, I., & Cranswick, L. (2006). The effect of pressure on the Morin transition in hematite (α-Fe$_2$O$_3$). *Physica B*, *385*, 391–393. https://doi.org/10.1016/j.physb.2006.05.081

Pauling, L., & Hendricks, S. B. (1925). The crystal structures of hematite and corundum. *Journal of the American Chemical Society*, *47*(3), 781–790. https://doi.org/10.1021/ja01680a027

Penn, R. L. (2004). Kinetics of oriented aggregation. *The Journal of Physical Chemistry B*, *108*(34), 12707–12712. https://doi.org/10.1021/jp036490+

Pollack, J. B., Pitman, D., Khare, B. N., & Sagan, C. (1970). Goethite on Mars: A laboratory study of physically and chemically bound water in ferric oxides. *Journal of Geophysical Research*, *75*(35), 7480–7490. https://doi.org/10.1029/JB075i035p07480

Porath, H. (1968). Stress induced magnetic anisotropy in natural single crystals of hematite. *Philosophical Magazine*, *17*(147), 603–608. https://doi.org/10.1080/14786436808217746

Posth, N. R., Köhler, I., Swanner, E. D., Schröder, C., Wellmann, E., Binder, B., et al. (2013). Simulating Precambrian banded iron formation diagenesis. *Chemical Geology*, *362*, 66–73. https://doi.org/10.1016/j.chemgeo.2013.05.031

Posth, N. R., Konhauser, K. O., & Kappler, A. (2011). Banded iron formations. In J. Reitner & V. Thiel (Eds.), *Encyclopedia of geobiology* (pp. 92–103). Springer. https://doi.org/10.1007/978-1-4020-9212-1_19

Potter, S. L., Chan, M. A., Petersen, E. U., Dyar, M., & Sklute, E. (2011). Characterization of Navajo Sandstone concretions: Mars comparison and criteria for distinguishing diagenetic origins. *Earth and Planetary Science Letters*, *301*(3–4), 444–456. https://doi.org/10.1016/j.epsl.2010.11.027

Powell, C. M., Oliver, N. H. S., Li, Z.-X., Martin, D. M., & Ronaszeki, J. (1999). Synorogenic hydrothermal origin for giant Hamersley iron oxide ore bodies. *Geology*, *27*(2), 175–178. https://doi.org/10.1130/0091-7613(1999)027<0175:shofgh>2.3.co;2

Prasad, P. S. R., Shiva Prasad, K., Krishna Chaitanya, V., Babu, E. V. S. S. K., Sreedhar, B., & Ramana Murthy, S. (2006). In situ FTIR study on the dehydration of natural goethite. *Journal of Asian Earth Sciences*, *27*(4), 503–511. https://doi.org/10.1016/j.jseaes.2005.05.005

Prasetyo, B., & Gilkes, R. (1994). Properties of iron-oxides from red soils derived from volcanic tuff in West Java. *Soil Research*, *32*(4), 781–794. https://doi.org/10.1071/SR9940781

Qin, H., Zhao, X., Liu, S. C., Paterson, G. A., Jiang, Z. X., Cai, S. H., et al. (2020). An ultra-low magnetic field thermal demagnetizer for high-precision paleomagnetism. *Earth Planets and Space*, *72*, 170. https://doi.org/10.1186/s40623-020-01304-0

Rasmussen, B., Krapež, B., & Meier, D. B. (2014). Replacement origin for hematite in 2.5 Ga banded iron formation: Evidence for postdepositional oxidation of iron-bearing minerals. *The Geological Society of America Bulletin*, *126*(3–4), 438–446. https://doi.org/10.1130/b30944.1

Rath, C., Sahu, K. K., Kulkarni, S. D., Anand, S., Date, S. K., Das, R. P., & Mishra, N. C. (1999). Microstructure-dependent coercivity in monodispersed hematite particles. *Applied Physics Letters*, *75*(26), 4171–4173. https://doi.org/10.1063/1.125572

Remazeilles, C., & Refait, P. (2007). On the formation of β-FeOOH (akaganéite) in chloride-containing environments. *Corrosion Science*, *49*(2), 844–857. https://doi.org/10.1016/j.corsci.2006.06.003

Ren, J., Long, X., Ji, J., Barrón, V., Torrent, J., Wang, Y., & Xie, S. (2020). Different enrichment patterns of magnetic particles modulated by primary iron-phosphorous input. *Geophysical Research Letters*, *47*(22), e2020GL090439. https://doi.org/10.1029/2020GL090439

Rendón, J. L., Cornejo, J., & de Arambarri, P. (1983). Grinding-induced effects on goethite (α-FeOOH). *Journal of Colloid and Interface Science*, *94*(2), 546–551. https://doi.org/10.1016/0021-9797(83)90294-1

Reufer, M., Dietsch, H., Gasser, U., Grobety, B., Hirt, A., Malik, V., & Schurtenberger, P. (2011). Magnetic properties of silica coated spindle-type hematite particles. *Journal of Physics: Condensed Matter*, *23*, 065102. https://doi.org/10.1088/0953-8984/23/6/065102

Reynolds, R. L. (1982). Post-depositional alteration of titanomagnetite in a Miocene sandstone, south Texas (U.S.A.). *Earth and Planetary Science Letters*, *61*(2), 381–391. https://doi.org/10.1016/0012-821X(82)90068-1

Reynolds, R. L., Cattle, S. R., Moskowitz, B. M., Goldstein, H. L., Yauk, K., Flagg, C. B., et al. (2014). Iron oxide minerals in dust of the Red Dawn event in eastern Australia, September 2009. *Aeolian Research*, *15*, 1–13. https://doi.org/10.1016/j.aeolia.2014.02.003

Rieder, R., Economou, T., Wänke, H., Turkevich, A., Crisp, J., Brückner, J., et al. (1997). The chemical composition of Martian soil and rocks returned by the mobile alpha proton X-ray spectrometer: Preliminary results from the X-ray mode. *Science*, *278*(5344), 1771–1774. https://doi.org/10.1126/science.278.5344.1771

Robb, G. L. (1949). Red bed coloration. *Journal of Sedimentary Research*, *19*(3), 99–103. https://doi.org/10.1306/D4269364-2B26-11D7-8648000102C1865D

Roberts, A. P. (2015). Magnetic mineral diagenesis. *Earth-Science Reviews*, *151*, 1–47. https://doi.org/10.1016/j.earscirev.2015.09.010

Roberts, A. P., Cui, Y. L., & Verosub, K. L. (1995). Wasp-waisted hysteresis loops: Mineral magnetic characteristics and discrimination of components in mixed magnetic systems. *Journal of Geophysical Research*, *100*(B9), 17909–17924. https://doi.org/10.1029/95JB00672

Roberts, A. P., Florindo, F., Chang, L., Heslop, D., Jovane, L., & Larrasoaña, J. C. (2013). Magnetic properties of pelagic marine carbonates. *Earth-Science Reviews*, *127*, 111–139. https://doi.org/10.1016/j.earscirev.2013.09.009

Roberts, A. P., Liu, Q. S., Rowan, C. J., Chang, L., Carvallo, C., Torrent, J., & Horng, C.-S. (2006). Characterization of hematite (α-Fe_2O_3), goethite (α-FeOOH), greigite (Fe_3S_4), and pyrrhotite (Fe_7S_8) using first-order reversal curve diagrams. *Journal of Geophysical Research*, *111*, B12S35. https://doi.org/10.1029/2006JB004715

Roberts, A. P., Zhao, X., Heslop, D., Abrajevitch, A., Chen, Y.-H., Hu, P., et al. (2020). Hematite (α-Fe_2O_3) quantification in sedimentary magnetism: Limitations of existing proxies and ways forward. *Geoscience Letters*, *7*(1), 8. https://doi.org/10.1186/s40562-020-00157-5

Robinson, P., Harrison, R. J., McEnroe, S. A., & Hargraves, R. B. (2002). Lamellar magnetism in the haematite-ilmenite series as an explanation for strong remanent magnetization. *Nature*, *418*(6897), 517–520. https://doi.org/10.1038/nature00942

Robinson, P., Harrison, R. J., McEnroe, S. A., & Hargraves, R. B. (2004). Nature and origin of lamellar magnetism in the hematite-ilmenite series. *American Mineralogist*, *89*(5–6), 725–747. https://doi.org/10.2138/am-2004-5-607

Robinson, P., McEnroe, S. A., & Jackson, M. J. (2017). Lamellar magnetism and exchange bias in billion-year-old metamorphic titanohematite with nanoscale ilmenite exsolution lamellae – II: Exchange-bias at 5 K after field-free cooling of NRM and after cooling in a 5 T field. *Geophysical Journal International*, *208*(2), 895–917. https://doi.org/10.1093/gji/ggw428

Robinson, S. G. (1986). The late Pleistocene palaeoclimatic record of North Atlantic deep-sea sediments revealed by mineral-magnetic measurements. *Physics of the Earth and Planetary Interiors*, *42*(1), 22–47. https://doi.org/10.1016/S0031-9201(86)80006-1

Rochette, P., Fillion, G., Ballou, R., Brunet, F., Ouaddiaf, B., & Hood, L. (2003). High pressure magnetic transition in pyrrhotite and impact demagnetization on Mars. *Geophysical Research Letters*, *30*(13), 1683. https://doi.org/10.1029/2003GL017359

Rochette, P., Mathé, P.-E., Esteban, L., Rakoto, H., Bouchez, J.-L., Liu, Q., & Torrent, J. (2005). Non-saturation of the defect moment of goethite and fine-grained hematite up to 57 Teslas. *Geophysical Research Letters*, *32*, L22309. https://doi.org/10.1029/2005GL024196

Ruan, H., & Gilkes, R. (1995). Acid dissolution of synthetic aluminous goethite before and after transformation to hematite by heating. *Clay Minerals*, *30*(1), 55–65. https://doi.org/10.1180/claymin.1995.030.1.06

Sato, M., Yamamoto, Y., Nishioka, T., Kodama, K., Mochizuki, N., Ushioda, M., et al. (2018). Constraints on the source of the Martian magnetic anomalies inferred from relaxation time of remanent magnetization. *Geophysical Research Letters*, *45*(13), 6417–6427. https://doi.org/10.1029/2018GL077498

Scheinost, A., Chavernas, A., Barrón, V., & Torrent, J. (1998). Use and limitations of second-derivative diffuse reflectance spectroscopy in the visible to near-infrared range to identify and quantity Fe oxide minerals in soils. *Clays and Clay Minerals*, *46*(5), 528–536. https://doi.org/10.1346/ccmn.1998.0460506

Scheinost, A., & Schwertmann, U. (1999). Color identification of iron oxides and hydroxysulfates: Use and limitations. *Soil Science Society of America Journal*, *63*(5), 1463–1471. https://doi.org/10.2136/sssaj1999.6351463x

Scheinost, A. C., Schulze, D. G., & Schwertmann, U. (1999). Diffuse reflectance spectra of Al substituted goethite: A ligand field approach. *Clays and Clay Minerals*, *47*(2), 156–164. https://doi.org/10.1346/ccmn.1999.0470205

Schlinger, C. M., & Veblen, D. R. (1989). Magnetism and transmission electron microscopy of Fe-Ti oxides and pyroxenes in a granulite from Lofoten, Norway. *Journal of Geophysical Research*, *94*(B10), 14009–14026. https://doi.org/10.1029/JB094iB10p14009

Scholz, C. H. (2002). *The mechanics of earthquakes and faulting*. Cambridge University Press. https://doi.org/10.1017/9781316681473

Schulze, D. (1984). The influence of aluminium on iron oxides. VIII. Unit cell dimensions of Al substituted goethites and estimation of Al from them. *Clays and Clay Minerals*, *32*(1), 36–44. https://doi.org/10.1346/CCMN.1984.0320105

Schwertmann, U. (1985). The effect of pedogenic environments on iron oxide minerals. *Advances in soil science* (pp. 171–200). Springer. https://doi.org/10.1007/978-1-4612-5046-3_5

Schwertmann, U. (1988). Occurrence and formation of iron oxides in various pedoenvironments. In J. W. Stucki, B. A.Goodman, & U.Schwertmann (Eds.), *Iron in soils and clay minerals* (pp. 267–308). Springer. https://doi.org/10.1007/978-94-009-4007-9_11

Schwertmann, U. (1993). Relations between iron oxides, soil color, and soil formation. In J. M. Bigham & E. J. Ciolkosz (Eds.), *Soil color* (pp. 51–69). SSSA Special PublicationSoil Science Society of America. https://doi.org/10.2136/sssaspecpub31.c4

Schwertmann, U., Carlson, L., & Murad, E. (1987). Properties of iron oxides in two Finnish lakes in relation to the environment of their formation. *Clays and Clay Minerals*, *35*(4), 297–304. https://doi.org/10.1346/ccmn.1987.0350407

Schwertmann, U., & Cornell, R. M. (2000). *Iron oxides in the laboratory: Preparation and characterization*. Wiley-VCH. https://doi.org/10.1002/9783527613229

Schwertmann, U., Fitzpatrick, R., Taylor, R., & Lewis, D. (1979). The influence of aluminum on iron oxides. Part II: Preparation and properties of Al substituted hematites. *Clays and Clay Minerals*, *27*, 105–112. https://doi.org/10.1346/ccmn.1979.0270205

Schwertmann, U., Fitzpatrick, R. W., & Le Roux, J. (1977). Al substitution and different disorder in soil hematites. *Clays and Clay Minerals*, *25*(5), 373–374. https://doi.org/10.1346/ccmn.1977.0250504

Schwertmann, U., Friedl, J., & Stanjek, H. (1999). From Fe (III) ions to ferrihydrite and then to hematite. *Journal of Colloid and Interface Science*, *209*(1), 215–223. https://doi.org/10.1006/jcis.1998.5899

Schwertmann, U., Friedl, J., Stanjek, H., & Schulze, D. (2000). The effect of clay minerals on the formation of goethite and hematite from ferrihydrite after 16 years' ageing at 25°C and pH 4–7. *Clay Minerals*, *35*(4), 613–623. https://doi.org/10.1180/000985500547034

Schwertmann, U., & Murad, E. (1983). Effect of pH on the formation of goethite and hematite from ferrihydrite. *Clays and Clay Minerals*, *31*(4), 277–284. https://doi.org/10.1346/ccmn.1983.0310405

Schwertmann, U., & Murad, E. (1988). The nature of an iron oxide-organic iron association in a peaty environment. *Clay Minerals*, *23*(3), 291–299. https://doi.org/10.1180/claymin.1988.023.3.06

Searle, C. (1967). On the pressure dependence of the low-temperature transition in hematite. *Physics Letters A*, *25*(3), 256–257. https://doi.org/10.1016/0375-9601(67)90890-0

Seguin, M. (1966). Instability of $FeCO_3$ in air. *American Journal of Science*, *264*(7), 562–568. https://doi.org/10.2475/ajs.264.7.562

Sheldon, N. D., & Tabor, N. J. (2009). Quantitative paleoenvironmental and paleoclimatic reconstruction using paleosols. *Earth-Science Reviews*, *95*(1), 1–52. https://doi.org/10.1016/j.earscirev.2009.03.004

Sherman, D. M., & Waite, T. D. (1985). Electronic spectra of Fe^{3+} oxides and oxide hydroxides in the near IR to near UV. *American Mineralogist*, *70*(11–12), 1262–1269. Retrieved from https://pubs.er.usgs.gov/publication/70012311

Shull, C. G., Strauser, W. A., & Wollan, E. O. (1951). Neutron diffraction by paramagnetic and antiferromagnetic substances. *Physical Review*, *83*(2), 333–345. https://doi.org/10.1103/PhysRev.83.333

Sileo, E. E., Daroca, D. P., Barrero, C. A., Larralde, A. L., Giberti, M. S., & Saragovi, C. (2007). Influence of the genesis on the structural and hyperfine properties of Cr-substituted hematites. *Chemical Geology*, *238*(1), 84–93. https://doi.org/10.1016/j.chemgeo.2006.10.017

Smith, R., & Fuller, M. (1967). Alpha-hematite: Stable remanence and memory. *Science*, *156*, 1130–1133. https://doi.org/10.1126/science.156.3778.1130

Smith, T. T. (1916). The magnetic properties of hematite. *Physical Review*, *8*(6), 721–737. https://doi.org/10.1103/physrev.8.721

Spencer, E., & Percival, F. G. (1952). The structure and origin of the banded hematite jaspers of Singhbhum, India. *Economic Geology*, *47*(4), 365–383. https://doi.org/10.2113/gsecongeo.47.4.365

Sprain, C. J., Feinberg, J. M., Renne, P. R., & Jackson, M. (2016). Importance of titanohematite in detrital remanent magnetizations of strata spanning the Cretaceous-Paleogene boundary, Hell Creek region, Montana. *Geochemistry, Geophysics, Geosystems*, *17*(3), 660–678. https://doi.org/10.1002/2015GC006191

Squyres, S. W., Grotzinger, J., Arvidson, R., Bell, J., Calvin, W., Christensen, P., et al. (2004). In situ evidence for an ancient aqueous environment at Meridiani Planum, Mars. *Science*, *306*(5702), 1709–1714. https://doi.org/10.1126/science.1104559

Squyres, S. W., & Knoll, A. H. (2005). Sedimentary rocks at Meridiani Planum: Origin, diagenesis, and implications for life on Mars. *Earth and Planetary Science Letters*, *240*(1), 1–10. https://doi.org/10.1016/j.epsl.2005.09.038

Srivasta, J. K., & Sharma, R. P. (1972). Magnetic dilution effects on Morin phase-transition in hematite. *Physica Status Solidi B*, *49*(1), 135–146. https://doi.org/10.1002/pssb.2220490112

Stacey, F. D. (1958). Thermo-remanent magnetization (TRM) of multidomain grains in igneous rocks. *Philosophical Magazine*, *3*(36), 1391–1401. https://doi.org/10.1080/14786435808233326

Stacey, F. D. (1963). The physical theory of rock magnetism. *Advances in Physics*, *12*(45), 45–133. https://doi.org/10.1080/00018736300101263

Stanjek, H., & Schwertmann, U. (1992). The influence of aluminum on iron oxides. Part XVI: Hydroxyl and aluminum substitution in synthetic hematites. *Clays and Clay Minerals*, *40*, 347–354. https://doi.org/10.1346/ccmn.1992.0400316

Stearns, C., & Van der Voo, R. (1987). A paleomagnetic reinvestigation of the Upper Devonian Perry Formation: Evidence for Late Paleozoic remagnetization. *Earth and Planetary Science Letters*, *86*(1), 27–38. https://doi.org/10.1016/0012-821X(87)90185-3

Steiner, M. B. (1983). Detrital remanent magnetization in hematite. *Journal of Geophysical Research*, *88*(B8), 6523–6539. https://doi.org/10.1029/JB088iB08p06523

Stevenson, D. J. (2001). Mars' core and magnetism. *Nature*, *412*(6843), 214–219. https://doi.org/10.1038/35084155

Stokking, L., & Tauxe, L. (1990a). Properties of chemical remanence in synthetic hematite: Testing theoretical predictions. *Journal of Geophysical Research*, *95*(B8), 12639–12652. https://doi.org/10.1029/JB095iB08p12639

Stokking, L. B., & Tauxe, L. (1990b). Multicomponent magnetization in synthetic hematite. *Physics of the Earth and Planetary Interiors*, *65*, 109–124. https://doi.org/10.1016/0031-9201(90)90080-H

Stokking, L. B., & Tauxe, L. (1987). Acquisition of chemical remanent magnetization by synthetic iron oxide. *Nature*, *327*(18), 610–612. https://doi.org/10.1038/327610a0

Suber, L., Imperatori, P., Mari, A., Marchegiani, G., Mansilla, M. V., Fiorani, D., et al. (2010). Thermal hysteresis of Morin transition in hematite particles. *Physical Chemistry Chemical Physics*, *12*(26), 6984–6989. https://doi.org/10.1039/B925371H

Šubrt, J., Pérez-Maqueda, L. A., Criado, J. M., Real, C., Boháček, J., & Večerníková, E. (2000). Preparation of nanosized hematite particles by mechanical activation of goethite samples. *Journal of the American Ceramic Society*, *83*(2), 294–298. https://doi.org/10.1111/j.1151-2916.2000.tb01188.x

Sugimoto, T., & Sakata, K. (1992). Preparation of monodisperse pseudocubic α-Fe_2O_3 particles from condensed ferric hydroxide gel. *Journal of Colloid and Interface Science*, *152*(2), 587–590. https://doi.org/10.1016/0021-9797(92)90062-Q

Sugimoto, T., Sakata, K., & Muramatsu, A. (1993). Formation mechanism of monodisperse pseudocubic α-Fe_2O_3 particles from condensed ferric hydroxide gel. *Journal of Colloid and Interface Science*, *159*(2), 372–382. https://doi.org/10.1006/jcis.1993.1336

Sugimoto, T., Waki, S., Itoh, H., & Muramatsu, A. (1996). Preparation of monodisperse platelet-type hematite particles from a highly condensed β-FeOOH suspension. *Colloids and Surfaces A*, *109*, 155–165. https://doi.org/10.1016/0927-7757(95)03454-4

Sugimoto, T., & Wang, Y. (1998). Mechanism of the shape and structure control of monodispersed α-Fe_2O_3 particles by sulfate ions. *Journal of Colloid and Interface Science*, *207*(1), 137–149. https://doi.org/10.1006/jcis.1998.5741

Sugimoto, T., Wang, Y. S., Itoh, H., & Muramatsu, A. (1998). Systematic control of size, shape and internal structure of monodisperse α-Fe_2O_3 particles. *Colloids and Surfaces A*, *134*(3), 265–279. https://doi.org/10.1016/S0927-7757(97)00103-9

Sun, J. M., Zhang, L. Y., Deng, C. L., & Zhu, R. X. (2008). Evidence for enhanced aridity in the Tarim Basin of China since 5.3 Ma. *Quaternary Science Reviews*, *27*(9–10), 1012–1023. https://doi.org/10.1016/j.quascirev.2008.01.011

Sun, L., Cao, M., & Hu, C. (2010). Synthesis and magnetic properties of hollow α-Fe_2O_3 nanospheres templated by carbon nanospheres. *Solid State Sciences*, *12*(12), 2020–2023. https://doi.org/10.1016/j.solidstatesciences.2010.08.020

Sun, Q., Lu, X., & Liang, G. (2010). Controlled template-free hydrothermal synthesis of hematite nanoplatelets. *Materials Letters*, *64*(18), 2006–2008. https://doi.org/10.1016/j.matlet.2010.06.025

Sun, Z., Yang, Z., Pei, J., Yang, T., & Wang, X. (2006). New Early Cretaceous paleomagnetic data from volcanic and red beds of the eastern Qaidam Block and its implications for tectonics of Central Asia. *Earth and Planetary Science Letters*, *243*(1), 268–281. https://doi.org/10.1016/j.epsl.2005.12.016

Sváb, E., & Krén, E. (1979). Neutron diffraction study of substituted hematite. *Journal of Magnetism and Magnetic Materials*, *14*(2–3), 184–186. https://doi.org/10.1016/0304-8853(79)90114-8

Swann, P., & Tighe, N. (1977). High voltage microscopy of the reduction of hematite to magnetite. *Metallurgical Transactions B*, *8B*(2), 479–487. https://doi.org/10.1007/BF02696936

Swanson-Hysell, N. L., Fairchild, L. M., & Slotznick, S. P. (2019). Primary and secondary red bed magnetization constrained by fluvial intraclasts. *Journal of Geophysical Research: Solid Earth*, *124*(5), 4276–4289. https://doi.org/10.1029/2018JB017067

Tadić, M., Čitaković, N., Panjan, M., Stojanović, Z., Marković, D., & Spasojević, V. (2011). Synthesis, morphology, microstructure and magnetic properties of hematite submicron particles. *Journal of Alloys and Compounds*, *509*(28), 7639–7644. https://doi.org/10.1016/j.jallcom.2011.04.117

Tan, X., Gilder, S., Kodama, K. P., Jiang, W., Han, Y., Zhang, H., et al. (2010). New paleomagnetic results from the Lhasa block: Revised estimation of latitudinal shortening across Tibet and implications for dating the India–Asia collision. *Earth and Planetary Science Letters*, *293*(3), 396–404. https://doi.org/10.1016/j.epsl.2010.03.013

Tan, X., & Kodama, K. (2002). Magnetic anisotropy and paleomagnetic inclination shallowing in red beds: Evidence from the Mississippian Mauch Chunk Formation, Pennsylvania. *Journal of Geophysical Research*, *107*(B11), 2311. https://doi.org/10.1029/2001JB001636

Tan, X., & Kodama, K. P. (2003). An analytical solution for correcting palaeomagnetic inclination error. *Geophysical Journal International*, *152*(1), 228–236. https://doi.org/10.1046/j.1365-246X.2003.01848.x

Tan, X., Kodama, K. P., Chen, H., Fang, D., Sun, D., & Li, Y. (2003). Paleomagnetism and magnetic anisotropy of Cretaceous red beds from the Tarim basin, northwest China: Evidence for a rock magnetic cause of anomalously shallow paleomagnetic inclinations from central Asia. *Journal of Geophysical Research*, *108*(B2), 2107. https://doi.org/10.1029/2001JB001608

Tan, X., Kodama, K. P., & Fang, D. (2002). Laboratory depositional and compaction-caused inclination errors carried by haematite and their implications in identifying inclination error of natural remanence in red beds. *Geophysical Journal International*, *151*(2), 475–486. https://doi.org/10.1046/j.1365-246X.2002.01794.x

Tan, X., Kodama, K. P., Gilder, S., & Courtillot, V. (2007). Rock magnetic evidence for inclination shallowing in the Passaic Formation red beds from the Newark basin and a systematic bias of the Late Triassic apparent polar wander path for North America. *Earth and Planetary Science Letters*, *254*(3–4), 345–357. https://doi.org/10.1016/j.epsl.2006.11.043

Tanikawa, W., Mishima, T., Hirono, T., Lin, W., Shimamoto, T., Soh, W., & Song, S. R. (2007). High magnetic susceptibility produced in high-velocity frictional tests on core samples from the Chelungpu fault in Taiwan. *Geophysical Research Letters*, *34*, L15304. https://doi.org/10.1029/2007gl030783

Tanikawa, W., Mishima, T., Hirono, T., Soh, W., & Song, S.-R. (2008). High magnetic susceptibility produced by thermal decomposition of core samples from the Chelungpu fault in Taiwan. *Earth and Planetary Science Letters*, *272*(1), 372–381. https://doi.org/10.1016/j.epsl.2008.05.002

Tauxe, L. (2010). *Essentials of paleomagnetism*. University of California Press.

Tauxe, L., & Kent, D. V. (1984). Properties of a detrital remanence carried by haematite from study of modern river deposits and laboratory redeposition experiments. *Geophysical Journal of the Royal Astronomical Society*, *76*(3), 543–561. https://doi.org/10.1111/j.1365-246X.1984.tb01909.x

Tauxe, L., & Kent, D. V. (2004). A simplified statistical model for the geomagnetic field and the detection of shallow bias in paleomagnetic inclinations: Was the ancient magnetic field dipolar? *AGU Geophysical Monograph*, *145*, 101–115. https://doi.org/10.1029/145GM08

Tauxe, L., Kent, D. V., & Opdyke, N. D. (1980). Magnetic components contributing to the NRM of Middle Siwalik red beds. *Earth and Planetary Science Letters*, *47*(2), 279–284. https://doi.org/10.1016/0012-821X(80)90044-8

Tauxe, L., Kodama, K. P., & Kent, D. V. (2008). Testing corrections for paleomagnetic inclination error in sedimentary rocks: A comparative approach. *Physics of the Earth and Planetary Interiors*, *169*(1), 152–165. https://doi.org/10.1016/j.pepi.2008.05.006

Tauxe, L., & Opdyke, N. D. (1982). A time framework based on magnetostratigraphy for the Siwalik sediments of the Khaur area, Northern Pakistan. *Palaeogeography, Palaeoclimatology, Palaeoecology*, *37*(1), 43–61. https://doi.org/10.1016/0031-0182(82)90057-8

Taylor, D., Dalstra, H. J., & Harding, A. E. (2001). Genesis of high-grade hematite orebodies of the Hamersley province, Western Australia–A reply. *Economic Geology*, *97*(1), 837–873. https://doi.org/10.2113/GSECONGEO.97.1.179

Taylor, R., & Schwertmann, U. (1980). The influence of aluminum on iron oxides. VII. Substitution of Al for Fe in synthetic lepidocrite. *Clays and Clay Minerals*, *28*(4), 267–271. https://doi.org/10.1346/ccmn.1980.0280404

Thomas, P., Grott, M., Morschhauser, A., & Vervelidou, F. (2018). Paleopole reconstruction of Martian magnetic field anomalies. *Journal of Geophysical Research: Planets*, *123*(5), 1140–1155. https://doi.org/10.1002/2017JE005511

Thorpe, A. N., Minkin, J. A., Senftle, F. E., Alexander, C., Briggs, C., Evans, H. T., & Nord, G. L. (1977). Cell dimensions and antiferromagnetism of lunar and terrestrial ilmenite single crystals. *Journal of Physics and Chemistry of Solids*, *38*(2), 115–123. https://doi.org/10.1016/0022-3697(77)90155-X

Till, J., Guyodo, Y., Lagroix, F., Morin, G., & Ona-Nguema, G. (2015). Goethite as a potential source of magnetic nanoparticles in sediments. *Geology*, *43*(1), 75–78. https://doi.org/10.1130/G36186.1

Tite, M. S., & Mullins, C. (1971). Enhancement of the magnetic susceptibility of soils on archaeological sites. *Archaeometry*, *13*(2), 209–219. https://doi.org/10.1111/j.1475-4754.1971.tb00043.x

Torrent, J., & Barrón, V. (2000). Key role of phosphorus in the formation of the iron oxides in Mars soils? *Icarus*, *145*(2), 645–647. https://doi.org/10.1006/icar.2000.6408

Torrent, J., & Barrón, V. (2002). Diffuse reflectance spectroscopy of iron oxides. In P. Somasundaran (Ed.), *Encyclopedia of surface and colloid science* (Vol. 239–240, pp. 1438–1446). Marcel Dekker. https://doi.org/10.1016/j.geoderma.2014.11.010

Torrent, J., & Barrón, V. (2003). The visible diffuse reflectance spectrum in relation to the color and crystal properties of hematite. *Clays and Clay Minerals*, *51*(3), 309–317. https://doi.org/10.1346/ccmn.2003.0510307

Torrent, J., & Barrón, V. (2008). Diffuse reflectance spectroscopy. In A. L. Ulery & R. Drees (Eds.), *Methods of soil analysis part 5: Mineralogical methods* (pp. 367–387). Soil Science Society of America.

Torrent, J., Barrón, V., & Liu, Q. S. (2006). Magnetic enhancement is linked to and precedes hematite formation in aerobic soil. *Geophysical Research Letters*, *33*, L02401. https://doi.org/10.1029/2005GL024818

Torrent, J., Guzman, R., & Parra, M. (1982). Influence of relative humidity on the crystallization of Fe (III) oxides from ferrihydrite. *Clays and Clay Minerals*, *30*(5), 337–340. https://doi.org/10.1346/CCMN.1982.0300503

Torrent, J., Liu, Q., & Barrón, V. (2010a). Magnetic minerals in Calcic Luvisols (Chromic) developed in a warm Mediterranean region of Spain: Origin and paleoenvironmental significance. *Geoderma*, *154*(3–4), 465–472. https://doi.org/10.1016/j.geoderma.2008.06.020

Torrent, J., Liu, Q., & Barrón, V. (2010b). Magnetic susceptibility changes in relation to pedogenesis in a Xeralf chronosequence in northwestern Spain. *European Journal of Soil Science*, *61*(2), 161–173. https://doi.org/10.1111/j.1365-2389.2009.01216.x

Torrent, J., Liu, Q., Bloemendal, J., & Barrón, V. (2007). Magnetic enhancement and iron oxides in the Upper Luochuan loess–paleosol sequence, Chinese Loess Plateau. *Soil Science Society of America Journal*, *71*(5), 1570–1578. https://doi.org/10.2136/sssaj2006.0328

Torrent, J., & Schwertmann, U. (1987). Influence of hematite on the color of red beds. *Journal of Sedimentary Research*, *57*(4), 682–686. https://doi.org/10.1306/212F8BD4-2B24-11D7-8648000102C1865D

Torrent, J., Schwertmann, U., Fechter, H., & Alferez, F. (1983). Quantitative relationships between soil color and hematite content. *Soil Science*, *136*(6), 354–358. https://doi.org/10.1097/00010694-198312000-00004

Torrent, J., Schwertmann, U., & Schulze, D. (1980). Iron oxide mineralogy of some soils of two river terrace sequences in Spain. *Geoderma*, *23*(3), 191–208. https://doi.org/10.1016/0016-7061(80)90002-6

Tronc, E., Chanéac, C., & Jolivet, J. (1998). Structural and magnetic characterization of ε-Fe$_2$O$_3$. *Journal of Solid State Chemistry*, *139*(1), 93–104. https://doi.org/10.1006/jssc.1998.7817

Tunstall, B. R., Martin, T., Walker, J., Gill, A., & Aston, A. (1976). *Soil temperatures induced by an experimental log pile fire: Preliminary data analysis*. CSIRO.

Umebayashi, H., Frazer, B., Shirane, G., & Daniels, W. (1966). Pressure dependence of the low-temperature magnetic transition in α-Fe$_2$O$_3$. *Physics Letters*, *22*(4), 407–408. https://doi.org/10.1016/0031-9163(66)91201-7

Urquhart, H. M., & Goldman, J. (1956). Magnetostrictive effects in an antiferromagnetic hematite crystal. *Physical Review*, *101*, 1443–1450. https://doi.org/10.1103/PhysRev.101.1443

Vandenberghe, R., Van San, E., De Grave, E., & da Costa, G. (2001). About the Morin transition in hematite in relation with particle size and aluminium substitution. *Czechoslovak Journal of Physics*, *51*(7), 663–675. https://doi.org/10.1023/A:1017697715646

Van der Voo, R., & Torsvik, T. H. (2012). The history of remagnetization of sedimentary rocks: Deceptions, developments and discoveries. *Geological Society, London, Special Publications*, *371*(1), 23–53. https://doi.org/10.1144/SP371.2

Van der Zee, C., Roberts, D. R., Rancourt, D. G., & Slomp, C. P. (2003). Nanogoethite is the dominant reactive oxyhydroxide phase in lake and marine sediments. *Geology*, *31*(11), 993–996. https://doi.org/10.1130/G19924.1

Van Houten, F. B. (1968). Iron oxides in red beds. *The Geological Society of America Bulletin*, *79*(4), 399–416. https://doi.org/10.1130/0016-7606(1968)79[399:IOIRB]2.0.CO;2

Van Houten, F. B. (1973). Origin of red beds: A review-1961-1972. *Annual Review of Earth and Planetary Sciences*, *1*, 39–61. https://doi.org/10.1146/annurev.ea.01.050173.000351

Van San, E. V., De Grave, E., Vandenberghe, R. E., Desseyn, H. O., Datas, L., Barrón, V., & Rousset, A. (2001). Study of Al-substituted hematites, prepared from thermal treatment of lepidocrocite. *Physics and Chemistry of Minerals*, *28*(7), 488–497. https://doi.org/10.1007/s002690100169

Varshney, D., & Yogi, A. (2011). Structural and electrical conductivity of Mn doped hematite (α-Fe_2O_3) phase. *Journal of Molecular Structure*, *995*(1), 157–162. https://doi.org/10.1016/j.molstruc.2011.04.011

Varshney, D., & Yogi, A. (2013). Influence of Cr and Mn substitution on the structural and spectroscopic properties of doped haematite: α-$Fe_{2-x}M_xO_3$ ($0.0 \leqslant x < 0.50$). *Journal of Molecular Structure*, *1052*, 105–111. https://doi.org/10.1016/j.molstruc.2013.08.052

Vaughan, R., & Drickamer, H. (1967). High-pressure Mössbauer studies on α-Fe_2O_3, $FeTiO_3$, and FaO. *The Journal of Chemical Physics*, *47*(4), 1530–1536. https://doi.org/10.1063/1.1712113

Vaughn, J., Kodama, K. P., & Smith, D. P. (2005). Correction of inclination shallowing and its tectonic implications: The Cretaceous Perforada Formation, Baja California. *Earth and Planetary Science Letters*, *232*(1–2), 71–82. https://doi.org/10.1016/j.epsl.2004.11.026

Wade, M. L., Agresti, D. G., Wdowiak, T. J., Armendarez, L. P., & Farmer, J. D. (1999). A Mössbauer investigation of iron-rich terrestrial hydrothermal vent systems: Lessons for Mars exploration. *Journal of Geophysical Research*, *104*(E4), 8489–8507. https://doi.org/10.1029/1998je900049

Walker, T. R. (1967a). Color of recent sediments in tropical Mexico: A contribution to the origin of red beds. *The Geological Society of America Bulletin*, *78*(7), 917–920. https://doi.org/10.1130/0016-7606(1967)78[917:CORSIT]2.0.CO;2

Walker, T. R. (1967b). Formation of red beds in modern and ancient deserts. *The Geological Society of America Bulletin*, *78*(3), 353–368. https://doi.org/10.1130/0016-7606(1967)78[353:forbim]2.0.co;2

Walker, T. R., Larson, E. E., & Hoblitt, R. P. (1981). Nature and origin of hematite in the Moenkopi Formation (Triassic), Colorado Plateau: A contribution to the origin of magnetism in red beds. *Journal of Geophysical Research*, *86*(B1), 317–333. https://doi.org/10.1029/JB086iB01p00317

Walter, D., Buxbaum, G., & Laqua, W. (2001). The mechanism of the thermal transformation from goethite to hematite. *Journal of Thermal Analysis and Calorimetry*, *63*(3), 733–748. https://doi.org/10.1023/a:1010187921227

Wang, C., Hu, X., Sarti, M., Scott, R. W., & Li, X. (2005). Upper Cretaceous oceanic red beds in southern Tibet: A major change from anoxic to oxic, deep-sea environments. *Cretaceous Research*, *26*(1), 21–32. https://doi.org/10.1016/j.cretres.2004.11.010

Wang, C., Huang, Y., Hu, X., & Li, X. (2004). Cretaceous oceanic red beds: Implications for paleoclimatology and paleoceanography. *Acta Geologica Sinica*, *78*(3), 873–877.

Watari, F., Delavignette, P., & Amelinckx, S. (1979). Electron microscopic study of dehydration transformations. II. The formation of "superstructures" on the dehydration of goethite and diaspore. *Journal of Solid State Chemistry*, *29*(3), 417–427. https://doi.org/10.1016/0022-4596(79)90198-1

Watari, F., Delavignette, P., Van Landuty, J., & Amelinckx, S. (1983). Electron microscopic study of dehydration transformations. Part III: High resolution observation of the reaction process $FeOOH \rightarrow Fe_2O_3$. *Journal of Solid State Chemistry*, *48*(1), 49–64. https://doi.org/10.1016/0022-4596(83)90058-0

Watari, F., Van Landuyt, J., Delavignette, P., & Amelinckx, S. (1979). Electron microscopic study of dehydration transformations. I. Twin formation and mosaic structure in hematite derived from goethite. *Journal of Solid State Chemistry*, *29*(1), 137–150. https://doi.org/10.1016/0022-4596(79)90218-4

Wayne, R., & Anderson, D. H. (1967). Pressure dependence of the Morin transition in the weak ferromagnet α-Fe_2O_3. *Physical Review*, *155*(2), 496–498. https://doi.org/10.1103/PhysRev.155.496

Weeks, R., Laj, C., Endignoux, L., Fuller, M., Roberts, A., Manganne, R., et al. (1993). Improvements in long-core measurement techniques: Applications in palaeomagnetism and palaeoceanography. *Geophysical Journal International*, *114*, 651–662. https://doi.org/10.1111/j.1365-246X.1993.tb06994.x

Wells, M., Fitzpatrick, R., Gilkes, R., & Dobson, J. (1999). Magnetic properties of metal-substituted haematite. *Geophysical Journal International*, *138*(2), 571–580. https://doi.org/10.1046/j.1365-246X.1999.00840.x

Wells, M., Gilkes, R., & Fitzpatrick, R. W. (2001). Properties and acid dissolution of metal-substituted hematites. *Clays and Clay Minerals*, *49*(1), 60–72. https://doi.org/10.1346/ccmn.2001.0490105

West, M. D., Clarke, J. D. A., Thomas, M., Pain, C. F., & Walter, M. R. (2010). The geology of Australian Mars analogue sites. *Planetary and Space Science*, *58*(4), 447–458. https://doi.org/10.1016/j.pss.2009.06.012

Westcott-Lewis, M. F. (1971). Grain size dependence of thermoremanence in ilmenite-haematites. *Earth and Planetary Science Letters*, *12*(1), 124–128. https://doi.org/10.1016/0012-821X(71)90063-X

Whidden, K. J., Lund, S. P., Bottjer, D. J., Champion, D., & Howell, D. G. (1998). Paleomagnetic evidence that the central block of Salinia (California) is not a far-traveled terrane. *Tectonics*, *17*, 329–343. https://doi.org/10.1029/97TC03021

Williams, H., Sherwood, R., & Remeika, J. (1958). Magnetic domains in α-Fe_2O_3. *Journal of Applied Physics*, *29*(12), 1772–1773. https://doi.org/10.1063/1.1723049

Wolska, E., & Schwertmann, U. (1989). Nonstoichiometric structures during dehydroxylation of goethite. *Zeitschrift für Kristallographie*, *189*(3–4), 223–237. https://doi.org/10.1524/zkri.1989.189.3-4.223

Woodland, A. B., Frost, D. J., Trots, D. M., Klimm, K., & Mezouar, M. (2012). In situ observation of the breakdown of magnetite (Fe_3O_4) to Fe_4O_5 and hematite at high pressures and temperatures. *American Mineralogist*, *97*(10), 1808–1811. https://doi.org/10.2138/am.2012.4270

Worlton, T., Bennion, R., & Brugger, R. (1967). Pressure dependence of the Morin transition in α-Fe_2O_3 to 26 kbar. *Physics Letters A*, *24*(12), 653–655. https://doi.org/10.1016/0375-9601(67)91009-2

Xiao, G. Q., Guo, Z. T., Dupont-Nivet, G., Lu, H. Y., Wu, N. Q., Ge, J. Y., et al. (2012). Evidence for northeastern Tibetan Plateau uplift between 25 and 20 Ma in the sedimentary archive of the Xining Basin, Northwestern China. *Earth and Planetary Science Letters*, *317–318*, 185–195. https://doi.org/10.1016/j.epsl.2011.11.008

Yamazaki, T., & Ioka, N. (1997). Environmental rock-magnetism of pelagic clay: Implications for Asian eolian input to the North Pacific since the Pliocene. *Paleoceanography*, *12*(1), 111–124. https://doi.org/10.1029/96PA02757

Yan, M., Van der Voo, R., Fang, X. M., Parés, J. M., & Rea, D. K. (2006). Paleomagnetic evidence for a mid-Miocene clockwise rotation of about 25° of the Guide Basin area in NE Tibet. *Earth and Planetary Science Letters*, *241*(1–2), 234–247. https://doi.org/10.1016/j.epsl.2005.10.013

Yan, M., Van der Voo, R., Tauxe, L., Fang, X., & Parés, J. M. (2005). Shallow bias in Neogene palaeomagnetic directions from the Guide Basin, NE Tibet, caused by inclination error. *Geophysical Journal International*, *163*(3), 944–948. https://doi.org/10.1111/j.1365-246x.2005.02802.x

Yang, T., Chen, J., Wang, H., & Jin, H. (2012). Magnetic properties of fault rocks from the Yingxiu–Beichuan fault: Constraints on temperature rise within the shallow slip zone during the 2008 Wenchuan earthquake and their implications. *Journal of Asian Earth Sciences*, *50*, 52–60. https://doi.org/10.1016/j.jseaes.2012.01.013

Yang, T., Chou, Y.-M., Ferré, E. C., Dekkers, M. J., Chen, J., Yeh, E.-C., & Tanikawa, W. (2020). Faulting processes unveiled by magnetic properties of fault rocks. *Reviews of Geophysics*, *58*(4), e2019RG000690. https://doi.org/10.1029/2019RG000690

Yang, T., Dekkers, M. J., & Zhang, B. (2016). Seismic heating signatures in the Japan Trench subduction plate-boundary fault zone: Evidence from a preliminary rock magnetic 'geothermometer'. *Geophysical Journal International*, *205*(1), 332–331. https://doi.org/10.1093/gji/ggw013

Yi, Z., Huang, B., Chen, J., Chen, L., & Wang, H. (2011). Paleomagnetism of early Paleogene marine sediments in southern Tibet, China: Implications to onset of the India–Asia collision and size of Greater India. *Earth and Planetary Science Letters*, *309*(1), 153–165. https://doi.org/10.1016/j.epsl.2011.07.001

Yogi, A., & Varshney, D. (2013). Magnetic and structural properties of pure and Cr-doped haematite: α-Fe$_{2-x}$Cr$_x$O$_3$ ($0 \leq x \leq 1$). *Journal of Advanced Ceramics*, *2*(4), 360–369. https://doi.org/10.1007/s40145-013-0084-7

Yoshida, H., Hasegawa, H., Katsuta, N., Maruyama, I., Sirono, S., Minami, M., et al. (2018). Fe-oxide concretions formed by interacting carbonate and acidic waters on Earth and Mars. *Science Advances*, *4*(12), eaau0872. https://doi.org/10.1126/sciadv.aau0872

Yoshikazu, I., & Yasuhiko, S. (1963). Order-disorder transformation and reverse thermo-remanent magnetism in the FeTiO$_3$-Fe$_2$O$_3$ system. *Journal of Physics and Chemistry of Solids*, *24*(4), 517–528. https://doi.org/10.1016/0022-3697(63)90147-1

Yuan, J., Yang, Z., Deng, C., Krijgsman, W., Hu, X., Li, S., et al. (2020). Rapid drift of the Tethyan Himalaya terrane before two-stage India-Asia collision. *National Science Review*, *8*, nwaa173. https://doi.org/10.1093/nsr/nwaa173

Zeese, R., Schwertmann, U., Tietz, G., & Jux, U. (1994). Mineralogy and stratigraphy of three deep lateritic profiles of the Jos Plateau (Central Nigeria). *Catena*, *21*(2), 195–214. https://doi.org/10.1016/0341-8162(94)90012-4

Zhang, C., Paterson, G. A., & Liu, Q. (2012). A new mechanism for the magnetic enhancement of hematite during heating: The role of clay minerals. *Studia Geophysica et Geodaetica*, *56*, 845–860. https://doi.org/10.1007/s11200-011-9018-4

Zhang, Q., Liu, Q., Li, J., & Sun, Y. (2018). An integrated study of the eolian dust in pelagic sediments from the North Pacific Ocean based on environmental magnetism, transmission electron microscopy, and diffuse reflectance spectroscopy. *Journal of Geophysical Research: Solid Earth*, *123*(B5), 3358–3376. https://doi.org/10.1002/2017JB014951

Zhang, W., Fang, X., Zhang, T., Song, C., & Yan, M. (2020). Eocene rotation of the Northeastern Central Tibetan Plateau indicating stepwise compressions and eastward extrusions. *Geophysical Research Letters*, *47*(17), e2020GL088989. https://doi.org/10.1029/2020GL088989

Zhang, W.-J., Huo, C.-F., Feng, G., Li, Y.-W., Wang, J., & Jiao, H. (2010). Dehydration of goethite to hematite from molecular dynamics simulation. *Journal of Molecular Structure*, *950*(1–3), 20–26. https://doi.org/10.1016/j.theochem.2010.03.013

Zhang, Y. C., Tang, J. Y., & Hu, X. Y. (2008). Controllable synthesis and magnetic properties of pure hematite and maghemite nanocrystals from a molecular precursor. *Journal of Alloys and Compounds*, *462*(1), 24–28. https://doi.org/10.1016/j.jallcom.2007.07.115

Zhang, Y. G., Ji, J., Balsam, W. L., Liu, L., & Chen, J. (2007). High resolution hematite and goethite records from ODP 1143, South China Sea: Co-evolution of monsoonal precipitation and El Niño over the past 600,000 years. *Earth and Planetary Science Letters*, *264*(1–2), 136–150. https://doi.org/10.1016/j.epsl.2007.09.022

Zhu, W., Cui, X., Wang, L., Liu, T., & Zhang, Q. (2011). Monodisperse porous pod-like hematite: Hydrothermal formation, optical absorbance, and magnetic properties. *Materials Letters*, *65*(6), 1003–1006. https://doi.org/10.1016/j.matlet.2010.12.053

Zolotov, M. Y., & Shock, E. L. (2005). Formation of jarosite-bearing deposits through aqueous oxidation of pyrite at Meridiani Planum, Mars. *Geophysical Research Letters*, *32*(21), L21203. https://doi.org/10.1029/2005GL024253

Zysler, R. D., Fiorani, D., Testa, A. M., Suber, L., Agostinelli, E., & Godinho, M. (2003). Size dependence of the spin-flop transition in hematite nanoparticles. *Physical Review B*, *68*(21), 212408. https://doi.org/10.1103/PhysRevB.68.212408